OPTIMAL VIBRATION SUPPRESSION OF BEAM-TYPE STRUCTURES USING PASSIVE AND SEMI-ACTIVE TUNED MASS DAMPERS

Fan Yang

A Thesis

In the Department

of

Mechanical and Industrial Engineering

Presented in Partial Fulfillment of the Requirements

For the Degree of Doctor of Philosophy at

Concordia University

Montreal, Quebec, Canada

September 2008

Your file Votre référence
ISBN: 978-0-494-45683-5
Our file Notre référence
ISBN: 978-0-494-45683-5

ABSTRACT

Optimal Vibration Suppression of Beam-Type Structures using Passive and Semi-Active Tuned Mass Dampers

Fan Yang, Ph.D.
Concordia University, 2008

The overall aim of this dissertation is to conduct a comprehensive investigation on the design optimization for passive and semi-active vibration suppression of beam-type structures utilizing the Tuned Mass Damper (TMD) and Semi-Active Mass Damper (SAMD) to prevent discomfort, damage or outright structural failure through dissipating the vibratory energy effectively.

The finite element model for general curved beams with variable curvatures under different assumptions (including/excluding the effects of the axial extensibility, shear deformation and rotary inertia) are developed and then utilized to solve the governing differential equations of motion for beam-type structures with the attached TMD system. The developed equations of motion in finite element form are then solved through the random vibration state-space analysis method to effectively find the variance of response under stationary random loading.

A hybrid optimization methodology, which combines the global optimization method based on Genetic Algorithm (GA) and the powerful local optimization method based on Sequential Quadratic Programming (SQP), is developed and then utilized to find the optimal design parameters (damping, stiffness and position) of the attached single and multiple TMD systems. Based on the extensive numerical investigation, a design

framework for vibration suppression of beam-type structures using TMD technology is then presented.

An in-house experimental set-up is designed to demonstrate the effectiveness of the developed optimal design approach for vibration suppression of beam-type structures using TMD technology.

Next, the Magneto-Rheological (MR) fluid damper is utilized to design the SAMD system. A new hysteresis model based on the LuGre friction model is developed to analyze the dynamic behavior of large-scale MR-damper (MR-9000 type) accurately and efficiently. The gradient based optimization technique and least square estimation method have been utilized to identify the characteristic parameters of MR-damper. Moreover, based on the developed hysteresis model, an effective inverse MR-damper model has also been proposed, which can be readily used in the design of semi-active vibration suppression devices.

The controller for SAMD system using MR-damper is designed based on the proposed inverse MR-damper model and H_2/LQG controller design methodology. The developed SAMD system along with the MR-damper model is then implemented to beam-type structures to suppress the vibration. It has been shown that the designed SAMD system using MR-damper can effectively suppress the vibration in a robust and fail-safe manner.

ACKNOWLEDGEMENTS

I would like to take this opportunity to express my deep sense of gratitude and profound feeling of admiration to my thesis supervisors, Dr. Ramin Sedaghati and Dr. Ebrahim Esmailzadeh. Advises I received from my supervisors concerning the scope and direction of this dissertation have been invaluable. The faculty members of Mechanical and Industrial Engineering Department in Concordia University, in particular, my committee members also deserve my sincere thanks.

I owe the biggest debt of gratitude to my family, without their understanding, love and support I would not be here.

TABLE OF CONTENTS

NOMENCLATURE

Symbols	Nomenclature
$A(s)/A(x)$	Beam cross-sectional area along the central line of beam
C	Beam structural damping
C_{TMD}	Linear viscous damping of the attached Tuned Mass Damper
$[C]$	Damping matrix
E	Elastic modulus
$\{F\}$	External force vector
G	Shear modulus
$[G]$	Controller
$I(s)/I(x)$	Beam cross-sectional area moment along the central line of beam
$J(s)/J(x)$	Beam cross-sectional mass moment along the central line of beam
$\bar{J}$	Jacobian for straight beam
$\bar{J}_c$	Jacobian for curved beam
K_{TMD}	Stiffness of the attached Tuned Mass Damper
$[K]$	Stiffness matrix
L	Beam's span length
$[M]$	Mass matrix
R	Circular beam's radius
S	Curved beam's curvilinear coordinate
T	Dimensionless transfer matrix
$\{U\}$	Curved beam's tangential direction response nodal vector
$\{W\}$	Beam's transverse response nodal vector
X, Y	Cartesian coordinate
f_{TMD}	Frequency ratio of the attached Tuned Mass Damper
$\{f\}$	Control force
h	Rise of Curved beam
k_q	Timoshenko beam's shear coefficient
l	Beam' length (curvilinear length)
s	Along curved beam's curvilinear coordinate (S)
$u(t)$	Curved beam's tangential direction displacement
v	Poisson's ratio
v_n	Measured noise
$w(t)$	Beam's transverse displacement

x	Along Cartesian coordinate X direction
$\{z\}$	State-space vector
Ω	Dimensionless frequency
Φ	Curved beam's span angle
ψ	Beam's rotation deformation due to bending
β	Beam's rotation deformation due to shear
γ	Material volumetric density
ξ_{TMD}	Damping factor of the attached Tuned Mass Damper
η	Natural coordinate [-1, 1]
η_{TMD}	Position of the attached Tuned Mass Damper in natural coordinate
ω	Natural frequency
λ	Eigenvalue
$\rho(s)$	Radius of curved beam
μ	Mass ratio of the attached Tuned Mass Damper

Math symbols	**Nomenclature**
[ ]	Matrix
{ }	Vector

Acronyms	**Nomenclature**
AMD	Active Mass Damper
ATMD	Active Tuned Mass Damper
AVS	Active Variable Stiffness
BFGS	Broyden Fletcher Goldfarb Shanno
COG	Mean Center of Gravity
DMF	Dynamic Magnification Factors
DOF	Degree of Freedom
DQM	Differential Quadrate Method
DTMD	Distributed Tuned Mass Damper
DVA	Dynamic Vibration Absorber
GA	Genetic Algorithm
H_2	H_2 controller design
H_2/LQG	H_2/LQG controller design
IIE	Interdependent Interpolation Element

LFT	Linear Fractional Transformation
LQR	Linear Quadratic Regulator
LQG	Linear Quadratic Gaussian
MDOF	Multi-Degree-of-Freedom
MR-damper	Magneto-Rheological fluid damper
MTMD	Multiple Tuned Mass Damper
PSD	Power Spectral Density
RMS	Root Mean Square
SAIVS	Semi-Active Independently Variable Stiffness
SAMD	Semi-Active Mass Damper
SDOF	Single-Degree-of-Freedom
SQP	Sequent Quadratic Programming
TLD	Tuned Liquid Damper
TLCD	Tuned Liquid Column Damper
TMD	Tuned Mass Damper
VSD	Variable Stiffness Device

Graphic symbols	**Nomenclature**
	Linear spring
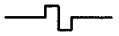	Linear viscous damper

LIST OF FIGURES

LIST OF TABLES

CHAPTER 1

INTRODUCTION AND LITERATURE REVIEW

1.1 Motivation

Beam-type structures have many applications in mechanical, aerospace and civil engineering fields. Due to their inherent low damping and recent trend for light weight design, these structures may easily vibrate in their low modes, which may subsequently lead to failure of structure[1]. Thus, one of the biggest challenges structural engineers face today is to protect structures from the damaging effects due to excessive vibrations.

One of the commonly adopted structural protecting devices is based on the Tuned Mass Damper (TMD) technology, which dissipates vibratory energy through a set of damper and spring connecting a small mass to the main structure. The natural frequency of this secondary structure is usually tuned to the dominant mode of the primary structure. Due to mechanical simplicity and low cost, TMD devices are effectively used for vibration suppression in many civil and mechanical engineering applications. A successful optimal TMD system design for beam-type structures requires not only a robust optimization approach, but also a reliable mathematical model to model beam-type structures and their combination with the TMD system.

As the stiffness and damping of an optimally designed TMD system are typically invariant, to improve the vibration suppression effectiveness of the TMD system, the

Active Mass Damper (AMD) or Semi-Active Mass Damper (SAMD) systems, in which a controllable device can be added to or replace the damper in TMD system, are developed. Magneto-Rheological (MR) fluid dampers are one of the most promising devices to provide controllable damping force. They offer large range damping force capacity with very low power consumption, highly reliable operation and robustness in a fail-safe manner.

Based on the above introduction, the main purpose of this dissertation is to present a comprehensive investigation on beam-type structures' vibration suppression using TMD, SAMD and MR-damper technologies.

1.2 Literature Review of the Pertinent Works

In the following sections, a brief introduction and relevant literature review of different aspects of the present subject are provided in a systematic way.

1.2.1 Finite element analysis for beam-type structures

The slim straight beam-type structures can be modeled as Euler-Bernoulli beam, and its equations of motion in the finite element form can be obtained utilizing the Hermitian interpolation[2, 3], which can be found in most finite element methods[3] and vibration theory[4] textbooks. For beams in which the effect of the cross-sectional dimension on frequencies cannot be neglected, and the study of higher modes are required (for instance for the case of random type loading), the Timoshenko theory which considers the effects of rotary inertia and shear deformation provides a better approximation to the true behavior of the beam.

The governing differential equations of motion for Timoshenko beam can be found in many vibration textbooks[4]. Most of works about solving Timoshenko beam using finite element method were published in the 70s[5-8] and the related interpolation methodology are available in commercial finite element method software packages, such as the Beam188/189 elements from Ansys®[9], in which the transverse displacement and rotation due to bending are assumed to be independent variables. Recently, Reddy[10] and Mukherjee *et al*[11] proposed a set of new shape functions, which were named as Interdependent Interpolation Element (IIE)[10], to study Timoshenko beam. As the interpolation methodology utilized by Ansys®[9] for the Beam188/189 elements is widely accepted by most of researchers, in this dissertation it will also be utilized to model the Timoshenko beam.

The study of the free in-plane vibration of a curved beam using the beam theory is more complicated than that of a straight beam, since the structural deformations in a curved beam depend on not only the rotation and radial displacement but also the coupled tangential displacement caused by the curvature of the structure. Many theories have been evolved to derive, simplify and solve the equations of motion for the free in-plane vibration of the curved beam. Henrych[12] utilized the first order equilibrium conditions for the external and internal forces to derive the general expression of the differential equations of motion for the curved (circular) beam and then provided sets of methodologies to solve the differential equations of motion based on different assumptions, considering and/or neglecting the shear deformation, rotary inertia and axial extensibility.

It should be noted that the solution of the differential equations of motion for curved (circular) beams are very complicated, if one takes into account the effects of shear deformation, rotary inertia and axial extensibility. Therefore, most of works in this area are to simplify the curved beam model based on different deformational assumptions. Auciello and Rosa[13] modeled the curved (circular) beam neglecting the shear deformation, rotary inertia and axial extensibility, and then summarized the results obtained through different numerical methodologies, which were available in published literatures, such as the Rayleigh-Ritz methodology by Laura *et al*[14], the Rayleigh-Schmidt methodology by Schmidt[15] and Bert[16] and the cell discretization method by Raithel and Franciosi[17]. Tong *et al*[18] modeled the curved (circular) beam using the same assumption as those adopted by Auciello and Rosa[13], and further simplified the tapered arch as sets of stepped arches. Veletsos *et al*[19] and Lee and Hsiao[20] modeled the curved (circular) beam neglecting the shear deformation and rotary inertia. Chidamparam and Leissa[21] studied the influence of axial extensibility for curved (circular) beams. The results[21] show that the axial extensibility causes a decrease in the natural frequencies, and it is significant for shallow arches. Thus, the model neglecting the axial extensibility, which has been adopted by many researchers in studying the vibration problem for circular beams, may not be accurate especially when the high vibration modes study is required, such as in random vibration analysis.

Henrych[12] has modeled the curved (circular) beam considering the shear deformation, rotary inertia and axial extensibility, and then provided a general approach to solve the related differential equations of motion. However, the approach presented by Henrych[12]

is quite complicated. In fact many methodologies, which are available in published literatures, have been successfully presented to solve the circular beam model. Austin and Veletsos[22] improved their study[19] and developed an approximation and simplified procedure to estimate the natural frequencies of circular arches. Irie *et al*[23] utilized the transfer matrix methodology to solve the curved beam, in which the central lines were modeled as different types of function. Issa *et al*[24] derived the general dynamic stiffness matrix for a uniform curved (circular) beam. Kang *et al*[25] utilized the Differential Quadrate Method (DQM) to compute the eigenvalues of the differential equations of motion governing the uniform curved (circular) beams. Tseng *et al*[26] adopted the Frobenius method[27] to solve the problem. Yildirim[28] utilized the transfer matrix method and then solved the problem based on the Cayley-Hamilton theorem[29]. The same method has also been adopted by Tüfekçí and Arpaci[30] and Tüfekçí and Ozdemirci[31]. Rubin and Tüfekçí[32] adopted the Cosserat point methodology, which was proposed by Rubin[33, 34], to extend the study to three-dimension problem. The natural frequencies for the elliptical, parabolic and sinusoidal arches can also be found in Oh *et al*[35].

There are still many papers in this area (curved (circular) beams' vibration problem, considering the shear deformation, rotary inertia and axial extensibility), in which their main differences are in the methodologies adopted to solve the governing differential equations of motion. However one assumption, which is commonly adopted in previous works, is to separate the radial and tangential displacements and the rotation variables, and then assume those variables as independent[12, 22-28, 30-35]. Although the methodologies

adopted in these literatures[22-28, 30-35] are simpler than those provided by Henrych[12], they are still too complicated to be utilized in engineering design optimization problem.

The earliest works about utilizing finite element method to solve the curved (circular) beams problem can be found in the 70's. In 1971 Petyr and Fleischer[36] utilized three kinds of interpolation functions and then proposed three two-node curved (circular) arch elements, in which two of them have three degree-of-freedom per node and the other one has four degree-of-freedom per node. In 1972 Davis *et al*[37] proposed the other two-node curved (circular) arch element with three degree-of-freedom per node. In 1974 Dawe[38] presented different kinds of two-node curved (circular) beam elements based on the polynomial interpolation with different definitions of the nodal degree of freedom. Balasubramanian and Prathap[39] utilized a three-order polynomial function to interpolate the radial and tangential displacements and rotation variables separately and finally developed a two-node curved (circular) beam element with six degree-of-freedom per node. Recently, Friedman and Kosmatka[40] utilized a set of interpolation function to describe the radial and tangential displacements and the rotation variables separately, and then derived a two-node curved (circular) beam element with three degree-of-freedom per node. Through comparison, one can easily find that the interpolation function utilized by Friedman and Kosmatka[40] is similar to that adopted by Davis *et al*[37] to interpolate the tangential direction displacement. Raveendranath *et al*[41] proposed three kinds of two-node curved (circular) beam elements, which are similar to those presented by Petyr and Fleischer[36] and Dawe[38]. Litewka and Rakowski[42] also utilized the similar methodology as those adopted by Friedman and Kosmatka[40]. Eisenberger and Efraim[43] again utilized the

polynomial function to interpolate the radial and tangential displacements and the rotation variable separately. Wu and Chiang[44] utilized the similar interpolation methodology as Davis *et al*[37] to study the curved (circular) beam problem. Ribeiro[45] studied the curved (circular) beam based on the *p*-version (high order) finite element method. ÖztÜrk *et al*[46] utilized the similar interpolation function as Dawe[38] to study the non-uniform circular beam.

Based on the above analysis, it can be found that: (1) most of works related to the curved (circular) beam using finite element method are based on the papers published by Petyr and Fleischer[36], Davis *et al*[37] and Dawe[38]; (2) the basic methodology is to interpolate the radial and tangential direction displacement variables (some papers adding the rotation variable) with a set of selected admissible functions, and then transfer the interpolation to be expressed as the nodal degrees of freedom to obtain a two-node element; (3) all papers are based on the circular type beam, in which the radius of curvature is constant and thus the problem can be simplified by interchanging the curvilinear coordinates with the arch angle. In 2008, Zhu and Meguid[47] extended the study to three-dimension case (an in-plane and out-plane vibration problem). Although they mentioned that the methodology can be utilized to study the curved beam with different curvatures, the provided numerical examples are all based on the circular beam-type structures.

In the present work, sets of curved beam elements, which can be utilized to investigate the curved beam-type structure with changing curvatures, will be presented and evaluated numerically based on the curvilinear integral along the central line of curve beam-type structures. The results perfectly agree with those available in published literatures. The

developed finite element method is then utilized in the optimal design of beam-type structures with the attached TMD system.

1.2.2 Tuned mass damper technology

One commonly adopted damping technology is to install damper between the structures and their related install bases, such as the passive base isolation system. Generally big size damping devices are required for this technology. The other type of damping method is based on the TMD technology, which dissipates vibratory energy through a set of damper and spring connecting a small mass to the main structure, as illustrated in Figure 1.1(a).

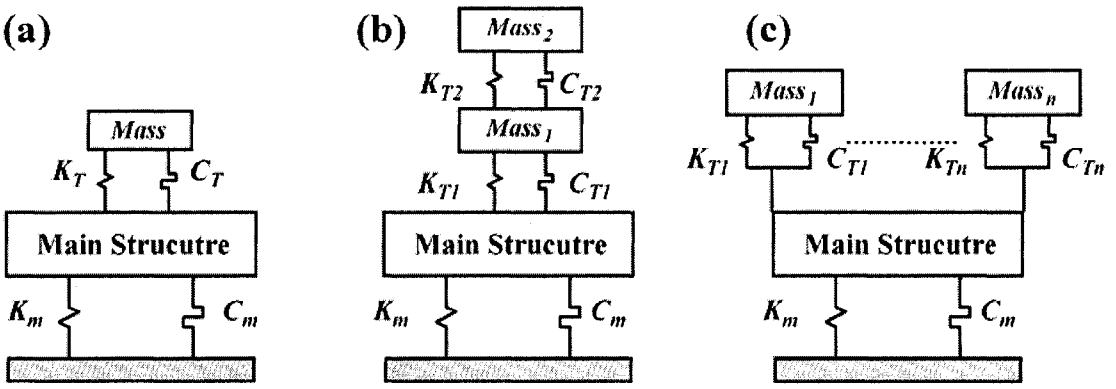

Figure 1.1 Typical TMD system and its modifications. (a) TMD system. (b) Composite Tuned Mass Damper system. (c) Distributed Tuned Mass Damper system (DTMD).

The TMD technology is developed based on the Tuned Mass system proposed by Frahm[48], in which a secondary system composed of a mass and a spring is implemented to a primary structure and its natural frequency is tuned to be very close to the dominant mode of the primary structure. Thus, a large reduction in the dynamic responses of the primary structure around the natural frequency of the dominant mode can be achieved.

However the combined system adds two resonant frequencies, one before the frequency of the primary system's dominant mode, and the other after that. The TMD system is to add a damper in the Tuned Mass system to suppress the vibration in these two added resonant frequencies. Here, it should be noted that in some papers and textbooks, the TMD system was also named as vibration absorber or Dynamic Vibration Absorber (DVA)[49].

Although the basic design concept of a TMD system is quite simple, its parameters (mass, damping and stiffness) must be determined through an optimal design procedure to attain the best vibration suppression performance. Therefore, the major task is to obtain the optimal design parameters of the TMD system to enhance the vibration suppression effectiveness. Since Den Hartog[49] first proposed an optimal design approach of TMD for an un-damped Single-Degree-of-Freedom (SDOF) structure, many optimal design methods of TMD system have been developed to suppress the structural vibration induced by various types of excitation sources. Crandall and Mark[50] adopted the random vibration theory to analyze a SDOF structure attached with a single TMD system under white noise base excitation. The results demonstrated that the TMD system can effectively reduce the vibration of the base-excited structure. Warburton[51, 52] studied SDOF system vibration suppression using TMD under different loading conditions. The topic for vibration suppression of a SDOF system using the attached optimal TMD system is not novel, and its optimal parameters for different loading conditions has been widely accepted and also can be found in many textbooks[49, 53] in structural vibration area. Therefore, just some typical literatures published recently would be presented here. Kwok and Samali[54] studied a SDOF system's vibration suppression problem using TMD

system under wind loading. Rana and Soong[55] summarized some optimal TMD system's results published before. Rüdinger[56] studied the relationship between the structural damper and the optimal TMD system.

The discrete Multi-Degree-of-Freedom (MDOF) system's vibration suppression using the optimal TMD system can also be found in many research works[52, 55]. As the modeling procedures and the adopted optimization methodologies are similar to those for SDOF system, here only some typical papers published recently will be presented. Hadi and Arfiadi[57] studied a discrete MDOF system, which represented a typical building structure, with the attached TMD system at the top floor, and selected the H_2 norm of the transfer function as the objective function for an optimization procedure, and then utilized the Genetic Algorithm (GA) optimization methodology to obtain the solution. Hwang *et al*[58] investigated the SDOF and discrete MDOF structures with the attached TMD system. Lee *et al*[59] studied the discrete MDOF structure with the attached single or multiple TMD system and utilized a gradient based optimization methodology. Marano *et al*[60] studied a MDOF structure with the attached single TMD system utilizing a constrained reliability-based optimization method.

There are two modified TMD design methodologies that can be found in published literatures, as illustrated in Figures 1.1(b) and 1.1(c). Based on the introduction presented by Nishimura *et al*[61], the modified TMD design illustrated in Figure 1.1(b) was named as Composite Tuned Mass Damper and invented by Yamada in 1998 (Japan Patent Bureau, S63-156171). Unfortunately we cannot find the original report about this patent. Lewandowski and Grzymislawska[62] investigated the performance of the Composite

Tuned Mass Damper system and added one controllable damper on the second TMD. Li and Zhu[63] studied Composite Tuned Mass Damper system utilizing the Dynamic Magnification Factors (DMF), which represents the magnitude of the structural response.

The other type of modified TMD design shown in Figure 11(c) was developed by Xu and Igusa[64, 65] and named as multiple Tuned Mass Dampers. In this dissertation, to distinguish it with the multiple Tuned Mass Damper design based on multiple natural frequencies of the main structure, the multiple Tuned Mass Damper design based on one special natural frequency, as illustrated in Figure 1.1(c), was named as Distributed Tuned Mass Damper (DTMD). As the modeling procedure for this kind of problem is simple, the main differences in this area are the adopted optimization methodologies, especially the selected (generated) objective function. Basically, two typical approaches have been utilized to solve this problem. The first one is to directly obtain the transfer function and then define the variance or the Dynamic Magnification Factors (DMF) as objective functions, which was utilized by most of researchers such as Xu and Igusa[64, 65], Kareem and Kline[66], Joshi and Jangid[67], Li[68], Li and Qu[69], Li and Ni[70] and Febbo and Vera[71]. The other methodology was developed by Zuo and Nayfeh[72-74], in which the transfer function was expressed as a dynamic model with an optimal H_2 controller. Although the vibration suppression performance for a DTMD system is better than the TMD system, one can improve the performance of the TMD system through adding one active or semi-active device with suitably designed controller, which can provide the same or better effectiveness and is more practical in real application than the DTMD system.

Previous introduction are mainly related to attaching single TMD or its modifications onto a structure modeled as SDOF or discrete MDOF systems. As the equations of motion for a SDOF or discrete MDOF structures with the attached TMD system is simple and the location of the attached TMD is usually obvious, the main differences in previous works[49-74] are typically the adopted optimization methodologies. For continuous systems, such as uniform beams, the optimal TMD design problem is more complicated than that for the SDOF or discrete MDOF structure, as the related mathematical model is not easy to be obtained and the design variables include not only the damping and the stiffness of the attached TMD system, but also the locations and number of the attached TMD system.

The earlier work about beam-type structures with the attached TMD system can be found by Jacquot[75] in 1978, in which a cantilever beam was modeled as Euler-Bernoulli beam and a single TMD was attached to the mid-span of the beam. Manikanahally and Crocker[76] studied a mass-load beam's vibration suppression with TMD. Recently, Gu *et al*[77] designed an optimal DTMD system based on the first vibration mode of the beam structure. You and Yang[78, 79] investigated the optimal DTMD system for different bridge structures. Kwon and Park[80] studied the same example as You and Yang[78, 79] and utilized the Genetic Algorithm (GA) optimization methodology to obtain the solution. Chen *et al*[81, 82] adopted the Timoshenko beam theory to model the bridge and design a set of TMD distributed symmetrically along the beam length to suppress the vibration related to the first vibration mode. Esmailzadeh and Jalili[83] and Younesian *et al* [84] studied the Timoshenko beam with the attached TMD system under different loading conditions.

Wu[85] analyzed the natural frequencies of a cantilever beam with the attached TMD system.

The basic methodology adopted in these literatures[75-82, 84, 85] is to typically simplify the equations of motion to a SDOF system based on the fundamental modal shape of the continuous system. However, this methodology has some restrictions as: (1) the fundamental modal shape of the continuous system will change with different boundary condition, thus one should repeat the whole procedure for different boundary conditions; (2) it is difficult to obtain the fundamental modal shape for the non-uniform structure and also the curved beam structure; (3) before utilizing the fundamental modal shape to decouple the differential equations of motion, the position of the attached TMD should be given, thus it is difficult to identify the position of the attached TMD as one of the design variables in an optimization procedure. The finite element method appears to be particularly promising in addressing those restrictions, which is one of the main topics of this dissertation.

1.2.3 Design optimization of the tuned mass damper system

As mentioned above, the basic design concept of a TMD system is quite simple, its parameters (mass, damping and stiffness) must be determined through an optimal design procedure to attain the best vibration suppression performance. Moreover, for beam-type structures one should also take into account the optimal position and number of the attached TMD system. Therefore, after establishing a reliable dynamic model for structures with the attached TMD system, the next essential part is the optimization.

Selecting a suitable objective function with design boundary is the most important issue for an optimization problem. Here, the classical TMD system design illustrated in Figure 1.1(a) will be utilized to introduce the objective function for the optimal TMD design. For random type loading, the objective function can be selected as the variance[52, 56, 61] or norm of the transfer function (H_2 norm)[57, 59], and then one can utilized some available command provided by MATLAB®[86] or function[87] to obtain the value of the objective function. These kinds of definitions are very clear.

However, there is not a criterion in average sense for harmonic type loading. Den Hartog[49] proposed a methodology to solve this problem, which was popularly accepted by researchers. As this is the first document related to the optimization methodology for the TMD system and the only available methodology to identify the optimal TMD design based on harmonic loading, a short discussion of the methodology adopted by Den Hartog[49] would be presented. As the design variables of a TMD system includes the damping and stiffness under a known input mass, in the first step Den Hartog[49] separated these two design variables. Let us recall a SDOF structure subjected to harmonic type base excitation, as illustrated in Figure 1.2(a). The related magnitude of the transfer function can be expressed as[49, 53]:

$$\left|\frac{X}{Y}\right| = \sqrt{\frac{K^2 + (C\omega)^2}{(K - M\omega^2)^2 + (C\omega)^2}} \tag{1.1}$$

This type of transfer function has an important property, which is the value of the magnitude is independent to the damping when excitation frequency equal to $\sqrt{2K/M}$.

The similar property can be found for the TMD system, as illustrated in Figure 1.2(b), in which the magnitude of transfer function can be expressed as[49]:

$$\left|\frac{X}{F_0}\right| = \sqrt{\frac{(k-m\omega^2)^2+(c\omega)^2}{[(K-M\omega^2)(k-m\omega^2)-mk\omega^2]^2+(c\omega)^2(K-M\omega^2-m\omega^2)^2}} \tag{1.2}$$

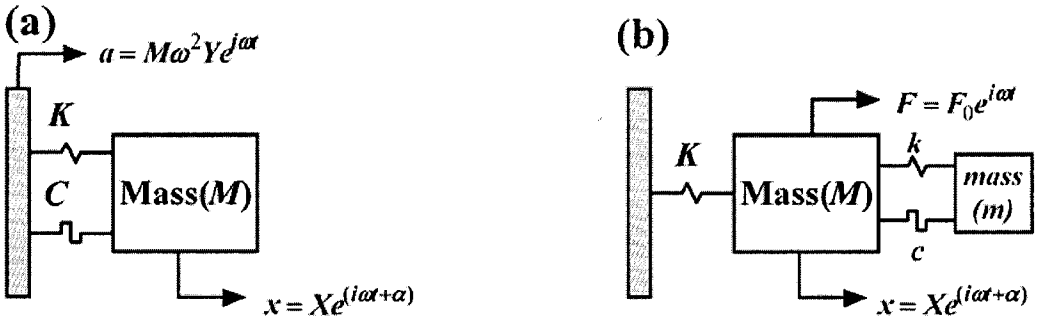

Figure 1.2 Typical SDOF system and SDOF system with the attached TMD system subjected to harmonic loading. (a) SDOF system. (b) SDOF system with the attached TMD system.

Den Hartog[49] utilized the properties of the transfer function stated in Equation (1.2), in which the magnitude is independent of damping (c) at two frequency values (ω_1 and ω_2) under given M, K, m and k, to separate the design variables (k and c). The second step adopted by Den Hartog[49] was to tune the magnitudes at these two special excitation frequencies (ω_1 and ω_2) are identical through suitably selected stiffness (k). The last step is to make the magnitude at these two special excitation frequencies (ω_1 and ω_2) to be the maximum value in the whole frequency domain response through an optimally designed damping (c). In fact, the methodology adopted by Den Hartog[49] is equal to minimize the maximum magnitude under the entire frequency range, which is also utilized in the

Distributed Tuned Mass Damper (DTMD) design based on Dynamic Magnification Factors (DMF).

Here it should be noted that one can also select the response of velocity or acceleration as objective[52] and the values of optimal damping (c) and stiffness (k) have slight difference from those utilized the displacement as objective under harmonic or random loading. As the adopted methodologies are exactly the same as those for displacement, in this dissertation the displacement will be utilized as the objective for an optimization procedure.

Optimization methodology is another important issue for an optimal design problem. Generally, the optimization methodologies adopted in the optimally designed TMD system can be classified into three main categories: (1) the analytical methodology[49]; (2) the gradient based optimization; (3) the global optimization methodologies, such as Genetic Algorithm (GA)[57] and Simulated Annealing(SA)[71]. Here, the gradient based optimization methodology plays an important role in the TMD design area. The simplest one can be seen in Den Hartog[49], in which the optimal damping (c) was obtained directly utilizing the first order (gradient function) and second order (Hessian matrix) criterion, which can be identified as the Karush-Kuhn-Tucker (KKT) conditions without constraint. Here, it should be noted that most gradient based optimization methodologies presented in published papers in the TMD area can be found in most optimization textbooks[88, 89], such as Lee *et al*[59], Li *et al*[70] and Zuo and Nayfeh[73] utilized the Steepest Decent Algorithm method. As the Sequential Quadratic Programming (SQP) is the most recently

developed and perhaps one of the best and most powerful methods of optimization[89], recently some researchers[84] utilized this method to obtain the optimal TMD design.

In present work, the SQP optimization technology will be utilized to find the optimal design variables (damping and stiffness) for an optimal TMD system. Then, a hybrid optimization methodology will be developed to obtain not only the optimal damping and stiffness, but also the optimal location of the attached TMD system in beam-type structures.

1.2.4 Active and semi-active mass dampers

The so-called Active Mass Damper (AMD) or Semi-Active Mass Damper (SAMD) system is developed to improve the vibration suppression performance of the optimal TMD system. Here, it should be mentioned that some researchers also called AMD as active TMD (ATMD). Nishimura *et al*[61, 90] developed the basic ATMD design method, and assumed the control force generated through a simple constant acceleration feedback gain. Chang and Yang[91] also studied ATMD design and utilized the constant displacement and velocity feedback gain to represent the control force. Both studies did not take into account the active device's dynamic properties.

The AMD system can provide good vibration suppression effectiveness[61, 90, 91], however there is a serious challenge regarding the device that can provide required control force, which should be considered before AMD can be used practically. Dyke *et al*[92] also summarized some other challenges such as the system reliability and robustness, reduction of capital cost and maintenance, eliminating reliance on external power and

gaining acceptance of nontraditional technology. On the other hand, the SAMD system provides controllable energy dissipation rate utilizing the controlled damper which does not induce energy to the controlled structure. Thus, it appears to be particularly promising in addressing those challenges.

Different kinds of semi-active devices have been investigated for the SAMD system design, such as variable orifice hydraulic actuator[93-97], Active Variable Stiffness (AVS)[98-103], Tuned Liquid Column Damper (TLCD)[104-112], Electro-Rheological (ER) fluid damper[113-117] and Magneto-Rheological (MR) fluid damper. In the following, the commonly adopted semi-active devices mentioned above will be briefly reviewed.

1.2.4.1 Variable Orifice Hydraulic Actuator

The operating principle for variable orifice hydraulic actuator is very simple, which is to change the energy dissipation rate through adjusting the orifice of the hydraulic actuator. This kind of device has been widely used in many areas, such as the commercial airplane's landing gear system[93]. Dyke[94] and Spencer Jr *et al*[95] and Zhuang[96] and Zhuang *et al*[97] utilized a hydraulic actuator as an semi-active device in the SAMD system, and combined the hydraulic actuator's dynamic properties with the structural dynamic equations to design a controller through adjusting the orifice of the hydraulic actuator to change the energy dissipation rate.

1.2.4.2 Active Variable Stiffness

The operating principle for Active Variable Stiffness (AVS) is to produce a non-stationary, non-resonant condition during severe external excitation through altering the

structural stiffness based on the nature of the excitation[98], which has been successfully utilized in building structure[98]. The Variable Stiffness Device (VSD) is the active (semi-active) device for an AVS system. Leavitt *et al*[99] proposed a VSD design. Renzi and De Angelis[100] studied the dynamic response of structure with AVS system. Nagarajaiah[101] proposed a Semi-Active Variable Stiffness (SAVIS), as illustrated in Figure 1.3, in which the stiffness (K) between points A and B can be adjusted through the relative displacement between points p_1 and p_2.

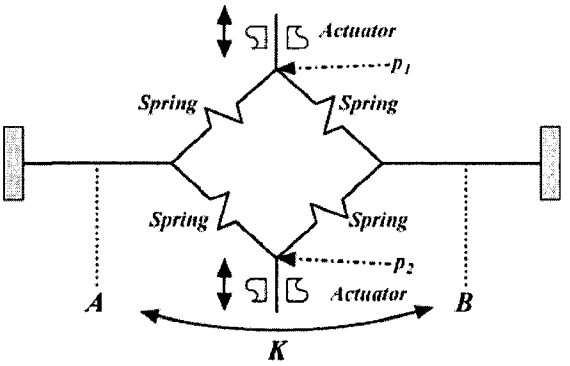

Figure 1.3 Schematic of Semi-Active Variable Stiffness (SAVIS) device.

Agrawal[102] studied the dynamic properties of the SAVIS devices illustrated in Figure 1.3. Recently Varadarajan and Nagarajaiah[103] combined the proposed SAVIS device with TMD system to present a SAVIS-TMD design.

1.2.4.3 Tuned Liquid Column Damper

The original design of Tuned Liquid Column Damper (TLCD)[105-107], as illustrated in Figure 1.4(b) is a passive device and a special type of Tuned Liquid Damper (TLD)[104], which suppresses the structural vibration through shallow liquid sloshing in a rigid tank,

as illustrated in Figure 1.4(a). The semi-active TLCD[108-112] is to adjust the damping through an added device illustrated in Figures 1.4(c)-(e).

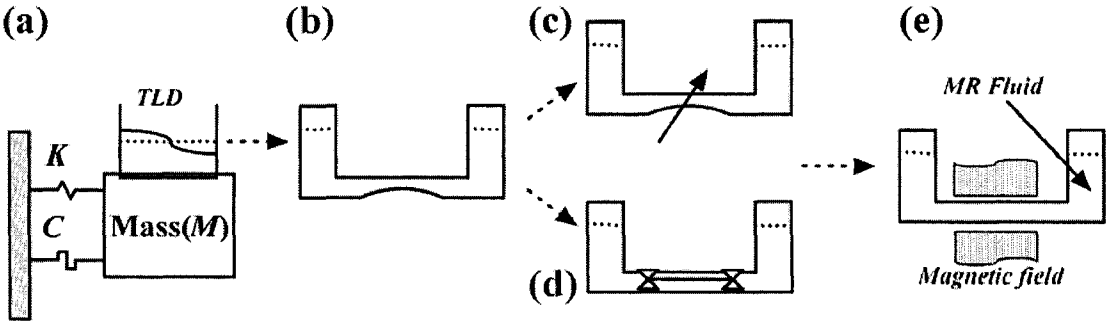

Figure 1.4 Schematics of typical Liquid Damper design. (a) Traditional Tuned Liquid Damper (TLD). (b) TLCD. (c) Semi-active TLCD with variable orifice. (d) Semi-active TLCD with propellers. (e) Semi-active TLCD using MR fluid with adjustable magnetic field.

Yalla *et al*[108, 109] and Hochrainer[110] proposed a device through adjusting the dimension of orifice to change the damping factor of TLCD, as illustrated in Figure 1.4(c). Chen and Ko[111] incorporated a set of controllable propellers in TLCD and then changed the damping factor of TLCD through adjusting the rotation speed of the propellers, as illustrated in Figure 1.4(d). Recently, Wang *et al*[112] replaced the liquid in the TLCD system with Magneto-Rheological (MR) fluid and then changed the damping factor of TLCD system through adjusting the magnetic field around the MR fluid, as illustrated in Figure 1.4(e).

1.2.4.4 Electro-Rheological Fluid and Damper

Electro-Rheological (ER) fluids are suspensions of extremely fine non-conducting particles in an electrically insulating fluid[113], which was invented by Winslow[114]. The

change in viscosity of ER fluids directly depends on the applied electric field and this characteristic makes ER fluids attractive for providing a rapid response interface in controlled mechanical devices. The most common application of ER fluids is the hydraulic valve, clutch, brake and absorber (damper)[115-118]. As the key operation modes for ER and MR fluids are similar and the mathematical model utilized to describe dynamic behavior of ER/MR devices are also similar, detail information about ER fluid operation modes and its relative devices will be presented in the next section, which is mainly focused on the MR fluid devices.

1.2.5 Magneto-Rheological fluid and damper

Magneto-Rheological (MR) fluids are a class of novel intelligent materials whose dynamic characteristics change rapidly and can be controlled easily in the presence of an applied magnetic field controlled by input current (voltage). Figure 1.5 illustrated the working principle of MR fluids[118].

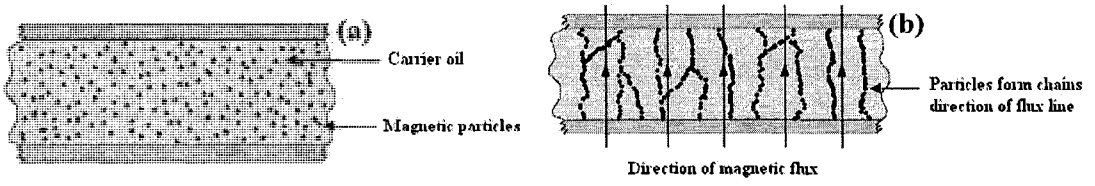

Figure 1.5 Operation principle of Magneto-Rheological (MR) fluids[118]. (a) Before applying magnetic field. (b) After applying magnetic field.

From Figure 1.5(a), it can be found that the magnetic particles are suspended within the carrier oil and distributed randomly. When a magnetic field is applied, as shown in Figure 1.5(b), the magnetic particles would be aligned along the magnetic flux line. Subsequently, the resulting chains of particles restrict the movement of the fluid, which is

perpendicular to the direction of flux, and thus increasing its viscosity. It should be noted that the working principle of ER fluids can also be illustrated through Figures 1.5 by changing the applied magnetic field to electric field and also the magnetic particles to non-conducting particles. There are three key operation modes[118, 119], as illustrated in Figure 1.6[119], for ER and MR fluids.

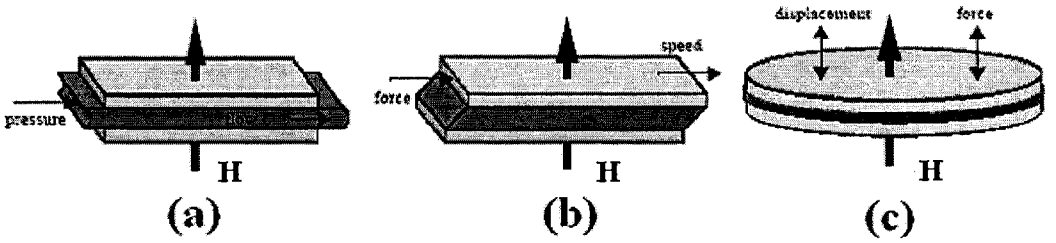

Figure 1.6 Schematics of ER/MR fluids' key operation modes[119]. (a) The flow mode. (b) The sheer mode. (c) The squeeze-flow mode. Note: "H" represents the applied magnetic or electric field.

In the flow mode illustrated in Figure 1.6(a), the smart fluid is contained between a pair of stationary plates. The resistance to the fluid flow is controlled by varying the strength of the electric or magnetic field across the electrodes (ER fluid) or poles (MR fluid). Practical application of the flow mode includes hydralic servo valve, damper and absorber[118, 119]. The shear mode shown in Figure 1.6(b) allows the relative motion, either rotational or translational, perpendicular to the direction of the applied field. Practical application of the shear mode includes controllable clutch and brake[118, 119]. The squeeze-flow mode shown in Figure 1.6(c) allows the smart fluid subject to tension/comperssion and some shearing of the fluid also occurs[118]. The squeeze-flow mode is most suitable for applications controlling small, millimeter-order movements but involving large forces[118-121]. As the MR fluid type device has larger working temperature range and working force

with smaller electric source than that for ER fluild type devices, the commercial applications of smart fluid are mainly based on MR fluid.

To date, MR fluid dampers are one of the typical devices for MR fluid's commercial applications[122]. This kind of devices can offer large range of damping force capacity, high reliable operation, and robustness in a reliable fail-safe manner with very low power requirements and then it is one of the most promising devices for structural semi-active control. A successful semi-active control system depends on two important issues, which are the selected semi-active device and its relative controller. This section will be focused on the mathematical model for MR-damper and the controller design for MR-damper will be presented in the next section.

Different mathematical models have been developed to model the dynamic behavior of ER/MR-dampers. Stanway *et al*[123, 124] and Peel *et al*[125] proposed the Bingham model, in which a coulomb friction element is placed in parallel with a linear viscous damper. Gamota and Filisko[126] presented the parametric viscoelastic-plastic model based on Bingham model[123]. Wereley *et al*[127] provided the nonlinear hysteretic biviscous model which can improve the pre-yield hysteresis behavior. Spencer *et al*[128] proposed a phenomenological model, which can capture the force roll-off in the low velocity region, based on the Bouc-Wen hysteresis model, which is a numerical model developed by Wen[129] in 1976 for modeling the hysteretic systems. Yang[119] summarized four types of modification of the Bouc-Wen models.

Recently, many research works have been conducted to model the dynamic behavior of MR-dampers. Li *et al*[130] developed a polynomial model. Choi *et al*[131] proposed a model

in which the MR-damper operates in two rheological domains, the pre-yield and pose-yield regions. Oh and Onode[132] proposed an equivalent structural model based on the combination of springs, dashpot and friction elements. Wang *et al*[133, 134] gave a numerical model based on the mathematical analysis of hysteresis behavior. Jimenez and Alvarez[135] proposed the modified LuGre friction model, and then they introduced the improved LuGre friction model[136], which can simulate the dynamic behavior of MR-damper more accurately than the modified LuGre friction model[135]. Xia[137] utilized the optimal neural network technique to model the dynamic behavior of MR-damper and then proposed an inverse MR-damper model. Kim *et al*[138] utilized the ANFIS toolbox provided by MATLAB®[86] directly to estimate the MR-damper's fuzzy model based on the experimental data. Dominguez *et al*[139] proposed a numerical model based on the solution of Bouc-Wen hysteresis equation, and then they[140] improved the model incorporating the frequency, current and magnitude relationships. Jin *et al*[141] utilized the nonlinear black box identification techniques to model the MR-damper. Wang and Kamath[142] utilized the phase-transition theory to model the MR-damper. Ikhouane and Dyke[143] adopted the Dahl friction model to characterize the hysteretic properties of MR-damper. Shivaram and Gangadharan[144] proposed a quadratic equation to predict the Root Mean Square (RMS) of the MR-damper's damping force.

Based on the above introduction, it can be found that although the earliest work for modeling the dynamic behavior of ER/MR-damper can be found in 1987[123], a significant number of papers continue to appear in this area. It is due to the fact that no mathematical

model is perfect, which can not only characterize the dynamic behavior accurately, but also be easily to be used.

1.2.6 Magneto-Rheological damper control methodology

The controller design is the other important issue for semi-active structure using MR-dampers. Basically, five most reported approaches have been utilized in designing the controller for MR-dampers:

(1) The first one is based on the Lyapunov stability theory. Leitmann[145] applied the Lyapunov's direct approach and selected the Lyapunov function as the 2-norm of state vector. McClamroch and Gavin[146] selected the Lyapunov function as the total vibratory energy (kinetic energy and potential energy) and then designed the decentralized Bang-Bang controller. Jansen and Dyke[147] selected the Lyapunov function as the relative vibratory energy. In numerical expression, these design methodologies will make controllers switch in two states utilized the Heaviside step function, and it is an "*on-off*" relationship. This type of controller has been popularly adopted by many researchers[133,134, 145-148];

(2) The second approach is based on the linear quadratic controller design method, such as Zhang and Roschke[149] designed a LQG/LTR controller;

(3) The third approach is based on the inverse MR-damper model, which is a numerical model to calculate the MR-damper's required control current (voltage) under a known control force[150, 151];

(4) The forth methodology is based on fuzzy controller design methodology, which has been conducted by many researchers recently. Battaini *et al*[152] designed a fuzzy

controller, which utilized the bell-shape membership function and the Mean Center of Gravity (COG) defuzzificaiton method. Schurter and Roschke[153] proposed a fuzzy controller design approach for vibration suppression using MR-damper , in which a target controller was design firstly, and then the structure response under the developed target controller were simulated and collected, finally utilized the ANFIS toolbox provided by MATLAB®[86] and the collected response data to train a fuzzy controller. Choi *et al*[154] and Liu *et al*[155] designed a fuzzy controller based on the triangular-shape membership function and the COG defuzzificaiton method. Wilson and Abdullah[156] utilized the same methodology as Liu *et al*[155] but proposed the other set of scaling factor for normalizing the universes of discourse, and then they[157] improved their study[156] by adding a self tuned scaling device, which can tune the scaling factor automatically. Zhou *et al*[158] proposed a fuzzy controller with adaptive tuning properties. Reigles and Symans[159] presented a fuzzy supervisory controller. The other direction in the fuzzy controller design is to utilize the GA optimization method to tune the parameters in membership function[138, 160,161];

(5) The last methodology is the stochastic optimal controller by Zhu and Ying[162], Ying *et al*[163] and Cheng *et al*[164].

In practical applications, some of above basic methodologies were combined together. Dyke[94] and Dyke and Spencer Jr *et al*[92, 165] combined linear quadratic optimal controller design method and Lyapunov stability theory and then proposed the Clipped-Optimal controller. Recently, Yoshioka *et al*[166] improved the Clipped-Optimal switching by adding a threshold. Yoshida and Dyke[167] added a function in the Clipped-Optimal switching, which can make the control current to obtain any values between zero and

maximum prescribed value. Sakai *et al*[168] utilized the modified LuGre friction model[135] to derive the inverse MR-damper model and then combined it with the Linear Quadratic Gaussian (LQG) controller to control the MR-damper command voltage. Wang *et al*[134] introduced the inverse MR-damper model based on the numerical model proposed by them, in which the dependence of the hysteresis property of MR-damper to input current has been neglected, and then combined it with the "*on-off*" controller[134].

In this dissertation, an inverse MR-damper model has been proposed based on the LuGre friction model, and then combined with a H_2/LQG controller, to provide effective vibration suppression performance for structure under random loading.

1.3 Present Works

This work is generally aimed to establish a comprehensive framework for design optimization and vibration suppression of structures using Tuned Mass Damper (TMD) and Semi-Active Mass Damper (SAMD) technologies. In particular, this work improves the design procedure for vibration suppression of beam-type structures using TMD technology through the development of finite element analysis and design optimization algorithm, and demonstrates the functionality and performance of vibration suppression using TMD technology and the validity of Magneto-Rheological (MR) fluid damper utilized as the semi-active device to design the SAMD system

Specifically, the important components and contributions in this dissertation can be summarized as:

- **Design Optimization of TMD system for beam-type structures**
  - ✓ Developing a hybrid optimization methodology, which combines the global optimization method based on Genetic Algorithm (GA) and the powerful local optimization method based on SQP.
  - ✓ Utilizing the developed hybrid optimization methodology to obtain the optimal design for vibration suppression of beam-type structures using TMD technology through the developments of finite element model and optimization approach.
- **Magneto-Rheological (MR) damper modeling**
  - ✓ Proposing a LuGre friction model to model the dynamic behavior of large-scale MR-damper (MR-9000 type[22]) effectively and accurately.
  - ✓ Developing an inverse MR-damper model based on the LuGre friction model, which can be readily used in the design of semi–active vibration suppression devices.
- **Vibration Suppression**
  - ✓ The effectiveness of vibration suppression for beam-type structure using the developed optimal MTMD design is investigated.
  - ✓ Developing an effective control methodology to suppress vibration using SAMD based on MR-damper technology.

1.4 Dissertation Organization

The first chapter contains the motivation and objective of the present work, an introduction of the concepts and methodologies used in this dissertation, and also a detailed review of the recent pertinent works in the relative area. The important

components and contributions of this research work have been summarized at the end of this chapter.

The straight Timoshenko beam and the curved beam-type structure's finite element models are formulated in Chapter 2. First, a simple procedure for the straight Timoshenko beam's finite element model is presented. Then, the whole investigation for the curved beam's finite element model is developed in a systemic way. Finally numerical examples are presented to verify the validity of the developed finite element models.

Chapter 3 addresses the optimal Tuned Mass Damper (TMD) design for Timoshenko beam using the finite element methodology. The equations of motion in finite element form for Timoshenko beam with the attached TMD system are derived first, and then utilized to establish the optimization problem for both random and harmonic excitations.

Chapter 4 is the extension of the study presented in Chapter 3 to curved beam-type structures. Through extensive numerical investigations, a throughout TMD design framework for beam-type structures with the attached TMD system is established in this chapter.

The validity of the developed design methodology for vibration suppression of beam-type structures using optimal TMD system is testified in Chapter 5 through experimental study. The structural response under both random and harmonic excitations is studied.

The MR-damper's numerical model is presented in Chapter 6. A detailed introduction of MR-damper model is presented followed by the proposed LuGre friction model for MR-9000 type damper[22].

Chapter 7 is devoted to semi-active vibration control using MR-damper. The whole control strategy for SAMD system using MR-damper is presented in this chapter. The simulation results are then utilized to verify the validity of the developed control strategy through different examples.

To conclude, a summary of work and major contributions of the dissertation and recommendations for future works are presented in Chapter 8.

CHAPTER 2

FINITE ELEMENT MODEL FOR BEAM-TYPE STRUCTURES

2.1 Introduction

The finite element model for beam-type structures, which will be utilized in the optimal Tuned Mass Damper (TMD) design, will be presented in this chapter. The differential equations of motion for the Timoshenko beam have been clarified in many vibration textbooks[4], and its equations of motion in finite element form can be obtained through the polynomial interpolation function[9].

Based on the introduction presented in Chapter 1, it can be realized that although the circular beam-type structure has been studied by many researchers, not much work has been done on either uniform or non-uniform curved beams with variable curvatures. In particular, no further work based on the finite element approach has been reported on curved beams with variable curvatures. Considering this fact, one of the main objectives of this chapter is to develop the finite element model for the general curved beam with variable curvature. The geometrical relationships for the curved beam's deformations will be introduced first, and then the governing differential equations of motion are derived using the extended Hamilton principle. Finally the weighted residual technique based on the Galerkin method is utilized to transfer the governing differential equations into the finite element form.

Initially, the finite element model of the curved beam including the effects of the axial extensibility, shear deformation and the rotary inertia (Case 1) is developed. Subsequently, the curved beam model excluding the axial extensibility, shear deformation and rotary inertia (Case 2) is investigated. Efficient numerical techniques, based on the curvilinear integral applied on the central line of the curvilinear beam and the Gaussian integral method[3] have been implemented to obtain the governing equations of motion in finite element form. The results for the natural frequencies, modal shapes and deformed configurations of different curved beams with different boundary conditions are obtained and compared with those available in published literatures.

2.2 Finite Element Model of Timoshenko Beam

A Timoshenko beam and its rotary deformations are illustrated in Figure 2.1.

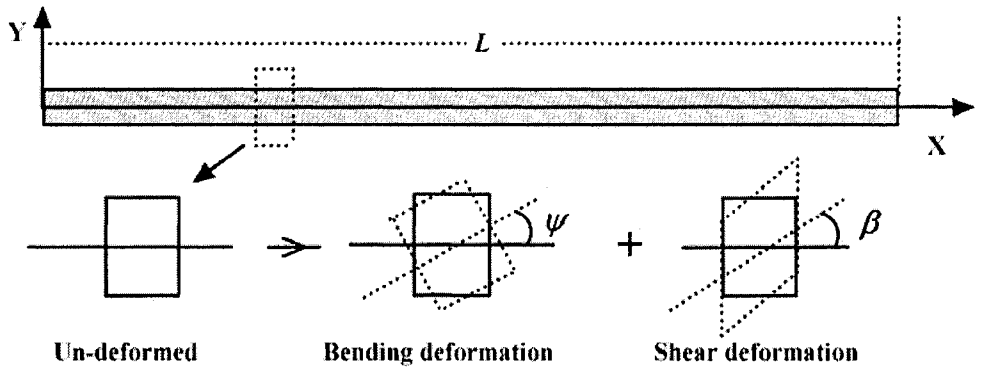

Figure 2.1 Typical Timoshenko beam and its rotary deformations.

In Figure 2.1, variables ψ and β represent the rotation due to bending and angle of distortion due to shear, respectively. Therefore, the deformation relationship for the Timoshenko beam can be expressed as:

$$\frac{\partial w(x,t)}{\partial x} = \psi(x,t) + \beta(x,t) \tag{2.1}$$

where w represents the transverse displacement. Based on Equation (2.1), one can easily obtain the governing differential equations of motion for free vibration, as stated in Equations (2.2)[4], by applying the extended Hamilton principle.

$$-m(x)\frac{\partial^2 w(x,t)}{\partial t^2} + \frac{\partial}{\partial x}\left[k_q GA(x)\left(\frac{\partial w(x,t)}{\partial x} - \psi(x,t)\right)\right] = 0 \tag{2.2a}$$

$$-J(x)\frac{\partial^2 \psi(x,t)}{\partial t^2} + \frac{\partial}{\partial x}\left(EI(x)\frac{\partial \psi(x,t)}{\partial x}\right) + k_q GA(x)\left(\frac{\partial w(x,t)}{\partial x} - \psi(x,t)\right) = 0 \tag{2.2b}$$

where E, G and k_q are the elastic modulus, shear modulus and sectional shear coefficient of the Timoshenko beam, respectively. The $m(x)$, $A(x)$, $I(x)$ and $J(x)$ are the linear density, cross-sectional area, area moment of inertia and mass moment of inertia density per unit length along the X coordinate, respectively. Here it should be noted that $J(x)$ is related to $I(x)$ as $J(x) = \gamma\ I(x)$, where γ is the material volumetric density. The sectional shear coefficient (k_q) is depended on the material and the cross-sectional geometrical properties[169, 170]. For beams with circular and thin rectangular cross-section, the widely accepted shear coefficient (k_q) are $6(1+\nu)^2/(7+12\nu+4\nu^2)$ and $5(1+\nu)/(6+5\nu)$, respectively, where ν is the Poisson's ratio.

The governing differential equations of motion, as stated in Equations (2.2), will be solved by the finite element method using the natural coordinate system and appropriate Lagrangian type shape functions. Beams' deformations (transverse displacement $w(x)$ and rotation due to the bending $\psi(x)$), coordinates (x) and geometrical properties (cross-section area $A(x)$ and area moment of inertia $I(x)$) can be related to their nodal values as:

$$w(\eta,t)=[N(\eta)]\{W(t)\},\ \psi(\eta,t)=[N(\eta)]\{\Psi(t)\},\ x(\eta)=[N(\eta)]\{X\},$$
$$A(\eta)=[N(\eta)]\{A\} \text{ and } I(\eta)=[N(\eta)]\{I\} \tag{2.3}$$

where η is the natural coordinate ($-1\leq \eta \leq 1$) and $\{W(t)\}$ and $\{\Psi(t)\}$ are the nodal displacement and rotation vectors for w and ψ deflection functions, respectively. $\{X\}$, $\{A\}$ and $\{I\}$ are the nodal vectors for x, A and I functions, respectively. $[N(\eta)]$ is the Lagrangian type shape function. Here it should be noted that one can utilize different order polynomial functions to interpolate the deformation (w and ψ), geometrical coordinate (x) and geometrical properties (A and I) separately, which will not affect the integral procedure to obtain the finite element formulation. Therefore, for the sake of simple expression, in this dissertation the shape function utilized to interpolate the deformation, geometrical coordinate and properties are assumed to be the same, except those defined specifically.

Now applying Galerkin weighted residual technique to Equations (2.2) and substituting the interpolation functions provided in Equations (2.3), the following governing equations of motion in finite element form can be obtained:

$$[M]\{\ddot{q}(t)\}+[K]\{q(t)\}=0 \tag{2.4}$$

where

$$[M]=\begin{bmatrix}[M_{ww}] & [0]\\ [0] & [M_{\psi\psi}]\end{bmatrix},\ [K]=\begin{bmatrix}[K_{ww}] & [K_{w\psi}]\\ [K_{\psi w}] & [K_{\psi\psi}]\end{bmatrix} \text{ and } \{q(t)\}=\begin{Bmatrix}\{W(t)\}\\ \{\Psi(t)\}\end{Bmatrix} \tag{2.5}$$

The sub-matrices for mass and stiffness matrices given in Equations (2.5) are provided in "Appendix A" and evaluated numerically using Gauss Quadrate technique.

2.3 Finite Element Model of Curved Beams

Based on the introduction presented in Chapter 1, it can be found that two basic assumptions for curved beam-type structures were widely studied by researchers, which are the curved beam including the effects of the axial extensibility, shear deformation and the rotary inertia (Case 1) and the curved beam model neglecting the effects of the axial extensibility, shear deformation and rotary inertia (Case 2). Therefore, both models will be studied in this dissertation. The geometry of the general curved beam is illustrated in Figure 2.2, in which L, Φ and h are the span length, curve angle and rise of the curved beam, respectively. The coordinate S is along the central line and $y(x)$ is the function describing the central line. Here, it should be noted that the coordinate definition is adopted the same as Tseng *et al*[26], Oh *et al*[35] and Chidamparam and Leissa[171]. The geometrical and deformational relationships for both curved beam models (Cases 1 and 2) are summarized in Table 2.1.

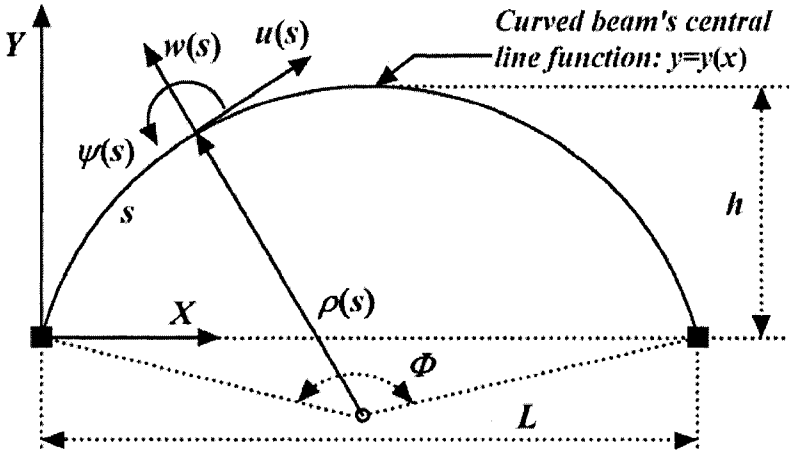

Figure 2.2 Curved beam's geometry.

Table 2.1 Geometrical and deformational relationships for different curved beam models.

Curved beam model	Case 1	Case 2
Radial displacement	$w(s)$	$w(s)$
Differential of the total tangential displacement	$du_T(s)/ds = du(s)/ds + w(s)/\rho(s)$	$0 = du(s)/ds + w(s)/\rho(s)$
Rotation due to the tangential displacement	$\varphi(s) = u(s)/\rho(s)$	$\varphi(s) = u(s)/\rho(s)$
Total rotation	$dw(s)/ds = \beta(s) + \psi(s) + \varphi(s)$	$dw(s)/ds = \psi(s) + \varphi(s)$

In Figure 2.2 and Table 2.1, $w(s)$, $u(s)$, $\varphi(s)$, $\psi(s)$ and $\beta(s)$ are the beam's radial displacement, tangential displacement, rotation due to tangential displacement, rotation due to bending and rotation due to shear along the S coordinate, respectively. Variables $\rho(s)$, $u_T(s)$, $dw(s)/ds$ and $w(s)/\rho(s)$ are the radius of curvature, beam's total tangential displacement, slope of radial deflection (w) curve and tangential displacement due to radial displacement along the S coordinate, respectively.

Next, the procedure for deriving the governing differential equations of motion and the equations of motion in finite element form for both curved beam models (Cases 1 and 2) will be presented. The extended Hamilton principle stated in Equation (2.6) will be utilized to derive the governing differential equations of motion.

$$\int_{t_1}^{t_2} (\delta T - \delta V + \delta W_{nc}) dt = 0; \qquad \delta(.) = 0 \text{ at } t = t_1, t_2 \tag{2.6}$$

where T, V and δW_{nc} represent the kinetic energy, potential energy and non-conservative virtual work, respectively. As the main purpose of this chapter is to study the free vibration of curved beam-type structures, the non-conservative virtual work (δW_{nc}), as stated in Equation (2.6), is assumed to be zero in the following sections.

2.3.1 Equations of motion for curved beam model (Case 1)

The curved beam model (Case 1) takes into account the rotary inertial, axial extensibility ($du_T(s)/ds$) and also the shear deformation. Therefore the kinetic energy (T) and the potential energy (V) in its most general form can be written as:

$$T = \frac{1}{2}\int_L m(s)\left(\frac{\partial w(s,t)}{\partial t}\right)^2 ds + \frac{1}{2}\int_L J(s)\left(\frac{\partial \psi(s,t)}{\partial t}\right)^2 ds + \frac{1}{2}\int_L m(s)\left(\frac{\partial u(s,t)}{\partial t}\right)^2 ds \tag{2.7}$$

$$V = \frac{1}{2}\int_L EI(s)\left(\frac{\partial \psi(s,t)}{\partial s}\right)^2 ds + \frac{1}{2}\int_L k_q GA(s)\beta^2(s,t)ds + \frac{1}{2}\int_L EA(s)\left(\frac{\partial u_T(s,t)}{\partial s}\right)^2 ds \tag{2.8}$$

where $m(s)$, $A(s)$, $I(s)$ and $J(s)$ are the linear density, area, area moment and mass moment of inertia density along S coordinate, respectively. Here it should be noted that the integral ($\int_L[.]$) represents curvilinear integral applied on S coordinate. The geometrical and deformational expressions for Case 1 in Table 2.1 were substituted into Equations (2.7) and (2.8), and then by identifying $w(s)$, u(s) and $\psi(s)$ as the independent variables, and applying Hamilton's principle stated in Equation (2.6), the following three governing differential equations of motion[26, 35, 171] will be obtained as:

$$-m(s)\frac{\partial^2 w(s,t)}{\partial t^2} + \frac{\partial}{\partial s}\left[k_q GA(s)\left(\frac{\partial w(s,t)}{\partial s} - \frac{u(s,t)}{\rho(s)} - \psi(s,t)\right)\right] - \frac{EA(s)}{\rho(s)}\left(\frac{\partial u(s,t)}{\partial s} + \frac{w(s,t)}{\rho(s)}\right) = 0 \tag{2.9a}$$

$$-m(s)\frac{\partial^2 u(s,t)}{\partial t^2} + \frac{k_q GA(s)}{\rho(s)}\left(\frac{\partial w(s,t)}{\partial s} - \frac{u(s,t)}{\rho(s)} - \psi(s,t)\right) + \frac{\partial}{\partial s}\left[EA(s)\left(\frac{\partial u(s,t)}{\partial s} + \frac{w(s,t)}{\rho(s)}\right)\right] = 0 \tag{2.9b}$$

$$-J(s)\frac{\partial^2 \psi(s,t)}{\partial t^2} + \frac{\partial}{\partial s}\left(EI(s)\frac{\partial \psi(s,t)}{\partial s}\right) + k_q GA(s)\left(\frac{\partial w(s,t)}{\partial s} - \frac{u(s,t)}{\rho(s)} - \psi(s,t)\right) = 0 \tag{2.9c}$$

The finite element model of the system will now be developed based on Equations (2.9). By using the natural coordinate system and the appropriate Lagrangian type shape functions, the Cartesian coordinate $x(s)$ and $y(s)$, radial displacement $w(s)$, tangential displacement $u(s)$, rotation due to bending $\psi(s)$, cross-sectional area $A(s)$ and area moment of inertia $I(s)$ can be related to their relative nodal values as:

$$\begin{gathered} x(\eta)=[N(\eta)]\{X\};\ y(\eta)=[N(\eta)]\{Y\};\ w(\eta,t)=[N(\eta)]\{W(t)\}; \\ u(\eta,t)=[N(\eta)]\{U(t)\};\ \psi(\eta,t)=[N(\eta)]\{\Psi(t)\};\ A(\eta)=[N(\eta)]\{A\};\ I(\eta)=[N(\eta)]\{I\} \end{gathered} \tag{2.10}$$

where η is the natural coordinate ($-1\leq \eta \leq 1$) and $[N(\eta)]$ is the Lagrangian type shape function and the vectors $\{W(t)\}$, $\{U(t)\}$ and $\{\Psi(t)\}$ are the nodal radial displacement, nodal tangential displacement and nodal rotation vectors associated with the radial displacement function (w), tangential displacement function (u) and rotation function (ψ), respectively. Similarly, $\{X\}$, $\{Y\}$, $\{A\}$ and $\{I\}$ are the nodal values associated with the x, y, A and I functions, respectively.

By applying the Galerkin weighted residual technique to Equations (2.9), substituting the functions with respect to their nodal values given in Equations (2.10), and then utilizing the Jacobin relationship between the Cartesian coordinate (X and Y), the curvilinear coordinate (S) and the natural coordinate (η), the following governing equations of motion in the finite element form can be obtained.

$$[M]\{\ddot{q}(t)\}+[K]\{q(t)\}=0 \tag{2.11}$$

where

$$[M]=\begin{bmatrix}[M_{ww}] & [0] & [0]\\ [0] & [M_{uu}] & [0]\\ [0] & [0] & [M_{\psi\psi}]\end{bmatrix},\ [K]=\begin{bmatrix}[K_{ww}] & [K_{wu}] & [K_{w\psi}]\\ [K_{wu}]^T & [K_{uu}] & [K_{u\psi}]\\ [K_{w\psi}]^T & [K_{u\psi}]^T & [K_{\psi\psi}]\end{bmatrix},\ \{q(t)\}=\begin{Bmatrix}\{W(t)\}\\ \{U(t)\}\\ \{\Psi(t)\}\end{Bmatrix} \tag{2.12}$$

The mass and stiffness sub-matrices in Equations (2.12), are presented in "Appendix B", and evaluated numerically using the Gauss Quadrate technique and the curvilinear integral applied on the central line of curvilinear.

2.3.2 Equations of motion for curved beam model (Case 2)

The curved beam model (Case 2) neglects the rotary inertial, axial extensibility ($du_T(s)/ds$) and also shear deformation. Therefore, one can easily cancel the energy related to the rotary inertial, axis extensibility ($du_T(s)/ds$) and also shear deformation in Equations (2.7) and (2.8) to obtain:

$$T = \frac{1}{2}\int_L m(s)\left(\frac{\partial w(s,t)}{\partial t}\right)^2 ds + \frac{1}{2}\int_L m(s)\left(\frac{\partial u(s,t)}{\partial t}\right)^2 ds \tag{2.13}$$

$$V = \frac{1}{2}\int_L EI(s)\left(\frac{\partial \psi(s,t)}{\partial s}\right)^2 ds \tag{2.14}$$

Substituting the geometrical and deformation relationships for Case 2 listed in Table 2.1 into Equations (2.13) and (2.14), and selecting $w(s)$ and u(s) as the variables and then applying the Hamilton's principle stated in Equation (2.6), the following two governing differential equations for Case 2 can be obtained:

$$m(s)\frac{\partial^2 w(s,t)}{\partial t^2} + \frac{\partial^2}{\partial s^2}\left(EI(s)\frac{\partial^2 w(s,t)}{\partial s^2}\right) - \frac{\partial^2}{\partial s^2}\left(\frac{EI(s)}{\rho(s)}\frac{\partial u(s,t)}{\partial s}\right) = 0 \tag{2.15}$$

$$m(s)\frac{\partial^2 u(s,t)}{\partial t^2} + \frac{\partial}{\partial s}\left(\frac{EI(s)}{\rho(s)}\frac{\partial^2 w(s,t)}{\partial s^2}\right) - \frac{\partial}{\partial s}\left(\frac{EI(s)}{\rho^2(s)}\frac{\partial u(s,t)}{\partial s}\right) = 0 \tag{2.16}$$

The detailed procedure for obtaining the above different equations of motion has been provided in "Appendix C". These two equations can be combined together by utilizing

the inextensibility assumption ($du_T(s)/ds=0$) for Case 2 listed in Table 2.1 to obtain a single governing differential equation of order 6 with respect to the tangential displacement (u), which will be identical to that provided by Chidamparam and Leissa[21] for uniform circular beam as:

$$m\left(\rho^2\frac{\partial^4 u(s,t)}{\partial s^2\partial t^2}-\frac{\partial^2 u(s,t)}{\partial t^2}\right)+EI\rho^2\frac{\partial^6 u(s,t)}{\partial s^6}+2EI\frac{\partial u^4(s,t)}{\partial s^4}+\frac{EI}{\rho^2}\frac{\partial u^2(s,t)}{\partial s^2}=0 \qquad (2.17)$$

Here, the equations of motion in finite element form for curved beam model (Case 2) will be developed based on Equations (2.15) and (2.16). For this case, the Lagrangian type shape function, similar to Case 1, is utilized to interpolate the Cartesian coordinate $x(s)$ and $y(s)$, cross-sectional area function $A(s)$ and area moment of inertia function $I(s)$ as:

$$x(\eta)=[N(\eta)]\{X\},\ y(\eta)=[N(\eta)]\{Y\},\ A(\eta)=[N(\eta)]\{A\},\ I(\eta)=[N(\eta)]\{I\} \qquad (2.18)$$

A polynomial equation of order 5, as stated in Equation (2.19), would then be used to interpolate the tangential displacement (u) for this case, as it will satisfy the governing differential equation with respect to the tangential displacement stated in Equation (2.17).

$$u(\eta)=C_0+C_1\eta+C_2\eta^2+C_3\eta^3+C_4\eta^4+C_5\eta^5 \qquad (2.19)$$

Using the deformation relationship for the beam model (Case 2 listed in Table 2.1), the radial displacement (w) and rotation (ψ) are related to the tangential displacement (u) as:

$$w(\eta)=-\frac{du(\eta)}{d\eta}\times\frac{\rho(\eta)}{\bar{J}_c(\eta)}\ \text{and}\ \psi(\eta)=\frac{dw(\eta)}{d\eta}\frac{1}{\bar{J}_c(\eta)}-\frac{u(\eta)}{\rho(\eta)} \qquad (2.20)$$

where Jacobian $\bar{J}_c(\eta)$ and radius $\rho(\eta)$ can be evaluated using the same methodology as that for curved beam model (Case 1), as the geometrical properties were interpolated using the same Lagrangian type shape function. The displacement function $u(\eta)$ can be

related to a two–node curved beam element (each node has three degrees of freedom U, W, Ψ) with nodes i and j as:

$$u(\eta) = [NN(\eta)]\{U_i \quad W_i \quad \Psi_i \quad U_j \quad W_j \quad \Psi_j\}^T \tag{2.21}$$

where $[NN(\eta)]$ is the shape function matrix, which can be obtained using Equations (2.19) and (2.20). The detailed information has been provided in "Appendix D". Finally, by applying the Galerkin weighted residual technique to the governing differential equations listed in Equations (2.15) and (2.16), the governing equations of motion in finite element form for Case 2, similar to that in Equation (2.11), can be obtained. For this case, the nodal displacement vector and the mass and the stiffness matrices for this case can be expressed as:

$$\{q\} = \{U_1, W_1, \Psi_1, \cdots, U_n, W_n, \Psi_n\}^T \tag{2.22}$$

$$[M] = \sum_{element} \left\{ \int_{-1}^{1} \left\{ \begin{array}{l} \dfrac{\rho^2(\eta)}{\bar{J}_c(\eta)} [B_N(\eta)]^T \gamma A(\eta) [B_N(\eta)] \\ + [NN(\eta)]^T \gamma A(\eta) [NN(\eta)] \bar{J}_c(\eta) \end{array} \right\} d\eta \right\} \tag{2.23}$$

$$[K] = \sum_{element} \left\{ \int_{-1}^{1} \left\{ \begin{array}{l} \dfrac{\rho^2(\eta)}{\bar{J}_c^{\,5}(\eta)} [D_N(\eta)]^T EI(\eta) [D_N(\eta)] + \dfrac{EI(\eta)}{\bar{J}_c^{\,3}(\eta)} [D_N(\eta)]^T [B_N(\eta)] + \\ \dfrac{EI(\eta)}{\bar{J}_c^{\,3}(\eta)} [B_N(\eta)]^T [D_N(\eta)] + \dfrac{EI(\eta)}{\rho^2(\eta) \bar{J}_c(\eta)} [B_N(\eta)]^T [B_N(\eta)] \end{array} \right\} d\eta \right\} \tag{2.24}$$

where n is the total number of nodes to model the curved beam, $[B_N(\eta)] = d[NN(\eta)]/d\eta$, and $[D_N(\eta)] = d^3[NN(\eta)]/d\eta^3$. The detailed procedure for obtaining Equations (2.23) and (2.24) has been provided in "Appendix E".

2.4 Numerical Results

In this section, illustrative examples are presented to clarify the generality and accuracy of the developed methodologies. As the dimensionless natural frequency, which will be studied in this section, has different definition in available published literatures, Table 2.2 will summarize those definitions for dimensionless natural frequency.

Table 2.2 Definitions of the dimensionless natural frequency.

	Definition 1	Definition 2
Dimensionless natural frequency	$\Omega_i = \sqrt{\lambda_i} l^2 \sqrt{\gamma A_0 / E I_0}$	$\Omega_i = \sqrt{\lambda_i} R^2 \sqrt{\gamma A_0 / E I_0}$

In Table 2.2, Ω_i and λ_i represent the i^{th} dimensionless natural frequency and eigenvalue, respectively. A_0, I_0, E and γ represent the area and area moment of the beam structure, and the material elastic modulus and volumetric density, respectively. l and R represent the beam length (curvilinear length) and the radius of circular beam, respectively.

2.4.1 Timoshenko beam

A typical non-uniform beam[172], as shown in Figure 2.3, will be utilized to investigate the presented methodology.

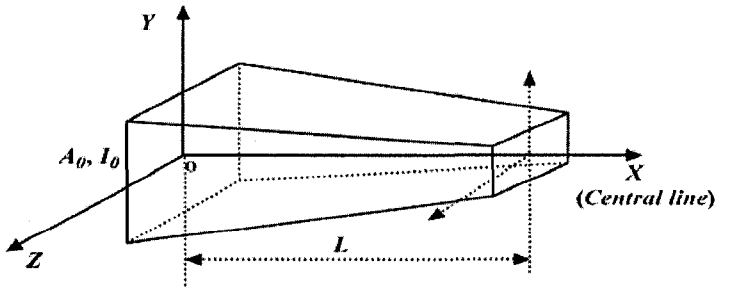

Figure 2.3 A typical non-uniform Timoshenko beam.

Here, the Timoshenko beam is modeled using 7 Timoshenko beam elements with 4 nodes per element. The dimensionless geometrical and physical properties of this beam have been summarized in Table 2.3.

Table 2.3 Dimensionless properties of the non-uniform Timoshenko beam[172].

Elastic modulus (E)/ Shear modulus (G)	2.6	Area moment (I_0)/Area (A_0)	0.0707^2
Shear coefficient(k_q)	5/6	Beam Length (L)	1
Density(γ)	1	Tapped rate (α)	-0.5, 0 , 1
Beam Area function		$A=A_0(1+\alpha x), \quad 0<x<L$	
Beam Area moment function		$I=I_0(1+\alpha x)^3, \quad 0<x<L$	

Note: *(1) the original reference papers did not provide the unit of each parameter and the value of density, as the dimensionless natural frequency will be studied, the effect of unit and detail value of physical properties will be cancelled finally; (2) The tapped rate (α) is utilized to evaluate the area and area moment function.*

In this example, the dimensionless natural frequency, as defined in "Definition 1" in Table 2.2, will be utilized to study the dynamic properties of the beam. The first five dimensionless natural frequencies evaluated through the presented finite element method, which is programmed utilizing the MATLAB®[86] software, have been provided in Table 2.4, and compared with those solved analytically in available literatures.

Table 2.4 The first five dimensionless natural frequencies comparison for non-uniform Timoshenko beam with pinned-pinned boundary.

α	-0.5			0 (uniform)			1		
Ω_i	Ref[172]	Ref[173]	Present	Ref[172]	Ref[173]	Present	Ref[172]	Ref[174]	Present
Ω_1	6.765	6.754	6.754	9.023	9.023	9.021	11.901	11.896	11.893
Ω_2	24.462	24.539	24.353	29.914	29.912	29.9	36.427	36.424	36.402
Ω_3	47.371	47.302	47.281	55.201	55.207	55.173	63.004	62.849	62.798
Ω_4	72.674	72.672	72.632	81.817	81.815	81.756	68.143	68.048	67.975
Ω_5	99.231	99.039	98.982	108.856	108.695	108.61	89.984	89.696	89.615

From Table 2.4, one can easily find that the results are in perfect agreement with those in published literatures. Here, it should be noted that the results are provided for both uniform (α=0) and non-uniform Timoshenko beams.

2.4.2 Curved beam model (Case 1)

The curved beam model (Case 1) takes into account the axial extensibility ($du_T(s)/ds$), shear deformation and rotary inertia. The challenge for the finite element methodology developed in this dissertation is to evaluate the mass, stiffness (also the damping and force) matrices utilizing the curvilinear integral applied on the central line of curvilinear beam numerically. Therefore in this section, first the circular beam-type structure will be studied to validate the developed finite element formulation, and then the study will be extended to non-circular beam with variable curvature, finally a non-circular beam with non-uniform cross-section will be presented. Here, it should be noted that all the curved beams studied in this section, are modeled using 10 developed 'curved beam element' with 4 nodes per element.

Example 1: Uniform circular curved beam with pinned-pinned boundary conditions

The uniform circular curved beam, as illustrated in Figure 2.2, with the pinned-pinned boundary condition is considered here. The beam's dimensionless material and geometrical characteristics are given in Table 2.5:

Table 2.5 Dimensionless properties of circular beam[22, 43].

Physical properties (k_qG/E)	0.3	Beam area Moment (I_0)	0.01
Beam Radius (R)	0.75	Beam area (A_0)	4
Density(γ)	1	Acre angle (Φ)	$\pi/2$

Note: *the original reference papers did not provide the unit of each parameter and the value of density, as the dimensionless natural frequency will be studied, the effect of unit and detail value of physical properties will be cancelled finally.*

The other parameters can be obtained through those listed in Table 2.5 as:

$$l = R\Phi,\ r=\sqrt{(I_0/A_0)}=0.05,\ R/r = 15 \text{ and } l/r = 23.56 \qquad (2.25)$$

The results for the first 10 dimensionless natural frequencies defined as "Definition 1" in Table 2.2, and the associated modal shapes and deformed configurations are provided in Table 2.6 and Figures 2.4 and 2.5, respectively. It can be realized that very good agreement between the present results and those presented by Austin and Veletsos[22] and Eisenberger and Efraim[43] does exist. It should be noted that the horizontal axis "non-dimensional beam curvilinear length" in Figure 2.4 is defined by the non-dimensional parameter s/l, in which, s is measured along the curved beam central line. Therefore, s/l varies between zero and one.

Table 2.6 Dimensionless frequencies of a uniform circular curved beam with the pinned-pinned boundary conditions (Case 1).

Mode	Austin and Veletsos[22]	Eisenberger and Efraim[43]	Present study
1	29.61	29.2799	29.2760
2	33.01	33.3049	33.3176
3	67.24	67.1235	67.1231
4	79.6	79.9708	79.9752
5	107.7	107.8511	107.8559
6	144.5	143.6175	143.6287
7	155.2	156.6656	156.6790
8	191.3	190.4771	190.5445
9	223.7	225.3611	225.3700
10	235.3	234.5235	234.7116

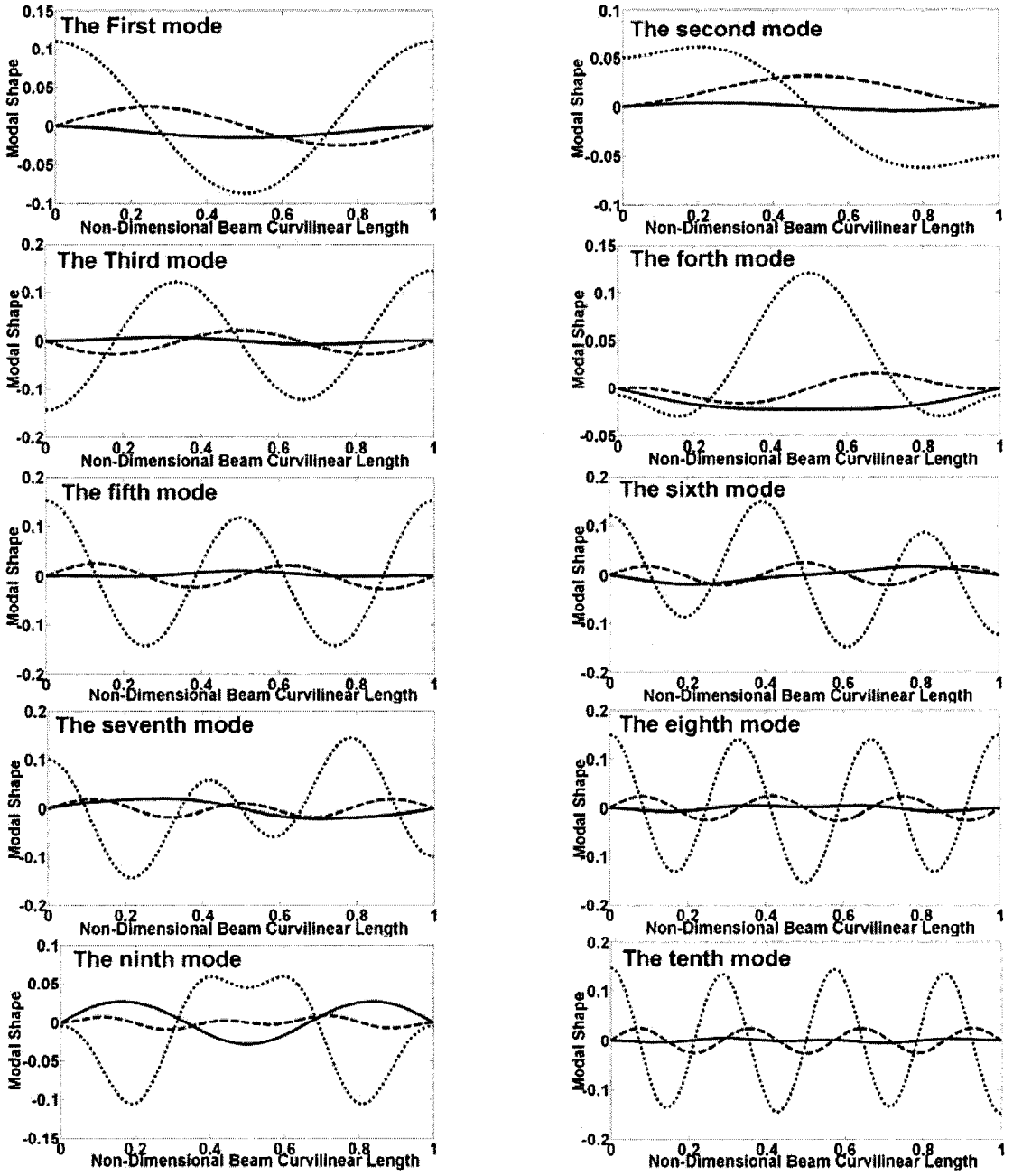

Figure 2.4 The first 10 vibration modal shapes of uniform circular curved beam with pinned-pinned boundary conditions. Solid, dashed and dotted lines represent modal shapes for u, w and ψ, respectively.

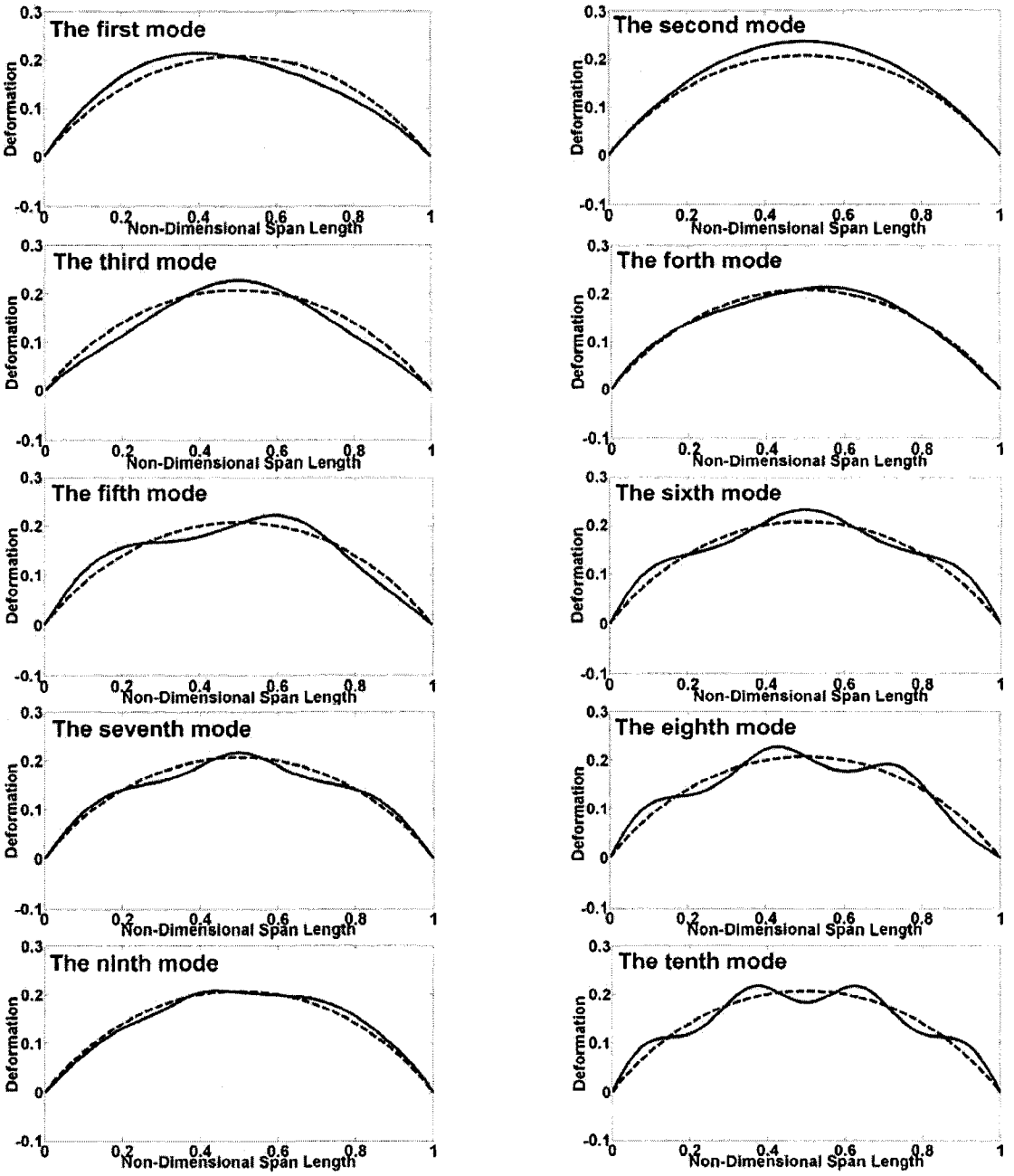

Figure 2.5 The deformations relative to the first 10 vibration modes for uniform circular curved beam with pinned-pinned boundary condition. Solid and dashed lines represent deformed and un-deformed configurations, respectively.

Example 2: Uniform circular curved beam with clamped-clamped boundary conditions

In this example, a uniform circular curved beam with the clamped-clamped boundary is studied. The dimensionless geometrical and material properties are given in Table 2.7.

Table 2.7 Dimensionless properties of circular beam[22, 43].

Physical properties (k_qG/E)	0.3	Beam area Moment (I_0)	0.0016
Beam arch length (l)	1	Beam area (A_0)	1
Density(γ)	1	Acre angle (Φ)	$\pi/2$

Note: *the original reference papers did not provide the unit of each parameter and the value of density, as the dimensionless natural frequency will be studied, the effect of unit and detail value of physical properties will be cancelled finally.*

The other parameters can be obtained through those listed in Table 2.7 as:

$$R = l/\Phi = 0.6366,\ r = \sqrt{(I_0/A_0)} = 0.04,\ R/r = 15.91 \text{ and } l/r = 25 \qquad (2.26)$$

The results for the first 10 dimensionless natural frequencies (Ω) defined as "Definition 1" in Table 2.2, and the associated modal shapes and the deformed configurations are presented in Table 2.8 and Figures 2.6 and 2.7, respectively.

Table 2.8 Dimensionless frequencies of uniform circular curved beam with clamped-clamped boundary conditions (Case 1).

Mode	Austin and Veletsos[22]	Eisenberger and Efraim[43]	Present study
1	36.81	36.7031	36.7130
2	42.44	42.2635	42.2588
3	82.5	82.2330	82.2328
4	84.3	84.4915	84.4935
5	122.5	122.3053	122.3108
6	155.1	154.9447	154.9510
7	167.7	168.2026	168.2192
8		204.4718	204.5467
9		238.9920	238.9938
10	249.6	249.0114	249.2148

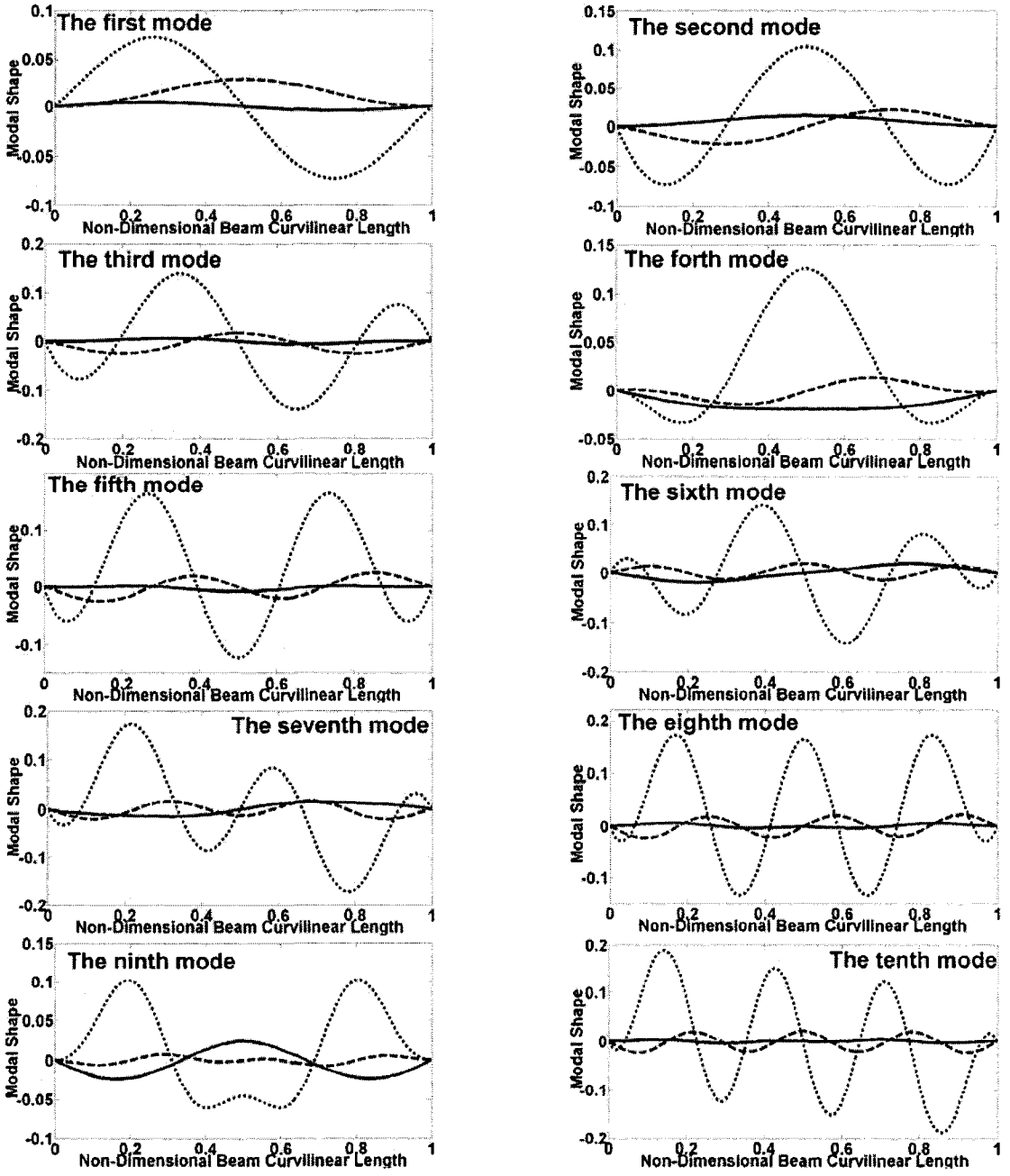

Figure 2.6 The first 10 vibration modal shapes of uniform circular curved beam with clamped-clamped boundary conditions. Solid, dashed and dotted lines represent modal shapes for u, w and ψ, respectively.

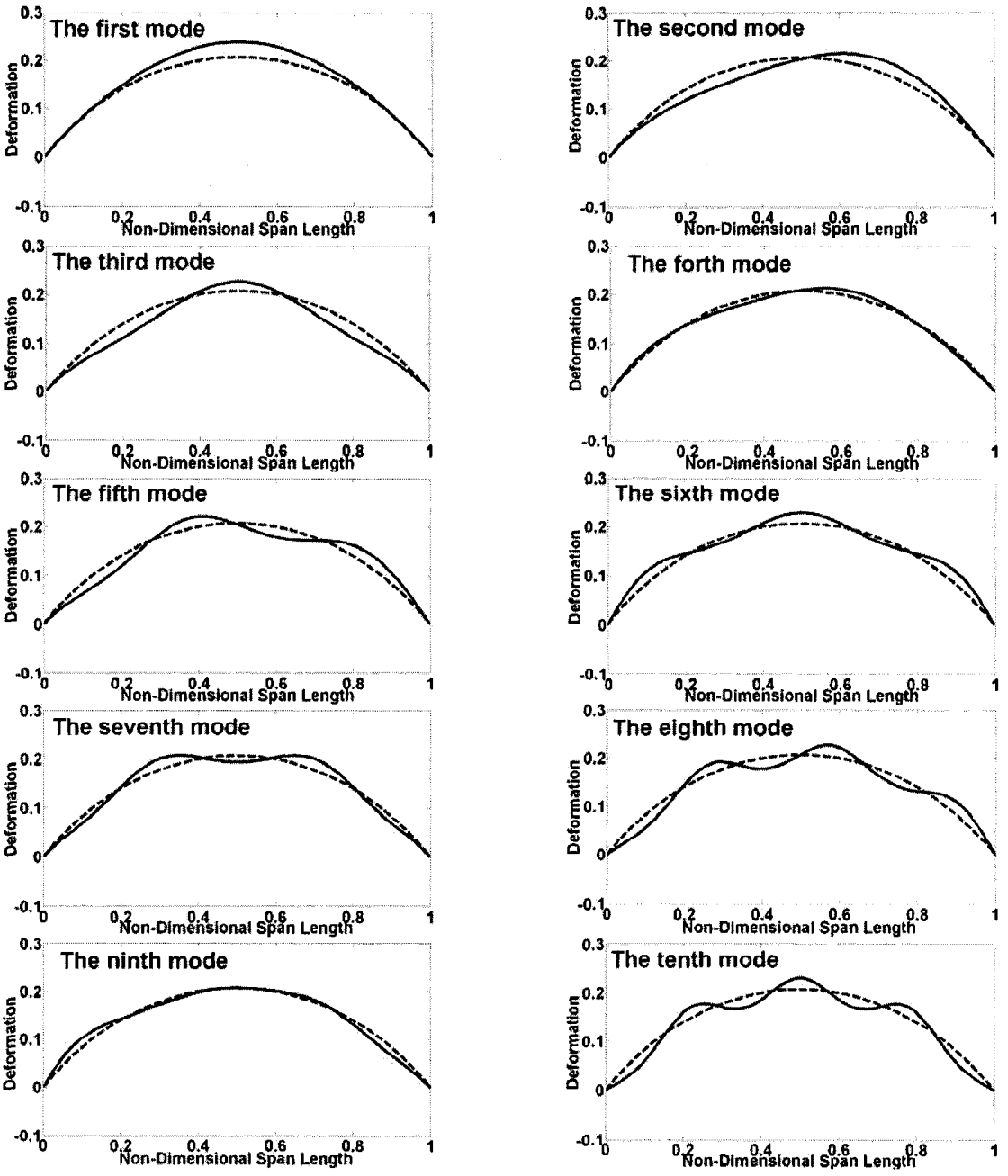

Figure 2.7 The deformations relative to the first 10 vibration modes for uniform circular curved beam with clamped-clamped boundary conditions. Solid and dashed lines represent deformed and un-deformed configurations, respectively.

Once again, it can be seen the results are in very close agreement with those reported in works by Austin and Veletsos[22] and Eisenberger and Efraim[43].

Example 3: Uniform circular beam with different arch angle

Above two examples are concentrated on the uniform circular beam with 90° arch angle. This example will be focused on circular beam with different arch angle. The dimensionless natural frequency defined as "Definition 2" in Table 2.2, will be evaluated utilizing the developed finite element methodology and then the results will be compared with those in available literatures. In this example, the cross-section of uniform circular beam is circular and the geometrical and physical parameters are listed in Table 2.9.

Table 2.9 Properties of circular beam[28, 43, 175].

Elastic module (E)	$2.1\times10^{11}(N/m^2)$	Shear coefficient (k_q)	0.909
Poisson's ratio (ν)	0.3	Beam area (A_0)	0.0004 (m^2)
Density(γ)	7850 (N/m^3)	Slenderness ratio	20

In Table 2.9, the slenderness ratio is defined as $2R/r$[43], in which R and r represent the radius of circular beam and the beam's cross-section, respectively. As it is a circular cross-section beam, the area moment can be easily obtained through $I=\pi\ (2r)^4/64$. The shear modules can be obtained through $G=E/2(1+\nu)$. The results for the first four dimensionless natural frequencies defined as "definition 2" in Table 2.2, are listed in Table 2.10. Again, excellent agreement is observed with the results in published literatures.

Now, the natural frequency of the circular beam with different boundary conditions and arch angles has been evaluated using the developed methodology, and the results show

perfect agreement with those in available literatures. Next, the proposed finite element approach will be utilized to evaluate the natural frequency of non-circular curved beam.

Table 2.10 Dimensionless frequencies of uniform circular beam with clamped-clamped boundary conditions (Case 1).

Arch angle (Φ)	Mode	Yildirim[28]	Eisenberger and Efraim[43]	Irie *et al*[175]	Present
60°	1	23.799	23.799185	23.75	23.8013
	2	39.144	39.144203	39.05	39.1433
	3	62.976	62.976120	62.38	62.9772
	4	71.042	71.041569	70.71	71.0424
120°	1	10.629	10.629336	10.61	10.6266
	2	15.194	15.193805	15.19	15.2006
	3	24.756	24.755831	24.72	24.7613
	4	30.598	30.598384	30.47	30.6
180°	1	4.160	4.160407	4.151	4.156
	2	8.546	8.545747	8.542	8.5437
	3	15.481	15.480691	15.46	15.4796
	4	17.921	17.921279	17.91	17.9454

Example 4: Parabolic, elliptical and sinusoidal uniform curved beams

In this example, the parabolic, sinusoidal and elliptical arches, as shown in Figure 2.8, are investigated for their dimensionless natural frequencies. To facilitate the numerical study, the following dimensionless variables are defined: $f = h/L$ (arch rise to the span length), $SR = L/\sqrt{(I/A)}$ (slenderness ratio) and $\xi = x/L$. The cross-sectional area, second moment of area of the beam, and all beam material properties are similar to those given in Example 1. The Dimensionless equation for the parabolic arch (Figure 2.8a) is defined as[35]:

$$y = 4f\xi(1-\xi); \qquad 0 \le \xi \le 1 \tag{2.27}$$

And the dimensionless equation for the sinusoidal arch (Figure 2.8b) is defined as[35]:

$$y = f - c_1 + c_1 \sin(c_2 \xi + \varepsilon c_2)\,;\ 0 \le \xi \le 1 \tag{2.28}$$

where

$$c_2 = \pi/(1+2\varepsilon)\,; c_1 = f/[1-\sin(\varepsilon c_2)] \tag{2.29}$$

The dimensionless equation for the elliptical arch (Figure 2.8c) can be written as:

$$y = b_2\sqrt{1-\{1-[\xi - b_1\cos(a)]/b_1\}^2} - b_2\sin(a)\,; \quad 0 \le \xi \le 1 \tag{2.30}$$

where

$$b_1 = \varepsilon + 0.5\,;\ a = \arccos(0.5/b_1);\ b_2 = f/[1-\sin(a)] \tag{2.31}$$

The numerical results for the first four dimensionless natural frequencies defined as "Definition 1" in Table 2.2, are listed in Table 2.11. As it can be realized that the results are in excellent agreement with those reported by Oh *et al*[35].

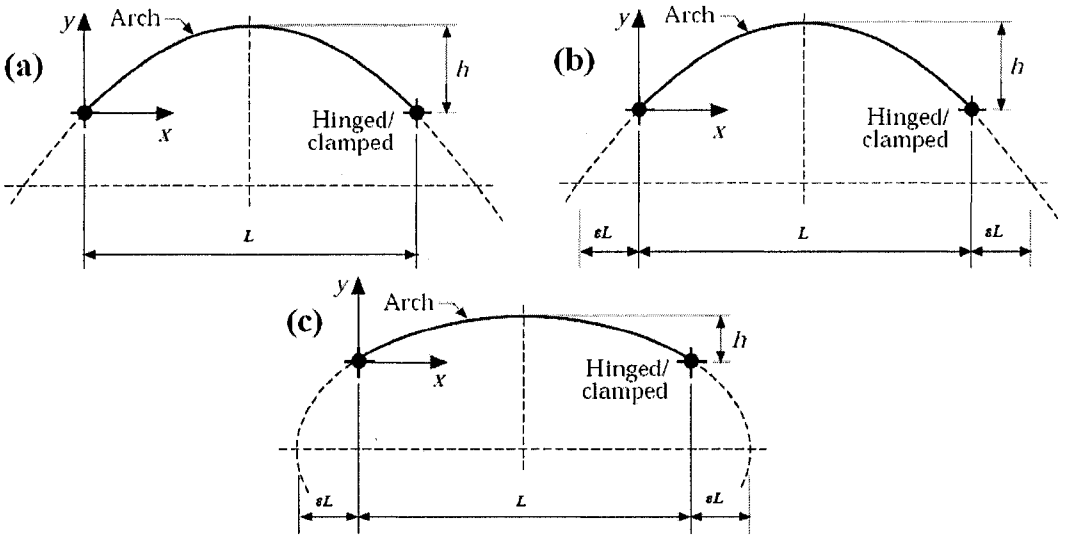

Figure 2.8 Different types of curved beams: (a) Parabolic; (b) Sinusoidal; (c) Elliptical.

Table 2.11 Dimensionless frequencies for the parabolic, elliptical and sinusoidal curved beams with different boundary conditions (Case 1).

Geometry of arch	Mode	Oh *et al*[35]	Present study
Parabolic	1	21.83	21.7478
pinned-pinned	2	56.00	55.4894
$f = 0.3$, $SR = 75$,	3	102.3	100.7214
$k_q G/E = 0.3$	4	113.4	113.4976
Elliptic ($\varepsilon = 0.5$)	1	35.25	34.892
pinned-clamped	2	57.11	56.766
$f = 0.2$, $SR = 50$,	3	83.00	81.420
$k_q G/E = 0.3$	4	128.2	124.288
Sinusoid ($\varepsilon = 0.5$)	1	56.3	56.0836
clamped-clamped	2	66.14	66.0952
$f = 0.1$, $SR = 100$,	3	114.3	113.4277
$k_q G/E = 0.3$	4	181.7	179.3567

Example 5: General non-uniform and non-circular curved beams

In above four examples, the natural frequencies for circular beams with different arch angles (Φ) and also different type of non-circular beam with different boundary conditions have been investigated and by comparing the results with those in available literatures, the validity of the proposed finite element approach has been verified. In this section a general curved beam with clamped-clamped boundary condition, which represents an overpass bridge shown in Figure 2.9, will be investigated. It should be noted that this type of curved beam has a variable radius of curvature. The physical properties of the curved beam are listed in Table 2.12.

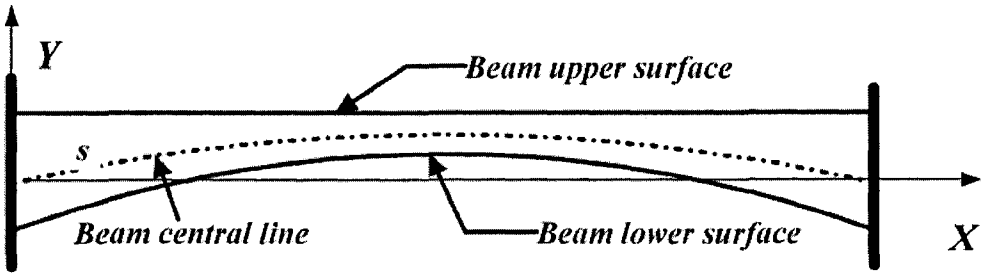

Figure 2.9 General non-uniform and non-circular curved beam representing an overpass bridge.

Table 2.12 Properties of the general non-uniform and non-circular curved beam.

Elastic modulus(E)	70 (*GPa*)	Shear coefficient(k_q)	0.8438
Shear modulus(G)	24.50 (*GPa*)	Beam width	2 (*m*)
Density(γ)	2777 (Kg/m^3)	Beam span length	40 (*m*)
Beam upper and lower surface functions	$y = 2$ (*m*), $y = -0.005\ x^2 + 0.2x - 2$ (*m*)		
Central line function	$y = -0.0025x^2 + 0.1x$ (*m*)		

The variations of the first four natural frequencies with respect to the number of elements for the finite element model are shown in Figure 2.10. The first four associated modal shapes and the beam's deformations are also illustrated in Figures 2.11 and 2.12, respectively.

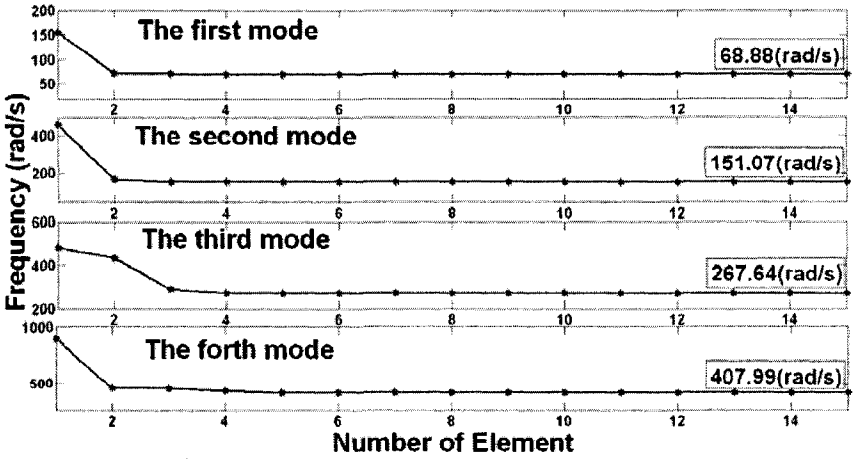

Figure 2.10 Finite element model convergence analysis for the clamped-clamped general non-uniform and non-circular curved beam.

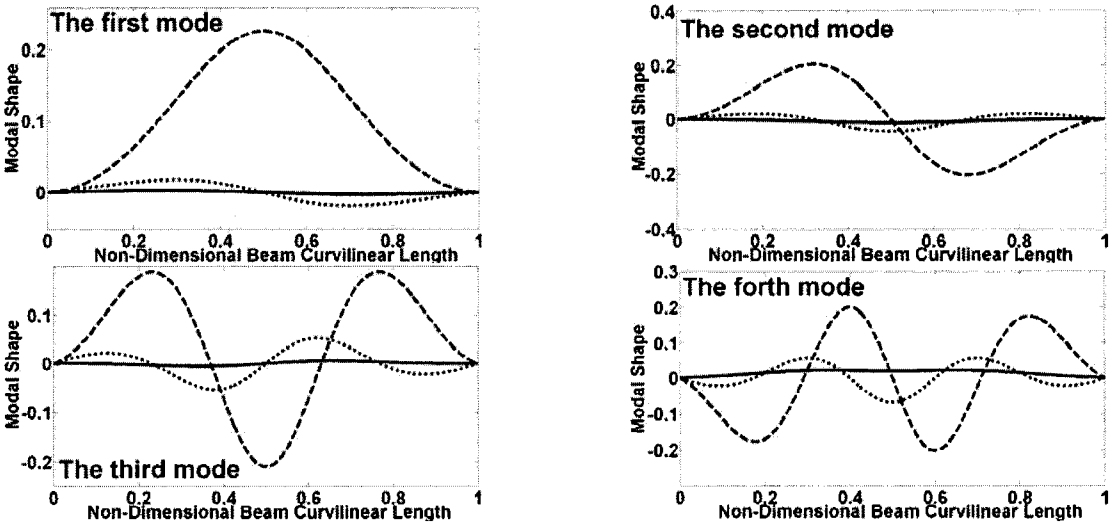

Figure 2.11 The first four vibration modal shapes of the general non-uniform and non-circular curved beam with the clamped-clamped boundary condition. Solid, dashed and dotted lines represent mode shapes for u, w and ψ, respectively.

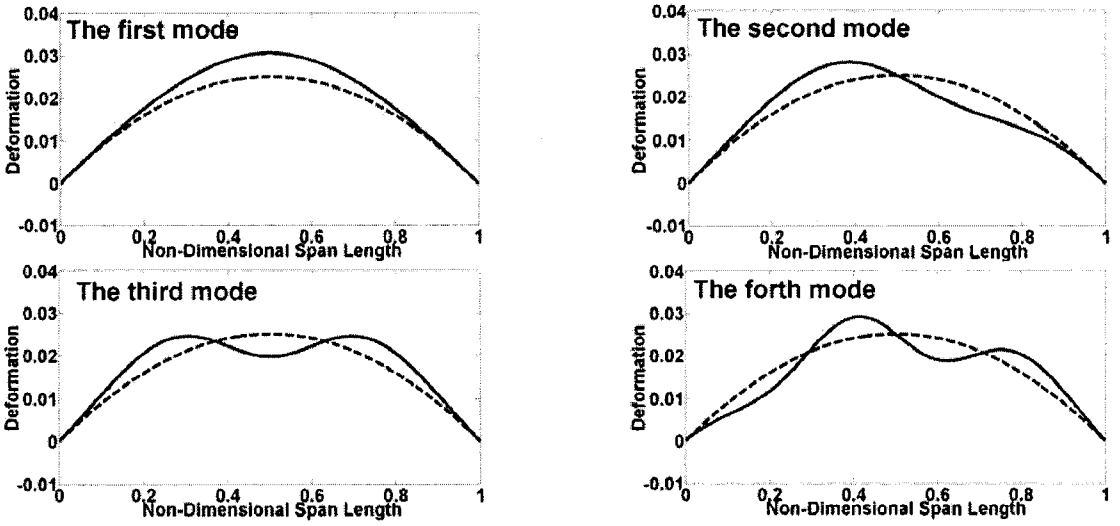

Figure 2.12 The deformations relative to the first four vibration modes for the general non-uniform and non-circular curved beam with the clamped-clamped boundary condition. Solid and dashed lines represent deformed and un-deformed configuration, respectively.

It can be realized from Figure 2.10 that the natural frequencies converge rapidly with the increase of the number of elements in the finite element model and there is no significant changes in the natural frequencies for the number of elements higher than 6.

2.4.3 Curved beam model (Case 2)

The natural frequencies of a uniform circular beam are once again studied in this section, but this time the effects of the axial extensibility ($du_T(s)/ds$), shear deformation and rotary inertia of the curved beam have all been neglected. The parameters related to the tangential inertial force, which are presented in Equations (2.13), (2.16) and (2.23), have also been neglected in order to compare the results with those reported in available literature[12]. The first 10 dimensionless natural frequencies defined as "Definition 2" in Table 2.2, of the circular beam with various curve angles and different boundary conditions are listed in Tables 2.13 to 2.16, and were compared with those presented by Henrych[12]. In this example 10 'curved beam elements' (4 nodes per element), similar to that for Case 1, is utilized to evaluate the nodal cross-sectional area, moment of inertia, radius of curvature and geometrical Jacobian matrix, and then 10 'curved beam elements' (2 nodes per element), as given in Equation (2.21), are employed to evaluate the nodal displacement vector for Case 2.

To compare the related results with those for curved beam model (Case 1), the last columns of Tables 2.13 and 2.14 are the dimensionless natural frequencies defined by "Definition 1" in Table 2.2 for the pinned-pinned and the clamped-clamped circular beam with the curve angle Φ of 90°, respectively.

Table 2.13 Dimensional natural frequencies of a uniform circular beam with the pinned-pinned boundary conditions (Case 2)

Mode	Φ=20° Henrych[12]	Φ=20° Present	Φ=40° Henrych[12]	Φ=40° Present	Φ=80° Henrych[12]	Φ=80° Present	Φ=120° Henrych[12]	Φ=120° Present	Φ=160° Henrych[12]	Φ=160° Present	Φ=90°
1	323.000	323.000	80.000	80.000	19.250	19.250	8.000	8.000	4.063	4.063	37.011
2	690.898	690.890	172.005	172.006	42.283	42.283	18.261	18.261	9.855	9.855	81.937
3	1295.000	1295.024	323.000	323.006	80.000	80.002	35.000	35.000	19.250	19.250	155.449
4	1988.835	1988.966	496.470	496.503	123.379	123.388	54.288	54.292	30.107	30.109	240.040
5	2915.000	2915.595	728.000	728.149	181.250	181.288	80.000	80.017	44.563	44.572	352.911
6	3933.560	3935.449	982.646	983.118	244.917	245.036	108.301	108.354	60.485	60.515	477.197
7	5183.000	5188.535	1295.000	1296.384	323.000	323.347	143.000	143.155	80.00	80.087	629.864
8	6525.941	6538.970	1630.739	1633.998	406.938	407.754	180.309	180.672	100.988	101.194	794.424
9	8099.000	8101.399	2024.000	2024.600	505.250	505.400	224.000	224.067	125.563	125.600	984.786
10	9766.176	9828.878	2440.797	2456.476	609.452	613.375	270.314	272.060	151.615	152.600	1195.293

Table 2.14 Dimensional natural frequencies of a uniform circular beam with the clamped-clamped boundary conditions (Case 2)

Mode	Φ=20° Henrych[12]	Φ=20° Present	Φ=40° Henrych[12]	Φ=40° Present	Φ=80° Henrych[12]	Φ=80° Present	Φ=120° Henrych[12]	Φ=120° Present	Φ=160° Henrych[12]	Φ=160° Present	Φ=90°
1	505.404	504.404	125.792	125.792	30.894	30.894	13.328	13.328	7.190	7.190	59.851
2	910.100	908.105	226.910	226.912	56.114	56.115	24.488	24.489	13.423	13.424	108.977
3	1639.391	1639.445	409.204	409.218	101.658	101.662	44.707	44.708	24.775	24.776	197.752
4	2374.823	2375.064	593.043	592.103	147.598	147.613	65.109	65.116	36.239	36.243	287.322
5	3421.348	3422.394	854.661	854.923	219.989	213.055	94.161	94.191	52.572	52.590	414.895
6	4483.458	4486.607	1120.178	1120.966	279.358	279.556	123.651	123.740	69.154	69.205	544.536
7	5851.325	5860.895	1462.137	1464.532	364.841	365.441	161.638	161.906	90.517	90.669	711.969
8	7238.872	7267.536	1809.018	1816.189	451.555	453.352	200.173	200.975	112.189	112.643	883.353
9	8929.311	8943.932	2231.623	2235.282	557.201	558.119	247.123	247.534	138.596	138.829	1087.599
10	10641.76	10704.02	2659.730	2675.387	664.224	668.143	294.686	296.431	165.348	166.076	1302.093

Table 2.15 Dimensional natural frequencies of a uniform curved beam with the clamped-pinned boundary conditions (Case 2)

Mode	Φ=20° Henrych[12]	Φ=20° Present	Φ=40° Henrych[12]	Φ=40° Present	Φ=80° Henrych[12]	Φ=80° Present	Φ=120° Henrych[12]	Φ=120° Present	Φ=160° Henrych[12]	Φ=160° Present
1	407.417	407.417	101.203	101.203	24.652	24.652	10.482	10.482	5.529	5.529
2	797.909	797.912	198.816	198.817	49.045	49.045	21.312	21.312	11.608	11.608
3	1460.549	1460.585	364.441	364.451	90.415	90.417	39.670	39.671	21.911	21.911
4	2178.817	2178.995	544.006	544.051	135.304	135.315	59.619	59.624	33.130	33.132
5	3161.588	3162.378	789.684	789.882	196.709	196.758	86.899	86.921	48.465	48.478
6	4205.315	4207.747	1050.615	1051.224	261.940	262.093	115.890	115.958	64.772	64.811
7	5510.606	5517.811	1376.930	1378.732	343.511	343.963	152.137	152.339	85.157	85.271
8	6879.112	6897.378	1719.056	1723.625	429.041	430.186	190.150	190.661	106.539	106.827
9	8507.617	8520.880	2126.177	2129.496	530.817	531.649	235.380	235.752	131.977	132.188
10	10200.606	10262.610	2549.424	2564.929	636.629	640.509	282.407	284.135	158.430	159.404

Table 2.16 Dimensional natural frequencies of a uniform circular beam with the clamped-free boundary conditions (Case 2)

Mode	Φ=20° Henrych[12]	Φ=20° Present	Φ=40° Henrych[12]	Φ=40° Present	Φ=80° Henrych[12]	Φ=80° Present	Φ=120° Henrych[12]	Φ=120° Present	Φ=160° Henrych[12]	Φ=160° Present
1	29.101	29.101	7.462	7.462	2.064	2.064	1.084	1.084	0.766	0.766
2	180.235	180.235	44.611	44.611	10.721	10.721	4.470	4.470	2.315	2.315
3	505.606	505.607	125.845	125.845	30.910	30.910	13.337	13.337	7.197	7.197
4	991.426	991.436	247.243	247.246	61.200	61.200	26.750	26.750	14.696	14.697
5	1639.392	1639.464	409.204	409.222	101.658	101.663	44.707	44.709	24.775	24.777
6	2449.366	2449.709	611.678	611.764	152.257	152.279	67.180	67.189	37.404	37.409
7	3421.348	3422.617	854.661	854.978	212.989	213.069	94.161	94.197	52.572	52.593
8	4555.335	4559.249	1138.147	1139.127	283.851	284.096	125.648	125.758	70.277	70.339
9	5851.325	5862.148	1462.137	1464.845	364.841	365.519	161.638	161.940	90.517	90.688
10	7309.317	7342.488	1826.630	1834.926	455.958	458.036	202.130	203.057	113.290	113.814

One can realize form Tables 2.13-2.16 that the dimensionless natural frequencies evaluated using the developed finite element approach agree perfectly with those provided by Henrych[12]. Comparing the natural frequencies listed in the last column of Tables 2.13 and 2.14 with the corresponding values in Tables 2.6 and 2.8 for Case 1, one can realize the significant effects of the shear deformation, rotary inertia and axial extensibility ($du_T(s)/ds$), especially, for the higher modes. For instance, the first non-dimensional fundamental natural frequency for the pinned-pinned circular beam with $\Phi = 90^\circ$ is 29.276 for Case 1 compared to 37.011 for Case 2, while the 10^{th} natural frequency of the beam is 234.116 for Case 1 compared to 1195.293 for Case 2. Similarly, the first non-dimensional fundamental natural frequency for the clamped-clamped circular beam with $\Phi = 90^\circ$ is 36.713 in Case 1 compared to 59.851 in Case 2 while the 10^{th} natural frequency of the beam is 249.2148 in Case 1 compared to 1302.093 in Case 2.

2.5 Conclusions and Summary

In this Chapter, the governing differential equations for the Timoshenko beam and general curved beam (including and excluding the effects of the axial extensity ($du_T(s)/ds$), shear deformation and rotary inertia) are derived using the extended Hamilton principle and then cast into finite element method.

A '4-node' Lagrangian type Timoshenko beam element with two-degree of freedom per node has been presented to solve both uniform and non-uniform Timoshenko beams. The results are in excellent agreement with those reported in published literatures. Moreover, a '4-node' Lagrangian type curved beam element with three-degree of freedom per node

has been developed to study the curved beam model considering the axial extensibility ($du_T(s)/ds$), shear deformation and rotary inertia (Case 1), and then combined with the curvilinear integral method to solve both the uniform and non-uniform curved beam with variable curvatures. The results for the conventional geometry (circular, parabolic, sinusoidal and elliptical curves) are in excellent agreement with those reported in published literatures.

Furthermore, a 'two-node' curved beam element with three-degree of freedom per node has also been proposed to study the curved beams' deformation relationship excluding the effects of the axial extensibility ($du_T(s)/ds$), shear deformation and rotary inertia (Case 2). The '4-node' Lagrangian type shape function are utilized to interpolate the geometrical properties of the curved beams. The equations of motion in finite element form were obtained by the curvilinear integral method and Gauss Quadrate technique. Results obtained are in excellent agreement with those available in literature for different boundary conditions and curve angles. It has been shown that the effect of the axial extensibility ($du_T(s)/ds$), shear deformation and rotary inertia is significant[21].

It has also been shown that by using the finite element method with appropriate shape functions, the dynamic property of the curved beam with different geometry and boundary conditions can be accurately obtained. Therefore, the beam elements developed in this chapter will be utilized to model and investigate the vibration suppression problem for beam-type structures using TMD and SAMD technologies, which will be presented in the following chapters.

CHAPTER 3

VIBRATION SUPPRESSION OF TIMOSHENKO BEAM USING TUNED MASS DAMPER

3.1 Introduction

Based on the literature review presented in Chapter 1, one can easily find that previous works about the Tuned Mass damper (TMD) system are mainly focused on attaching TMD onto Single-Degree-of-Freedom (SDOF) or discrete Multi-Degree-of-Freedom (MDOF) systems. For continuous systems, such as uniform beams, the problems are typically simplified to a SDOF system based on the fundamental modal shape of the continuous system[84]. This methodology has some restrictions, which have been summarized in Chapter 1. Therefore, this chapter concentrates on studying the uniform Timoshenko beam with one attached TMD. Subsequently, the optimal TMD parameters will be compared with those reported in published literatures, to verify the validity of the optimal TMD design for beam-type structures using the developed design optimization algorithm.

3.2 Equations of Motion for Timoshenko Beam with Attached TMD

In this section, a detailed and comprehensive procedure for the equations of motion in finite element form for Timoshenko beam with the attached TMD system, as illustrated in Figure 3.1, is presented. Here, for the sake of simplicity, the formulation for the

Timoshenko beam with one TMD system has been derived using the extended Hamilton principle. However, the mathematical modeling procedure can be easily extended to multiple TMD system.

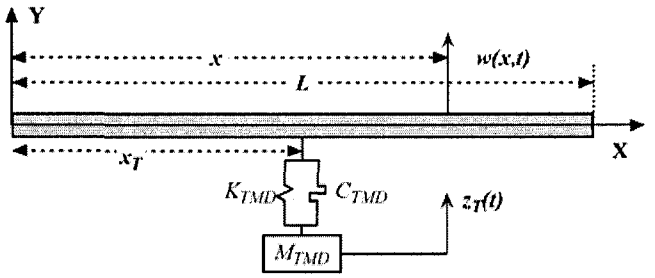

Figure 3.1 The Timoshenko beam with the attached Tuned Mass Damper (TMD) system.

In Figure 3.1, K_{TMD}, C_{TMD} and M_{TMD} represent the spring stiffness, damping and mass of the designed TMD system, respectively, and L is the beam length. The extended Hamilton principle can be described as:

$$\int_{t_1}^{t_2}(\delta T - \delta V + \delta W_{nc})dt = 0\ ;\quad \delta(.)=0 \text{ at } t=t_1, t_2 \tag{3.1}$$

where the kinetic (T) and potential (V) energies and the non–conservative virtual work (δW_{nc}) for the Timoshenko beam with one attached TMD system could be described as:

$$T = \frac{1}{2}\int_0^L m(x)\left(\frac{\partial w(x,t)}{\partial t}\right)^2 dx + \frac{1}{2}\int_0^L J(x)\left(\frac{\partial \psi(x,t)}{\partial t}\right)^2 dx + \frac{1}{2}M_{TMD}\,\dot{z}_T(t)^2 \tag{3.2}$$

$$V = \frac{1}{2}\int_0^L EI(x)\left(\frac{\partial \psi(x,t)}{\partial x}\right)^2 dx + \frac{1}{2}\int_0^L k_q GA(x)\beta^2(x,t)dx + \frac{1}{2}K_{TMD}\left(w(x_T,t)-z_T(t)\right)^2 \tag{3.3}$$

$$\delta W_{nc} = \int_0^L f(x,t)\delta w dx + L\int_0^L -C\dot{w}(x,t)\delta w dx - C_{TMD}(\dot{w}(x_T,t)-\dot{z}_T(t))\delta(w(x_T,t)-z_T(t)) \tag{3.4}$$

where E, G, k_q, $m(x)$, $A(x)$, $I(x)$, $J(x)$, l, w, β and ψ have the same definitions as those presented in Equations (2.2). C represents the viscous damping. z_T and $w(x_T,t)$ represent the displacement of the attached TMD and beam's transverse displacement at the point (x_T) of attachment TMD system, respectively. $f(x,t)$ represents the external force. Considering the Timoshenko beam's deformation relationship ($\partial w/\partial x = \psi + \beta$), as stated in Equation (2.1), and Equations (3.2)-(3.4), and then applying the Hamilton's principle, as stated in Equation (3.1), the following three governing differential equations of motion may be obtained.

$$\begin{aligned} &-m(x)\frac{\partial^2 w(x,t)}{\partial t^2} - C\frac{\partial w(x,t)}{\partial t} + \frac{\partial}{\partial x}\left[k_q GA(x)\left(\frac{\partial w(x,t)}{\partial x} - \psi(x,t)\right)\right] + f(x,t) \\ &-C_{TMD}\left(\frac{\partial w(x_T,t)}{\partial t} - \dot{z}_T(t)\right)\vartheta(x-x_T) - K_{TMD}(w(x_T,t) - z_T(t))\vartheta(x-x_T) = 0 \end{aligned} \tag{3.5a}$$

$$-J(x)\frac{\partial^2 \psi(x,t)}{\partial t^2} + \frac{\partial}{\partial x}\left(EI(x)\frac{\partial \psi(x,t)}{\partial x}\right) + k_q GA(x)\left(\frac{\partial w(x,t)}{\partial x} - \psi(x,t)\right) = 0 \tag{3.5b}$$

$$M_{TMD}\ddot{z}_T + C_{TMD}(\dot{z}_T(t) - \dot{w}(x_T,t)) + K_{TMD}(z_T - w(x_T,t)) = 0 \tag{3.5c}$$

where the symbol $\vartheta(x-x_T)$ is set to unity when $x = x_T$, otherwise is equal to zero. Now, utilizing Equations (3.5), and the finite element approach presented in Chapter 2, the following equations of motion in the finite element form can be obtained:

$$[M]\{\ddot{q}(t)\} + [C]\{\dot{q}(t)\} + [K]\{q(t)\} = \{F(t)\} \tag{3.6}$$

where

$$\{q\} = \{\{W(t)\} \quad \{\Psi(t)\} \quad z_T(t)\}^T \tag{3.7a}$$

$$[M] = \begin{bmatrix} [M_{ww}] & [0] & [0] \\ [0] & [M_{\psi\psi}] & [0] \\ [0] & [0] & M_{TMD} \end{bmatrix} \tag{3.7b}$$

$$[C]=\begin{bmatrix}[C_{ww}]+[C_{wTMD}] & [0] & -[C_{zTMD}] \\ [0] & [0] & [0] \\ -[C_{zTMD}]^T & [0] & C_{TMD}\end{bmatrix} \tag{3.7c}$$

$$[K]=\begin{bmatrix}[K_{ww}]+[K_{wTMD}] & [K_{w\psi}] & -[K_{zTMD}] \\ [K_{w\psi}]^T & [K_{\psi\psi}] & [0] \\ -[K_{zTMD}]^T & [0] & K_{TMD}\end{bmatrix} \tag{3.7d}$$

$$\{F(t)\}=\left\{\sum_{element}\begin{bmatrix}\int_{-1}^{1}\{[N(\eta)]f(\eta,t)\bar{J}(\eta)d\eta\}, & \{0\}_{\psi}, & 0\end{bmatrix}\right\}^T, \tag{3.7e}$$

where $[N(\eta)]$ and $\bar{J}(\eta)$ are the shape function and Jacobian between the natural coordinates and physical coordinates, which have been defined in Chapter 2 and presented in "Appendix A". In equivalent nodal force vector $\{F(t)\}$, expression $\{0\}_{\psi}$ represents the null vector with the same size as $\{\Psi(t)\}$. The sub-matrices $[M_{ww}]$, $[M_{\psi\psi}]$, $[K_{ww}]$, $[K_{w\psi}]$ and $[K_{\psi\psi}]$ in the mass and stiffness matrices have the same definitions as Equations (2.5) and presented in "Appendix A". All the other sub-matrices are defined in the "Appendix F". For the sake of numerical stability, the following transform matrix is defined to transfer the nodal displacement vector to a dimensionless vector.

$$[T]=\begin{bmatrix}L_e[I]_w & [0] & [0] \\ [0] & [I]_{\psi} & [0] \\ [0] & [0] & L_e\end{bmatrix} \tag{3.8}$$

where L_e is the length between two nodes for Timoshenko beam element and $[I]_w$ and $[I]_{\psi}$ are the identity matrices with sizes corresponding to vectors $\{W\}$ and $\{\Psi\}$, respectively. Thus the nodal displacement vector $\{q\}$ can be expressed as $\{q\}=[T]\{q_d\}$, where $\{q_d\}$ is a dimensionless vector, and then Equation (3.6) can be transferred to the following form:

$$[M_d]\{\ddot{q}_d(t)\}+[C_d]\{\dot{q}_d(t)\}+[K_d]\{q_d(t)\}=\{F_d(t)\} \tag{3.9}$$

where $[M_d]=[T]^T[M][T]$, $[C_d]=[T]^T[C][T]$, $[K_d]=[T]^T[K][T]$ and $\{F_d(t)]=[T]^T\{F(t)\}$. Therefore, the response, which will be defined in numerical example, will be also dimensionless.

3.3 Random Vibration State-Space Analysis

Structural systems are typically subjected to the random type loading. In this work, the optimal design of TMD systems are also been studied for structures under random loading. For a typical random vibration problem, the mean value of the response can be obtained through static analysis, thus the problem would be focused on structures subject to random loading with zero mean value. In general, the random vibration analysis are concentrated on two important criterions, the variance and Power Spectral Density (PSD) function, in which the first one reflects the performance in time domain and the second one represents that in frequency domain. The PSD function can be obtained directly through the transfer function. The general procedure to obtain the variance of response can be summarized as: Decoupling the equations of motion utilizing the fundamental modal shape (eigenvector), then analyzing each vibration mode as a SDOF system, finally using some numerical methodologies, such as Square Root of the Sum of Squares method, Absolute Method, Naval Research Laboratory method, Closed Method, Modified Root Sum of Squares method or Combined Quadratic Combination method[87], to obtain the variance of response. For more detail information about the methodologies presented above, one can consult the textbook by Wirsching[87].

In this dissertation, the random vibration matrix analysis method[176] will be utilized to find the variance of structural response, which will be considered subsequently as the

objective function of the optimal TMD design problem. The basic idea of the random vibration matrix analysis method is to transfer the equations of motion stated in Equation (3.9) to the following state-space form, which is a first-order differential equation.

$$\{\dot{z}(t)\} = [A]\{z(t)\} + [B]\{F_d(t)\} = [A]\{z(t)\} + \{Q(t)\}, \tag{3.10}$$

where $\{z\}$ is the state vector $\{q_d, \dot{q}_d\}^T$, and

$$[A] = \begin{bmatrix} [0] & [I] \\ -[M_d]^{-1}[K_d] & -[M_d]^{-1}[C_d] \end{bmatrix} \text{ and } [B] = \begin{bmatrix} [0] \\ [M_d]^{-1} \end{bmatrix} \tag{3.11}$$

It should be noted that the mean value is assumed to be zero, thus the variance is equal to the mean-square-value, the covariance is equal to the correlation and the autocovariance is also equal to the autocorrelation. In the frequency domain, knowing the PSD function of external excitation $[S_{QQ}(\omega)]$, the PSD of state-space vector, as stated in Equation (3.10), can be obtained through:

$$[S_{zz}(\omega)] = [i\omega[I] + [A_s]]^{-1}[S_{QQ}(\omega)]([-i\omega[I] + [A_s]]^{-1})^T \tag{3.12}$$

where $[A_s]$=-$[A]$. It is noted that for the stationary random process, the PSD of external excitation is a constant matrix, and thus $[S_{QQ}(\omega)]$ can be simplified as $[S_0]$, and then the expression of state-space covariance equation can be simplified as[176]:

$$[A_s][C_{zz}] + [C_{zz}][A_s]^T = 2\pi[S_0] \tag{3.13}$$

where $[C_{zz}]$ represents the covariance matrix, in which the diagonal components are the variance of every variables in the state-space vector $\{z(t)\}$ and other components are the covariance. A simple derivative procedure for Equation (3.13) has been provided in "Appendix G", and for more information one can consult the textbook by Lutes and

Sarkani[176]. In fact, the Equation (3.13) is a Lyapunov equation and can be easily solved. The RMS of response is basically the square root of variance.

3.4 Optimization Approach

In this section the objective function for the optimal TMD design approach will be established first. As the established objective function will be utilized in this chapter and also next chapter (Chapter 4), the objective function in general form will also be presented in this section. Then, the Sequential Quadratic Programming (SQP) method will be implemented to find the optimal design TMD parameters in this chapter.

3.4.1 Optimization problem

In this dissertation, the objective of the design optimization problem is to find the optimal values of the location, damping coefficient and stiffness of the TMD system in order to minimize the RMS of the beam's deflection subjected to random loading. For the sake of numerical stability, the following dimensionless parameters are defined for the attached TMD system.

$$\mu_i = \frac{M_{TMDi}}{M_{structure}},\ f_{TMD_i} = \frac{\omega_{TMDi}}{\omega_n} \text{ and } \xi_{TMD_i} = \frac{C_{TMDi}}{2\sqrt{K_{TMDi} M_{TMDi}}} \tag{3.14}$$

where ω_n and $M_{structure}$ are the n^{th} natural frequency and mass of the main structure. M_{TMDi}, K_{TMDi}, C_{TMDi} and $\omega_{TMDi} = \sqrt{K_{TMDi} / M_{TMDi}}$ are the mass, stiffness, viscous damping and natural frequency of the i^{th} attached TMD, respectively. Dimensionless variables μ_i, f_{TMDi} and ξ_{TMDi} are mass ratio, frequency ratio and damping factor of the i^{th} attached TMD, respectively. Now the optimization problem for the beam with attached TMD system under given mass ratio (μ), subjected to random excitation can be described as:

$$
\begin{array}{lll}
\text{Find the design variables:} & \{DV\}=\{\xi_{TMDi}, f_{TMDi}, \eta_{TMDi}\} & \\
\text{To minimize:} & \textit{RMS of Deflection} & (3.15) \\
\text{Subjected to:} & 0\leq \xi_{TMDi}\leq 1,\ 0\leq f_{TMDi}\leq 2.5,\ -1\leq \eta_{TMDi}\leq 1. &
\end{array}
$$

where η_{TMDi} represents the position of the i^{th} attached TMD system in the natural coordinate (η), and the objective function is the solution of Equation (3.13). It is noted that the mass ratio (μ) is a given input in the optimization problem and practically the ratio of the total mass of the attached TMD system to the mass of the beam should not be greater than 10%, otherwise the attached TMD will change the structural dynamic properties significantly[82]. As the numerical examples provided in this chapter are based on the single attached TMD with fixed position, the design optimization problem stated in Equation (3.15) would be simplified as:

$$
\begin{array}{lll}
\text{Find the design variables:} & \{DV\}=\{f_{TMD}, \xi_{TMD}\} & \\
\text{To minimize:} & \textit{RMS of Deflection} & (3.16) \\
\text{Subjected to:} & 0\leq f_{TMD}\leq 2.5,\ 0\leq \xi_{TMD}\leq 1 &
\end{array}
$$

3.4.2 Optimization algorithm

Sequential Quadratic Program (SQP) technique, which is a powerful and robust gradient based optimization algorithm, has been employed to solve the optimization problem stated in Equation (3.16). Here the most essential issues of the SQP technique will be reviewed. For more details information about SQP optimization methodology, one may consult the books by Arora[88] or Rao[89]. The main idea of the SQP optimization method is to generate a Quadratic Programming (QP) problem based on the quadratic approximation of the Lagrangian function described as[88, 89]:

$$
L(\{DV\},\lambda) = f(\{DV\}) + \sum_{i=1}^{m} \lambda_i g_i(\{DV\}) \tag{3.17}
$$

where $\{DV\}$, $\{g_i\}$ and $\{\lambda_i\}$ are the design variable vector, the i^{th} constraint and Lagrange multiplier, respectively. $f(.)$ represents the objective function. The SQP implementation consists of three main steps: (1) a QP Sub-problem solution; (2) a linear searching based on the value of objective function; (3) updating the Hessian matrix of the Lagrangian function given by Equation (3.17). The procedure proceeds by solving a QP sub-problem at each major iteration. The solution of the QP sub-problem generates an estimate of the Lagrange multiplier (λ) and a search direction vector $\{d\}$ in each iteration (k), which is utilized to generate a new iteration as:

$$\{q\}_{k+1} = \{q\}_k + \alpha_k \{d\}_k \tag{3.18}$$

where α_k represents the step length at the k^{th} iteration and it should be determined by using an appropriate line search technique (one-dimensional minimization) in order to produce a sufficient decrease in the merit function. Then the Hessian of the Lagrangian, which is required for the solution of the next positive definitive quadratic programming problem, is updated using the Broyden Fletcher Goldfarb Shanno (BFGS) formula[88, 89]. It should be noted that the SQP optimization methodology is a typical local optimization technology, which is capable to find the local optimum points. In this chapter the SQP algorithm has been executed for multitude of random initial points to ensure that the global optimal point has been caught.

3.5 Numerical Results

A uniform Timoshenko beam with the attached mid-span TMD, as illustrated in Figure 3.1, will be investigated in this section. The boundary condition is clamped-clamped. The physical and geometrical properties of the beam have been listed in Table 3.1.

Table 3.1 Properties of the Timoshenko beam[84].

Elastic Modulus	29.43 (*GPa*)	Second moment of area	8.72 (m^4)
Shear Modulus	24.50 (*GPa*)	Shear coefficient (k_q)	0.41
Mass per unit length	36056 (*Kg/m*)	Beam structural damping	0
Cross Sectional Area	7.94 (m^2)	Beam length (*L*)	40 (*m*)

The first five natural frequencies of the beam are evaluated using the finite element method presented in Chapter 2, and then compared with those obtained analytically[84], as provided in Table 3.2.

Table 3.2 The first five natural frequencies of the Timoshenko beam.

	ω_1 (*rad/s*)	ω_2 (*rad/s*)	ω_3 (*rad/s*)	ω_4 (*rad/s*)	ω_5 (*rad/s*)
Analytical Solutions[84]	36.280	93.550	168.125		
finite element Method	35.451	92.084	168.609	259.10	359.64

In this chapter, the optimal TMD design based on both random and harmonic loadings will be presented, and the results will be compared with those available in published literatures. Here, it should be noted that the beam has been modeled using 7 Timoshenko beam elements with 4 nodes per element, which has been presented in Chapter 2.

3.5.1 Optimization based on random excitation

In this section, the random loading is assumed to be in the form of white noise with PSD function of 10^{10} ($N^2 rad/s$) applied uniformly perpendicular to the central line of beam. Here three different cases have been investigated. In Case (1), the RMS of the first vibration modal response has been considered as the objective function, in Case (2), the RMS of the beam's mid-span transverse response (w) has been selected as objective function and in Case (3) the optimal results based on simplified SDOF system under random loading would be investigated, which is obtained based on utilizing the

eigenvector of ($[M_d]^{-1}[K_d]$), as stated in Equation (3.9), to separate the first vibration mode as:

$$M_1\ddot{q}_1(t) + K_1 q_1(t) = F_1(t) \tag{3.19}$$

where M_1, K_1, and q_1 represent the modal mass, modal stiffness and modal displacement for the first vibration mode, respectively. It is also assumed that the structural damping is zero and the mass ratio (μ), as defined in Equation (3.14), is changed to $\mu=M_{TMD}/M_1$. As the effect of attached TMD has been assumed to be restricted in the first vibration mode[84] in the numerical model, The problem in Case (3) can be considered as a classical TMD design problem, in which a single TMD is attached to an un-damped SDOF structure. The analytical solution for optimal TMD parameters for an un-damped SDOF structure under the white noise random excitation can be found in Warburton[52] as:

$$f_{TMD} = \frac{\sqrt{1+\mu/2}}{1+\mu} \text{ and } \xi_{TMD} = \sqrt{\frac{\mu(1+3\mu/4)}{4(1+\mu)(1+\mu/2)}} \tag{3.20}$$

For Case (3), the obtained optimal parameters are compared with those based on Equation (3.20) to verify the validity the proposed optimization approach for TMD system as well as the random vibration state-space analysis methodology utilized in this dissertation for TMD design. The optimal frequency ratio (f_{TMD}) and damping factor (ξ_{TMD}) for Cases (1)-(3) and the value of objective function for Cases (1) and (2) with respect to the input mass ratio (changing from 0.01-0.1) have been obtained based on the design optimization problem stated in Equation (3.16). The results are shown in Figure 3.2 and compared with those obtained analytically based on Equation (3.20).

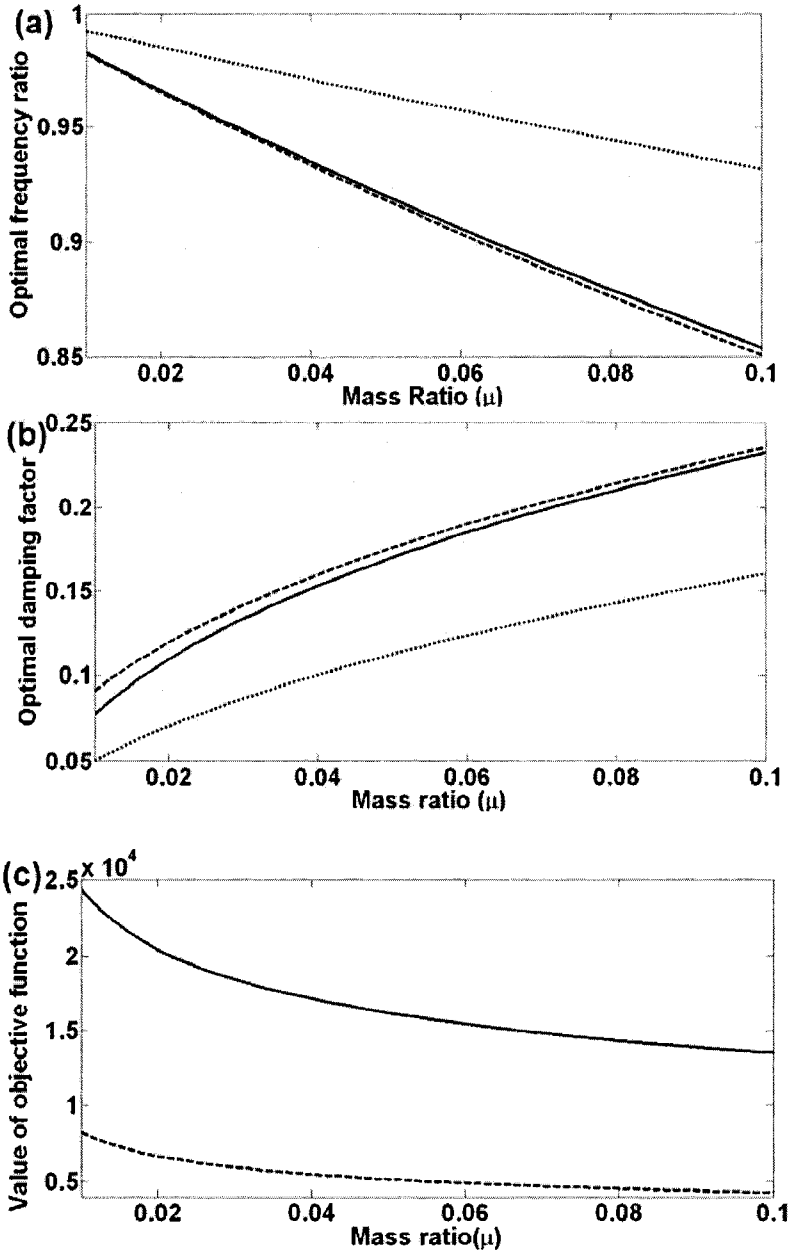

Figure 3.2 Optimal Tuned Mass Damper (TMD) parameters and objective function *vs.* input mass ratio (μ). (a) Optimal frequency ratio (f_{TMD}). (b) Optimal damping factor (ξ_{TMD}). (c) Value of objective function. Solid, dashed and dotted lines represent Cases (1), (2) and (3), respectively. Note: in (a) and (b) the dotted line coincides with Equation (3.20).

One can realize from Figure 3.2 that the optimal parameters for Cases (1) and (2) are in close agreement as expected. This is mainly due to the fact that the first vibration mode is the dominant mode in this example. The optimal results for Case (3) are exactly matching those obtained by Warburton[52], as stated in Equation (3.20), however, they are significantly different from those in Cases (1) and (2). Thus, one can make the conclusion that for the continuous structure with the attached TMD system under the random loading the simplified assumptions made in Case (3) would not generate accurate optimal results. Furthermore, based on the result for Case (3) and its comparison with the analytical solution, one can also find that the developed optimization approach stated in Equation (3.16) are effective in optimal TMD design.

To illustrate the efficiency of the optimal TMD design and also the system response for different cases, typical optimal TMD parameters for mass ratio (μ) equal to 0.01 are selected and provided in Table 3.3. As expected there is not significant different for the optimal frequency ratio (f_{TMD}) between Case (1) and Case (2), which is exactly in agreement with the working principle of the optimal TMD system and also due to the fact that the first vibration mode is the dominant mode in this example.

Table 3.3 Optimal Tuned Mass Damper (TMD) parameters for mass ratio (μ=0.01) under random excitation.

	Optimal Damping Factor (ξ_{TMD})	Optimal Frequency Ratio (f_{TMD})
Case (1)	0.0779367	0.982632
Case (2)	0.0915456	0.982311

The PSD of the beam mid-span transverse displacement (w) without and with the optimal TMD systems given in Table 3.3 for Cases (1) and (2) are compared in Figure 3.3.

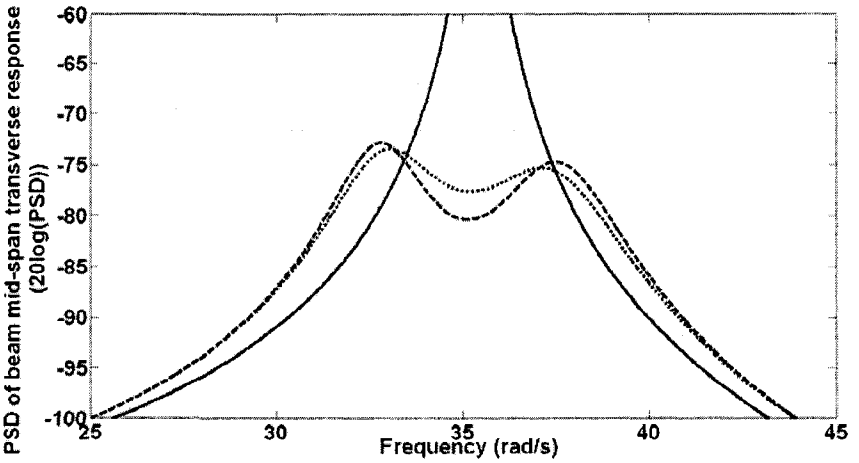

Figure 3.3 PSD of the beam's mid-span transverse displacement (w). Solid, dashed and dotted lines represent the uncontrolled structure, structure with optimal TMD Case (1) and Case (2) listed in Table 3.3, respectively.

It can be seen from Figure 3.3 that the TMD system significantly decreases the system response corresponding to the fundamental frequency. Furthermore, it can also be realized that in this example as the fundamental mode is the dominant vibration mode, the PSD of the middle point deflection for Cases (1) and (2) are close to each other.

To illustrate the efficiency of these optimal parameters of the TMD system, the sensitivity analysis has been carried around optimal point provided in Table 3.3 for Case (2). The PSD of the beam mid-span transverse displacement (w) with respect to 20% deviation of the optimal TMD parameters provided in Table 3.3 for Case (2) are illustrated in Figure 3.4. Figure 3.5 shows how the off–tuning of the damping factor (ξ_{TMD}) and the frequency ratio (f_{TMD}) of the TMD can affect the performance of the system response. In Figure 3.5 the horizontal axis is the percentage of the TMD design parameter off–tunings, ξ_{TMD}/ξ_{optTMD}, and f_{TMD}/f_{optTMD}, the vertical axis shows the deviations of the objective function with respect to the optimal system.

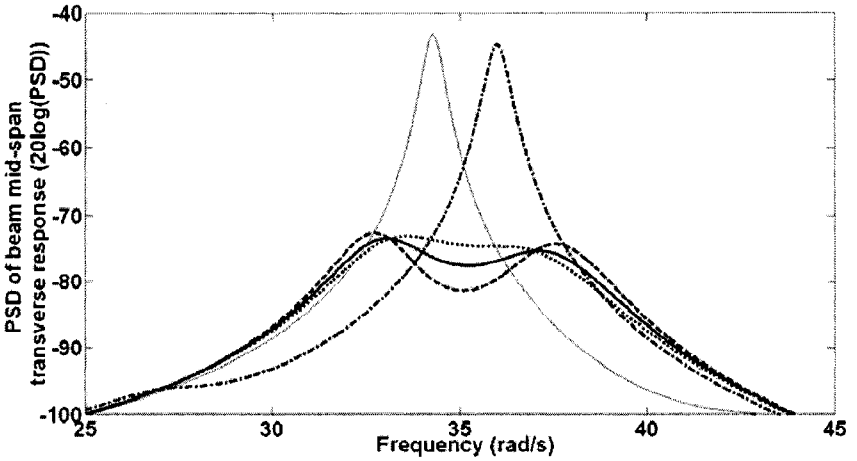

Figure 3.4 PSD of beam mid-span transverse displacement (w) with respect to the optimal TMD parameters' off-tuning for Case (2) in Table 3.3. Solid, dashed, dotted, dashed-dotted and solid (light) lines represent structure with optimal TMD, TMD with -20% and +20% deviations from optimal damping factor (ξ_{TMD}) and frequency ratio (f_{TMD}), respectively.

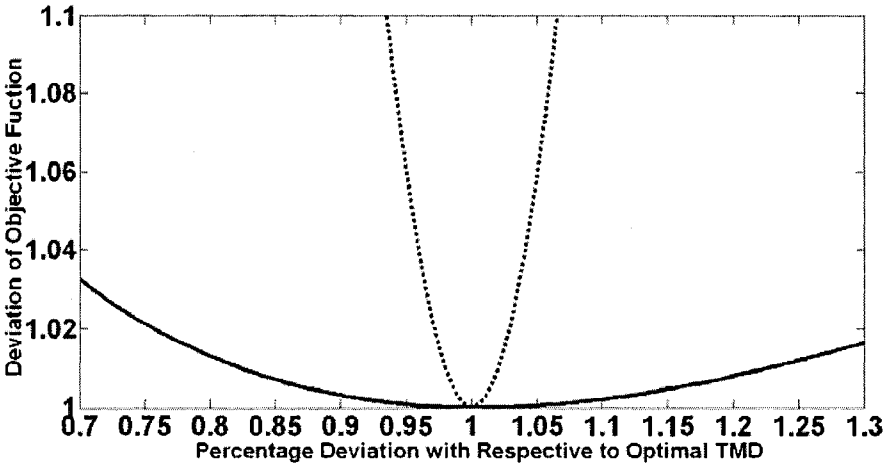

Figure 3.5 Analysis for optimal TMD parameters' off–tunings under random excitation. Solid and dotted lines represent the off-tunings for optimal damping factor (ξ_{TMD}) and frequency ratio (f_{TMD}), respectively.

From Figures 3.4 and 3.5, it can be realized that: (1) the effect of the deviation of frequency ratio (f_{TMD}) from its optimal value is higher than that of the damping factor (ξ_{TMD}) and small deviation of frequency ratio (f_{TMD}) from its optimal value may cause

significant change in the system performance; (2) the effect of the negative deviation of the damping factor is more than the positive deviation. The results shown here are exactly agreed with the working principle of optimally designed TMD system and also perfectly agreed with those presented by Younesian *et al*[84].

3.5.2 Optimization based on harmonic excitation

The optimal TMD design based on harmonic excitation will be studied in this section. The objective function in this section would be to minimize the maximum magnitude in the frequency range around the first mode, which is different from that for random excitation, as stated in Equation (3.16). Thus the optimization problem in this section can be expressed as:

$$\begin{aligned} &\text{Find the design variables:} && \{DV\}=\{f_{TMD}, \xi_{TMD}\} \\ &\text{To minimize:} && Max\ (Magnitude(\omega)\ of\ the\ transfer\ function) \\ &\text{Subjected to:} && 0.7\ \omega_1 \le \omega \le 1.3\ \omega_1,\ 0 \le f_{TMD} \le 2.5,\ 0 \le \xi_{TMD} \le 1 \end{aligned} \tag{3.21}$$

where ω_1 represents the structural first natural frequency, which is 35.451 (*rad/s*) provided in Table 3.2. The harmonic loading is assumed to be applied uniformly perpendicular to the central line of beam. Three different cases, similar to those for random loading will be investigated. In Case (1), the magnitude of the transfer function for the first vibration mode has been considered as the objective function, in Case (2), the magnitude of the transfer function for the beam's mid-span transverse displacement (w) has been selected as objective function and Case (3) is the optimal results based on SDOF system under harmonic loading. As discussed in the last section, the optimization problem in Case (3) is an simplified un-damped SDOF system with one attached TMD,

and the analytical solutions for optimal TMD parameters based on harmonic loading have been proposed by Den Hartog[49] as:

$$f_{TMD} = \frac{1}{1+\mu} \text{ and } \xi_{TMD} = \sqrt{\frac{3\mu}{8(1+\mu)}} \tag{3.22}$$

The optimal frequency ratio (f_{TMD}) and damping factor (ξ_{TMD}) for Cases (1)-(3) and the value of objective function for Cases (1) and (2) with respect to the input mass ratio (changing from 0.01-0.1) have been obtained based on the optimization problem stated in Equation (3.21). The results are shown in Figure 3.6 and compared with those obtained analytically based on Equation (3.22). Here it should be noted that for the sake of stability of the SQP method, in this section the value of the objective function has been enlarged by 10^{10}.

From Figure 3.6, it can be found that the optimal results for Case (3) are exactly similar to those obtained by Den Hartog[52], as stated in Equation (3.22), however they are significantly different from those for Cases (1) and (2). This confirms that for continue structures with attached TMD, the simplified assumptions made in Case (3) would not generate accurate optimal results. Through comparing the optimal results with those shown in Figure 3.2, one can also find that no significant difference exist between the optimal TMD frequency ratio (f_{TMD}) obtained based on random loading and harmonic loading. This is due to the fact that the basic working principle of the TMD system is to tune its natural frequency to one of the natural frequency of main structure.

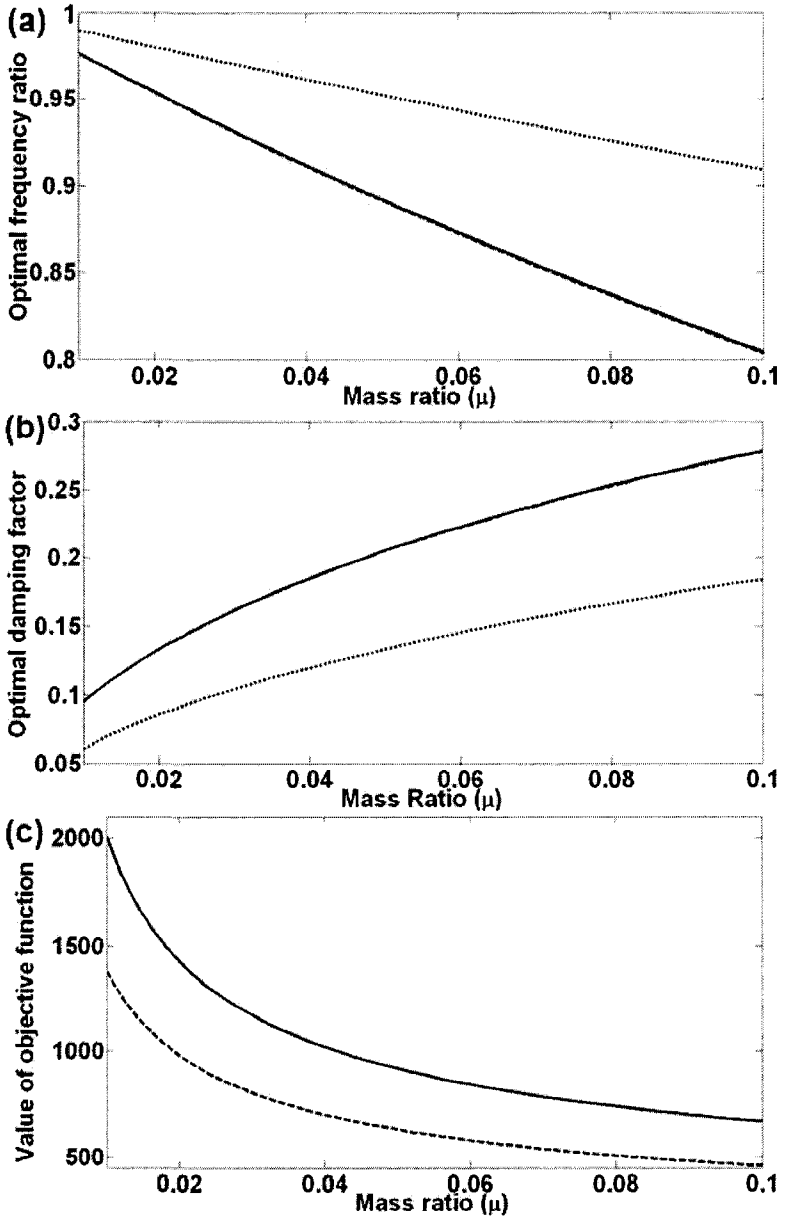

Figure 3.6 Optimal Tuned Mass Damper (TMD) parameters and objective function *vs.* input mass ratio (μ). (a) Optimal frequency ratio (f_{TMD}). (b) Optimal damping factor (ξ_{TMD}). (c) Value of objective function. Solid, dashed and dotted lines represent Cases (1), (2) and (3), respectively. Note: in (a) and (b) the solid and dashed lines coincide with each other and dotted line coincides with Equation (3.22).

Again, to illustrate the efficiency of the optimal TMD design and the system response for different cases, typical optimal TMD parameters for the mass ratio (μ) equal to 0.01 are selected and have been listed in Table 3.4.

Table 3.4 Optimal Tuned Mass Damper (TMD) parameters for mass ratio (μ=0.01) under harmonic loading.

	Optimal Damping Factor (ξ_{TMD})	Optimal Frequency Ratio (f_{TMD})
Case (1)	0.0951483	0.976533
Case (2)	0.0952205	0.976364

From Table 3.4, it can be found that the optimal results for these two cases are almost identical. The magnitude (transfer function) of the mid-span transverse displacement (w) of the beam without and with the optimal TMD system provided in Table 3.4 for Case (2) under harmonic loading is illustrated in Figure 3.7.

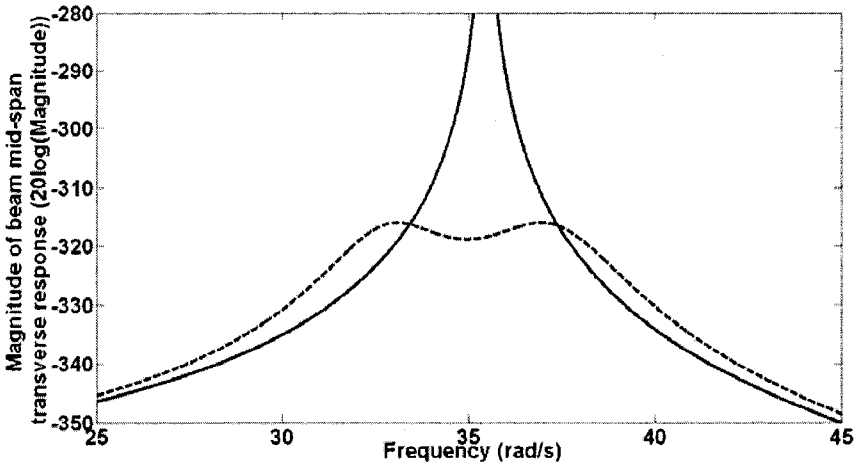

Figure 3.7 Magnitude (transfer function) of the beam's mid-span transverse displacement (w) under harmonic excitation. Solid and dashed lines represent the response for uncontrolled structure and structure with the optimal TMD provided in Table 3.4 for Case (2), respectively.

It can be found from Figure 3.7 that the TMD system significantly decreases the system response corresponding to the fundamental frequency. It is interesting to note that extremes of the magnitude for structure with attached optimal TMD are the same which actually agrees with that reported by Den Hartog[49].

Similar to the random excitation analysis, and in order to illustrate the efficiency of these optimal parameters of the TMD system for harmonic excitation, the sensitivity analysis has also been performed. The magnitude (transfer function) of the beam's mid-span transverse displacement (w) with respect to 20% deviations from the optimal TMD parameters listed in Table 3.4 for Case (2) are illustrated in Figure 3.8.

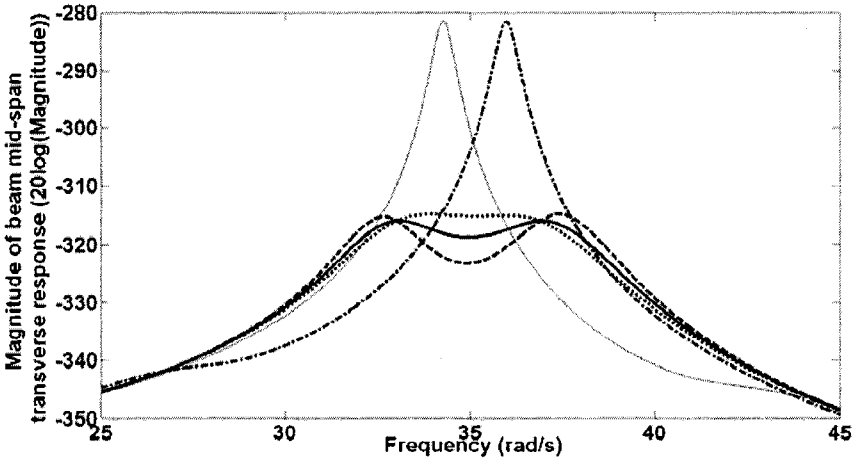

Figure 3.8 Magnitude (transfer function) of the beam mid-span transverse displacement (w) with respect to the optimal TMD parameters' off-tuning under harmonic excitation. Solid, dashed, dotted, dashed-dotted and solid (light) lines represent structure with optimal TMD, TMD with -20% and +20% deviations from optimal damping factor (ξ_{TMD}) and frequency ratio (f_{TMD}), respectively.

The results show that the deviations from the optimal TMD parameters may result in the system response to be far from the optimal condition and the effect of the deviations of

the frequency ratio from the optimal value is significantly higher than that for damping factor. Similarly, Figure 3.9 shows how the off–tuning of the damping factor and the frequency ratio of the TMD system can affect the performance of the system response. In this figure the definitions of the axes are the same as those in Figure 3.5. The same phenomenon can be found in Figure 3.9 as those illustrated in Figure 3.5.

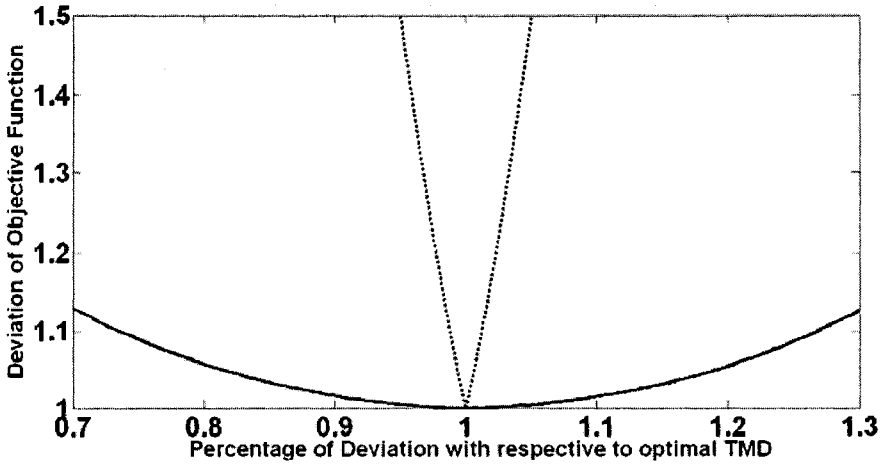

Figure 3.9 Analysis for optimal TMD's parameters' off–tunings under harmonic loading. Solid and dotted lines represent the off–tunings for damping factor (ξ_{TMD}) and frequency ratio (f_{TMD}), respectively.

3.6 Conclusions and Summary

In this chapter, the equations of motion for the Timoshenko beam with the attached Tuned Mass Damper (TMD) system has been successfully derived utilizing the finite element methodology derived in Chapter 2, and been combined with the gradient based numerical optimization technique based on Sequential Quadratic Programming (SQP) to find the optimal parameters of the TMD system subjected to both random and harmonic loadings. The effectiveness of the developed techniques, which include the equations of motion in finite element form for beam structures with the attached TMD system, the

selected objective function and the optimization methodology, have been testified through the illustrated example, in which the structural response comparison for uncontrolled structure and structure with attached optimal TMD and optimal TMD design parameters' sensitivity analysis have been conducted and also the results has been compared with those available in published literatures.

The numerical examples provided in this chapter were based on the symmetry beam with symmetry boundary condition and the first vibration mode is the dominant mode. Due to these, the optimal TMD parameters are very close for Case (1) and (2) under both random and harmonic excitation. However, if multiple dominant vibration modes exist for a beam structure, the optimal design for the attached TMD system would be more complicated than those investigated in this chapter. This issue will be discussed in Chapter 4.

CHAPTER 4

MUTIPLE TUNED MASS DAMPERS DESIGN

4.1 Introduction

In previous chapters, the developed finite element formulation for general curved beam-type structures and the design optimization approach of the attached single Tuned Mass Damper (TMD) system for the Timoshenko beam were validated. This chapter will extend the study to the structural vibration suppression of the curved beam using multiple Tuned Mass Damper (MTMD) technology. As investigated in Chapter 2 that the curved beam modeled considering the axial extensibility ($du_T(s)/ds$), shear deformation and rotary inertia provides better approximation to the true behavior of the beam, in this chapter this curved beam model will be utilized to investigate the optimal TMD system design for curved beam-type structures.

First, the governing differential equations of motion of curved beams with the attached MTMD system are derived through the extended Hamilton principle, and then transformed to the finite element form using the Galerkin weighted residual method. The Root Mean Square (RMS) of the curved beam's responses under random loading is obtained through the random vibration state-space analysis methodology and considered as the objective function for an optimization procedure, as discussed in Chapter 3. A hybrid optimization methodology, which combines the global optimization method based on Genetic Algorithm (GA) and the powerful local optimization method based on

Sequential Quadratic Programming (SQP), has been developed and then utilized to obtain the optimally designed parameters of the TMD system, which includes not only the damping factor and stiffness but also the position of the attached TMD system. Illustrated examples have been provided to verify the validity of the proposed methodology. A parametric sensitivity study for the system response with respect to small deviations from the parameters of the optimally designed TMD system has also been carried out. Furthermore, the theoretical principle for the optimum number and also the optimum position of the attached TMD system will be established based on the results obtained from the numerical examples.

4.2 Equations of Motion for Curved Beams with Attached TMD

Considering a general curved beam with attached MTMD system, as shown in Figure 4.1.

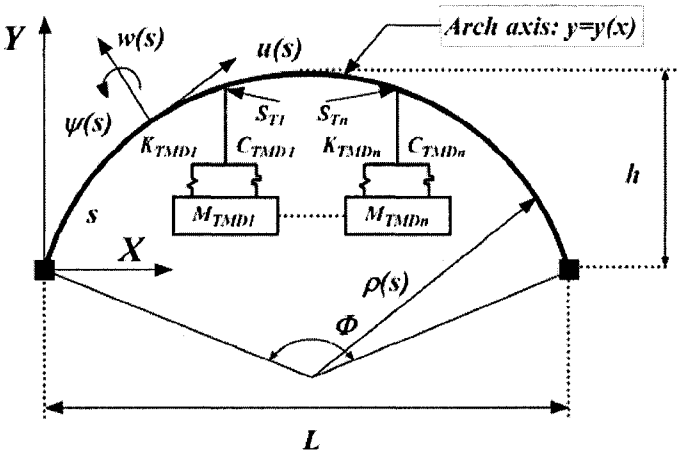

Figure 4.1 General curved beam with the attached MTMD system.

In Figure 4.1, L, Φ, h, $y(x)$ and $\rho(s)$ have the same definitions as those shown in Figure 2.2 and S_{Ti}, K_{TMDi}, C_{TMDi} and M_{TMDi} are the position along the S coordinate, stiffness, viscous damping and mass of the i^{th} attached TMD, respectively. The curved beam's

deformation relationships considering the effects of the axial extensibility ($du_T(s)/ds$), shear deformation and rotary inertia have been listed in Table 2.1 for Case 1.

In this section the governing differential equations of motion will be derived through the extended Hamilton principle, as stated in Equation (3.1). For the sake of simplicity, the formulations presented here are based on two attached TMD. One can easily extend the formulations to any desired number of TMD utilizing the same approach. The kinetic energy (T), potential energy (V) and non-conservative virtual work (δW_{nc}) for curved beams with two attached TMD can be described as:

$$T = \frac{1}{2}\int_L m(s)\left(\frac{\partial w(s,t)}{\partial t}\right)^2 ds + \frac{1}{2}\int_L J(s)\left(\frac{\partial \psi(s,t)}{\partial t}\right)^2 ds + \frac{1}{2}\int_L m(s)\left(\frac{\partial u(s,t)}{\partial t}\right)^2 ds + \frac{1}{2}M_{TMD1}\dot{z}_{T1}(t)^2 + \frac{1}{2}M_{TMD2}\dot{z}_{T2}(t)^2 \tag{4.1a}$$

$$V = \frac{1}{2}\int_L EI(s)\left(\frac{\partial \psi(s,t)}{\partial s}\right)^2 ds + \frac{1}{2}\int_L k_q GA(s)\beta^2(s,t)ds + \frac{1}{2}\int_L EA(s)\left(\frac{\partial u_T(s,t)}{\partial s}\right)^2 ds + \frac{1}{2}K_{TMD1}[w(s_{T1},t)\cos(\alpha_{s_{T1}}) + u(s_{T1},t)\sin(\alpha_{s_{T1}}) - z_{T1}(t)]^2 + \frac{1}{2}K_{TMD2}[w(s_{T2},t)\cos(\alpha_{s_{T2}}) + u(s_{T2},t)\sin(\alpha_{s_{T2}}) - z_{T1}(t)]^2 \tag{4.1b}$$

$$\begin{aligned}\delta W_{nc} = {} & \int_L f(s,t)\delta w ds + \int_L - C_w \dot{w}(s,t)\delta w ds + \int_L - C_u \dot{u}(s,t)\delta u ds \\ & - C_{TMD1}[\dot{w}(s_{T1},t)\cos(\alpha_{s_{T1}}) + \dot{u}(s_{T1},t)\sin(\alpha_{s_{T1}}) - \dot{z}_{T1}(t)] \\ & \times \delta[w(s_{T1},t)\cos(\alpha_{s_{T1}}) + u(s_{T1},t)\sin(\alpha_{s_{T1}}) - z_{T1}(t)] \\ & - C_{TMD2}[\dot{w}(s_{T2},t)\cos(\alpha_{s_{T2}}) + \dot{u}(s_{T2},t)\sin(\alpha_{s_{T2}}) - \dot{z}_{T2}(t) \\ & \times \delta[w(s_{T2},t)\cos(\alpha_{s_{T2}}) + u(s_{T2},t)\sin(\alpha_{s_{T2}}) - z_{T2}(t)]\end{aligned} \tag{4.1c}$$

where $m(s)$, $A(s)$, $I(s)$, $J(s)$, E, G and k_q have the same definitions as those illustrated in Equations (2.7) and (2.8). C_w and C_u are the viscous damping of the curve beam's radial and tangential direction, respectively. K_{TMD1} (K_{TMD2}) and C_{TMD1} (C_{TMD2}) are the stiffness and damping of the attached first (second) TMD, respectively. S_{T1} (S_{T2}) and α_{ST1} (α_{ST2})

represent the position and the angle between the curved beam central line tangential direction and the X axis at the location of the attached first (second) TMD along the S coordinate, respectively. $w(s_{T1},t)$ ($w(s_{T2},t)$) and $u(s_{T1},t)$ ($u(s_{T2},t)$) are the radial and tangential displacements of the curved beam at the position of the attached first (second) TMD, respectively. z_{T1} (z_{T2}) represents the displacement of the attached first (second) TMD. The integral $\int_L[.]ds$ is the curvilinear integral applied on the S coordinate. $f(s,t)$ is the external force perpendicular to the central line of curved beam. It should be noted that through parameter S_T, one can easily extend Equations (4.1) to any desired number of attached TMD.

Substituting the geometrical and deformational relations for the curved beam model Case 1 listed in Table 2.1, into Equations (4.1), and then applying Hamilton's principle stated in Equation (3.1), the following five governing differential equations of motion for the curved beam with the attached MTMD system can be obtained:

$$\begin{aligned}
&-m(s)\frac{\partial^2 w(s,t)}{\partial t^2}+\frac{\partial}{\partial s}\left[k_q GA(s)\left(\frac{\partial w(s,t)}{\partial s}-\frac{u(s,t)}{\rho(s)}-\psi(s,t)\right)\right]-\frac{EA(s)}{\rho(s)}\left(\frac{\partial u(s,t)}{\partial s}+\frac{w(s,t)}{\rho(s)}\right)\\
&-K_{TMD1}[w(s_{T1},t)\cos(\alpha_{s_{T1}})+u(s_{T1},t)\sin(\alpha_{s_{T1}})-z_1]\cos(\alpha_{s_{T1}})\vartheta(s-s_{T1})\\
&-C_{TMD1}[\dot{w}(s_{T1},t)\cos(\alpha_{s_{T1}})+\dot{u}(s_{T1},t)\sin(\alpha_{s_{T1}})-\dot{z}_1]\cos(\alpha_{s_{T1}})\vartheta(s-s_{T1})\\
&-K_{TMD2}[w(s_{T2},t)\cos(\alpha_{s_{T2}})+u(s_{T2},t)\sin(\alpha_{s_{T2}})-z_2]\cos(\alpha_{s_{T2}})\vartheta(s-s_{T2})-C_w\dot{w}(s,t)\\
&-C_{TMD2}[\dot{w}(s_{T2},t)\cos(\alpha_{s_{T2}})+\dot{u}(s_{T2},t)\sin(\alpha_{s_{T2}})-\dot{z}_2]\cos(\alpha_{s_{T2}})\vartheta(s-s_{T2})+f(s,t)=0
\end{aligned} \tag{4.2a}$$

$$\begin{aligned}
&-m(s)\frac{\partial^2 u(s,t)}{\partial t^2}+\frac{k_q GA(s)}{\rho(s)}\left(-\psi(s,t)+\frac{\partial w(s,t)}{\partial s}-\frac{u(s,t)}{\rho(s)}\right)+\frac{\partial}{\partial s}\left(EA(s)(\frac{\partial u(s,t)}{\partial s}+\frac{w(s,t)}{\rho(s)})\right)\\
&-K_{TMD1}[w(s_{T1},t)\cos(\alpha_{s_{T1}})+u(s_{T1},t)\sin(\alpha_{s_{T1}})-z_1]\sin(\alpha_{s_{T1}})\vartheta(s-s_{T1})\\
&-C_{TMD1}[\dot{w}(s_{T1},t)\cos(\alpha_{s_{T1}})+\dot{u}(s_{T1},t)\sin(\alpha_{s_{T1}})-\dot{z}_1]\sin(\alpha_{s_{T1}})\vartheta(s-s_{T1})\\
&-K_{TMD2}[w(s_{T2},t)\cos(\alpha_{s_{T2}})+u(s_{T2},t)\sin(\alpha_{s_{T2}})-z_2]\sin(\alpha_{s_{T2}})\vartheta(s-s_{T2})\\
&-C_{TMD2}[\dot{w}(s_{T2},t)\cos(\alpha_{s_{T2}})+\dot{u}(s_{T2},t)\sin(\alpha_{s_{T2}})-\dot{z}_2]\sin(\alpha_{s_{T2}})\vartheta(s-s_{T2})-C_u\dot{u}(s,t)=0
\end{aligned} \tag{4.2b}$$

$$-J(s)\frac{\partial^2\psi(s,t)}{\partial t^2}+\frac{\partial}{\partial s}\left(EI(s)\frac{\partial\psi(s,t)}{\partial s}\right)+k_qGA(s)\left(\frac{\partial w(s,t)}{\partial s}-\psi(s,t)-\frac{u(s,t)}{\rho(s)}\right)=0 \tag{4.2c}$$

$$\begin{aligned}&M_{TMD1}\ddot{z}_1+C_{TMD1}[\dot{z}_1-\dot{w}(s_{T1},t)\cos(\alpha_{s_{T1}})-\dot{u}(s_{T1},t)\sin(\alpha_{s_{T1}})]\\&+K_{TMD1}[z_1-w(s_{T1},t)\cos(\alpha_{s_{T1}})-u(s_{T1},t)\sin(\alpha_{s_{T1}})]=0\end{aligned} \tag{4.2d}$$

$$\begin{aligned}&M_{TMD2}\ddot{z}_2+C_{TMD}[\dot{z}_2-\dot{w}(s_{T2},t)\cos(\alpha_{s_{T2}})-\dot{u}(s_2,t)\sin(\alpha_{s_{T1}})]\\&+K_{TMD2}[z_2-w(s_{T2},t)\cos(\alpha_{s_{T1}})-u(s_{T2},t)\sin(\alpha_{s_{T1}})]=0\end{aligned} \tag{4.2e}$$

where the symbol $\vartheta(s-s_T)$ is unity when S=S_{T1} (S_{T2}), otherwise zero. Utilizing the same approach derived in Chapter 3, the governing differential equations of motion stated in Equations (4.2) can be transferred to the finite element form as:

$$[M]\{\ddot{q}(t)\}+[C]\{\dot{q}(t)\}+[K]\{q(t)\}=\{F(t)\} \tag{4.3}$$

where

$$\{q\}=\left\{\{W(t)\}\quad\{U(t)\}\quad\{\Psi(t)\}\quad z_{T1}(t)\quad z_{T2}(t)\right\}^T \tag{4.4a}$$

$$[M]=\begin{bmatrix}[M_{ww}] & [0] & [0] & [0] & [0]\\ [0] & [M_{uu}] & [0] & [0] & [0]\\ [0] & [0] & [M_{\psi\psi}] & [0] & [0]\\ [0] & [0] & [0] & M_{TMD1} & [0]\\ [0] & [0] & [0] & [0] & M_{TMD2}\end{bmatrix} \tag{4.4b}$$

$$[K]=\begin{bmatrix}[K_{ww}]+[K_{wwT1}]+[K_{wwT2}] & [K_{wu}]+[K_{wuT1}]+[K_{wuT2}] & [K_{w\psi}] & [K_{wz1}] & [K_{wz2}]\\ [K_{wu}]^T+[K_{wuT1}]^T+[K_{wuT2}]^T & [K_{uu}]+[K_{uuT1}]+[K_{uuT2}] & [K_{u\psi}] & [K_{uz1}] & [K_{uz2}]\\ [K_{w\psi}]^T & [K_{u\psi}]^T & [K_{\psi\psi}] & [0] & [0]\\ [K_{wz1}]^T & [K_{uz1}]^T & [0] & K_{TMD1} & [0]\\ [K_{wz2}]^T & [K_{uz2}]^T & [0] & [0] & K_{TMD2}\end{bmatrix} \tag{4.4c}$$

$$[C]=\begin{bmatrix}[C_{ww}]+[C_{wwT1}]+[C_{wwT2}] & [C_{wu}]+[C_{wuT1}]+[C_{wuT2}] & [0] & [C_{wz1}] & [C_{wz2}]\\ [C_{wu}]^T+[C_{wuT1}]^T+[C_{wuT2}]^T & [C_{uu}]+[C_{uuT1}]+[C_{uuT2}] & [0] & [C_{uz1}] & [C_{uz2}]\\ [0] & [0] & [0] & [0] & [0]\\ [C_{wz1}]^T & [C_{uz1}]^T & [0] & C_{TMD1} & [0]\\ [C_{wz2}]^T & [C_{uz2}]^T & [0] & [0] & C_{TMD2}\end{bmatrix} \tag{4.4d}$$

$$\{F(t)\} = \left\{ \sum_{element} \left[\int_{-1}^{1} ([N(\eta)] f(\eta,t) \bar{J}_c(\eta)) d\eta, \quad \{0\}_u, \quad \{0\}_\psi, \quad 0, \quad 0 \right] \right\}^T \tag{4.4e}$$

where in equivalent nodal force vector $\{F(t)\}$, expression $\{0\}_u$ and $\{0\}_\psi$ represents the null vector with the same size as $\{U(t)\}$ and $\{\Psi(t)\}$, respectively. $\bar{J}_c(\eta)$ is the Jacobian between Cartesian coordinate (x, y), curvilinear coordinate (S) and natural coordinate (η), which has been defined in Chapter 2. The sub-matrices $[M_{ww}]$, $[M_{uu}]$, $[M_{\psi\psi}]$, $[K_{ww}]$, $[K_{uu}]$, $[K_{\psi\psi}]$, $[K_{wu}]$, $[K_{w\psi}]$ and $[K_{u\psi}]$ in the mass, stiffness and damping matrices have the same definitions as those in Chapter 2. All other sub-matrices have been defined in "Appendix H". For the sake of numerical stability, the following transform matrix has been defined to transfer the nodal displacement vector to a dimensionless vector.

$$[T] = \begin{bmatrix} L_e[I]_w & [0] & [0] & [0] & [0] \\ [0] & L_e[I]_u & [0] & [0] & [0] \\ [0] & [0] & [I]_\psi & [0] & [0] \\ [0] & [0] & [0] & L_e & [0] \\ [0] & [0] & [0] & [0] & L_e \end{bmatrix} \tag{4.5}$$

where L_e is the curvilinear length between two nodes for a curved beam element. $[I]_w$, $[I]_u$ and $[I]_\psi$ are the identity matrices with sizes corresponding to vectors $\{W\}$, $\{U\}$ and $\{\Psi\}$, respectively. Thus the nodal displacement vector $\{q\}$ can be expressed as $\{q\}=[T]\{q_d\}$, where $\{q_d\}$ is a dimensionless vector, and then the equations of motion described in Equation (4.3), can be transferred as:

$$[M_d]\{\ddot{q}_d(t)\} + [C_d]\{\dot{q}_d(t)\} + [K_d]\{q_d(t)\} = \{F_d(t)\} \tag{4.6}$$

where $[M_d]=[T]^T[M][T]$, $[C_d]=[T]^T[C][T]$, $[K_d]=[T]^T[K][T]$ and $\{F_d(t)]=[T]^T\{F(t)\}$. Therefore, the response, which will be defined in numerical example, will be also dimensionless.

4.3 Hybrid Design Optimization

The optimization problem in a general form has been established in Equation (3.15), and the methodology to obtain the solution of objective function has also been presented in Section 3.3. Here it should be noted that the optimization problem established in this chapter includes the position of the attached TMD system as well, and thus its relative objective function would have complex cost (objective) surface. Therefore the local optimization technique based on SQP presented in Chapter 3 may not provide accurate optimum results. Considering these, a hybrid optimization methodology, which combines the global optimization method based on GA and the powerful local optimization method based on SQP, has been developed to accurately find the global optimal solution. Figure 4.2 illustrates the schematic of the developed hybrid optimization methodology for a typical global optimization problem, in which the curve represents the variation of the objective function with respect to a design variable.

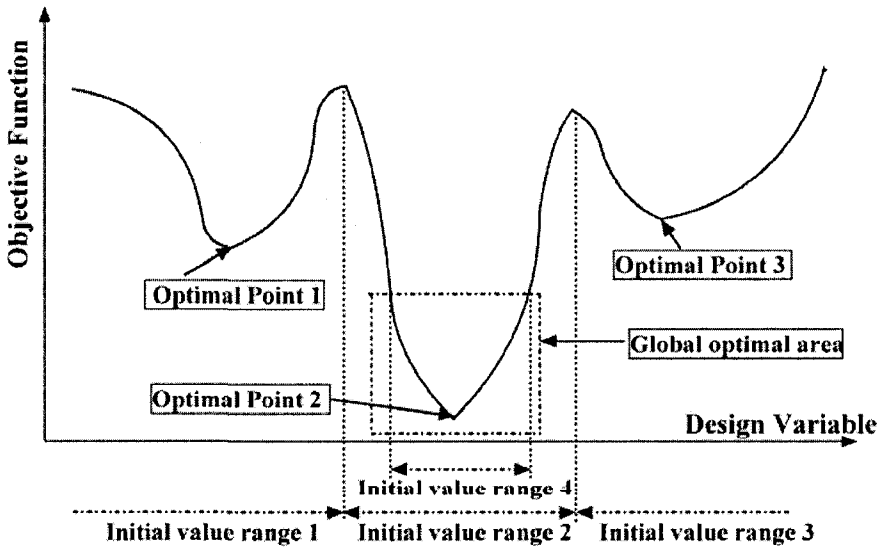

Figure 4.2 The schematic of the hybrid optimization method for a global optimization problem.

For an optimization problem illustrated in Figure 4.2, solved by a local optimization technology, in general (not always, this will depend on the selected optimization parameters, such as step size, and also the properties of a practical optimization problem) one would obtain the "Optimal points 1, 2 and 3" related to the initial values located in "Initial value ranges 1, 2 and 3", respectively. Obviously, only "Optimal point 2" is the global optimal point, thus the local optimization techniques may not be able to solve the global problem accurately. The developed hybrid optimization method consists of two procedures: (1) utilizing the global optimization technology to obtain the approximate optimum value, which is illustrated in Figure 4.2 as "Global optimal area"; (2) utilizing the results obtained in the last procedure as the initial value, which is illustrated in Figure 4.2 as "Initial value range 4", for a local optimization procedure. Finally the whole hybrid optimization procedure can catch the global optimum point —"Optimal point 2" accurately and efficiently. The essential issue for this developed hybrid optimization methodology is to make the global optimization procedure be able to catch the "Global optimal area". In this study the GA global optimization methodology will be utilized to search for the "Global optimal area".

The GA is a global optimization technique based on the principle of genetics and natural selection developed by Holland[177]. Goldberg[178] summarized the original work proposed by Holland[177] and then developed the theoretical basis for the GA through his schema theorem. Since then many versions of modification of GA programming have been published and successfully utilized to solve different problems. The advantages of GA include: it can be used to solve optimization problems with complex cost (objective) surface; optimization can be carried out with continuous or discrete variables; it does not

require derivative information. Haupt[179] also presented other advantages and summarized the previous work about GA. The schematic of GA for continuous design variables, which will be utilized in this dissertation, has been illustrated in Figure 4.3.

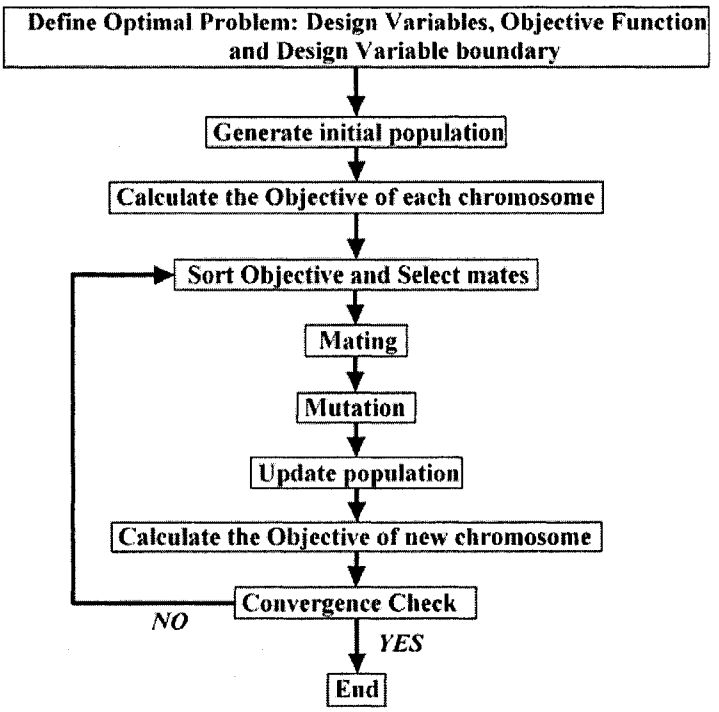

Figure 4.3 The schematic of GA global optimization method for continuous design variables.

The required steps in GA, as illustrated in Figure 4.3, will be discussed in following sub-sections. For the sake of programming simplicity, in GA programming all design variables will be transferred in the range of [0.0, 1.0]. This can be done by the mapping technique based on the boundary of each design variable using the following equation:

$$q_i = (DV_i - a_i) / (b_i - a_i) \tag{4.7}$$

where DV_i is the i^{th} design variable and a_i, b_i and q_i are the low and high boundaries and the uniformed design variable for DV_i, respectively.

4.3.1 Generating initial population

First, the definitions of population and chromosome will be presented. The chromosome represents a set of design variables as:

$$\text{Chromosome} = \{q_1 \ldots q_N\} \tag{4.8}$$

where q_i represents the i^{th} design variable. Here the chromosome has N variables (an N-dimensional optimization problem). Population represents the number of chromosome. Let us define N_{var} and N_{pop} to represent the dimension of chromosome (number of design variables) and number of chromosome (size of population), respectively. One can simply randomly generate a $N_{pop} \times N_{var}$ size matrix with each element between 0 and 1 to represent the initial population.

4.3.2 Sorting the objective and selecting the mates

The value of objective function for the initial population will be obtained first. Based on the selected population size, the objective function would be evaluated N_{pop} times. Next, the N_{pop} value of objective with the associated chromosomes will be sorted from the lowest cost (objective) to highest cost (objective). Then, a selection rate (X_{rate}) will be defined to select N_{keep} population from the sorted list using the following equation:

$$N_{keep} = ceil\,(X_{rate} \times N_{pop}) \tag{4.9}$$

where "*ceil*" represents the command to round the variable ($X_{rate} \times N_{pop}$) to the nearest integer larger than or equal to it. Thus, only the first N_{keep} population with lowest (best) cost (objective) would be kept, which can be defined as selection pool.

Next, the parents which will be utilized to generate (N_{pop}–N_{keep}) offspring (new chromosome) would be picked from the selection pool. In this study, the rank weighting

methodology[179] will be adopted as the selection method. To present the rank weighting methodology clearly, let us assume N_{pop} =8, X_{rate} =0.5 and thus N_{keep}=4, and then establish the following table for the chromosomes in the selection pool.

Table 4.1 Rank weighting selection methodology[179].

Index of Chromosome in selection pool (n)	Value of Objective	P_n	CP_n
1	Lowest	0.4	0.4
2	↓	0.3	0.7
3		0.2	0.9
4	Highest	0.1	1.0

In Table 4.1, P_n and CP_n represent the probability and cumulative probability related to each chromosome in the selection pool, and they are defined as[179]:

$$P_n = (N_{keep} - n + 1) / \left(\sum_{n=1}^{N_{keep}} n \right) \text{ and } CP_n = \sum_{i=1}^{n} P_i \tag{4.10}$$

where n is the index of chromosome in the selection pool, as listed in Table 4.1. One 2-component random vector on the unit interval, in which one component represents "father" and the other for "mother", will be generated to be compared with the cumulative probability (CP_n) given in Table 4.1. Starting from the top of Table 4.1, the first chromosome that the related cumulative probability (CP_n) is greater than the generated random number will be selected as parents. For example, assuming the generated random vector is [0.5, 0.8], then 0.4 < 0.5 < 0.7 and 0.7 < 0.8 < 0.9, thus chromosome No. 2 and 3 in Table 4.1 will be selected as one set of parents. All the selected parents can be defined as mating pool. Sometimes, the selected parents are identical, which will lead to poor convergence or bad optimal result. In this case, one can

easily exchange the "father" or "mother" with the other set of parents in the generated mating pool.

4.3.3 Mating

Mating is the method to generate offspring from set of parents in the mating pool, which has been established in last section. The mating methodology adopted in this dissertation can be expressed as[179]:

$$\begin{aligned} \{Offspring\ _1\} &= \{Ma\}.-\{\beta\}.\times(\{Ma\}.-\{Fa\}) \\ \{Offspring\ _2\} &= \{Ma\}.+\{\beta\}.\times(\{Ma\}.-\{Fa\}) \end{aligned} \tag{4.11}$$

where $\{Ma\}$ and $\{Fa\}$ represent one set of parents. β is a $1\times N_{var}$ vector with the same dimension as $\{Ma\}$ and $\{Fa\}$, and generated randomly on the unit interval. Symbols ".-", ".+" and ".×" represent element-element minus, plus and product, respectively. It should be noted that using Equation (4.11) to generate the offspring, sometimes some elements in the offspring would go outside of the boundary of design variable. One can simply generate a random number on the unit interval to replace the element which goes outside the design boundary or directly utilize the boundary to replace them. Utilizing the methodology introduced above, N_{pop}–N_{keep} offspring will be generated, which will keep the N_{pop} constant in every searching circle.

4.3.4 Mutation

Mutation is one of the essential steps in GA optimization methodology. Through mutation, GA can search outside of the current design variable region freely. However, too many mutation would lead to slow convergence. Here, we keep the best chromosome

(the lowest cost) stable and define the mutation rate as M_{rate}, and then the total mutation of the variables in the population would be:

$$N_{mute}=ceil\ (M_{rate}(N_{pop}-1)N_{var}) \tag{4.12}$$

where "*ceil*" has the same definition as that in Equation (4.9). Then one can randomly select N_{mute} elements in the population (excluding the best chromosome) to be replaced with generated random elements on the unit interval.

4.3.5 Updating population

In this step, the objective function for each chromosome in the generated new population will be evaluated and sorted from minimum to maximum. It should be noted that the best chromosome in the last population does not need to be recalculated and will be transferred to the new population without change.

4.3.6 Convergence checking

"Convergence checking" will depend on the property of a practical optimization problem. In theory, an optimization problem can be solved and one can obtain the global optimum point using GA through a suitably selected convergence checking method, but sometimes it is computationally expensive. In this dissertation, we only require that GA can catch the "Global optimal area", as illustrated in Figure 4.2. Therefore, the following convergence checking methodology would be utilized:

$$(\text{Cost\_list}\ (N_{keep})-\text{Cost\_list}\ (1))/\ \text{Cost\_list}\ (1) \leq \chi \tag{4.13}$$

where "Cost_list" is the value of objective function for the sorted new generated population, which has the same form as that shown in Table 4.1 and χ is a selected small value.

Now, assuming the optimization problem, as stated in Equation (3.15), has been solved by the GA optimization methodology and the optimal solution obtained through GA is located in the "Global optimal area", as illustrated in Figure 4.2. Then, this optimal solution will be used as the initial value for the powerful gradient based SQP technique presented in Chapter 3 to find the optimal design variables accurately.

4.4 Numerical Analysis

Here illustrative examples are provided to demonstrate the developed methodology and also the theoretical principle for designing the continuous structure with the attached MTMD system is proposed based on the results obtained from the numerical examples. The curved beam with the attached MTMD system shown in Figure 4.1 has been considered. The material and geometrical properties of the curved (circular) beam are given in Table 4.2.

Table 4.2 Properties of the circular uniform beam.

Elastic modulus	70 (GPa)	Shear coefficient	0.8438
Shear modulus	24.50 (GPa)	Beam Radius	40 (m)
Area moment	0.01 (m^4)	Cross-Sectional Area	4 (m^2)
Density	2777 (Kg/m^3)	Beam Curve Angle (Φ)	40°

It is noted that the other parameters such as the curve span (L), curve length (l) and rise of curved beam (h), as shown in Figure 4.1, can be obtained from the parameters listed in Table 4.2. The boundary condition for this example is clamped-clamped. The curved

beam has been modeled using 7 curved beam elements with 4 nodes per element, as derived in Chapter 2. Thus, the first five natural frequencies for the curved beam are found to be 19.4705, 35.2407, 64.4729, 90.5644 and 123.2884 (*rad/s*), respectively. The random loading is in the form of white noise with PSD of 10^{10} (N^2/*rad/s*) applied uniformly perpendicular to the central line. The responses of beam's mid-span transverse displacement (w), tangential displacement (u) and rotation (ψ) under this random loading have been shown in Figure 4.4.

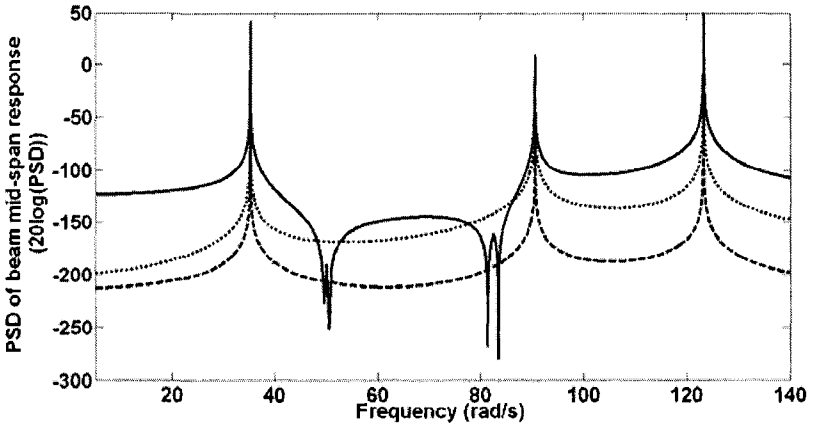

Figure 4.4 PSD of curved beam's mid-span responses. Solid, dashed and dotted lines represent the transverse displacement (w), tangential displacement (u) and rotation (ψ), respectively.

It can be found from Figure 4.4 that in the low frequency range (smaller than 140 *rad/s*), the structural responses mainly depend on the 2nd, 4th and 5th vibration modes, and thus to obtain the best vibration suppression performance, the TMD system should be designed based on the 2nd, 4th and 5th vibration modes. Considering these, the illustrative numerical examples presented in this chapter consists of four parts as:

(1) To design single TMD system based on the 2nd, 4th and 5th vibration modes separately. The optimal TMD parameters will be obtained by the GA, hybrid and SQP optimization

methodologies, and then by comparing the results the validity of the developed GA and hybrid optimization methods can be verified;

(2) To design two symmetrically attached TMD system using the developed hybrid optimization methodology based on the 2^{nd}, 4^{th} and 5^{th} vibration modes separately. The validity of each set of optimal TMD design will be demonstrated by the sensitivity analysis based on the small deviation of the design variables from their relative optimum values and also the convergence analysis for the optimum results obtained by GA;

(3) To design three attached TMD system utilizing the developed hybrid optimization methodology based on the 5^{th} vibration mode;

(4) Based on the results obtained in above parts, an optimal MTMD system will be developed to suppress the structural vibration effectively.

Finally, based on the above investigations, the theoretical basis for optimally designed TMD system for beam-type structures will be established. Here it should be emphasized that as mentioned in Chapter 1, in order to distinguish the multiple TMD design based on multiple vibration modes from that based on one special vibration mode, the former was named as MTMD and the latter as Distributed TMD (DTMD).

4.4.1 Single attached tuned mass damper system

One TMD is assumed to be attached onto the beam mid-span, as the curved beam structure and boundary condition studied in this chapter are both symmetry. The optimization problem has the same as that established in Equation (3.16). One of the main purposes of this subsection is to verify the validity of the developed GA and hybrid optimization methodologies through comparing the optimum results obtained by the GA and hybrid optimization methods with those by the formal SQP technique. Four different

cases have been investigated in this subsection: Case a- The response (RMS) of the 2nd vibration modal deflection is considered as the objective function; Case b- The response (RMS) of the 4th vibration modal deflection is considered as the objective function; Case c- The response (RMS) of the 5th vibration modal deflection is considered as the objective function; Case d- The response (RMS) of circular beam's mid-span transverse displacement (w) is considered as the objective function and the 2nd natural frequency is assumed as the base frequency ω_n in Equation (3.14) for the evaluation of the frequency ratio (f_{TMD}). The following parameters given in Table 4.3 have also been defined for the GA optimization.

Table 4.3 Parameters of GA optimization.

N_{pop}	8	X_{rate}	0.5	χ	1×10^{-4}
N_{var}	2	M_{rate}	0.4		

Tables 4.4–4.6 compare the parameters of the optimally designed TMD system obtained using the GA and hybrid optimization methodologies and also the SQP with initial values of {0.1, 0.1} for the TMD with mass ratio (μ) equal to 0.01, 0.015 and 0.02, respectively. It should be noted that as mentioned in Section 4.3, the design variables for GA optimization have been uniformed using Equation (4.7). Therefore, in Tables 4.4–4.6 (also the other tables related to GA optimum results in this chapter) the GA optimum results have been transferred back based on Equation (4.7). Here, it should be emphasized that in Tables 4.4–4.6 (also other tables in this chapter), the final parameters for the optimally designed TMD system have been illustrated as Italic and bold form.

Figures 4.5–4.7 illustrate the best value (lowest cost) of the objective function for each generated population by GA versus the GA calculating cycle, which was defined as "generation" by Haupt[179], for mass ratio (μ) equal to 0.01, 0.015 and 0.02, respectively.

Table 4.4 Optimal result comparison for curved beam with the attached single TMD with mass ratio (μ=0.01).

Optimal methodology	Optimal Strategies							
	2nd vibration mode-Case a		4th vibration mode-Case b		5th vibration mode-Case c		Mid-span transverse displacement-Case d	
	ξ_{TMD}	f_{TMD}	ξ_{TMD}	f_{TMD}	ξ_{TMD}	f_{TMD}	ξ_{TMD}	f_{TMD}
GA	0.094	0.9512	0.0542	0.9814	0.1403	0.9946	0.6318	1.826
Hybrid	***0.093***	***0.9592***	***0.0379***	***1.0063***	***0.0758***	***0.9634***	***0.6328***	***1.832***
SQP	0.093	0.9592	0.0379	1.0063	0.0758	0.9634	0.6328	1.832

Table 4.5 Optimal result comparison for curved beam with the attached single TMD with mass ratio (μ=0.015).

Optimal methodology	Optimal Strategies							
	2nd vibration mode-Case a		4th vibration mode-Case b		5th vibration mode-Case c		Mid-span transverse displacement-Case d	
	ξ_{TMD}	f_{TMD}	ξ_{TMD}	f_{TMD}	ξ_{TMD}	f_{TMD}	ξ_{TMD}	f_{TMD}
GA	0.1065	0.9508	0.0507	1.0055	0.103	0.9163	0.6688	1.9608
Hybrid	***0.1118***	***0.9402***	***0.0487***	***1.0091***	***0.0923***	***0.9458***	***0.6484***	***1.7940***
SQP	0.1118	0.9402	0.0487	1.0091	0.0923	0.9458	0.6484	1.7940

Table 4.6 Optimal result comparison for curved beam with the attached single TMD with mass ratio (μ=0.02).

Optimal methodology	Optimal Strategies							
	2nd vibration mode-Case a		4th vibration mode-Case b		5th vibration mode-Case c		Mid-span transverse displacement-Case d	
	ξ_{TMD}	f_{TMD}	ξ_{TMD}	f_{TMD}	ξ_{TMD}	f_{TMD}	ξ_{TMD}	f_{TMD}
GA	0.132	0.9249	0.082	1.0155	0.1574	0.8857	0.6947	1.6851
Hybrid	***0.1265***	***0.9222***	***0.0589***	***1.0117***	***0.1059***	***0.9288***	***0.6328***	***1.7559***
SQP	0.1265	0.9222	0.0589	1.0117	0.1059	0.9288	0.6328	1.7559

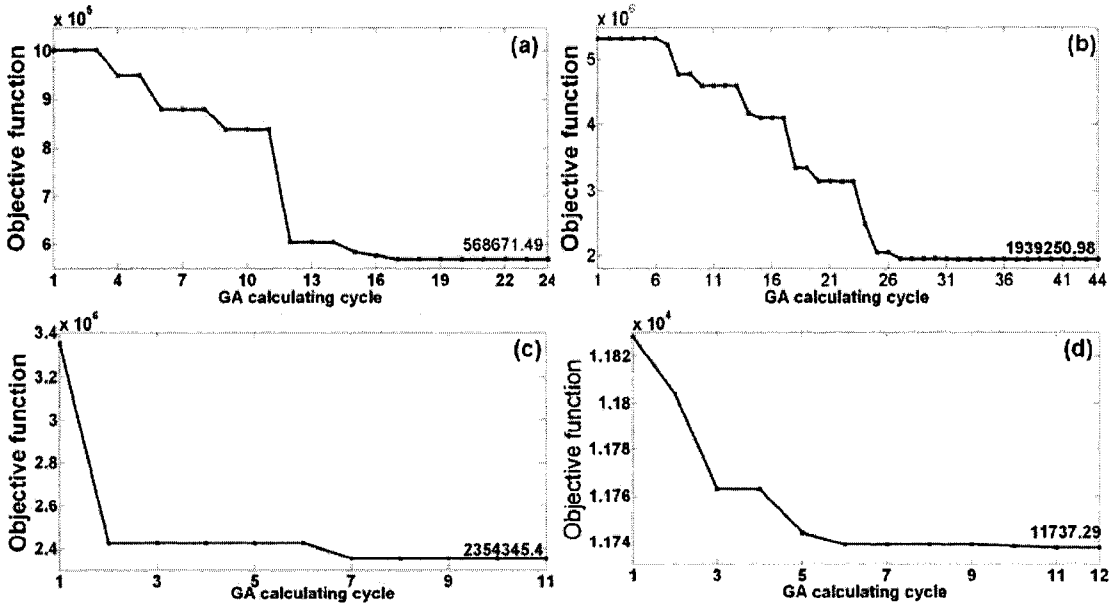

Figure 4.5 GA convergence analysis for curved beam with the attached single mid-span TMD with mass ratio (μ=0.01). (a) Based on the 2nd mode-Case a. (b) Based on the 4th mode-Case b; (c) Based on the 5th mode-Case c; (d) Based on the curved beam mid-span transverse displacement (w)-Case d.

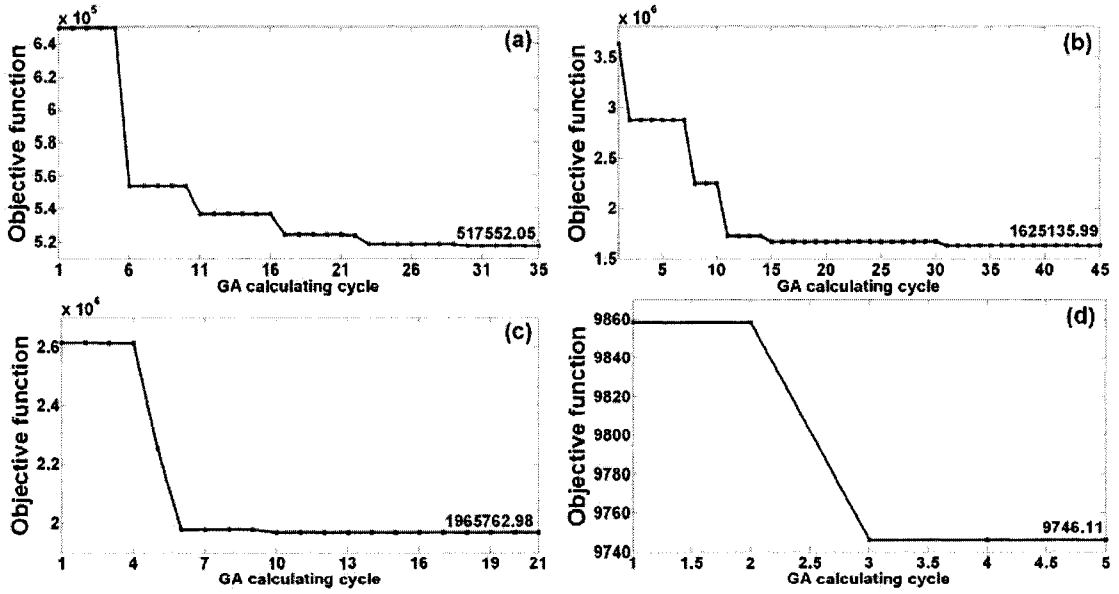

Figure 4.6 GA convergence analysis for curved beam with the attached single mid-span TMD with mass ratio (μ=0.015). (a) Based on the 2nd mode-Case a. (b) Based on the 4th mode-Case b; (c) Based on the 5th mode-Case c; (d) Based on the curved beam mid-span transverse displacement (w)-Case d.

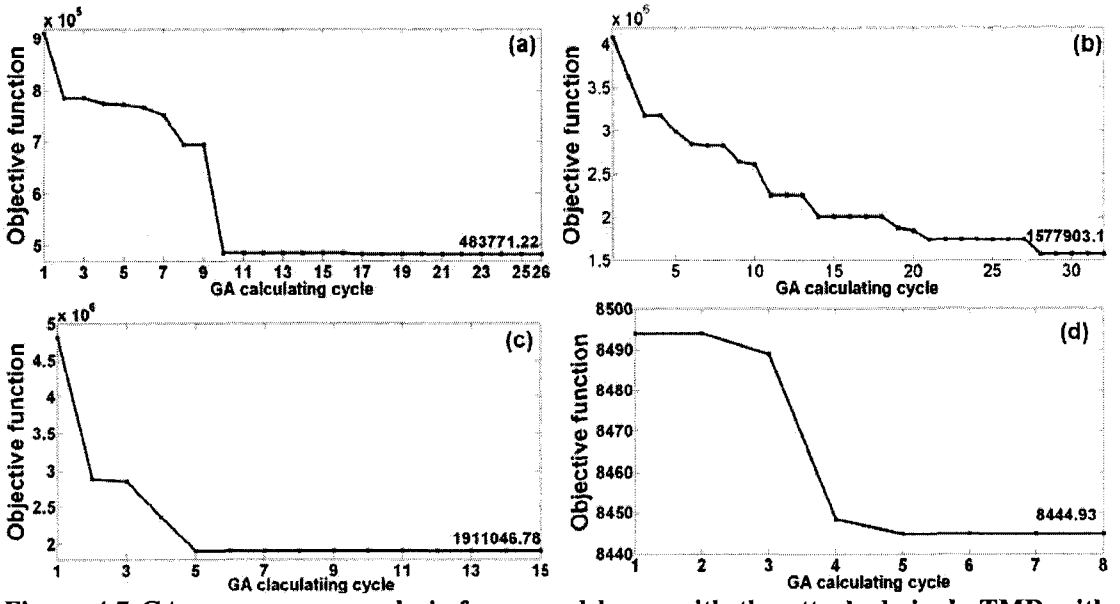

Figure 4.7 GA convergence analysis for curved beam with the attached single TMD with mass ratio (μ=0.02). (a) Based on the 2nd mode-Case a. (b) Based on the 4th mode-Case b; (c) Based on the 5th mode-Case c; (d) Based on the curved beam mid-span transverse displacement (w)-Case d.

From Tables 4.4–4.6 and Figures 4.5–4.7, one can easily find that: (1) the optimum results obtained using GA are closed to those obtained using hybrid optimization method, especially for the obtained optimum frequency ratio (f_{TMD}). This means that the GA has successfully caught the neighborhood of the global optimum point; (2) the optimum results obtained through the hybrid and SQP methods are the same. Also different initial points for the SQP optimization method have been tested and similar optimum results are found. From Tables 4.4–4.6, one can also find that the optimum frequency ratio (f_{TMD}) for Case b (based on the 4th vibration mode) will not exactly decrease with the increase of input mass ratio (μ), which is different from those for Cases a, c and d. To investigate this phenomenon, Figure 4.8 illustrates the optimal TMD parameters based on Cases a-d, for mass ratio (μ) changing from 0.01 to 0.1.

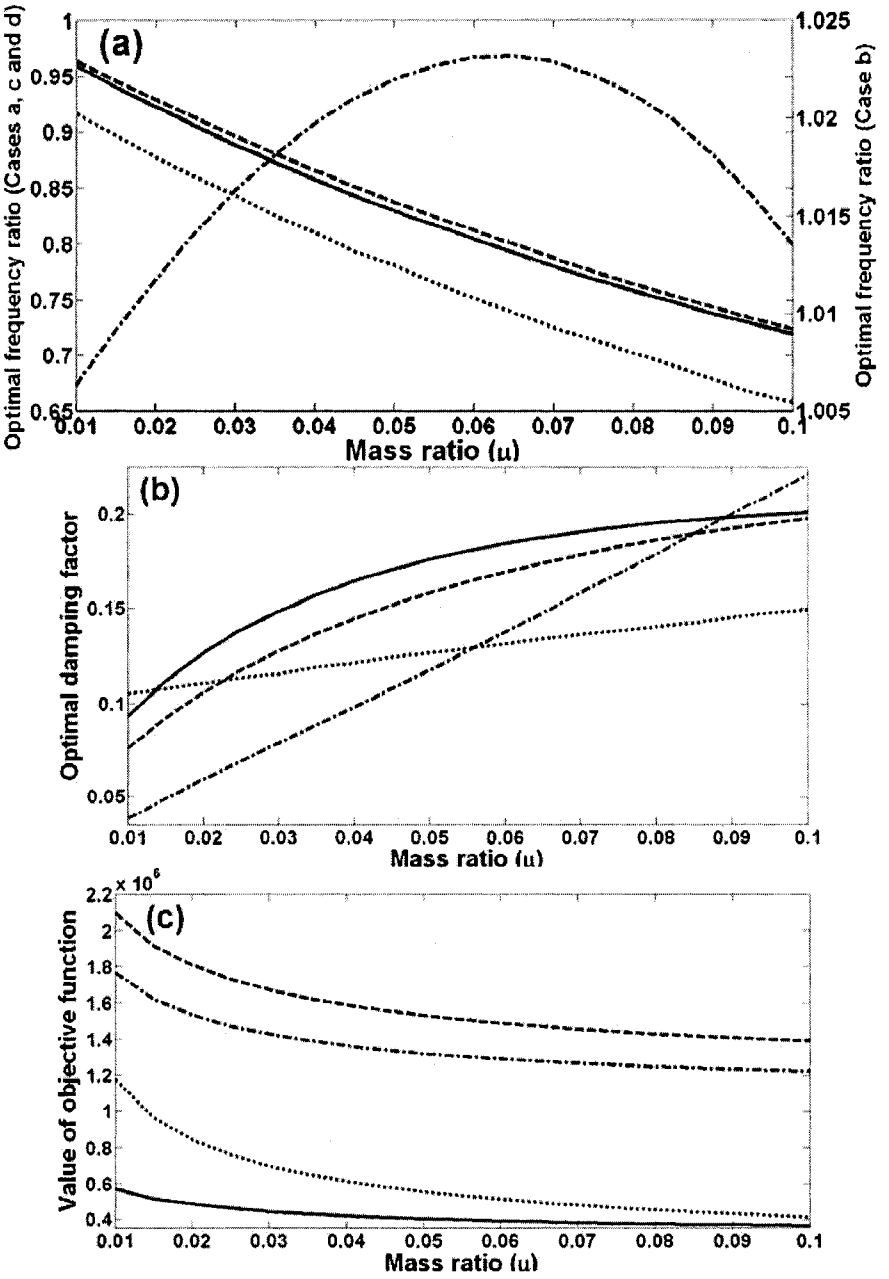

Figure 4.8 Optimal TMD parameters and value of objective function *vs.* input mass ratio (μ) for the curved beam with the attached single mid-span TMD. (a) Optimal frequency ratio (f_{TMD}). (b) Optimal damping factor (ξ_{TMD}). (c) Value of objective function. Solid, dashed-dotted, dashed and dotted lines represent Cases a-d, respectively. Note: in (a), (b) and (c) the dotted line has been divided by 2 and 6, and multiplied 100, respectively.

Here, it should be noted that in Figure 4.8, the optimal frequency ratio (f_{TMD}), damping factor (ξ_{TMD}) and value of objective function for Case d have been mapped by 1/2, 1/6 and 100, respectively, in order to facilitate the reader observing the trend of the optimal TMD parameters with the increase of input mass ratio (μ). It can be realized from Figure 4.8 that the value of objective function will decrease and the optimal damping factor (ξ_{TMD}) will increase with the increase of input mass ration (μ) for Cases a–d; the optimal frequency ratio (f_{TMD}) for Cases a, c and d will decrease with the increase of input mass ration (μ), but the optimal frequency ratio (f_{TMD}) for Case b will increase and then decrease with the increase of input mass ration (μ). Furthermore, one can also find that the optimal frequency ratio (f_{TMD}) for Case b changes in very small range. The reason is that the single attached TMD system is not a suitable selection to suppress the vibration due to the 4^{th} vibration mode, which will be illustrated in the following sections.

From Tables 4.4–4.6 and Figure 4.8, one can also find that there are significant differences for the optimal TMD parameters between Cases a and d, which is different from the results shown in Chapter 3. This is mainly due to the fact that the structure studied in this chapter does not have single dominant mode.

To illustrate the effect of the attached optimal single TMD design provided in Tables 4.4–4.6, optimal TMD parameters for Case a in Table 4.4 (μ=0.01); Case b in Table 4.6 (μ=0.02); Case c in Table 4.5 (μ=0.015); Case d in Table 4.4 (μ=0.01), have been selected for studying the curved beam's mid-span responses. The results for transverse displacement (w) have been illustrated in Figure 4.9. The tangential displacement (u) and rotation (ψ) responses have been presented in "Appendix I".

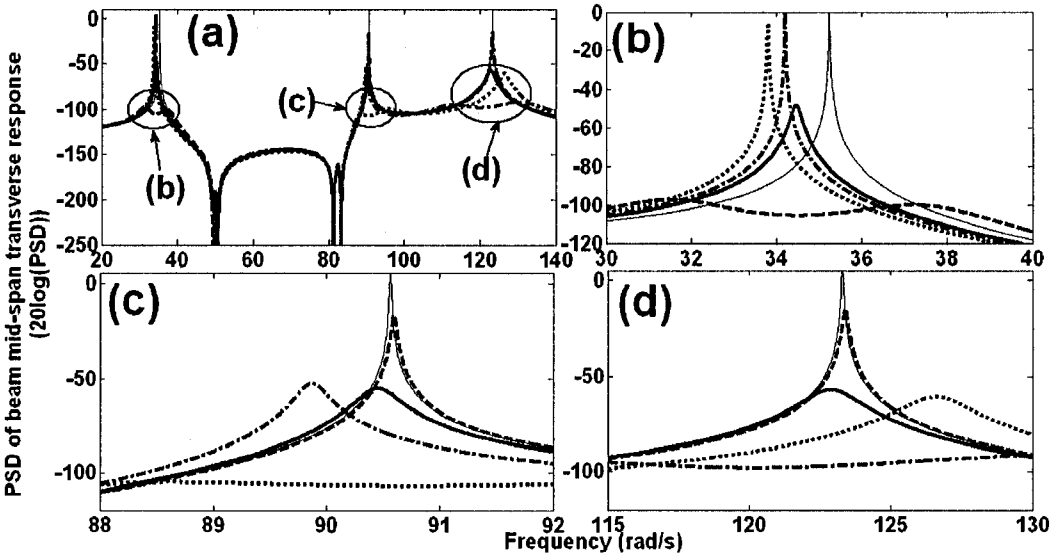

Figure 4.9 PSD of curved beam mid-span transverse displacement (w). (a) Frequency range 20-140 (*rad/s*). (b) Around the 2nd natural frequency. (c) Around the 4th natural frequency. (d) Around the 5th natural frequency. Solid (light), dashed, dotted, dotted-dashed and solid lines represent uncontrolled structure, structure with optimal TMD Case a in Table 4.4, Case b in Table 4.6, Case c in Table 4.5 and Case d in Table 4.4, respectively.

From Figure 4.9 and "Appendix I", it can be found that: (1) the effects of the optimally designed TMD systems for Cases a–c, as illustrated in Tables 4.4–4.6, are restricted in their related tuned natural frequencies, and thus for the structure with multiple dominant vibration modes, it is possible to design an optimal TMD system based on different vibration modes, separately, and then combine them together to provide a MTMD design to suppress vibration efficiently; (2) as single dominant mode dose not exist in this example, thus although the optimal TMD design strategy based on Case d can also suppress the vibration in each vibration mode effectively, its working principle is not TMD any more, which is to tune the frequency of the secondary system to one of the structural vibration modes.

Next, the developed hybrid optimization methodology will be utilized to find the optimal design variables of the attached DTMD system, which includes the position, damping factor and frequency ratio, based on each vibration mode. In fact the number of the attached DTMD system should also be identified as one of the design variables. However, it is very difficult to find a suitable optimal criterion to combine the number of the attached DTMD system in an optimization procedure. Therefore, at the beginning the number of the attached DTMD system is assumed to be a given input, and finally, a design principle will be established, which can be utilized to identify the best number of the attached DTMD system.

4.4.2 Distributed tuned mass dampers design methodology

The design variable describing the position of the attached TMD includes one discrete variable, which represents which elements the attached TMD would be located in, and one continuous variable, which represents the location of TMD in those elements. It is difficult to solve this kind of optimization problem, in which the design variables include both discrete and continuous variables. One simple way is to solve the TMD located in each different element's combination and then compare the objective to find the optimal TMD design. This is a simple approach but is computationally very expensive. In this work, an efficient and accurate design optimization approach has been proposed to find the location and parameters of the attached TMD system. The optimization procedure consists of two steps, as illustrated in Figure 4.10.

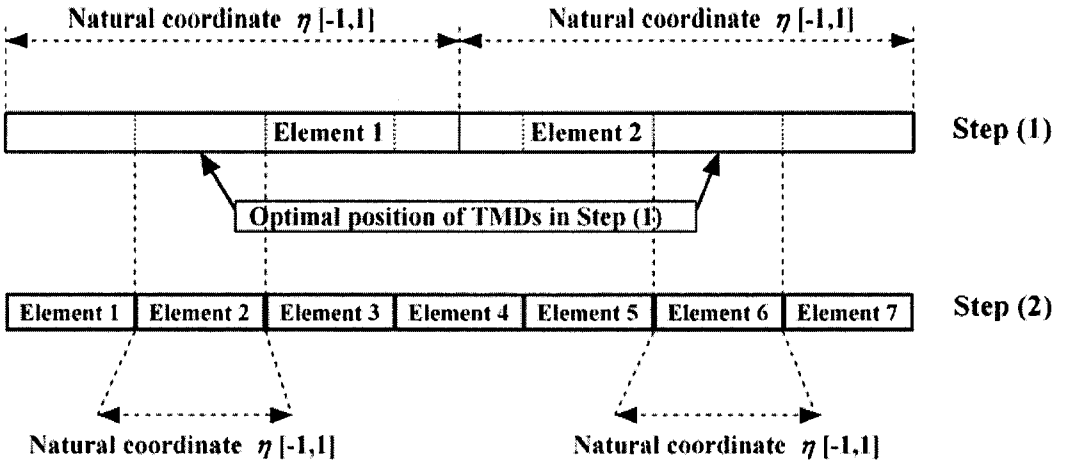

Figure 4.10 Optimization procedures.

In Step (1), the curved beam is modeled using 2 elements with 12 nodes per element, thus the position of the attached TMD can be simply expressed by one continuous variable defined in natural coordinate (η). In Step (2), the curved beam is modeled using 7 elements with 4 nodes per element. Then utilizing the optimal location of the attached TMD system obtained from Step (1), one can easily find in which element the TMD system should be located in this 7 elements model using Equation (4.14). The location of TMD in one special element can still be a continuous variable defined in the natural coordinate (η). Assuming the optimal position of the attached TMD obtained through Step (1) can be defined as η_1, and then its related position in Step (2) can be obtained through:

$$X=0.25\,N\,(1+\eta_1) \text{ and } N_e=ceil\,(X) \tag{4.14}$$

where N is the number of element to model the beam in Step (2), and "*ceil*" has the same definition as that in Equation (4.9). N_e represents the optimal element, in which the attached TMD should be located in the N elements finite element model. This optimal procedure is based on the fact that the 2-element model in Step (1) can describe the

dynamic properties of the curved beam with acceptable accuracy, and then one can catch the neighborhood of the optimal result. This issue has been verified through comparing the structural response for the finite element models in Steps (1) and (2). Obviously, one can model the curved beam using 1 or 2 elements with many nodes per element, which can still model the dynamic behavior of the curved beam accurately and also obtain accurate optimal TMD parameters, but it is computationally expensive due to the slow convergence of the finite element model. Based on the methodology presented above, the DTMD design will be presented in the following subsections.

4.4.3 Two symmetrically attached tuned mass damper system

For the curved beam, as shown in Figure 4.1, with symmetrical physical and geometrical conditions and also symmetrical boundary condition, it is obvious that the attached DTMD system should also be symmetry. As assuming two symmetrical TMD will be designed to suppress the vibration with respect to each vibration mode separately, the dimension of design variables can be simplified to 3, and the optimization problem can be expressed as:

$$\begin{aligned} &\text{Find the design variables:} && \{DV\}=\{\xi_{TMD}, f_{TMD}, \eta_{TMD}\} \\ &\text{To minimize:} && \textit{RMS of response for } 2^{nd}, 4^{th} \textit{ and } 5^{th} \\ & && \textit{vibration modes, respectively} \\ &\text{Subjected to:} && 0\le \xi_{TMD} \le 1,\ 0\le f_{TMD} \le 2.5,\ -1\le \eta_{TMD} \le 1 \end{aligned} \tag{4.15}$$

Based on the optimization problem established in Equation (4.15), the parameters for GA optimization methodology are defined as those listed in Table 4.7.

Table 4.7 Parameters of GA optimization.

N_{pop}	8	X_{rate}	0.5	χ	1×10^{-4}
N_{var}	3	M_{rate}	0.4		

The optimal results based on each vibration modes obtained using the GA, hybrid and SQP optimization methods and the convergence analysis for the GA optimization method will be presented to illustrate the validity of the developed optimization approach.

4.4.3.1 Design based on the 2nd vibration mode

Table 4.8 compares the optimal two symmetrical DTMD design parameters based on the 2nd vibration mode obtained using the GA, hybrid optimization methods and the SQP technique with different initial values for Step (1), as shown in Figure 4.10. The mass ratio (μ) is assumed to be 0.005 for each attached TMD, and thus total mass ratio (μ) would be 0.01. Here it should be noted that for comparison purposes, in Table 4.8 (also the other tables in this chapter) the value of TMD position has been expressed as the relative position along the curved beam's curvilinear length.

Table 4.8 The optimal two symmetrical DTMD parameters based on the 2nd vibration mode with mass ratio (μ=0.005) for each TMD—Step (1).

Design Variables	Optimal Methodologies				
	GA	Hybrid	SQP-1	SQP-2	SQP-3
ξ_{TMD}	0.0922	***0.0936***	0.0936	0.0537	0.0936
f_{TMD}	0.9615	***0.9595***	0.9595	1.0069	0.9595
Position_TMD1	0.4965	***0.5***	0.5	0.1915	0.5
Position_TMD2	0.5035	***0.5***	0.5	0.8085	0.5
Objective ($\times 10^5$)	5.6633	***5.6572***	5.6572	7.5881	5.6572

In Table 4.8, the SQP-1, SQP-2 and SQP-3 represent the results obtained using the SQP optimization method with the initial values of {0.1, 1, -0.9}, {0.1, 1, 0} and {0.1, 1, 1}, respectively. Examination of the results shows that: (1) the SQP provides different optimal results with respect to different initial values. This means that the optimization

problem has multiple local optimal points and SQP can easily trapped into one of the local optimal points without any mechanism to climb out; (2) the optimal results obtained using the GA methodology can catch the neighborhood of the global optimal values, especially the obtained optimal location of the attached DTMD system.

Next, utilizing the optimal parameters obtained in Step (1) and Equation (4.14), one can easily find that the optimal element that the two symmetrical DTMD should be located in the 7 elements beam model in Step (2) is the Element 4. The Step (2), as shown in Figure 4.10, is basically designed to accurately find the optimal location and parameters for the DTMD system. The optimal results for Step (2) based on the GA, hybrid and SQP optimization techniques are provided in Table 4.9.

Table 4.9 The optimal two symmetrical DTMD parameters based on the 2nd vibration mode with mass ratio (μ=0.005) for each TMD—Step (2).

Design Variables	Optimal Methodologies				
	GA	Hybrid	SQP-1	SQP-2	SQP-3
ξ_{TMD}	0.0927	***0.093***	0.093	0.093	0.093
f_{TMD}	0.9585	***0.9592***	0.9592	0.9592	0.9592
Position_TMD1	0.4983	***0.5***	0.5	0.5	0.5
Position_TMD2	0.5017	***0.5***	0.5	0.5	0.5
Objective ($\times 10^5$)	5.6766	***5.6762***	5.6762	5.6762	5.6762

Here, the SQP-1, SQP-2, and SQP-3 represent the SQP optimization methodology using the initial value as {0.1, 1, -0.9}, {0.1, 1, 1} and {0.0936, 0.9595, 0} (the optimal value obtained from Step (1)), respectively. It can be realized from Table 4.9 that these two symmetrical DTMD is exactly attached in the mid-span of the curved beam. Figure 4.11 illustrates the GA optimization convergence analysis for Steps (1) and (2).

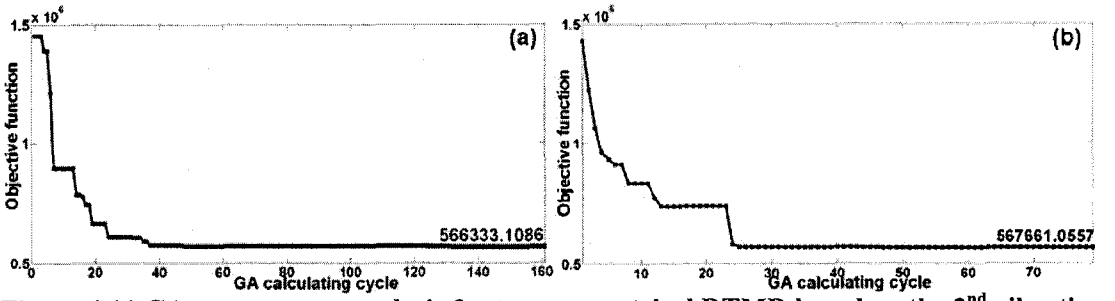

Figure 4.11 GA convergence analysis for two symmetrical DTMD based on the 2nd vibration mode with mass ratio (μ=0.005) for each TMD. (a) Step (1). (b) Step (2).

To illustrate the effectiveness of these set of optimal DTMD design, the structural response of transverse displacement (w) comparison and sensitivity analysis based on small deviation (±10%) from the optimal parameters have been investigated and shown in Figure 4.12. The investigations for the tangential displacement (u), rotation (ψ) and the 2nd modal responses have been provided in "Appendix J".

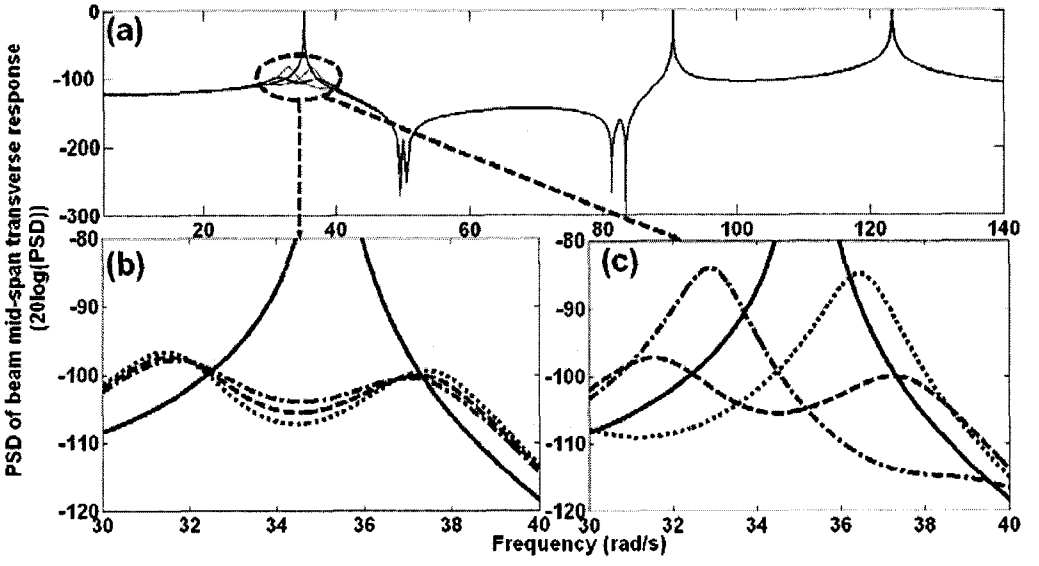

Figure 4.12 PSD of curved beam mid-span transverse displacement (w) and design parameters' sensitivity analysis. (a) Frequency range 5-140 (*rad/s*). (b) Sensitivity analysis for optimal damping factor (ξ_{TMD}). (c) Sensitivity analysis for optimal frequency ratio (f_{TMD}). Solid, dashed, dotted and dashed-dotted lines represent uncontrolled structure, structure with optimal DTMD, as stated in Tables 4.9, structure with DTMD having -10% and +10% deviations from designed optimal values, respectively.

It can be realized from Figure 4.12 and "Appendix J" that the optimally design DTMD system can significantly reduce the vibration due to the 2nd mode, and also it can be concluded that: (1) the optimally designed DTMD system is much more sensitive to the frequency ratio (f_{TMD}) than to the damping factor (ξ_{TMD}); (2) the effectiveness of the attached DTMD is restricted around its tuned natural frequency, thus it is possible to design a MTMD system based on different vibration modes separately.

Comparing the optimal DTMD parameters with those for single TMD provided in Table 4.4 (Case 1) for the 2nd mode with mass ratio (μ=0.01), one can easily find that there are approximately the same. Here it should be noted that the optimal two symmetrical DTMD in this section has mass ratio of 0.005 for each TMD and thus total mass ratio is 0.01. Thus, one may make the conclusion that the effects of these two optimally designed TMD systems are similar. Therefore, the final scheme for the optimal TMD design based the 2nd vibration mode would be selected as that listed in Table 4.4 for Case a, in which one TMD with mass ratio (μ=0.01) would be attached in the curved beam's mid-span.

4.4.3.2 Design based on the 4th vibration mode

Following the same procedure as those for studying the 2nd vibration mode, the optimal design procedure for two symmetrical DTMD system based on the 4th vibration mode will be presented in this section. The optimization problem and parameters for the GA optimization are the same as those provided in Equation (4.15) and Table 4.7. The mass ratio (μ) for each attached TMD is assumed as 0.01, thus total mass ratio (μ) is equal to 0.02. Table 4.10 compares the optimal results obtained using the GA, hybrid optimization and SQP technique with different initial values for Step (1).

Table 4.10 The optimal two symmetrical DTMD parameters based on the 4th vibration mode with mass ratio (μ=0.01) for each TMD—Step (1).

Design Variables	Optimal Methodologies				
	GA	Hybrid	SQP-1	SQP-2	SQP-3
ξ_{TMD}	0.1783	***0.1402***	0.1403	0.1401	0.0681
f_{TMD}	0.9057	***0.9278***	0.9278	0.9256	1.0186
Position_TMD1	0.3045	***0.3170***	0.3170	0.3095	0.5
Position_TMD2	0.6955	***0.6830***	0.6830	0.6905	0.5
Objective ($\times 10^5$)	9.18428	***9.0205***	9.0205	9.0218	14.099

In Table 4.10, the SQP-1, SQP-2 and SQP-3 have the same definitions as those in Table 4.8. It can be realized that: using different initial points, the optimization approach based on SQP presents different local optimum points; GA can catch near global optimum solution; the hybrid optimization method can accurately catch the global optimum points. The results based on Step (1) show that the two TMD should be attached to Elements 3 and 5 in Step (2). The accurate position and the optimal damping and stiffness of the DTMD system in their relative elements for Step (2) are obtained. The results are provided in Table 4.11.

Table 4.11 The optimal two symmetrical DTMD parameters based on the 4th vibration mode with mass ratio (μ=0.01) for each TMD—Step (2).

Design Variables	Optimal Methodologies				
	GA	Hybrid	SQP-1	SQP-2	SQP-3
ξ_{TMD}	0.1409	***0.1427***	0.1427	0.1427	0.1427
f_{TMD}	0.9255	***0. 9238***	0. 9238	0. 9238	0. 9238
Position_TMD1	0.3054	***0.3058***	0.3058	0.3058	0.3058
Position_TMD2	0.6945	***0.6942***	0.6942	0.6942	0.6942
Objective ($\times 10^5$)	9.29139	***9.29071***	9.29071	9.29071	9.29071

In Table 4.11, the SQP-1, SQP-2 and SQP-3 represent the optimal results obtained from SQP optimization methodology with initial values of {0.1, 1, -0.9}, {0.1, 1, 1} and

{0.1403, 0.9278, -0.5616} (the optimal value obtained from Step (1)), respectively. Figure 4.13 illustrates the GA optimal results convergence analysis for optimal Steps (1) and (2) listed in Figure 4.10.

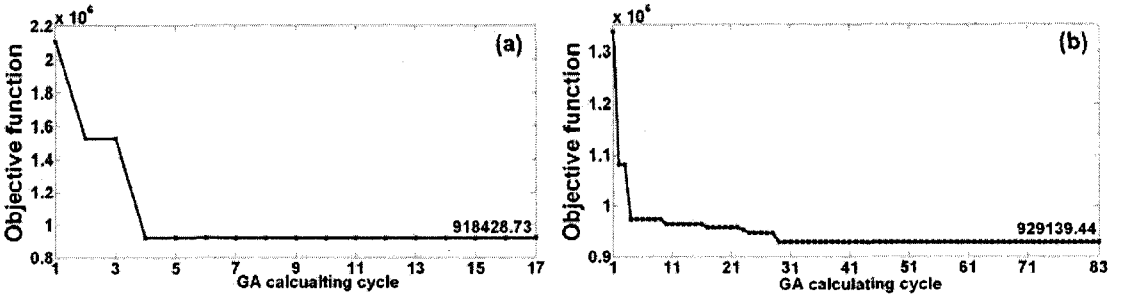

Figure 4.13 Convergence analysis for two symmetrical DTMD based on the 4th vibration mode with mass ratio (μ=0.01) for each TMD. (a) Step (1). (b) Step (2).

Again, to illustrate the validity of this set of optimal DTMD design, the structural response comparison for transverse displacement (w) and sensitivity analysis based on small deviation from the optimal parameters listed in Table 4.11 have been investigated and shown in Figure 4.14. The investigations for the tangential displacement (u), rotation (ψ) and the 4th modal responses have been provided in "Appendix K". As the design variables include the position of the attached DTMD system, the small deviation from the optimal position is selected as ±0.1 from the optimal parameter in the natural coordinate (η), which is about ±0.35% deviation relative to the beam's curvilinear length, and the small deviation for the damping and frequency ratio of the DTMD system are still selected as ±10% from their relative optimal values. It can be seen from Figure 4.14 and "Appendix K" that the optimally designed DTMD system based on the 4th mode can effectively suppress the vibration due to the 4th mode.

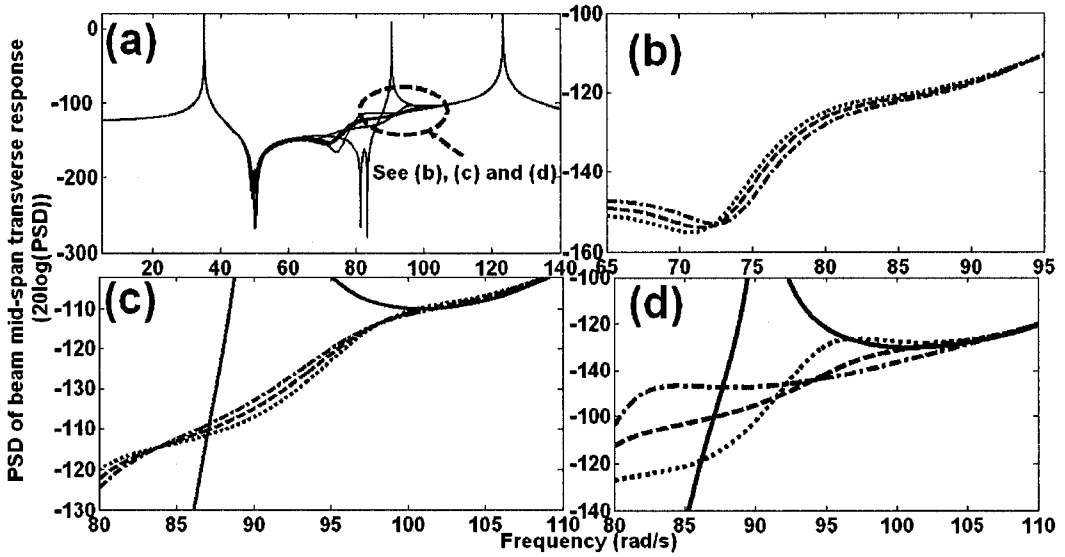

Figure 4.14 PSD of curved beam mid-span transverse displacement (w) and design parameters' sensitivity analysis. (a) Frequency range 5-140 (*rad/s*). (b) Sensitivity analysis for optimal position. (c) Sensitivity analysis for optimal damping factor (ξ_{TMD}) (d) Sensitivity analysis for optimal frequency ratio (f_{TMD}). Solid, dashed, dotted and dashed-dotted lines represent uncontrolled structure, structure with optimal DTMD, as listed in Table 11, structure with DTMD having -10% (-0.1) and +10% (+0.1) deviations from designed optimal values, respectively.

Figure 4.15 compares the structural response around the 4th vibration mode for curved beam with the optimal two symmetrical DTMD system provided in this section and the optimal single mid-span TMD presented in Table 4.6 for Case b, which has the same mass (total) ratio as the optimal two symmetrical DTMD system presented in Table 4.11.

Results provided in Figures 4.14 and 4.15 show that: (1) the optimal two symmetrical DTMD design proposed in this section can provide much better vibration suppression effectiveness than that for the single attached mid-span optimal TMD under the same mass (total) ratio; (2) the optimal DTMD design proposed in this section has almost no effect on other vibration modes. This property is very important for the design of MTMD system.

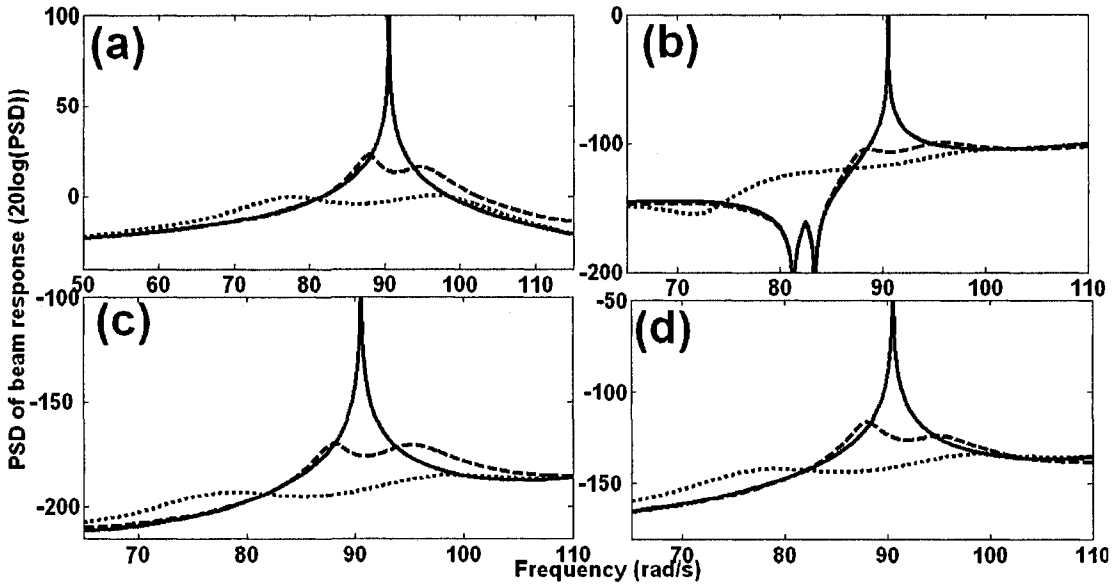

Figure 4.15 PSD of curved beam response comparison around the 4th natural frequency for different optimal TMD designs based on the 4th vibration mode. (a) The 4th vibration modal response. (b) Curved beam mid-span's transverse displacement (w) (c) Curved beam mid-span's tangential direction displacement (u). (d) Curved beam mid-span's rotation (ψ). Solid, dashed and dotted lines represent uncontrolled structure, structure with single optimal TMD in Table 4.6 (Case b) and with optimal two symmetrical DTMD in Table 4.11, respectively.

4.4.3.3 Design based on the 5th vibration mode

Following the same procedure as those for studying the 2nd and 4th modes, the optimal two symmetrical DTMD system related to the 5th vibration mode has been studied in this section. The optimization problem and parameters for GA optimization was the same as those listed in Equation (4.15) and Table 4.7. The mass ratio (μ) for each attached TMD is assumed to be 0.0075. Table 4.12 compares the optimal results obtained using the GA, hybrid optimization methods and SQP with different initial values for Step (1).

Table 4.12 The optimal two symmetrical DTMD parameters based on the 5th vibration mode with mass ratio (μ=0.0075) for each TMD—Step (1).

Design Variables	Optimal Methodologies				
	GA	Hybrid	SQP-1	SQP-2	SQP-3
ξ_{TMD}	0.0857	***0.096***	0.096	0.096	0.0994
f_{TMD}	0.9557	***0.9679***	0.9679	0.9679	0.9475
Position_TMD1	0.1836	***0.1873***	0.1873	0.1873	0.5
Position_TMD2	0.8164	***0.8127***	0.8127	0.8127	0.5
Objective ($\times 10^6$)	1.8573	***1.8416***	1.8416	1.8416	1.8744

In Table 4.12, the SQP-1, SQP-2, and SQP-3 have the same definition as those presented in Tables 4.8 and 4.10. Again it can be realized from Table 4.12 that the hybrid optimization can accurately catch the global optimum point. From the optimal results obtained in Step (1) and Equation (4.14), it can be easily found that the two TMD should be attached onto Elements 2 and 6 in Step (2). Table 4.13 compares the optimal results obtained through the GA, hybrid methods and SQP with different initial values for Step (2). In Table 4.13, the SQP-1, SQP-2, and SQP-3 represent the SQP optimization methodology based on the initial values of {0.1, 1, -0.9}, {0.1, 1, 1} and {0.096, 0.9679, -0.3887} (the optimal value obtained from Step (1)), respectively. Figure 4.16 illustrates the GA optimization convergence analysis for Steps (1) and (2).

Table 4.13 The optimal two symmetrical DTMD parameters based on the 5th vibration mode with mass ratio (μ=0.0075) for each TMD—Step (2).

Design Variables	Optimal Methodologies				
	GA	Hybrid	SQP-1	SQP-2	SQP-3
ξ_{TMD}	0.0992	***0.0953***	0.0953	0.0953	0.0953
f_{TMD}	0.9667	***0.9634***	0.9634	0.9634	0.9634
Position_TMD1	0.1759	***0.1715***	0.1715	0.1715	0.1715
Position_TMD2	0.8241	***0.8285***	0.8285	0.8285	0.8285
Objective ($\times 10^6$)	1.8584	***1.8570***	1.8570	1.8570	1.8570

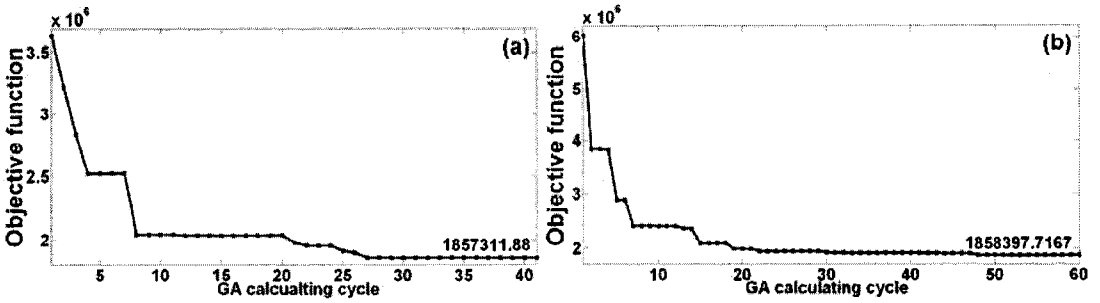

Figure 4.16 GA convergence analysis for two symmetrical DTMD based on the 5th vibration mode with mass ratio (μ=0.0075) for each TMD. (a) Step (1). (b) Step (2).

Similar to the previous cases, it can be realized from Table 4.13 that in Step (2) the optimal results obtained from the proposed hybrid optimization method and the SQP technique with different initial values are the same. Again, to illustrate the validity of this set of optimal DTMD design, the response comparison for structural transverse displacement (w) and sensitivity analysis based on small deviation from the optimal parameters listed in Table 4.13 have been investigated and shown in Figure 4.17. The investigations for the tangential displacement (u), rotation (ψ) and 5th modal response have been provided in "Appendix L". The definitions of small deviation from optimal values are the same as those for Figure 4.14.

It can be seen from Figure 4.17 and "Appendix L" that this set of optimally designed DTMD system for the 5th vibration mode can effectively suppress the vibration due to the 5th vibration mode. Figure 4.18 compares the structural response around the 5th vibration mode for the curved beam with the optimal symmetrical DTMD proposed in this section and the single mid-span optimal TMD presented in Table 4.5 for Case c, which has the same mass (total) ratio (μ) as the optimal two symmetrical DTMD system provided in Table 4.13.

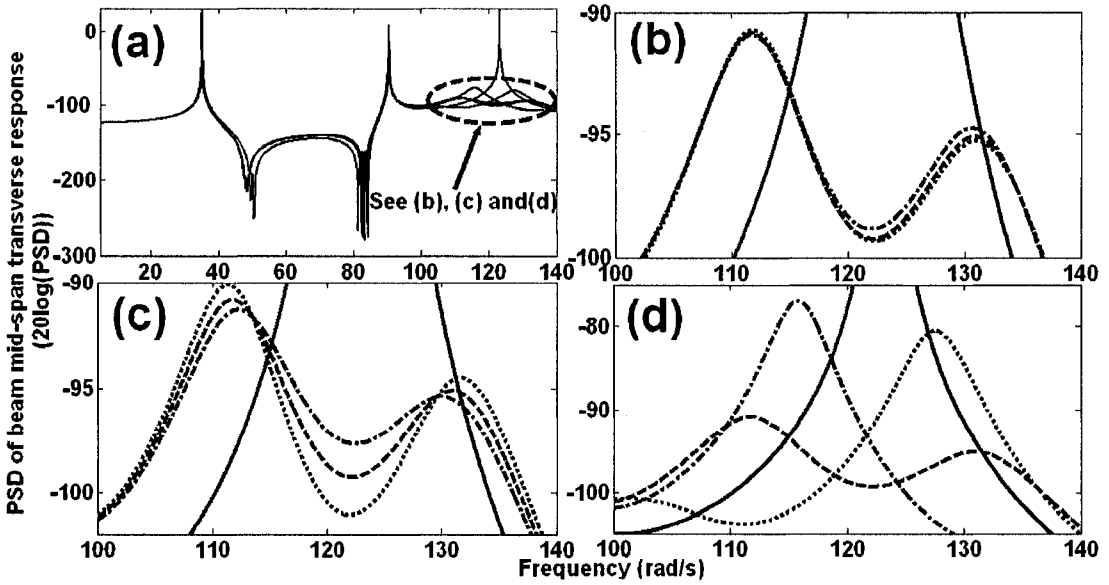

Figure 4.17 PSD of curved beam's mid-span transverse displacement (w) and design parameters' sensitivity analysis. (a) Frequency range 5-140 (*rad/s*). (b) Sensitivity analysis for optimal position. (c) Sensitivity analysis for optimal damping factor (ξ_{TMD}). (d) Sensitivity analysis for optimal frequency ratio (f_{TMD}). Solid, dashed, dotted and dashed-dotted lines represent uncontrolled structure, structure with optimal DTMD, as stated in Table 13, structure with DTMD having -10% (-0.1) and +10% (+0.1) deviations from designed optimal values, respectively.

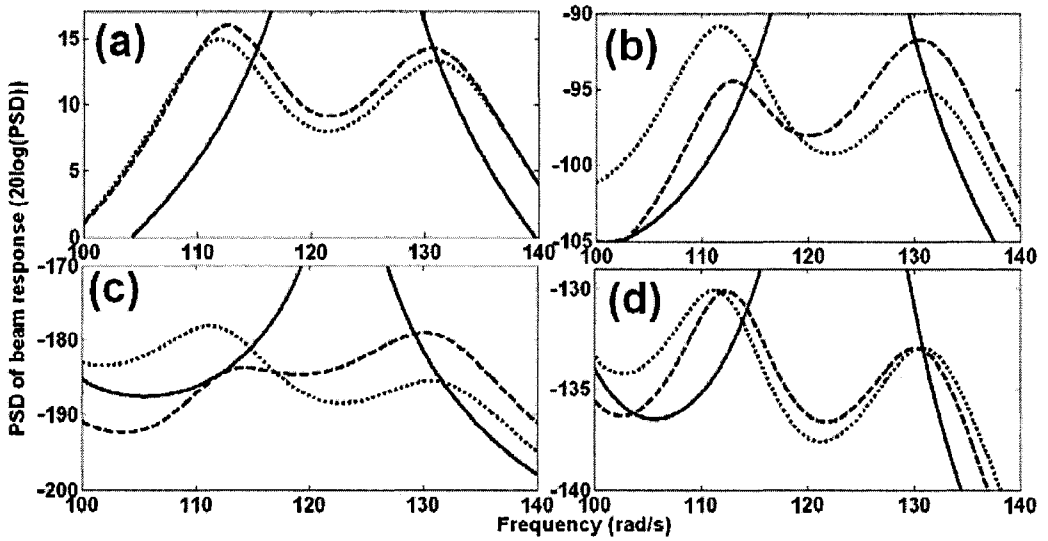

Figure 4.18 PSD of curved beam response comparison around the 5th natural frequency for different optimal TMD designs based on the 5th vibration mode. (a) The 5th vibration modal response comparison. (b) Curved beam mid-span's transverse displacement (w). (c) Curved beam mid-span's tangential direction displacement (u). (d) Curved beam mid-span's rotation (ψ). Solid, dashed and dotted lines represent uncontrolled structure, structure with single optimal TMD in Table 4.5 (Case c) and with optimal two symmetrical DTMD in Table 4.13, respectively.

It can be found from Figure 4.18 that the optimally designed two symmetrical DTMD system developed in this section performs slightly better than those shown in Table 4.5 Case c for one mid-span attached TMD under the same mass (total) ratio (μ=0.015), but not significantly compared with those for the 4th mode. It may due to the fact that the optimal two symmetrical DTMD system is not much effective and more TMD may be required for 5th vibration mode. This issue has been discussed in the following sections.

4.4.4 Three attached tuned mass damper system

Now let us assume three TMD will be attached to the curved beam to suppress the structural vibration due to the 5th vibration mode. As the curved beam structure and the boundary in this example are both symmetry, obviously two of these three attached TMD would be symmetry and one should be attached in the mid-span. Here, two design methods have been adopted: Method (1), all attached TMD have the same values of damping factor (ξ_{TMD}) and frequency ratio (f_{TMD}); Method (2), only the attached symmetrical TMD have similar damping factor (ξ_{TMD}) and frequency ratio (f_{TMD}).

It is noted that the mass ratio (μ) for each attached TMD has been assumed to be 0.005, thus the total mass ratio for these three DTMD system would be 0.015, which is the same as that for the optimal design of two symmetrical DTMD system and single mid-span TMD system stated in Tables 4.13 and 4.5 for Case c, respectively.

Method (1)

As in this design method all the attached three TMD have the same damping factor (ξ_{TMD}) and frequency ratio (f_{TMD}), thus the optimal problem and the parameters of the GA

optimization methodology will be similar to those stated in Equation (4.15) and Table 4.7, respectively. Following the same procedure as those for studying the two symmetrical DTMD, the optimal results' comparison for Steps (1) and (2), as illustrated in Figure 4.10, are provided in Tables 4.14 and 4.15, respectively. As one of the three TMD is attached to the mid-span, in Tables 4.14 and 4.15 only the position of the symmetrical TMD has been listed. Here it should be noted that based on the results obtained in Step (1), the symmetrical TMD is still located in Elements 2 and 6 for the 7-element finite element model in Step (2).

Table 4.14 The optimal three DTMD based on the 5th vibration mode for Method (1) with mass ratio (μ=0.005) for each TMD —Step (1).

Design	Optimal Methodologies				
Variables	GA	Hybrid	SQP-1	SQP-2	SQP-3
ξ_{TMD}	0.118	***0.0982***	0.0982	0.0982	0.0994
f_{TMD}	0.9147	***0.9759***	0.9759	0.9759	0.9475
Position_TMD1	0.1713	***0.1895***	0.1895	0.1895	0.5
Position_TMD2	0.8287	***0.8105***	0.8105	0.8105	0.5
Objective ($\times 10^6$)	1.9632	***1.8290***	1.8290	1.8290	1.8744

Table 4.15 The optimal three DTMD based on the 5th vibration mode for Method (1) with mass ratio (μ=0.005) for each TMD —Step (2).

Design	Optimal Methodologies				
Variables	GA	Hybrid	SQP-1	SQP-2	SQP-3
ξ_{TMD}	0.1322	***0.0959***	0.0959	0.0959	0.0959
f_{TMD}	1.0443	***0.9709***	0.9709	0.9709	0.9709
Position_TMD1	0.1905	***0.1785***	0.1785	0.1785	0.1785
Position_TMD2	0.8095	***0.8215***	0.8215	0.8215	0.8215
Objective ($\times 10^6$)	2.1056	***1.8587***	1.8587	1.8587	1.8587

In Table 4.14, the SQP-1, SQP-2 and SQP-3 have the same definitions as those presented in Tables 4.8, 4.10 and 4.12. In Table 4.15, the SQP-1, SQP-2 and SQP-3 represent the

SQP optimization methodology based on the initial value of {0.1, 1, -0.9}, {0.1, 1, 1} {0.0982, 0.9759, -0.3476} (the optimal value obtained from Step (1)), respectively. Figure 4.19 also illustrates the GA convergence analysis for the optimal results shown in Tables 4.14 and 4.15.

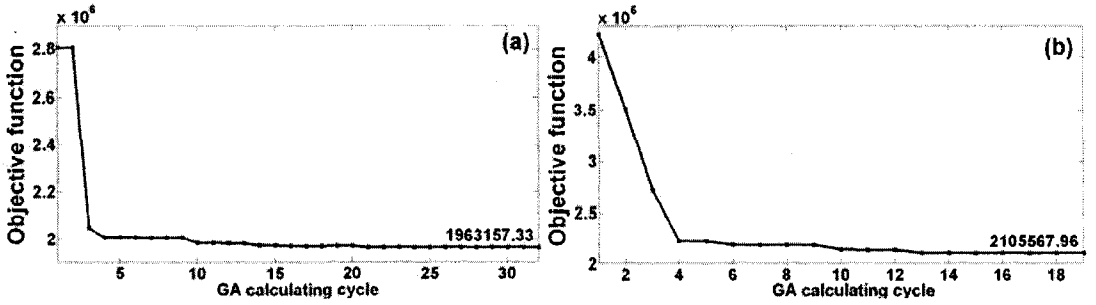

Figure 4.19 GA convergence analysis for three DTMD design Method (1) based on the 5th vibration mode with mass ratio (μ=0.005). (a) Step (1). (b) Step (2).

Again, it can be seen from Figure 4.19 that the GA optimization methodology provides good convergence property and also from the optimal results shown in Tables 4.14 and 4.15, it can be found that the optimal results obtained through the developed GA optimization methodology have successfully caught the neighborhood of the global optimum point. The structural response comparison for transverse displacement (w) and the optimal parameters' sensitivity analysis have been provided in Figure 4.20 to verify the validity of this set of optimal DTMD design. The results for the tangential displacement (u), rotation (ψ) and 5th modal responses have been provided in "Appendix M". It should also be noted that the small deviations from the optimal parameters have the same definitions as those in Figures 4.14 and 4.17.

It can be seen from Figure 4.20 and "Appendix M" that the optimally designed DTMD system for design Method (1) is effective to suppress the vibration due to the 5th mode.

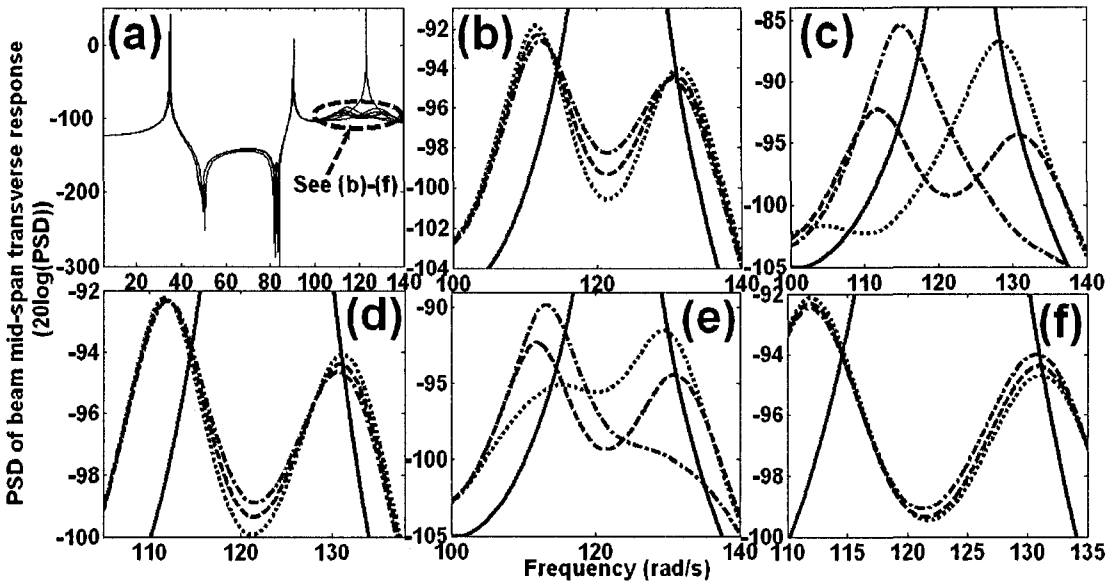

Figure 4.20 PSD of curved beam's mid-span transverse displacement (w) and optimal parameters' sensitivity analysis for three DTMD design Method (1). (a) Frequency range 5-140 (*rad/s*) (b) Sensitivity analysis for optimal damping factor for the two symmetrical TMD. (c) Sensitivity analysis for optimal frequency ratio for the two symmetrical TMD. (d) Sensitivity analysis for optimal damping factor for the mid-span TMD. (e) Sensitivity analysis for optimal frequency ratio for the mid-span TMD. (f) Sensitivity analysis for optimal position for the two symmetrical TMD. Solid, dashed, dotted and dashed-dotted lines represent uncontrolled structure, structure with optimal DTMD listed in Table 4.15, structure with DTMD having -10% (-0.1) and +10% (+0.1) deviations from designed optimal values, respectively.

Method (2)

In this design method, the mid-span TMD is assumed to have different damping factor (ξ_{TMD}) and frequency ratio (f_{TMD}) from those of the symmetrical TMD. Therefore, the optimization problem has five design variables and can be stated as:

$$\begin{aligned} &\text{Find the design variables:} && \{X\}=\{\xi_{sTMD}, f_{sTMD}, \eta_{TMD}, \xi_{TMD}, f_{TMD}\} \\ &\text{To minimize:} && \textit{RMS of response for the } 5^{th} \textit{ vibration mode} \\ &\text{Subjected to:} && -1\le \eta_{TMD} \le 1,\ 0\le \xi_{sTMD} \le 1,\ 0\le f_{sTMD} \le 2.5 \\ & && 0\le \xi_{TMD} \le 1,\ 0\le f_{TMD} \le 2.5 \end{aligned} \quad (4.16)$$

where parameters ξ_{sTMD}, f_{sTMD}, ξ_{TMD} and f_{TMD} represent the damping factor, frequency ratio for the symmetrical and mid-span TMD, respectively and η_{TMD} is the position of the

symmetrical TMD. The mass ratio (μ) for each attached TMD is assumed to be 0.005, and thus the total mass ratio (μ) is equal to 0.015. Based on Equation (4.16), the parameters for the GA optimization method are defined in Table 4.16.

Table 4.16 Parameters of GA optimization.

N_{pop}	12	X_{rate}	0.5	χ	1×10^{-4}
N_{var}	5	M_{rate}	0.2		

It should be noted that the GA optimization technique is kind of random searching method, which can not guarantee that the GA optimum results can converge to the same (close) values each time. In fact, all of the GA optimum results presented above for the 2 and 3-dimension design variables cases have been checked five times and each time they all converged to the same (close) optimum values, which means that the GA optimization technique developed in this study is very stable and robustness. However, the optimization problem stated in Equation (4.16) has five design variables, thus to investigate the accuracy and convergence of the developed hybrid and GA optimization techniques, in this section the developed hybrid optimization technique has been repeated 6 times. The optimum results obtained by the GA and hybrid optimization methods in Step (1), as illustrated in Figure 4.10, have been provided in Table 4.17. Figure 4.21 illustrates the GA convergence analysis for each calculation shown in Table 4.17.

Here, it should be noted that in Table 4.17 (also 4.18), the "position" represents the position of one of the symmetrically attached TMD. One can easily find from Table 4.17 that the optimal locations obtained using the GA and also hybrid techniques converge to two different points, one is around the middle of the beam (the 5th and 6th calculations), the other is around 0.18 along the curved beam's S coordinate (the 1st to 4th calculations)

with close values of objective function. It is noted that if DTMD system based on one special vibration mode is attached in one point, we will replace them with single TMD design as done for the 2nd vibration mode.

Table 4.17 The optimal three DTMD based on the 5th vibration mode for Method (2) with mass ratio (μ=0.005) for each TMD —Step (1).

Times	Optimal method	Design Variables					Objective function ($\times 10^6$)
		ξ_{sTMD}	f_{sTMD}	Position	ξ_{TMD}	f_{TMD}	
1	GA	0.0833	0.9362	0.1760	0.5418	2.48	2.1556
	Hybrid	0.0767	0.9814	***0.1915***	0.5	2.5	2.0240
2	GA	0.0984	0.9825	0.1854	0.4372	1.2716	2.0485
	Hybrid	0.0782	0.9780	***0.1823***	0.0001	1.128	2.0272
3	GA	0.1284	0.8902	0.1770	0.6436	1.0543	2.4564
	Hybrid	0.0782	0.9781	***0.1823***	0.8115	2.42	2.0272
4	GA	0.0906	0.9429	0.1765	0.7063	1.2192	2.1176
	Hybrid	0.0782	0.9781	***0.1821***	1	2.2892	2.0272
5	GA	0.1370	0.9255	0.4999	0.0309	2.5	2.2298
	Hybrid	0.081	0.9647	0.5	0.9985	2.48	2.044
6	GA	0.1655	0.9118	0.4870	0.2687	1.3450	2.3849
	Hybrid	0.081	0.9647	0.5	0.0001	1.125	2.0436

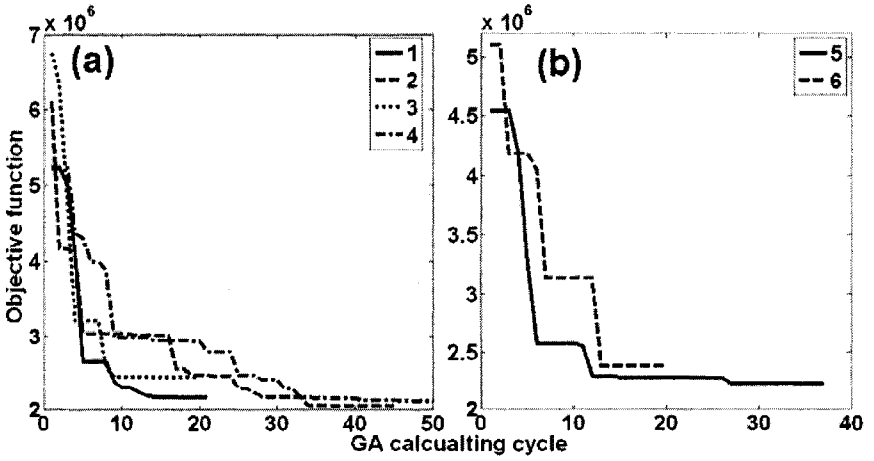

Figure 4.21 GA convergence analysis for each calculation as listed in Table 4.17. (a) For the 1st to 4th calculation. (b) For the 5th and 6th calculations.

From the 1st to 4th calculations in Table 4.17, one can find that different optimal values of the design variables can provide the same (close) values of objective, which basically means that the optimization problem established in Equation (4.16) is a very complex problem having multiple optimal points with close value of objective function and the developed GA and hybrid techniques are capable to catch all these points. As mentioned before, the main purpose of Step (1) is to catch the optimal elements for the 7 elements beam model in Step (2). Based on this, one can also find that although the optimal damping factor and frequency ratio especially for the mid-span TMD are significantly different in the 1st to 4th calculations, the optimal locations for the symmetrically attached TMD are very close, which are located in the Elements 2 and 6 for the 7 elements model in Step (2). Therefore, one can make the conclusion that the developed GA optimization method has successfully caught the global optimal region in Step (1).

In Step (2), the GA and hybrid optimization methods have been repeated 8 times, and the results have converged to two sets of parameters, as provided in Table 4.18. Figure 4.22 illustrates the GA convergence analysis for all the 8 calculations stated in Table 4.18.

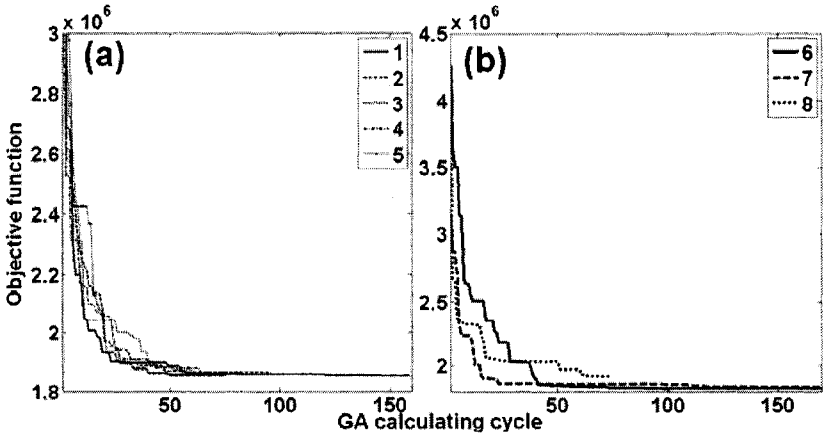

Figure 4.22 GA convergence analysis for each calculation as stated in Table 4.18. (a) For the 1st -5th times. (b) For 6th -8th times.

Table 4.18 The optimal three DTMD based on the 5th vibration mode for Method (2) with mass ratio (μ=0.005) for each TMD —Step (2).

Times	Optimal method	Design Variables					Objective function ($\times 10^6$)
		ξ_{sTMD}	f_{sTMD}	Position	ξ_{TMD}	f_{TMD}	
1	GA	0.098	0.9823	0.1751	0.226	0.2120	1.8509
	Hybrid	***0.0637***	***1.0245***	***0.1862***	***0.0525***	***0.9034***	***1.8076***
2	GA	0.1222	1	0.1777	0.0755	0.9292	1.8652
	Hybrid	***0.0637***	***1.0245***	***0.1862***	***0.0525***	***0.9034***	***1.8076***
3	GA	0.1119	0.9855	0.1709	0.0780	0.9308	1.8593
	Hybrid	***0.0637***	***1.0245***	***0.1862***	***0.0525***	***0.9034***	***1.8076***
4	GA	0.0939	0.9742	0.1775	0.0995	0.9545	1.8571
	Hybrid	***0.0637***	***1.0245***	***0.1862***	***0.0525***	***0.9034***	***1.8076***
5	GA	0.1038	0.9892	0.1799	0.0814	0.9447	1.8543
	Hybrid	***0.0637***	***1.0245***	***0.1862***	***0.0525***	***0.9034***	***1.8076***
6	GA	0.077	0.9283	0.1709	0.0692	1.0478	1.8233
	Hybrid	0.0735	0.9280	0.1710	0.0288	1.0529	1.8136
7	GA	0.0823	0.9442	0.1751	0.0795	1.0480	1.8323
	Hybrid	0.0735	0.9280	0.1710	0.0288	1.0529	1.8136
8	GA	0.129	0.9127	0.1732	0.0776	0.9678	1.9133
	Hybrid	0.0735	0.9280	0.1710	0.0288	1.0529	1.8136

From Table 4.18 and Figure 4.22, it can be found that: (1) in the 1st to 5th calculations, the optimal results obtained through the developed hybrid optimization method are exactly the same, although the relative results obtained through GA have different values. This means that the developed GA optimization method has successfully caught the global optimal region; (2) From the 6th to 8th calculations, the same conclusion can be found as those in the 1st to 5th calculations; (3) the optimization problem in this part has two optimal regions with very close value of objective function; (4) comparing the optimal result obtained from the 1st to 8th calculations, it can be found that the results for the 1st to 5th calculations is the best.

Again the effectiveness of the optimally designed three DTMD system based on Method (2) will be tested through the structural response comparison and the optimal parameter's sensitivity analysis. The result for the transverse displacement (w) has been shown in Figure 4.23. The investigations for the tangential displacement (u), rotation (ψ) and 5th modal responses have been provided in "Appendix N". Again it should also be noted that the small deviations from the optimal parameters have the same definition as those in Figures 4.14 and 4.17.

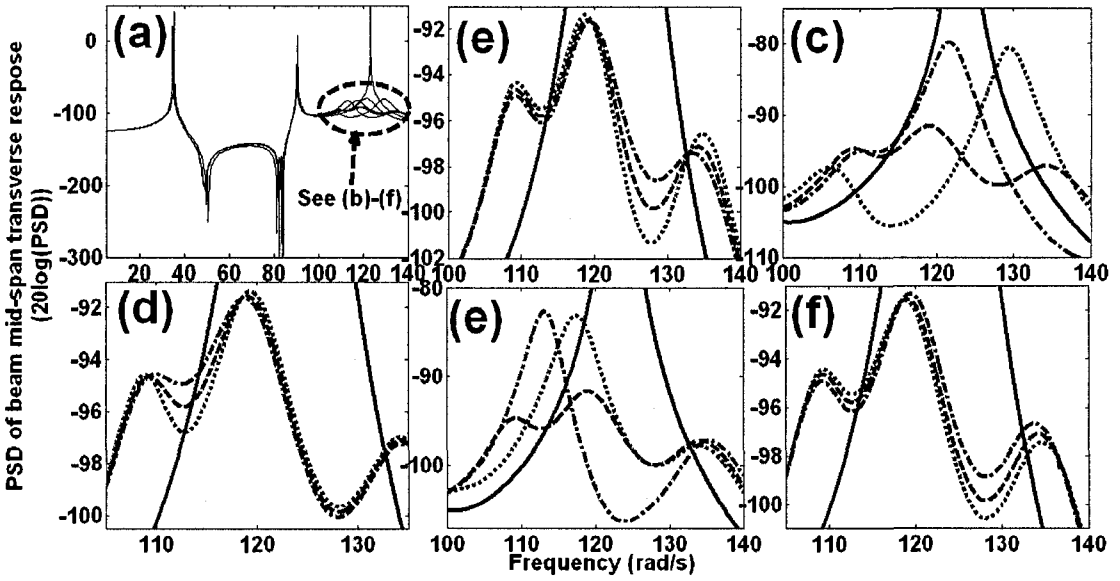

Figure 4.23 PSD of curved beam's mid-span transverse displacement (w) and optimal parameters' sensitivity analysis for three DTMD design Method (2). (a) Frequency range 5-140 (*rad/*s). (b) Sensitivity analysis for optimal damping factor for the two symmetrical attached TMD. (c) Sensitivity analysis for optimal frequency ratio for the two symmetrical attached TMD. (d) Sensitivity analysis for optimal damping factor for the mid-span attached TMD. (e) Sensitivity analysis for optimal frequency ratio for the mid-span attached TMD. (f) Sensitivity analysis for optimal position for the two symmetrical attached TMD. Solid, dashed, dotted and dashed-dotted lines represent uncontrolled structure, structure with optimal DTMD, as stated in Table 4.18, structure with DTMD having -10% (-0.1) and +10% (+0.1) deviations from designed optimal values, respectively.

From Figure 4.23 and "Appendix N", it can be found that: (1) this set of three optimally designed DTMD system is effective; (2) this set of three optimally designed DTMD system adds two sets of TMD around the 5th mode of the uncontrolled structure, thus the combined structure has three resonance frequencies around the 5th mode, and the optimal damping is to decrease the response at the added resonant frequencies.

Till now four different sets of optimal TMD system design based on the 5th vibration mode have been proposed with the same input mass (total) ratio of 0.0015, which include: one mid-span attached TMD (Tables 4.5 Case c); two symmetry DTMD (Table 4.13); three DTMD (method (1) in Table 4.15); three DTMD (Method (2) in Table 4.18). Table 4.19 summarizes the optimal parameters and results for the TMD designs based on the 5th vibration mode.

Table 4.19 The TMD design based on the 5th vibration mode for total mass ratio (μ=0.0015). Method a: one mid-span TMD. Method b: two symmetrical DTMD. Method c: three DTMD Method (1). Method d: three DTMD Method (2).

Methods	No of TMD	Mass ratio of each TMD	Design Variables			Objective function ($\times 10^6$)
			Position	ξ_{TMD}	f_{TMD}	
a (Table 4.5 Case c)	1	0.015	0.5	0.0923	0.9458	1.9180
b (Table 4.13)	2	0.0075	{0.1715, 0.8285}	0.0953	0.9634	1.8570
c (Table 4.15)	3	0.005	{0.1785, 0.8215} 0.5	0.0959	0.9709	1.8587
d (Table 4.18)	3	0.005	{0.1862, 0.8138} 0.5	0.0637 0.0525	1.0245 0.9034	1.8076

Figure 4.24 compared the structural responses for the different optimal TMD designs stated in Table 4.19. From Figure 4.24, one can easily find that: (1) the optimal Methods

b and c listed in Table 4.19 provide almost the same vibration suppression performance; (2) The optimal Method d listed in Table 4.19 is the best design based on the 5th mode.

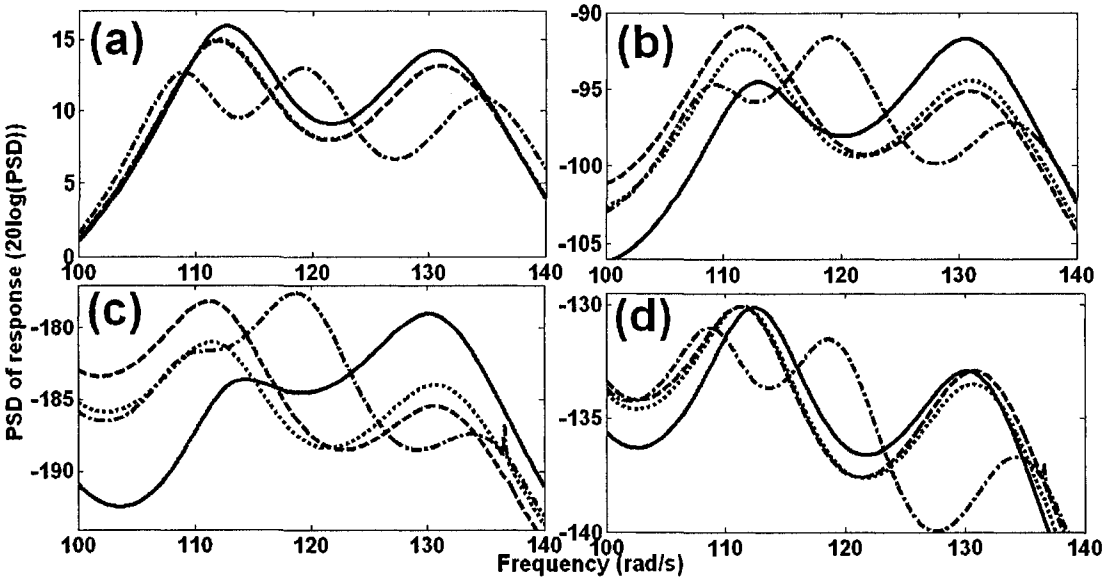

Figure 4.24 PSD of structural responses around the 5th vibration mode. (a) The 5th vibration modal response. (b) The curved beam mid-span transverse displacement (w). (c) The curved beam mid-span tangential displacement (u). (d) The curved beam mid-span rotation (ψ). Solid, dashed, dotted and dashed-dotted lines represent different optimal design methods based on the 5th vibration mode given in Methods a, b, c and d listed in Table 4.19, respectively. Note: in (a) the dashed and dotted lines almost coincides with each other.

4.4.5 Design based on multiple vibration modes

The curved beam's vibration suppression using TMD technology based on the 2nd, 4th and 5th vibration modes has been investigated in above sections. The sensitivity analysis based on small deviation from the optimal values and the response comparisons for each part of optimally designed TMD system have been conducted to verify the validity of the designed optimal TMD system. Based on the results presented above, the final optimal MTMD system can be illustrated through Figure 4.25. It should be noted that to clearly

show the position of the attached TMD, in Figure 4.25, the curved beam's S coordinate has been mapped to natural coordinate [0.0, 1.0].

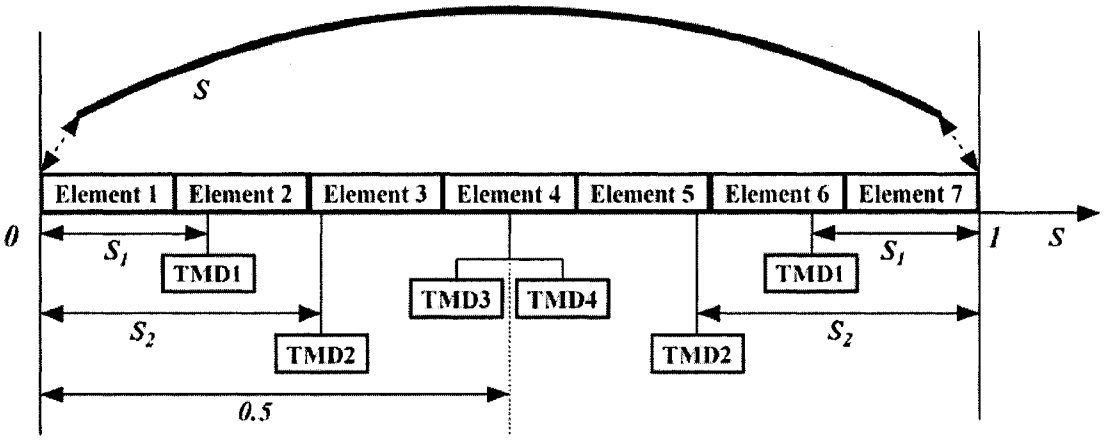

Figure 4.25 Optimal MTMD design.

In Figure 4.25, "TMD3" is the optimal single TMD based on the 2nd vibration mode listed in Table 4.4 for Case a. "TMD2" is the optimal DTMD based on the 4th vibration mode listed in Table 4.11. "TMD1" and "TMD4" are the optimal DTMD based on the 5th vibration mode listed in Table 4.18. Parameters S_1 and S_2 are the optimal locations of the attached TMD system. It should be noted that the exact parameters of the optimal TMD system will also depend on the selected mass ratio (μ). Next, to verify the validity of the proposed optimal MTMD schematic, three sets of optimal MTMD design with the same mass (total) ratio (μ) for each vibration modes, as summarized in Table 4.20, will be investigated.

Table 4.20 Optimal MTMD design strategies: Strategy 1, Three attached MTMD in the curved beam mid-span and using the optimal parameters, as listed in Table 4.4 Case a, Table 4.6 Case b and Table 4.5 Case c; Strategy 2, Six attached MTMD, as illustrated in Figure 4.25, using the optimal parameters, as listed in Tables 4.4 Case a, Table 4.11 and Table 4.18. Strategy 3, Six attached MTMD as illustrated in Figure 4.25, using the optimal parameters, as listed in Tables 4.4 Case a, Table 4.11 and Table 4.15. Note: Parameters S_1 and S_2 are defined in Figure 4.25.

Optimal Strategies	Optimal parameters	Vibration modes		
		2nd (Table 4.4 Case a)	4th (Table 4.6 Case b)	5th (Table 4.5 Case c)
Strategy 1 (Total mass ratio (μ) 4.5%)	Number of TMD	1	1	1
	Mass ratio	0.01	0.02	0.015
	(Mid-span) ξ_{TMD}	0.093	0.0598	0.0923
	(Mid-span) f_{TMD}	0.9592	1.0117	0.9458
		2nd (Table 4.4 Case a)	4th (Table 4.11)	5th (Table 4.18)
Strategy 2 (Total mass ratio (μ) 4.5%)	Number of TMD	1	2	3
	Mass ratio	0.01	0.01	0.005
	(Mid-span) ξ_{TMD}	0.093		0.0525
	(Mid-span) f_{TMD}	0.9592		0.9034
	Position	Mid-span	S_2= 0.3058	S_1= 0.1862
	(Symmetry) ξ_{TMD}		0.1427	0.0637
	(Symmetry) f_{TMD}		0. 9238	1.0245
		2nd (Table 4.4 Case a)	4th (Table 4.11)	5th (Table 4.15)
Strategy 3 (Total mass ratio (μ) 4.5%)	Number of TMD	1	2	3
	Mass ratio	0.01	0.01	0.005
	Position	Mid-span	S_2= 0.3058	S_1= 0.1785
	ξ_{TMD}	0.093	0.1427	0.0959
	f_{TMD}	0.9592	0. 9238	0.9709

As the optimal MTMD Strategies 2 and 3 listed in Table 4.20, includes 6 TMD: one for the 2nd vibration mode, which is the same as that in the Strategy 1; two for the 4th vibration mode with mass ratio (μ=0.01) for each TMD, thus the mass ratio (μ) in the Strategy 1 for the 4th vibration mode should be selected as 0.02 (Table 4.6 Case b); three for the 5th vibration mode with mass ratio (μ=0.005) for each TMD, thus the mass ratio (μ) in the Strategy 1 for the 5th vibration mode should be selected as 0.015 (Table 4.5 Case c). Therefore, the total mass ratio (μ) for each vibration mode and also for the whole MTMD system is the same for the three strategies listed in Table 4.20. Figures 4.26–4.28 illustrate the beam mid-span responses for transverse displacement (w), tangential displacement (u) and rotation (ψ) for uncontrolled structure and the structure with attached optimal MTMD system as listed in Table 4.20, respectively.

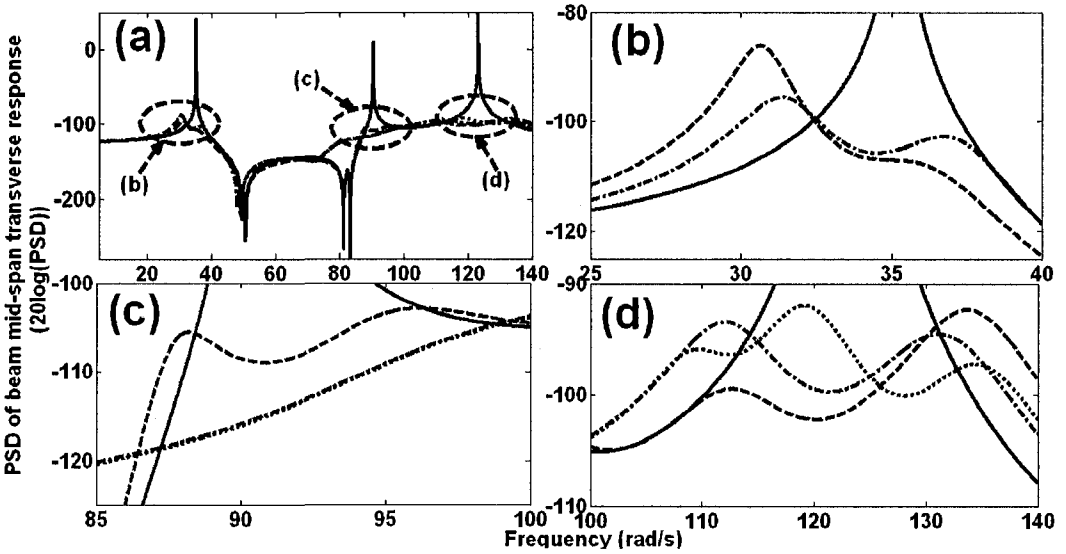

Figure 4.26 PSD of curved beam mid-span transverse displacement (w) comparison. (a) Frequency range 5-140 (*rad/s*). (b) Around the 2nd natural frequency. (c) Around the 4th natural frequency. (d) Around the 5th natural frequency. Solid, dashed, dotted and dashed-dotted lines represent the uncontrolled structure, structure with optimal MTMD Strategies 1, 2 and 3 listed in Table 4.20, respectively. Note: in (b) and (c) dotted and dashed-dotted lines coincide with each other.

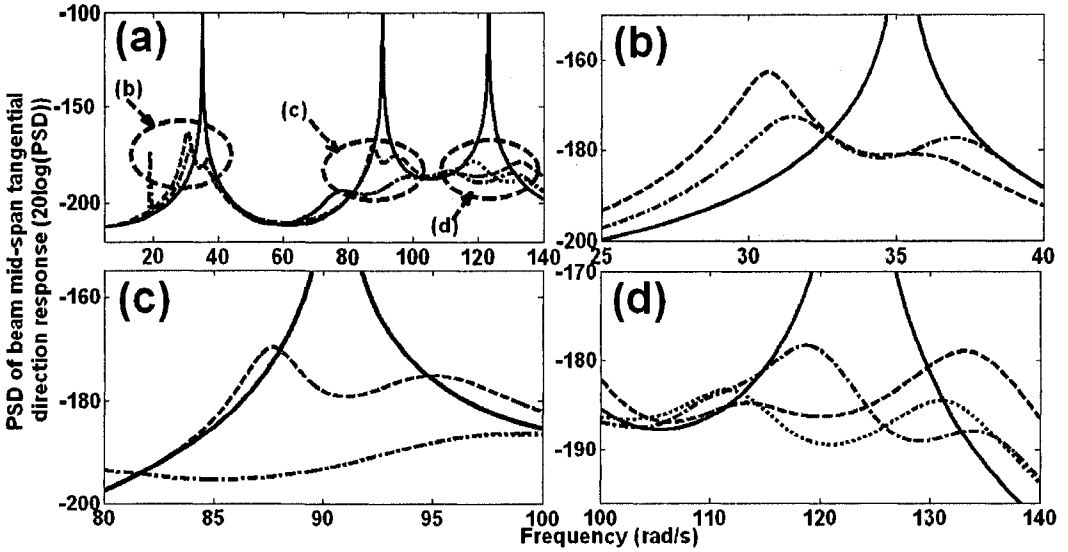

Figure 4.27 PSD of curved beam mid-span tangential (u) direction displacement comparison. (a) Frequency range 5-140 (*rad/s*). (b) Around the 2nd natural frequency. (c) Around the 4th natural frequency. (d) Around the 5th natural frequency. Solid, dashed, dotted and dashed-dotted lines represent the uncontrolled structure, structure with optimal MTMD Strategies 1, 2 and 3 listed in Table 4. 20, respectively. Note: in (b) and (c) dotted and dashed-dotted lines coincide with each other.

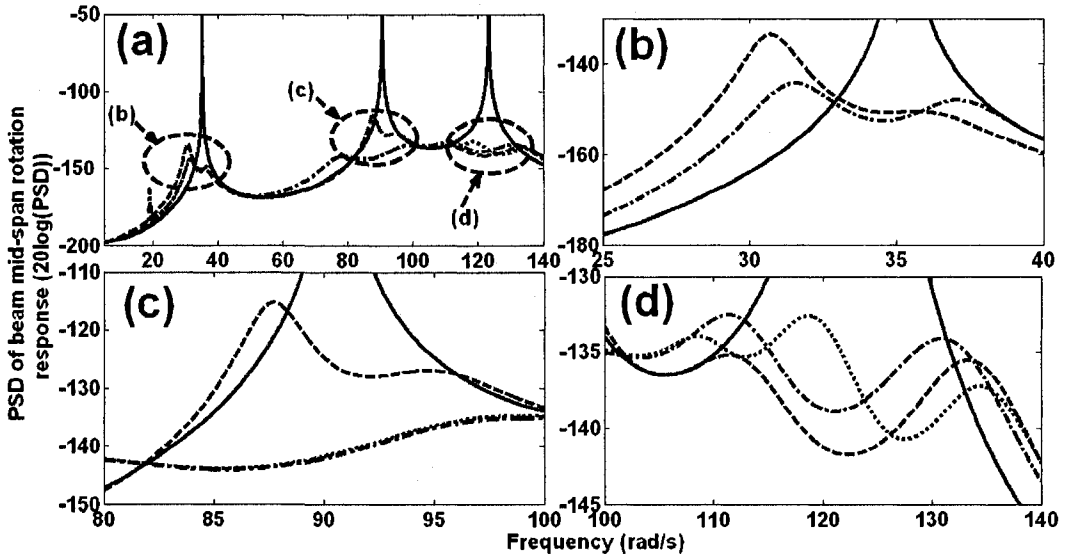

Figure 4.28 PSD of curved beam mid-span rotation (ψ) displacement comparison. (a) Frequency range 5-140 (*rad/s*). (b) Around the 2nd natural frequency. (c) Around the 4th natural frequency. (d) Around the 5th natural frequency. Solid, dashed, dotted and dashed-dotted lines represent the uncontrolled structure, structure with optimal MTMD Strategies 1, 2 and 3 listed in Table 20, respectively. Note: in (b) and (c) dotted and dashed-dotted lines coincide with each other.

From Figures 4.26–4.28, one can find that: (1) the optimal Strategies 2 and 3 listed in Table 20 provide better vibration suppression effectiveness than the optimal Strategy 1; (2) the structural response around the 2nd vibration mode for the optimal Strategy 1 has significant deviation from its relative design condition, as shown in Figures 4.9 and 4.12. The reason is due to the effect of the attached TMD system to the original structural dynamic properties, which will be analyzed in detail through Table 4.21, which illustrates the first 6 natural frequencies for the uncontrolled structure and the frequencies for the structure with the attached optimal TMD system for different optimal methodologies studied above.

From Table 4.21, it can be found that:

(1) For optimal TMD based on one special vibration mode:

(a) For the optimal one mid-span TMD based on the 2nd vibration mode (Table 4.4 Case a), the natural frequencies of the 4th and 5th vibration modes would shift +0.0378% (from 90.5644 to 90.5986 *rad/s*) and +0.0946 % (from 123.2884 to 123.405 *rad/s*) from the original condition, respectively. These are very small deviation and then would not affect the structural response around the 4th and 5th vibration modes, as shown in Figures 4.9 and 4.12.

(b) For the optimal one mid-span TMD based on the 4th vibration mode (Table 4.6 Case b), the natural frequencies of the 2nd and 5th vibration modes would shift -4.08% (from 35.2407 to 33.8045 *rad/s*) and +2.8588 % (from 123.2884 to 126.813 *rad/s*) from the original condition, respectively. These are very big deviations and it is the main reason that the response for the optimal MTMD Strategy 1 has significant deviation around the 2nd mode, as shown in Figures

4.26-4.28. However, the natural frequencies of the 2nd and 5th vibration modes would just shift -0.0358% (from 35.2407 to 35.2281 *rad/s*) and +0.0913 % (from 123.2884 to 123.401 *rad/s*) from the original condition, respectively for two symmetrical optimal DTMD design (Table 4.11). These small deviations would not affect the structural response around the 2nd and 5th vibration modes, as shown in Figures 4.26-4.28 for the Strategies 2 and 3.

(c) For the three types of optimal TMD methods based on the 5th vibration mode (Tables 4.5 Case d, 4.15 and 4.18), no significant shifts for the 2nd and 4th vibration modes from the original system exist. However the maximum deviation happens in the one mid-span TMD optimal design method (Table 4.5 Case b).

(2) For optimal MTMD Strategies 1, 2 and 3 shown in Tables 4.20 and 4.21:

(a) For the optimal MTMD Strategy 1, one can easily find that: (1) the natural frequencies around the 2nd vibration mode shift -2.96% (from 31.3078 to 30.3825 *rad/s*) and -3.8% (from 37.9841 to 36.5395 *rad/s*), from the design condition, respectively; (2) the natural frequencies around the 4th vibration mode shift -0.24% (from 87.3188 to 87.108 *rad/s*) and -0.42% (from 95.7043 to 95.3023 *rad/s*) from the design condition, respectively; (3) the natural frequencies around the 5th vibration mode shift 0.56% (from 111.397 to 112.0194 *rad/s*) and 1.95% (from 132.842 to 135.4281 *rad/s*) from the design condition, respectively.

(b) For optimal MTMD Strategies 2 and 3, no significant shifts from the design condition for the natural frequencies around the 2nd, 4th and 5th vibration modes.

Table 4.21 The natural frequencies analysis for uncontrolled structure and structure with the attached TMD system using different optimal strategies.

Natural Frequency (rad/s)	Uncontrolled structure	Based on 2nd mode (Table 4.4 Case a)	Based on 4th mode		Based on 5th mode			**Strategy 1** (Table 4.20)	**Strategy 2** (Table 4.20)	**Strategy 3** (Table 4.20)
			1 TMD (Table 4.6 Case b)	2 TMD (Table 4.11)	1 TMD (Table 4.5 Case c)	3 TMD (Table 4.15)	3 TMD (Table 4.18)			
1	19.4705	19.4705	19.4705	19.0545	19.4705	19.3684	19.3582	19.4705	18.9499	18.9596
2	**35.2407**	**31.3078** **37.9841**	**33.8045**	**35.2281**	**34.2065**	**34.6902**	**34.6852**	**30.3825** **36.5395**	**31.1252** **37.5908**	**31.1269** **37.5941**
3	64.4729	64.4729	64.4729	64.0156	64.4729	63.6275	63.7146	64.4729	63.2396	63.1541
4	**90.5644**	**90.5986**	**87.3188** **95.7043**	**75.9888** **85.2732** **99.4835**	**89.8283**	**90.2318**	**90.2419**	**87.108** **95.3023**	**75.9658** **85.2729** **98.9118**	**75.9582** **85.273** **98.9808**
5	**123.2884**	**123.405**	**126.813**	**123.401**	**111.397** **132.842**	**110.7266** **121.2436** **121.3372** **133.3781**	**108.8132** **119.2057** **127.9538** **135.6402**	**112.0194** **135.4281**	**109.2102** **119.2708** **128.013** **135.7157**	**111.0693** **121.3024** **121.3725** **133.4642**
6	136.545	136.545	136.545	137.541	136.545	136.9794	136.7633	136.545	137.711	137.9252

Based on the above investigations, one can easily make the conclusion that the Strategy 2 as stated in Tables 4.20 and 4.21 is the best MTMD design strategy which can provide the best vibration suppression performance for the structural response due to the 2^{nd}, 4^{th} and 5^{th} vibration modes and have the smallest effect to the structural dynamic properties and also the smallest deviation from their design condition.

4.4.6 Theoretical basis for the optimal MTMD design

In the above investigations, the optimal DTMD systems design based on each vibration mode have been conducted through the proposed hybrid optimal methodology and then combined together to provide an optimal MTMD design. As mentioned above, the number and position of the attached DTMD system play important roles in an optimal MTMD design problem and in above optimization procedure the number of the attached DTMD system is assumed to be a given value.

Here, we will present a theoretical principle to explain why one, two and three attached TMD are necessary for the optimal TMD system based on the 2^{nd}, 4^{th} and 5^{th} vibration modes, respectively, and also the optimal positions for the attached TMD system. Table 4.22 summarizes the positions for the optimal TMD design based on the 2^{nd}, 4^{th} and 5^{th} vibration modes taken from Tables 4.4 for Case a, 4.11, 4.15 and 4.18, respectively, which were utilized to combined the optimal MTMD Strategies 2 and 3 listed in Table 4.20. Figure 4.29 illustrates the modal shapes for the 2^{nd}, 4^{th} and 5^{th} vibration modes in the transverse displacement (w).

Table 4.22 Optimal location summarization (Tables 4.4 for Case a, 4.11, 4.15 and 4.18).

	2^{nd} mode (Table 4.4 Case a)	4^{th} mode (Table 4.11)	5^{th} mode	
Number of TMD	1	2 symmetry	3 (2 symmetry, 1 mid-span)	
			(Table 4.15)	(Table 4.18)
Position 1		0.3058	0.1785	0.1862
Position 2		0.6942	0.8215	0.8138
Position 3	0.5		0.5	0.5

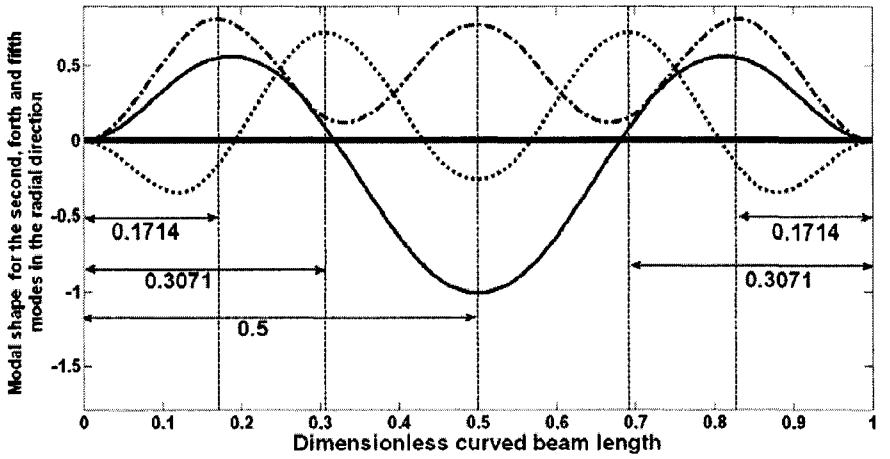

Figure 4.29 Modal shapes for the beam transverse displacement (w). Solid, dotted and dotted-dashed lines represent the modal shapes for the 2^{nd}, 4^{th} and 5^{th} modes, respectively.

Comparing the optimal position illustrated in Table 4.22 with Figure 4.29, one can easily find that the optimal position of the attached DTMD system is located around the relative maximum deflection points in the modal shapes and the required number of the DTMD system is equal to the number of the maximum deflection points in the modal shape:

(1) For the 2^{nd} vibration mode, one maximum deflection point in the modal shape is located in the beam mid-span, thus the optimal locations obtained for the two symmetrically attached DTMD system presented in Table 4.9 are exactly in the mid-span;

(2) For the 4th vibration mode, two symmetrical maximum deflection points exist in the modal shape. Therefore, one can easily explain some phenomenon investigated before: (a) the two symmetrical DTMD design method provided in Table 4.11 can provide much better vibration suppression performance around the 4th natural frequency than the one mid-span attached TMD provided in Table 4.6 (Case b); (b) from Figure 4.8 for the one mid-span TMD design based on the 4th vibration mode, one can find the optimal frequency ratio will not exactly decrease with the increase of the mass ratio, which is also due to the fact that the one mid-span TMD is not suitable choice for the vibration suppression based on the 4th vibration mode;

(3) For the 5th vibration mode, three maximum deflection points exist in the modal shape, in which two are symmetry and one locates in the mid-span. Therefore, one can also easily explain some phenomenon observed above: (a) the two symmetrical DTMD design method stated in Table 4.13 can provide better vibration suppression performance around the 5th vibration mode than the one mid-span attached TMD stated in Table 4.5 for Case c, but not significantly comparing with those for the 4th vibration mode illustrated in Figure 4.15. This is due to the fact that the mid-span is one of the maximum deflection points in the 5th modal shape; (b) from the optimal results given in Table 4.17, one can find that the one possible optimal locations for the symmetrical TMD is the mid-span, which is also due to the fact that the mid-span is one of the maximum deflection points in the 5th modal shape.

Based on above analysis, one can easily make the conclusion that the theoretical principle for continuous structure with attached MTMD system is the modal shape. For beam-type structure, as the transverse displacement is more important than the other degrees of

freedom, its modal shape should be utilized to design the optimal MTMD system. Therefore a design procedure for beam-type structures with attached MTMD system should include the following four main steps:

Step A: Through studying the uncontrolled structural dynamic properties, one can decide which vibration mode(s) is dominant. For instance, the example shown in Chapter 3 has single dominant mode, thus the TMD system design just need to be focused on this dominant mode.

Step B: From the modal shape(s) of dominant mode(s), one can decide how many TMD are required to suppress the vibration based on each dominant mode effectively. Moreover one can also obtain the initial positions of the attached DTMD system, which is close to the maximum deflection point(s) in the dominant modal shape(s).

Step C: Utilizing the optimization methodology proposed in this chapter to obtain the optimal TMD parameters. Here it should be noted that in Step B, the initial position of the DTMD system can be obtained through the modal shape, thus one can directly go to the Step (2), as illustrated in Figure 4.10, and then utilize the proposed hybrid optimal methodology to find the optimal DTMD parameters.

Step D: Based on the results obtained in above steps, the MTMD system can be obtained by simply combining the designed optimal DTMD systems.

Here, it should be noted that although the proposed optimal design principle for beam-type structures with the attached optimal MTMD system is derived based on the example provided in this chapter, it is suitable for general beams with different boundary condition. For example it can be utilized to analysis the optimal TMD design presented in Chapter 3.

4.5 Conclusions and Summary

This chapter presents a thorough investigation on vibration suppression of curved beam-type structures under random loading using multiple Tuned Mass Dampers (MTMD) technique. The finite element formulation for the curved beam with the attached MTMD system has been successfully derived. The finite element method provides general approach and can be efficiently used for design optimization of continuous curved structures with the attached TMD system and also through finite element method the position of the attached TMD can be identified as one of the design variables. It should be noted that based on the developed finite element formulation one can easily extend the study to curved beam with attached single or multiple TMD under different boundary and geometrical conditions. A hybrid optimization methodology, which combines the global optimization method based on GA and the powerful local optimization method based on SQP, has been established and then utilized to find the optimal design parameters (damping, stiffness and position) of the attached multiple TMD system. The validity of the developed GA and hybrid optimization methodologies has been verified through numerous illustrated examples.

Furthermore based on the results shown in the numerical examples, the theoretical principle for designing optimal MTMD system for beam-type structures has been proposed. Based on this, one can easily design the TMD system to suppress the vibration of beam-type structures with different geometrical and boundary conditions effectively and accurately.

CHAPTER 5

EXPERIMENTAL SETUP

5.1 Introduction and Experimental Setup

A uniform cantilever steel beam subjected to base excitation is investigated in this chapter. An optimally designed Tuned Mass Damper (TMD) system will be connected to the steel beam to suppress the vibration effectively. The absolute acceleration of the steel beam's end-point with and without attaching the optimally designed TMD system will be evaluated using the finite element approach presented in Chapters 2 and 3, and also measured by the accelerometer.

The schematic and physical experimental setups are illustrated in Figures 5.1 and 5.2, respectively. Here, a uniform aluminum beam with attached masses, which acts as a MTMD system, is connected to the steel beam, and the aluminum beam's natural frequencies can be tuned to the steel beam's vibration modes through an optimally designed locations and weights of its attached masses. Therefore, through this experimental study, one can validate the optimal design methodologies for the single and multiple attached TMD systems presented in Chapters 3 and 4. Here it should be noted that in Figure 5.1 the aluminum beam has been assumed to be connected to the tip of the steel beam, and the reason for this will be presented in Section 5.3.1.

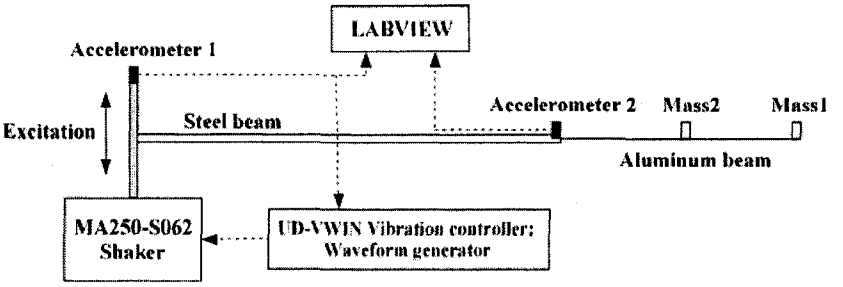

Figure 5.1 Schematic diagram of the experimental setup.

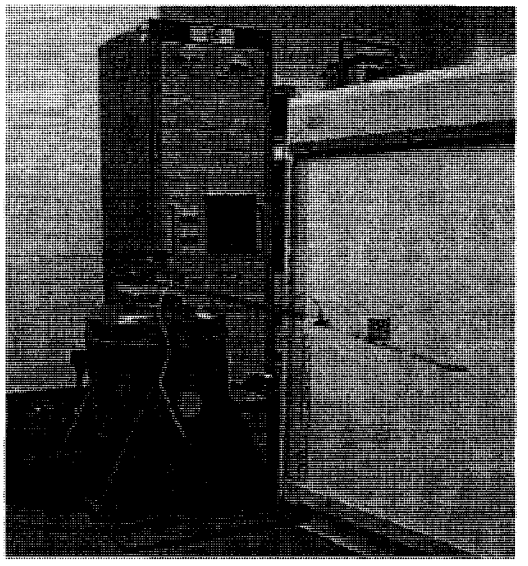

Figure 5.2 Physical diagram of the experimental setup.

In Figure 5.1, "Accelerometer 1" is the accelerometer installed in the MA250-S062 type shaker; "Accelerometer 2" is Minature DeltaTron type 4508 accelerometer, which is utilized to measure the absolute acceleration of the steel beam's end-point; "UD-VWIN vibration controller" is utilized to control the random excitation generated by MA250-S062 type shaker; Agilent 332204 type "Waveform generator" is utilized to control the harmonic excitation generated by MA250-S062 type shaker; analysis software "LABVIEW" with build-in Analogy-Digital-Card (ADC) will be utilized to analysis the experimental data.

It should be noted that in the following experimental study the beam has been subjected to random base excitation with the PSD function of acceleration as the form shown in Figure 5.3, in which the "Expected Excitation signal" is controlled by "UD-VWIN vibration controller" with ±3 (dB) boundary and the cutoff frequencies were set to 2 and 100 (*Hz*), respectively.

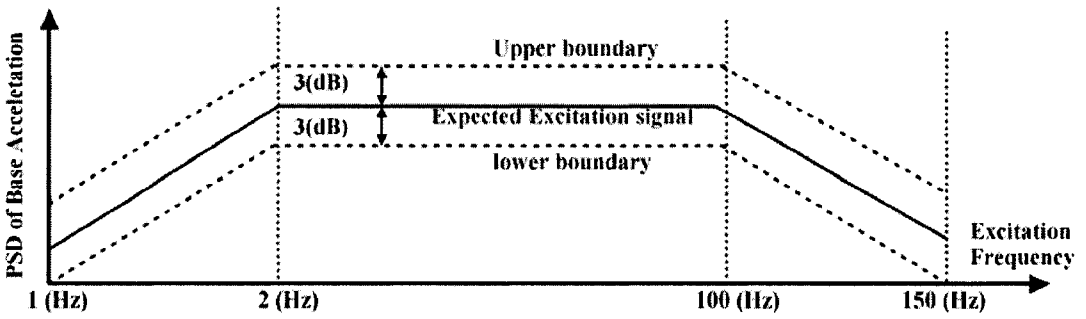

Figure 5.3 Random excitation signal generated by MA250-S62 type shaker controlled by "UD-VWIN vibration controller".

5.2 Dynamic Properties of Beams

Table 5.1 lists the physical and geometrical parameters of the steel and aluminum beams, which will be utilized in this experimental study.

Table 5.1 The physical and geometrical parameters of the steel and aluminum beams[189].

Parameters		Steel Beam	Aluminum Beam
Material		1018-Steel	6061-T6 Aluminum
Elastic modules		2.05×10^{11} (N/m^2)	6.9×10^{9} (N/m^2)
Poisson's ratio		0.29	0.33
Density		7870 (Kg/m^3)	2700 (Kg/m^3)
Length		1(m)	0.5(m)
Rectangle Cross section	Width	38.1 (mm) (1.5 *inch*)	19.38 (mm) (0.76 *inch*)
	Height	6.4 (mm) (0.25 *inch*)	3.12 (mm) (0.123 *inch*)

As both beams' cross-sectional area is rectangle, the shear coefficient for the Timoshenko beam theory can be obtained through $k_q=5(1+\nu)/(6+5\nu)$, where ν is the Poisson's ratio. The equations of motion for beam-type structures subjected to the base excitation can be expressed as:

$$[M]\{\ddot{q}(t)\}+[C]\{\dot{q}(t)\}+[K]\{q(t)\}=[E_s]\ddot{x}_g \tag{5.1}$$

where mass $[M]$ and stiffness $[K]$ matrices have the same definitions as those stated in Equation (2.5). The nodal displacement $\{q\}$, velocity $\{\dot{q}\}$ and acceleration $\{\ddot{q}\}$ vectors are all relative to the base. $\ddot{x}_g$ represents the base excitation. Matrix $[E_s]$ is the direction matrix for base excitation, which can be defined as:

$$[E_s]=\left\{\sum_{element}\left[-\gamma A\int_{-1}^{1}[N(\eta)]\bar{J}(\eta)d\eta,\quad \{0\}_\psi\right]\right\}^T \tag{5.2}$$

where γ and A represent the density and the beam's cross-sectional area, respectively. $[N(\eta)]$ and $\bar{J}(\eta)$ are the shape function and Jacobian between the natural and physical coordinates, as defined in Chapter 2. Expression $\{0\}_\psi$ has the same definition as that in Equation (3.5e). Utilizing the same methodology as stated in Equations (3.10) and (3.11), Equation (5.2) can be transferred to the state-space form as:

$$\{\dot{z}(t)\}=[A]\{z(t)\}+[B]\ddot{x}_g=[A]\{z(t)\}+\{Q(t)\}, \tag{5.3}$$

where $\{z\}$ is the state vector $\{q,\dot{q}\}^T$, and

$$[A]=\begin{bmatrix}[0] & [I]\\ -[M]^{-1}[K] & -[M]^{-1}[C]\end{bmatrix}\text{ and }[B]=\begin{bmatrix}[0]\\ [M]^{-1}[E_s]\end{bmatrix} \tag{5.4}$$

Now utilizing Equation (3.12), one can easily obtain the PSD function of state vector $\{z\}$. As the absolute acceleration would be measured in the experimental study, according to the properties of PSD function, one can evaluate the PSD of absolute acceleration as:

$$[S_{\ddot{q}_a}(\omega)] = \left[-[M]^{-1}[K] \quad -[M]^{-1}[C]\right] [S_z(\omega)] \left[-[M]^{-1}[K] \quad -[M]^{-1}[C]\right]^T \tag{5.5}$$

where $\{\ddot{q}_a\}$ represents the absolute acceleration of nodal variables; $[S_z(\omega)]$ and $[S_{\ddot{q}_a}(\omega)]$ are the PSD of the state-space vector and absolute acceleration. Here it should be noted that in this chapter the beams have been modeled using 7 Timoshenko beam elements with 4 nodes per element, as discussed in Chapter 2.

Next, the dynamic behavior for both steel and aluminum beams will be evaluated using the finite element model stated in Equation (5.1), and then the results would be compared with the experimental data.

5.2.1 Dynamic properties of the steel beam

Figure 5.4 compares the PSD of absolute acceleration of the steel beam' end-point evaluated using the finite element model and obtained from the experimental data.

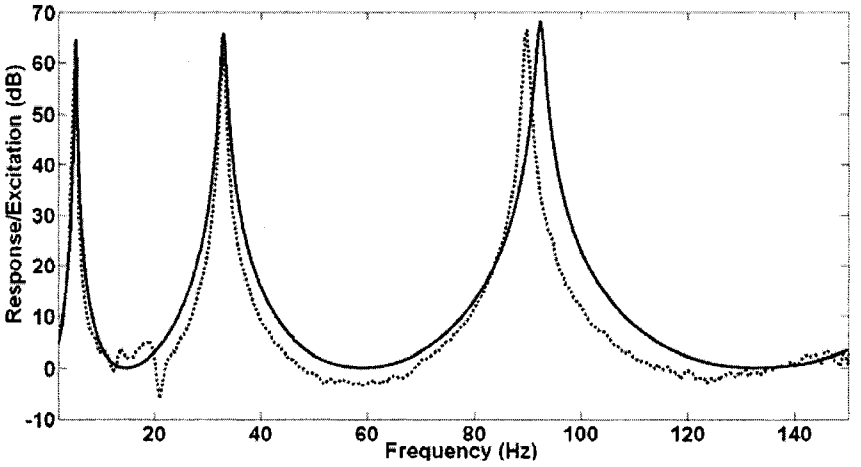

Figure 5.4 Steel beam's end-point acceleration response comparison. Solid and dotted lines represent the results from the finite element model and experimental data, respectively.

Here, it should be noted that in the finite element model, the steel beam's damping factors were selected as 0.031, 0.0161 and 0.0084 for the first three vibration modes, respectively, and 0.0002 for all higher vibration modes. Table 5.2 compares the first three natural frequencies evaluated using the finite element model and the resonant frequencies obtained from the experimental data.

Table 5.2 Natural frequencies of the steel beam's finite element model and the resonant frequencies from experimental data.

	ω_1 (Hz)	ω_2 (Hz)	ω_3 (Hz)
Experimental data	5	32.75	89.75
Finite element Method	5.2599	32.9612	92.3405

5.2.2 Dynamic properties of the aluminum beam

The PSD of the absolute acceleration of the aluminum beam' end-point obtained from experimental data and evaluated through the finite element model is compared in Figure 5.5.

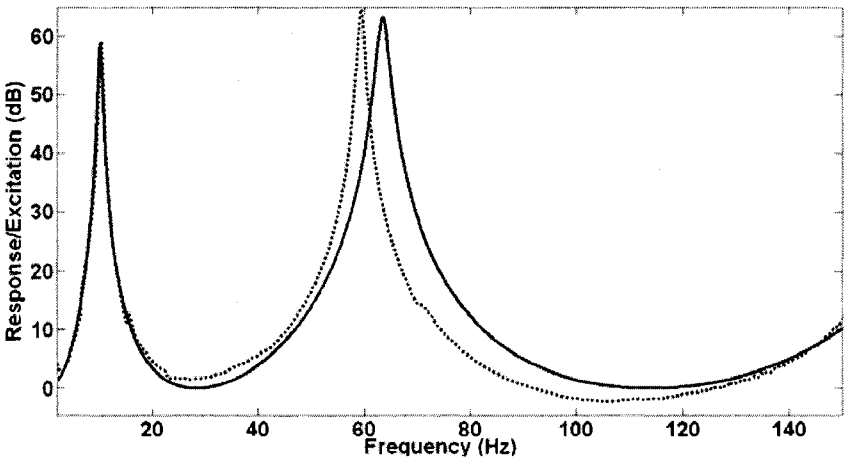

Figure 5.5 Aluminum beam's end-point acceleration response comparison. Solid and dotted lines represent the results from the finite element model and experimental data, respectively.

Here, the aluminum beam's damping factors were selected as 0.0415 and 0.0184 for the first and second vibration mode, and 0.002 for higher vibration modes. Table 5.3 illustrates the first three natural frequency evaluated using the finite element model and the resonant frequencies obtained from the experimental data.

Table 5.3 Natural frequencies of the Aluminum beam's finite element model and the resonant frequencies from experimental data.

	ω_1 (*Hz*)	ω_2 (*Hz*)	ω_3 (*Hz*)
Experimental data	10.15	59.78	
Finite element Method	10.1212	63.8634	178.9144

It can be seen from Figures 5.4 and 5.5 and Tables 5.2 and 5.3 that good agreement exists between the numerical model and experimental data for natural frequencies of both steel and aluminum beams. Therefore, in the following sections the established finite element model for both steel and aluminum beams will be utilized to design the TMD system.

5.3 Optimal Tuned Mass Damper Design

Based on the experimental investigation for the steel beam shown in Figure 5.4 and Table 5.2, it can be found that it is a very flexible beam in which there is not just single dominant mode. Therefore, to suppress the vibration effectively, in this chapter the TMD system has been designed based on the steel beam's first and second vibration modes, as considering the dynamic properties of the aluminum beam, it is difficult to decrease the aluminum beam's third natural frequency from around 180 (*Hz*) to around 90 (*Hz*), which is the third natural frequency of the steel beam, through adding small masses. The theoretical basis for optimally designed TMD system proposed in Chapter 4 will be utilized to determine the optimal location of attached aluminum beam, and then the whole

optimization procedure will be redefined based on this designed experimental investigation.

5.3.1 Optimal location of the attached aluminum beam

Based on the theory proposed in Chapter 4, one can utilize the modal shape to determine the number and initial position of the attached MTMD system. Figure 5.6 illustrates the steel beam's first two vibration modal shapes for transverse response.

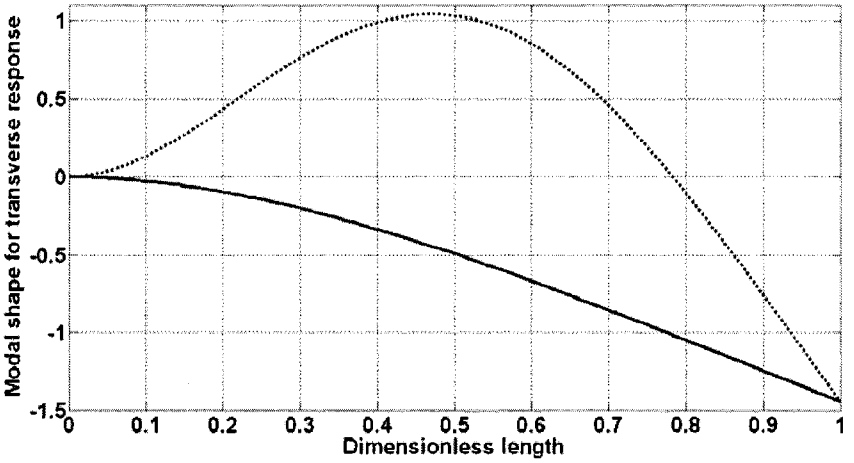

Figure 5.6 Steel beam's first two vibration modal shapes for transverse response. Solid and dotted lines represent the first and second vibration modes, respectively.

It can be found from Figure 5.6 that the maximum deflections in the first two vibration modal shapes are both located at the end of the beam and only one maximum point exists. Therefore two TMD will be attached at the end of beam, in which the natural frequencies of these two TMD were tuned to the steel beam's first two vibration modes, separately.

Based on the above investigations, the natural frequencies of the aluminum beam, which will be connected at the end of the steel beam, will be tuned to the steel beam's first two vibration modes through two attached small masses, as shown in Figure 5.1. Therefore,

the aluminum beam with the attached masses would operate similar to two sets of optimal TMD system.

The optimal TMD designs presented in Chapter 3 and 4 and those available in published literatures[75-85] are all based on given mass of the attached TMD system and the optimal parameters are the stiffness and damping of the attached TMD system. However, as the properties of the attached aluminum beam can not be changed, the optimal problem in this chapter would be transferred to select suitable masses and also their locations to tune the natural frequencies of the aluminum beam to the steel beam's first two vibration modes.

The equations of motion in finite element form for the steel beam end-connected to the aluminum beam with the attached masses under base excitation can be also expressed as Equation (5.1). Here it should be noted that the stiffness $[K]$ and damping $[C]$ matrices and the nodal displacement $\{q\}$, velocity $\{\dot{q}\}$ and acceleration $\{\ddot{q}\}$ vectors are the combination of both steel and aluminum beams' finite element models, and the mass $[M]$ and direction $[E_s]$ matrices are the combination of not only steel and aluminum beams' finite element model but also the effect of the attached mass. Let us assumed one mass (m) is connected to the j^{th} element of the aluminum beam's finite element model and its position in this j^{th} element can be expressed as (η_m). Therefore, the effect of the attached mass (m) to the mass $[M]$ and direction $[E_s]$ matrices stated in Equation (5.1) can be expressed as:

$$[M]_e = \sum_{element=j} \left\{ [N(\eta_m)]^T [N(\eta_m)] m \right\}_j \text{ and } [E_s]_e = \sum_{element=j} \left\{ [N(\eta_m)]^T m \right\}_j \qquad (5.6)$$

where $[M]_e$ and $[E_s]_e$ represent the effect of the attached mass (m) to the mass $[M]$ and direction $[E_s]$ matrices, as stated in Equation (5.1) and $[N(\eta)]$ is the shape function. Here it should be noted that the position of the attached mass (m) can be identified as a design variable through parameter η_m. Next the optimization methodology utilized in this experimental study will be presented in detail.

5.3.2 Design based on the steel beam's first vibration mode

Based on the data listed in Tables 5.2 and 5.3, it can be found that the first natural frequencies for the steel and aluminum beams are 5.2599 and 10.1212 (Hz), respectively. Obviously, to decrease the natural frequency of the aluminum beam from 10.1212 (Hz) to around 5 (Hz), a simple methodology is to connect a small mass ("Mass 1" shown in Figure 5.1) at the end of the aluminum beam. Therefore, the optimal problem in this section would be transferred to find the optimal value of this attached mass.

As mentioned before, in the traditional TMD design, the mass of the TMD system is a given input and restricted to be not more than the 10% of the original structural mass, otherwise the dynamic properties of the original structure will be changed significantly[82]. Moreover, based on the investigations presented in Figure 3.2 and those in available literatures[84], one can find that with the increase of input mass ratio, the effectiveness of the optimally designed TMD system would be increased. Based on those facts, as the optimization problem in this section is to find optimal value of the attached mass, which is the only design variable, it is difficult to define a suitable objective function for the optimization problem presented in this section.

Fortunately, based on the working principle of an optimally designed TMD system and also the investigations presented in Chapters 3 and 4, one can find that the frequency ratio defined in Equation (3.14) for an optimally designed TMD system is close to 1. Moreover, considering the fact that in the next section a second mass will be attached to the aluminum beam, which will also affect the dynamic property of the aluminum beam's first vibration mode. Therefore, in this section, the first natural frequency of the aluminum beam will be tuned to around 5.3 (Hz), which is the first natural frequency of the steel beam, through "Mass 1" illustrated in Figure 5.1, and the approach can be expressed as the following optimization problem:

$$\begin{aligned} &\text{Find the design variables:} && \{DV\}=\{mass\} \\ &\text{To make:} && \textit{first natural frequency of the aluminum beam with the attached tip mass equal to 5.3 (Hz)} \end{aligned} \tag{5.7}$$

Finally, one can easily find that the mass of the attached mass ("Mass 1" in Figure 5.1) is about 50 (g). Figure 5.7 shows the dynamic property of the aluminum beam with end-attached 50 (g) mass.

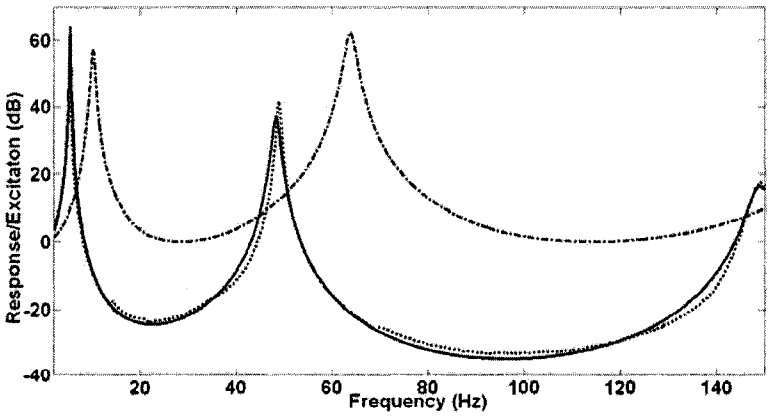

Figure 5.7 Aluminum beam's end-point acceleration response comparison. Solid, dotted and dashed-dotted lines represent the finite element model and experimental data for aluminum beam with tip attached 50 (g) mass, and the finite element model for original aluminum beam, respectively.

From Figure 5.7, it can be found that the first natural frequency of the aluminum beam has been tuned to 5.3 (*Hz*) through the end-attached mass. Next, a second mass ("Mass 2" in Figure 5.1) will be connected to the aluminum beam to suppress the steel beam's vibration due to the second mode.

5.3.3 Design based on the steel beam's second vibration mode

Here the end-attached mass 50 (*g*) will be kept, as it has successfully tuned the natural frequency of the aluminum beam to the first mode of the steel beam, and then a 54 (*g*) small mass ("Mass 2" in Figure 5.1) will be added to the aluminum beam to tuned the second natural frequency of the aluminum beam to the second mode of the steel beam. As the mass is given, the optimization problem is to find the best location for this attached mass to suppress the steel beam's vibration around the second vibration mode, which can be expressed as:

$$\begin{aligned} &\text{Find the design variables:} && \{DV\}=\{location\} \\ &\text{To minimize:} && RMS\ of\ the\ response\ of\ the\ 2^{nd}\ vibration\ mode \\ &\text{Subjected to:} && location\ along\ the\ length\ of\ the\ aluminum\ beam \end{aligned} \tag{5.8}$$

One can easily utilize the hybrid optimization methodology proposed in Chapter 4 to obtain the solution. However, as the optimization problem stated in Equation (5.8) is one-dimensional case and then it can be solved graphically. In order to clearly clarify the property of this optimization problem, Figure 5.8 illustrates the value of objective function versus the changing of the design variable, form which one can easily find that the optimal location of the attached second mass is around 0.66, which is about 32.5 (*cm*) from the connection point of the steel and aluminum beams.

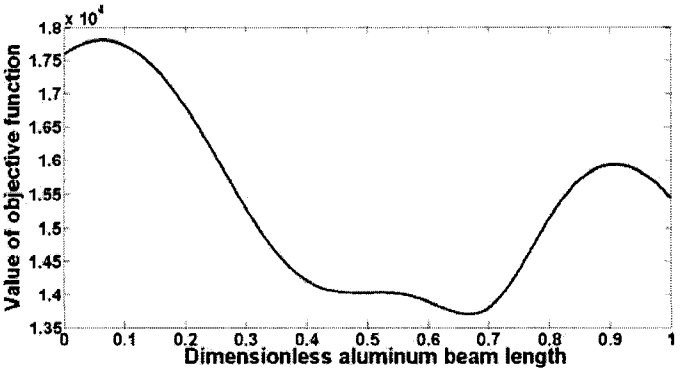

Figure 5.8 Value of objective function *vs.* position of the attached second mass.

5.3.4 Vibration suppression comparison under random excitation

To verify the validity of the optimal TMD design presented in the above two subsections, the vibration suppression performances will be compared in this section. Five different cases, as shown in Table 5.4, have been investigated.

Table 5.4 Vibration suppression strategies comparison.

Strategies	Schematics
Case 1	Excitation, Steel beam
Case 2	Excitation, Steel beam, Aluminum beam
Case 3	Excitation, Steel beam, Aluminum beam, 50 (*g*)
Case 4	Excitation, Steel beam, Aluminum beam, 54 (*g*), 50 (*g*), 32.5 (cm)
Case 5	Excitation, Steel beam, Aluminum beam, 54 (*g*), 50 (*g*), 23(cm)

Here it should be noted that Case 3 in Table 5.4 is the optimal design based on the steel beam's first vibration mode and Case 4 in Table 5.4 is the optimal design based on the beam's both first and second vibration modes. For the sake of clear expression, the five

cases listed in Table 5.4 have been categorized to two groups as: Group 1 for Cases 1, 2 and 3 and Group 2 for Cases 1, 3, 4 and 5. Therefore, Case 2 can be treated as the deviation from the optimal design based on the first vibration mode, as shown in Case 3; Cases 3 and 5 can also be identified as the deviation from the optimal design based on the second vibration mode, as shown in Case 4.

To testify the validity of the finite element model, Figure 5.9 compare the PSD of absolute acceleration of steel beam's end-point evaluated using the finite element model and obtained from the experimental data for Cases 2 and 3 listed in Table 5.4. The acceleration response of the tip point of the steel beam for Cases 4 and 5 based on finite element analysis and experimental data are compared in Figure 5.10. From Figures 5.9 and 5.10, one can find that the results evaluated from the finite element model are very close to the experimental data.

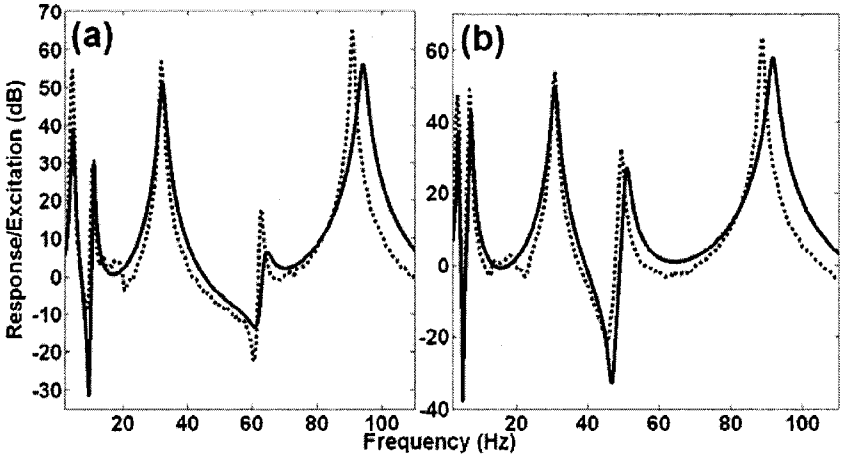

Figure 5.9 Steel beam's end point acceleration response comparison. Solid and dotted lines represent the results from the finite element model and experimental data, respectively. (a) For Case 2 listed in Table 5.4. (b) For Case 3 listed in Table 5.4.

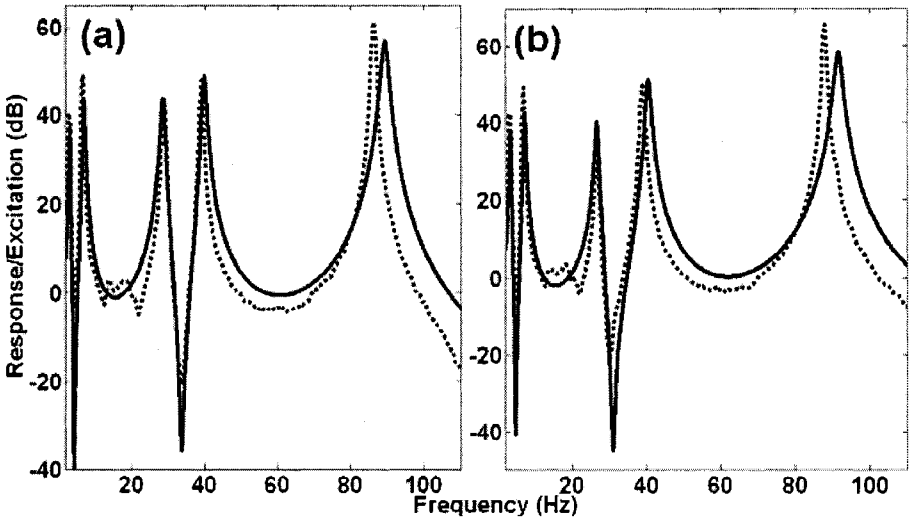

Figure 5.10 Frequency domain acceleration response comparison for steel beam's end point. Solid and dotted lines represent the results from the finite element model and experimental data, respectively. (a) For Case 4 listed in Table 5.4. (b) For Case 5 listed in Table 5.4.

The steel beam's dynamic property (end-point acceleration) for Cases 1, 2 and 3 (Group 1) for the results evaluated through the finite element model and obtained from the experimental data are shown in Figure 5.11. The comparisons of the acceleration response of the tip point of the steel beam for Cases 1, 3, 4 and 5 (Group 2) are shown in Figure 5.12.

From Figures 5.11 and 5.12, one can also find that the proposed TMD design methodology has successfully suppressed the vibration around the steel beam's first and second vibration modes.

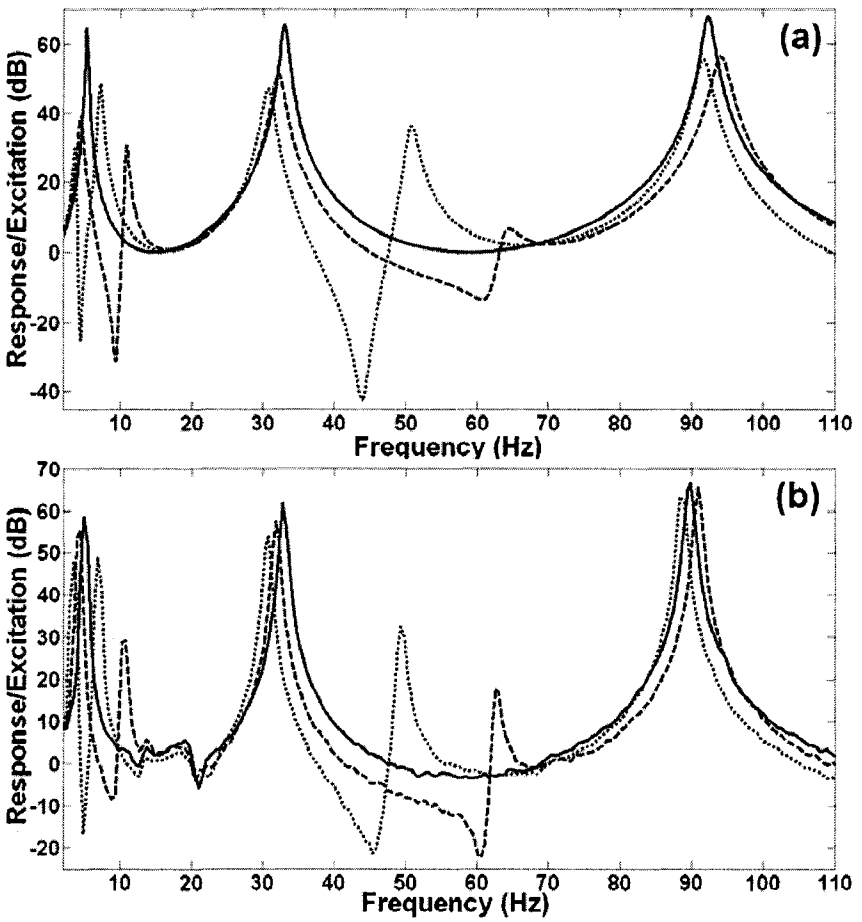

Figure 5.11 Frequency domain acceleration response comparison for steel beam's end point. Solid, dashed and dotted lines represent the Cases 1, 2 and 3, as listed in Table 5.4, respectively. (a) The results evaluated from finite element model. (b) The experimental data.

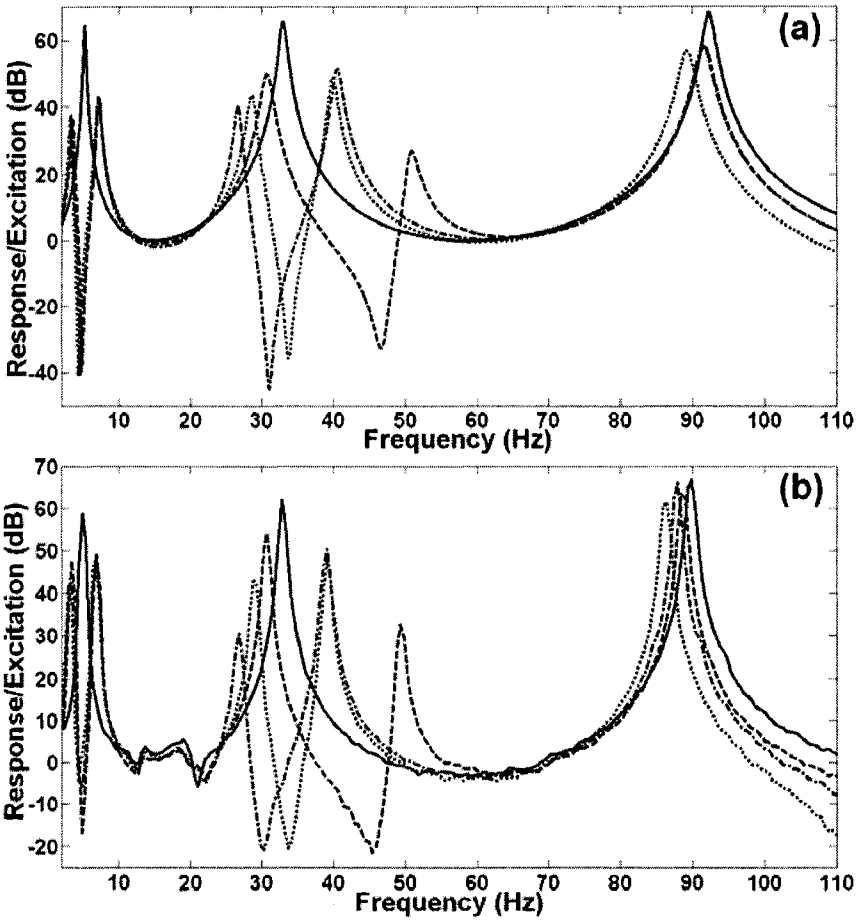

Figure 5.12 Frequency domain acceleration response comparison for steel beam's end point. Solid, dashed, dotted and dashed-dotted lines represent the Cases 1, 3, 4 and 5 listed in Table 5.4, respectively. (a) The result from finite element model. (b) The experimental data.

5.3.5 Vibration suppression comparison under harmonic excitation

The steel beam's response (tip acceleration) comparison for random loading has been conducted in above section, from which one can find that the vibration suppression performance for Cases 3–5 listed in Table 5.4 are very close at excitation frequency equal to 5 (*Hz*). Therefore, in this section only the Cases 1, 2 and 3 listed in Table 5.4 under harmonic excitation with excitation frequencies at 5 (*Hz*), which is the first resonant frequency of the steel beam, will be presented. Figure 5.13 illustrates the experimental

data for steel beam's end-point acceleration response in time domain under harmonic excitation with 5 (*Hz*) excitation frequency for Cases 1, 2 and 3 listed in Table 5.4. Here it should be noted that the data shown in Figure 5.13 have been filtered by a 5 order low-pass Butterworth type filter with cut-off frequency of 10 (*Hz*) and directly recorded by "LABVIEW" and then simply divided by the amplitude of excitation without any average processing.

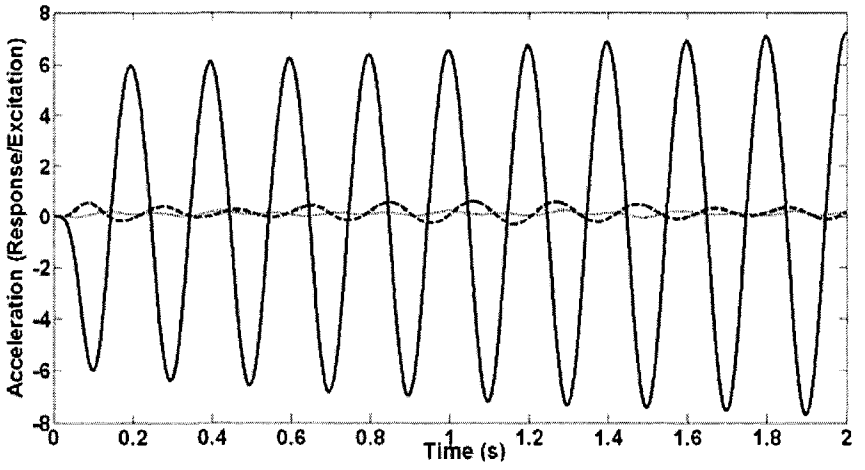

Figure 5.13 Steel beam's end point acceleration time domain response comparison under harmonic excitation with 5 (*Hz*) excitation frequency. Solid, dashed and dotted lines represent Cases 1, 2 and 3 listed in Table 5.4, respectively.

From Figure 5.13, one can find that the proposed TMD design methodology has successfully decreased the response around the steel beam's first natural frequency.

5.3.6 Natural frequency analysis for tuned mass damper system

The optimal TMD design and their response under both random and harmonic excitation have been investigated experimentally and computed using finite element model in above sections, and the results shows that the proposed TMD design is very effective. Table 5.5 summarizes the natural frequencies around the original steel beam's first two vibration

modes for different cases listed in Table 5.4, to clearly clarify the effectiveness of the proposed TMD design methodology.

Table 5.5 Natural frequencies comparison for Cases 1-5 listed in Table 5.4 around the first two vibration modes of the steel beam.

Cases listed in Table 5.4	Steel beam's natural frequency (*Hz*)			
	First mode		Second mode	
Case 1	5.2599		32.9612	
Case 2	4.4731	10.8896	32.1163	
Case 3	3.6269	7.2414	30.7476	
Case 4	3.2803	7.1576	28.6578	39.8982
Case 5	3.4114	7.2372	26.7607	40.5519

From Table 5.5, one can easily find that the proposed TMD design methodology adds two resonant frequencies around their relative tuned natural frequencies, which exactly agrees with the working principle of the classical optimally designed TMD system.

5.4 Conclusions and Summary

Through the experimental study presented in this chapter, the validities of the finite element model for Timoshenko beam presented in Chapter 2, the optimal Tuned Mass Damper (TMD) design utilizing the finite element method and the optimization methodologies proposed in Chapters 3 and 4, and also the optimal TMD design principle for beam-type structures presented in Chapter 4 have been investigated.

Moreover, the optimal TMD design method presented in this chapter, which connects a small beam with attached masses to the original beam structure, is novel.

CHAPTER 6

MODEL DYNAMIC BEHAVIOR OF MAGNETO-RHEOLOGICAL FLUID DAMPERS

6.1 Introduction

The finite element model for beam-type structures has been derived in the Chapter 2, and then utilized to design the Timoshenko beam and curved beam with the attached Tuned Mass Damper (TMD) system in Chapters 3 and 4. A design principle for beam-type structures with the attached TMD system has also been proposed in Chapter 4. In this chapter and the next chapter, the Semi-Active Mass Damper (SAMD) design using Magneto-Rheological (MR) fluid dampers, which is one of the most promising devices to provide semi-actively controlled damping force, will be investigated. The MR-damper can offer large range of damping force capacity, robustness in a fail-safe manner with very low power requirements. The two main issues regarding the SAMD system based on MR-damper are: 1- Development of the mathematical models, which can not only simulate the MR-damper's dynamic behavior accurately but also can easily be used; 2- Development of the control strategy. This chapter is dedicated to the aspect of modeling the MR-damper's dynamic behavior, and the development of control strategy will be presented in the next chapter.

Many mathematical models[123-144] for simulating the MR-damper's dynamic behavior have been developed. In general, all of these mathematical models can be categorized

into two different groups. One group is the mechanical model, in which a set of mechanical parts are utilized to model the MR-damper's dynamic behavior, such as the Bingham model[123-125]. The other group is the non-parametric model, in which a set of numerical equations are utilized to interpolate the dynamic behavior of MR-damper, such as the Fuzzy model[138], polynomial model[130] and the model proposed by Wang *et al*[133,134]. The development of the mechanical models can be summarized in Figure 6.1.

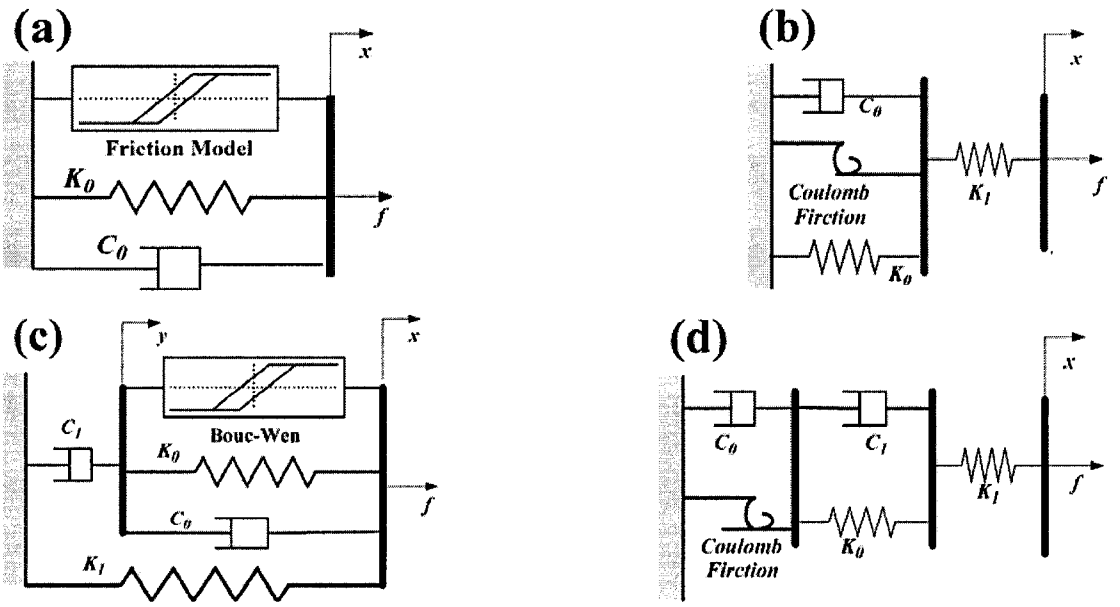

Figure 6.1 Typical Magneto-Rheological (MR) fluid damper's mechanical models. (a) Friction model. (b) Mechanical model by Oh and Onode[132]. (c) Phenomenological model by Spencer Jr *et al*[128]. (d) Parametric viscoelastic-plastic model by Gamota and Filisko[126].

In Figure 6.1, parameters K_0 (K_1) and C_0 (C_1) represent the stiffness and viscous damping, respectively and x, y and f are the MR-damper's external excitation, the inner state of the phenomenological model and the MR-damper's output damping force, respectively. By selecting different "friction model" illustrated in Figure 6.1(a), one can design different mechanical models, such as the Bingham model[123-125] utilized a coulomb friction element

and K_0 is assumed to be zero; the nonlinear biviscous model[127] utilized a nonlinear biviscous friction element; Bouc-Wen model[128,139,140] utilized the Bouc-Wen hysteresis element; LuGre friction model[135, 136] utilized the LuGre friction element. Figure 6.1(b) shows the mechanical model proposed by Oh and Onode[132]. Figure 6.1(c) illustrates the phenomenological model (modified Bouc-Wen model) proposed by Spencer Jr *et al*[128]. Figure 6.1(d) represents the parametric viscoelastic-plastic model proposed by Gamota and Filisko[126].

To date, most of the available literatures in this area are focused on small-scale MR-damper, especially for RD-1005 type MR-damper provided by Lord Company[122], but large-scale MR-damper is seldom reported by researchers. Yang *et al* [119, 180] developed a phenomenological model[128] with mass element for MR-9000 type damper, which is a large-scale MR-damper provided by Lord Company[122], and then they[181] proposed a phenomenological model based on the modified Bouc-Wen hysteresis model[128] and provided the relationships for the characteristic parameters with variable current input. Investigations of different mathematical models for RD-1005 type MR-damper show that although most of mathematical models can accurately simulate MR-damper's dynamic behavior, some of them are very difficult to be used in accurate control design. Among different modes, the LuGre friction model[136] is found to be simpler, more accurate and easily to be used than other models.

In this chapter, a LuGre friction model for MR-9000 type damper will be proposed. The gradient based optimization method[88] and the least square technique[182] will be utilized to identify the characteristic parameters of the proposed model. The dynamic properties of

the proposed model will be compared with those obtained by the modified Bouc-Wen model[181] under different types of excitation and input current to validate the proposed model.

6.2 Large-Scale MR-damper

The MR-9000 type damper is provided by Lord Company[122]. The schematic diagram of this type MR-damper has been shown in Figure 6.2 and its design parameters have been presented in Table 6.1[122,181].

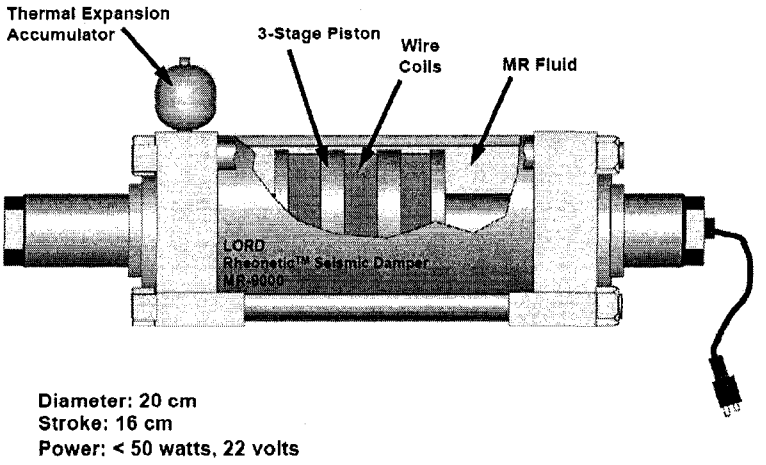

Figure 6.2 Schematic diagram of the MR-9000 type damper provided by Lord Company[122].

Table 6.1 Design parameters for MR-9000 type damper[122, 181].

Stroke	± 8 (*cm*)	Total mass	250 (*Kg*)
Max. input power	< 50 (*w*)	Total length	~ 1 (*m*)
Max. force (nominal)	200,000 (*N*)		

Yang *et al*[181] proposed a modified Bouc-Wen model, as shown in Figure 6.1(c), for MR-9000 type damper, in which the hysteresis damping force can be expressed as:

$$f = c_1\dot{y} + k_1(x - x_0) \tag{6.1}$$

$$\dot{y} = \frac{1}{c_0 + c_1}[\alpha z + c_0\dot{x} + k_0(x - y)] \tag{6.2}$$

$$\dot{z} = -\gamma|\dot{x} - \dot{y}||z||z|^{n-1} - \beta(\dot{x} - \dot{y})|z|^n + A(\dot{x} - \dot{y}) \tag{6.3}$$

where k_0, k_1, c_0, and c_1 are the stiffness at high speed, the stiffness of the accumulator, the viscous damping at high speed and for force roll-off at low speed, respectively. Variables x and f are the MR-damper's external excitation and output damping force, respectively. x_0, y and z are MR-damper's initial displacement, inner state and the evolutionary variable of modified Bouc-Wen model, respectively. The characteristic parameters A, γ, β, k_0, k_1, x_0 and n are constant and current independent and their values have been provided in Table 6.2[181]. The current dependent parameters (α, c_0 and c_1) can be expressed as[181]:

$$\alpha(i) = 16566i^3 - 87071i^2 + 168326i + 15114 \tag{6.4}$$

$$c_0(i) = 437097i^3 - 1545407i^2 + 1641376i + 457741 \tag{6.5}$$

$$c_1(i) = -9363108i^3 + 5334183i^2 + 48788640i - 2791630 \tag{6.6}$$

where variable i is the input current.

Table 6.2 Current independent characteristics parameters for MR-9000 type damper[181].

A	2679.0 (m^{-1})	n	10
γ, β	647.46 (m^{-1})	x_0	0.18 (m)
k_0	137,810 ($N\,m^{-1}$)	k_1	617.31 ($N\,m^{-1}$)

Yang *et al*[181] compared the dynamic behavior evaluated using this modified Bouc-Wen model with the experimental data, and found that this model can accurately simulate the dynamic behavior of MR-9000 type damper in a large working range. Therefore, in this

chapter we will utilize the simulation results of the dynamic behavior evaluated using the modified Bouc-Wen model[181] provided Equations (6.1)-(6.6) and Table 6.2, to identify the characteristic parameters of the proposed LuGre friction model. As the proposed model is based on the LuGre friction model[136], in the next part a general description of the LuGre friction model will be presented and also some properties of the LuGre friction element will be studied in detail, which are very important to derive the LuGre friction model for MR-9000 type damper.

6.3 LuGre Friction Model

The schematic diagram of the LuGre friction MR-damper model has been shown in Figure 6.1(a), and the damping force can be expressed as[136]:

$$\frac{1}{\alpha}\dot{y} = \dot{x} - |\dot{x}|\, y \tag{6.7a}$$

$$f = \frac{\beta}{\alpha} y + \gamma\dot{x} + \delta x + \frac{\varepsilon}{\alpha}\dot{y} + f_0 \tag{6.7b}$$

where x and f are the MR-damper's external excitation and output damping force, respectively. y is the inner state of the LuGre friction model. Characteristic parameters γ, δ and f_0 represent the viscous damping, stiffness and initial force, respectively. Parameters α, β and ε are the characteristic parameters related to the inner state (y).

Here, the hysteresis behavior equation (LuGre friction element) stated in Equation (6.7a) plays an important role in this model. Thus the properties of Equation (6.7a) need to be studied first. For a harmonic excitation $x = X \sin(\omega t)$, Equation (6.7a) can be expressed as:

$$\dot{y} = \alpha X\omega[\cos(\omega t) - |\cos(\omega t)|\, y] \tag{6.8}$$

It can be found from Equation (6.8) that the inner state (y) depends on the value of parameter (α) and the amplitude of excitation (X) for a given excitation frequency (ω). The simulation results for inner state (y) under harmonic excitation (frequency ω =1 *Hz*) with αX of 3000, 30 and 0.3, respectively, are illustrated in Figure 6.3.

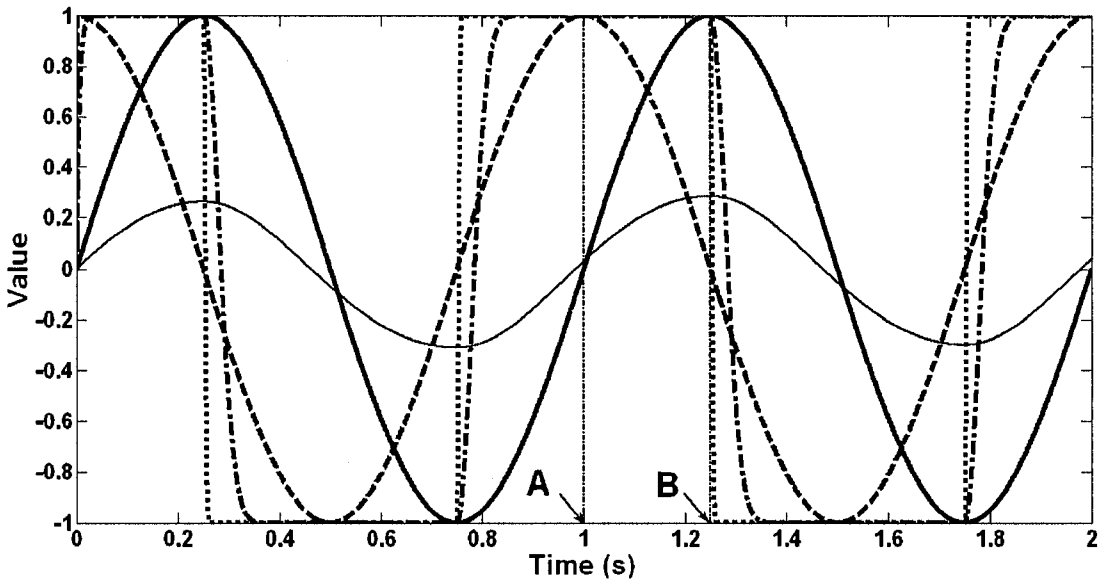

Figure 6.3 Simulation of Equation (6.7a) under harmonic excitation (frequency=1 *Hz*). Solid, dashed, dotted, dotted-dashed and solid (light) lines represent dimensionless displacement, dimensionless velocity and inner state (y) for αX of 3000, 30 and 0.3, respectively.

In Figure 6.3, the "dimensionless displacement" and "dimensionless velocity" in the caption mean the excitation displacement (x) and velocity ($\dot{x}$) divided by their maximum value, respectively; points "A" and "B" are related to the time points for harmonic excitation reaching the maximum velocity and maximum displacement points, respectively. It is noted that for the sake of clarity, the points "A" and "B" in Figure 6.3 are illustrated for one positive half period.

Now using Figure 6.3, some important properties of Equation (6.7a) under harmonic excitation ($x = X\sin(\omega t)$) will be studied.

(1) The time point "B" represents the zero excitation velocity point, and also reflects the point of inflection of the inner state (y). This property can be directly found in Equation (6.7a) by assuming $\dot{x}$=0, and then the differential of inner state (y) would also be zero, thus it represents the extreme point of inner state (y).

(2) The inner state (y) would be close to unit value between time point "A" and "B" under large value of αX. To illustrate this property, one can rearrange Equation (6.7a) as:

$$\dot{y} + \alpha |\dot{x}| y = \alpha\dot{x} \tag{6.9}$$

This is a Bernoulli Equation and its solution can be expressed as[27]:

$$y(t) = e^{-h}[\int e^{h}\alpha\dot{x}(t)dt + C_0], \qquad h = \int\alpha |\dot{x}(t)|dt \tag{6.10}$$

where C_0 represents the initial condition. Now let us assume that the excitation is harmonic loading ($x = X\sin(\omega t)$), the initial condition is zero and $0 < t \leq \pi/2\omega$ (the first quarter period). Therefore Equation (6.10) can be solved as:

$$\begin{aligned}
y(t) &= e^{-\alpha X\sin(\omega t)}\int e^{\alpha X\sin(\omega t)}\alpha X\omega\cos(\omega t)dt \\
&= e^{-\alpha X\sin(\omega t)}[\alpha X\sin(\omega t)e^{\alpha X\sin(\omega t)} - \int(\alpha X)^2 e^{\alpha X\sin(\omega t)}\sin(\omega t)\cos(\omega t)d(\omega t)] \\
&= \alpha X\sin(\omega t) - e^{-\alpha X\sin(\omega t)}\int(\alpha X)^2 e^{\alpha X\sin(\omega t)}\sin(\omega t)\cos(\omega t)d(\omega t) \\
&= \alpha X\sin(\omega t) - e^{-\alpha X\sin(\omega t)}\int(\alpha X)^2 e^{\alpha X\sin(\omega t)}\sin(\omega t)d(\sin(\omega t)) \\
&= \alpha X\sin(\omega t) - \frac{(\alpha X\sin(\omega t))^2}{2} + e^{-\alpha X\sin(\omega t)}\int\frac{(\alpha X)^3}{2}\sin^2(\omega t)e^{\alpha X\sin(\omega t)}d(\sin(\omega t)) \\
&= \alpha X\sin(\omega t) - \frac{(\alpha X\sin(\omega t))^2}{2} + \frac{(\alpha X\sin(\omega t))^3}{6} \\
&\quad - e^{-\alpha X\sin(\omega t)}\int\frac{(\alpha X)^4}{6}\sin^3(\omega t)e^{\alpha X\sin(\omega t)}d(\sin(\omega t))
\end{aligned} \tag{6.11}$$

Then, one can obtain:

$$y(t) = -\sum_{n=1}^{\infty} \frac{(-\alpha X \sin(\omega t))^n}{n!} \tag{6.12}$$

This is part of Taylor series of the exponential function and can be expressed as:

$$y(t) = 1 - \exp(-\alpha X \sin(\omega t)) \tag{6.13}$$

The solution in other quadrants is similar to Equation (6.13) with different initial values. As the value of the exponential function in Equation (6.13) will converge to zero very fast for large value of αX, Thus the inner state (y) in time range between points "A" and "B", which converges to (1 - exp (-αX)), will be close to unit value under large value of αX, as illustrated in Figure 6.3 for αX equal to 3000 and 30.

(3) From Equation (6.13), one can also find that the boundary of inner state (y) is (-1, 1), which has also been shown in Figure 6.3.

(4) From Equation (6.12), one can find that for small value of αX, the solution of inner state can be simplified as $y(t) = \alpha X \sin(\omega t)$, as shown in Figure 6.3 for αX equal to 0.3.

Based on the above investigations, the following assumption may be made: in most of MR-damper's working range, the inner state (y) for the LuGre friction model becomes (close to) unity between time points "A" and "B", as shown in Figure 6.3, under suitably selected characteristic parameter α. In the following sections, a LuGre friction model for MR-9000 type damper will be derived based on this assumption. Here, it should be emphasized that since the identification of the characteristic parameters is based on this assumption, the final value of characteristic parameter α should be checked for this assumption under the MR-damper's working range. It should be noted that the effect of excitation frequency to the inner state (y) is to change the response frequency of inner state and not the properties of time points "A" and "B", as shown in Figure 6.3.

6.4 Development of LuGre Friction Model for MR-9000 Type Damper

Comparing the Bouc-Wen model[181], as stated in Equations (6.1)-(6.6), with the general form of LuGre friction model, as stated in Equations (6.7), one can easily find that it is difficult to directly identify the characteristic parameters of LuGre friction model through mathematical derivation. Therefore, we will identify the characteristic parameters of LuGre friction model for MR-9000 type damper step by step, based on the simulation data obtained from the modified Bouc-Wen model[181]. For the sake of generality, we assume the characteristic parameters as stated in Equations (6.7) are all current, frequency and amplitude dependent. Before characterizing the MR-damper, let us examine a typical MR-damper's force-velocity (*f*-*v*) relationship, as shown in Figure 6.4.

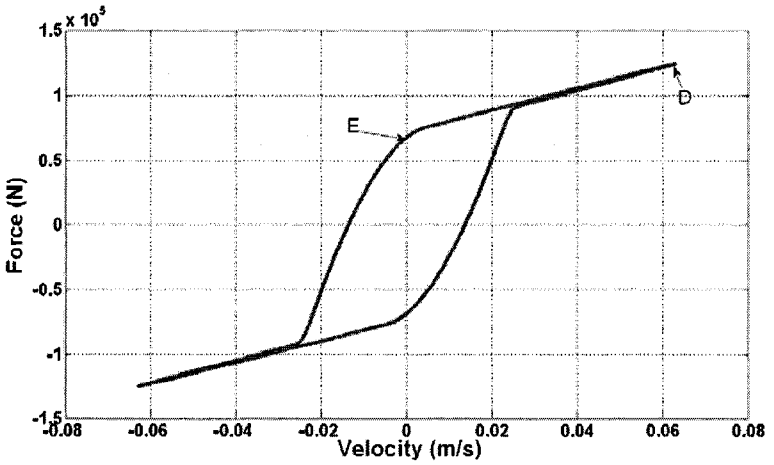

Figure 6.4 Typical MR-damper's force-velocity (*f*-*v*) curve.

Here, points "D" and "E" represent the force at time points "A" and "B", as shown in Figure 6.3, respectively. Based on the analysis for inner state (y) presented in the last section, these two special points will be utilized to evaluate the proposed LuGre friction model for MR-9000 type damper. Substituting Equation (6.7a) into (6.7b), we have:

$$f = (\frac{\beta}{\alpha} - \varepsilon |\dot{x}|)y + (\gamma + \varepsilon)\dot{x} + \delta x + f_0 \tag{6.14}$$

Next, Equation (6.14) will be utilized to identify the characteristic parameters for the proposed LuGre friction model under harmonic excitation, $x = X \sin(\omega t)$.

6.4.1 Estimation of initial force "f_0"

The parameter f_0 can easily be evaluated, because it represents the force when MR-damper stays in the middle condition and it mainly reflects the effect of the gas accumulator in the MR-damper. Thus, according to Equation (6.1) of the modified Bouc-Wen model[181], "f_0" can be estimated as $-k_1 x_0$, as it is the only parameter related to the damping force and also independent to the excitation and input current. Therefore, considering Table 6.2, "f_0" is equal to –111.1158 (N).

6.4.2 Estimation of characteristic parameters "γ" and "β/α"

At point "D", as shown in Figure 6.4, the inner state (y) is equal (close) to 1 and the displacement is zero, as illustrated in Figure 6.3 for time point "A". Thus the MR-damper's damping force, as stated in Equation (6.14), can be simplified as:

$$f = \frac{\beta}{\alpha} + \gamma \dot{x}_{\max} + f_0 = \frac{\beta}{\alpha} + \gamma(X\omega) + f_0 \tag{6.15}$$

where X and ω are the amplitude and frequency of the harmonic excitation, respectively. The amplitude, frequency and current dependency of parameters γ and β/α will be examined through Equation (6.15) in the following subsections.

6.4.2.1 *Amplitude dependency*

Based on Equation (6.15), if parameters β/α and γ are both amplitude independent, the MR-damper's damping force difference (Δf) under the same input current, for harmonic

excitation with the same excitation frequency and different amplitudes, should be proportional to the difference of amplitude as:

$$\Delta f = f_2 - f_1 = \gamma (X_2 - X_1)\omega = \gamma \Delta X \omega \tag{6.16}$$

where f_1 and f_2 represent the damping force stated in Equation (6.15), under the same input current for harmonic excitation with same excitation frequency (ω) and different amplitudes X_1 and X_2, respectively. Here, two sets of harmonic test signals, as listed in Table 6.3, will be utilized to study the amplitude dependency of the parameters γ and β/α.

Table 6.3 Test signals for studying the amplitude dependency of parameters β/α and γ.

Test Signal	Amplitude (*cm*)					
X_1 (Test signal set 1)	0.5	1	2	3	4	5
X_2 (Test signal set 2)	0.75	1.5	3	4.5	6	7.5
$\Delta X = X_2 - X_1$	0.25	0.5	1	1.5	2	2.5

Now the difference of damping force (Δf) measured at point "D" illustrated in Figure 6.4, for the two sets of test signals listed in Table 6.3, are evaluated using the modified Bouc-Wen model[181]. Table 6.4 provides the results for the harmonic excitation with frequency 1 (*Hz*) and the input current of 1 (*A*).

Table 6.4 The damping force difference (Δf) at point "D" (Figure 6.4) under harmonic excitation (frequency=1 (*Hz*) and amplitude listed in Table 6.3) with input current of 1 (*A*).

f_1 (*N*) (Test signal set 1)	148950.27	179358.38	240176.25	300994.45	361812.79	422631.11
f_2(*N*) (Test signal set 2)	164154.12	209767.18	300994.45	392221.95	483449.47	574677.02
$\Delta f = f_2 - f_1$ (*N*)	15203.85	30408.80	60818.20	91227.50	121636.68	152045.91

It can be seen from Table 6.4 that the Δf is exactly proportional to ΔX given in Table 6.3, thus β/α and γ should be amplitude independent parameters. The parameter Δf generated

by the test signals given in Table 6.3 for different excitation frequencies (0.5, 1, 2, 5, 7.5 and 10 (*Hz*)) and input currents (0, 0.1, 0.2, 0.4, 0.6, 0.8 and 1 (*A*)) has also been obtained. The results are shown in Figure 6.5, in which the "Dimensionless force" represents Δf divided by its minimum value at $\Delta X = 0.25$ (*cm*) listed in Table 6.3 under the same frequency and input current value, and "Amplitude-Difference" represents the ΔX given in Tables 6.3. It should be noted that in Figure 6.5 the results obtained for different current input under the same frequency are exactly the same. Considering these, it can be concluded that that Δf is exactly proportional to ΔX under different frequency and input current. Thus, parameters β/α and γ are both independent of the amplitude of harmonic excitation.

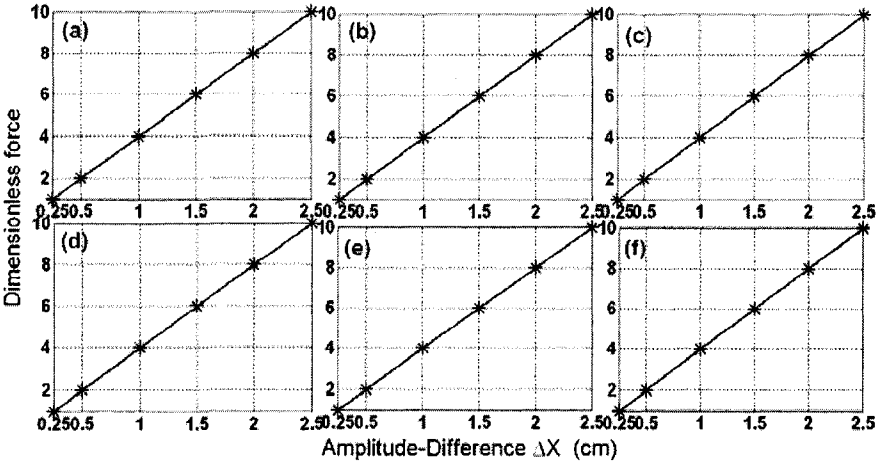

Figure 6.5 Variation of dimensionless force Δf *vs.* ΔX under different input current and excitation frequency. (a) 0.5 (*Hz*). (b) 1 (*Hz*). (c) 2 (*Hz*). (d) 5 (*Hz*). (e) 7.5 (*Hz*). (f) 10 (*Hz*). Note: the results for different input current are coincided under the same excitation frequency.

6.4.2.2 Frequency dependency

Based on Equation (6.15), if parameters β/α and γ are frequency independent, the MR-damper damping force difference (Δf) under the same input current and fixed ΔX with

different excitation frequency, should be proportional to excitation frequency, as stated in Equation (6.16). Therefore, using the same approaches as those for studying the amplitude dependence relationship, we can verify whether parameters β/α and γ are frequency dependent using the frequency test signal given in Table 6.5.

Table 6.5 Test signals for studying the frequency dependency of parameters β/α and γ.

Test signal amplitude	Frequency (*Hz*)					
Similar amplitude signals in Table 6.3	0.5	1	2	5	7.5	10

The damping forces difference (Δf) measured at point "D" for these test signals are evaluated using the modified Bouc-Wen model[181]. The results for the input current of 0.5 (A) and amplitudes of X_1=1 (cm) and X_2=1.5 (cm) (ΔX=0.5 cm), are listed in Table 6.6.

Table 6.6 The damping force difference (Δf) measured at point "D" (Figure 6.4) for test signals listed in Table 6.5 with input current =0.5 (A), amplitudes X_1= 1 (cm) and X_2= 1.5 (cm) (ΔX=0.5 cm).

Current=0.5 (A),	Frequency (*Hz*)					
ΔX=0.5 (cm)	0.5	1	2	5	7.5	10
f_1 (N) (X_1=1 (cm))	110405.94	138908.61	195991.88	366923.37	509434.37	651943.61
f_2 (N) (X_2=1.5 (cm))	124665.71	167410.25	252916.05	509434.53	723201.12	936966.09
$\Delta f = f_2 - f_1$ (N)	14259.77	28501.64	56924.17	142511.16	213766.75	285022.48

From Table 6.6, it can be found that the values of Δf are exactly proportional to the value of frequency under the same input current and fixed ΔX. Different excitation amplitudes as given in Table 6.3 and current input (0, 0.1, 0.2, 0.4, 0.6, 0.8 and 1 (A)) have also been tested to verify the frequency independent property. Figure 6.6 shows the variation of Δf with respect to excitation frequency under fixed amplitude difference (ΔX), in which the "Dimensionless force" is Δf divided by its minimum value at frequency ω=0.5 (Hz) under the same input current and fixed ΔX, as given in Table 6.3, and "Frequency" represents

the test signals' frequencies provided in Table 6.5. It should be noted that the results obtained from different current input under the same value of amplitude difference (ΔX) and excitation frequency are exactly the same. Considering these, it can be confirmed that Δf is exactly proportional to the frequency of harmonic excitation under the same input current and the fixed amplitude difference.

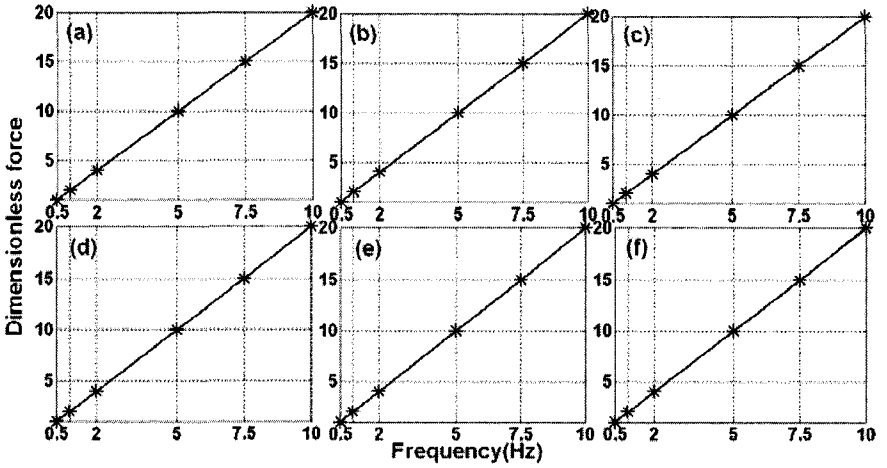

Figure 6.6 Variation of dimensionless Δf *vs.* ω under different amplitude difference and current input: (a) ΔX = 0.25 (cm); (b) ΔX=0.5 (cm); (c) ΔX =1 (cm); (d) ΔX =1.5 (cm); (e) ΔX =2 (cm); (f) ΔX =2.5 (cm). Note: the results for different input current are coincided under the fixed ΔX.

Based on the above investigation, it can be concluded that based on the MR-damper's dynamic behaviors obtained from the modified Bouc-Wen model[181], the parameters β/α and γ for the proposed LuGre friction model are both independent of the excitation frequency and amplitude.

6.4.2.3 Current dependency

It can be found that the damping force evaluated through the modified Bouc-Wen model for MR-9000 type damper[181] will not exactly increase with the increase of input current

when current value locates between 1 (A) and 2 (A) in the harmonic excitation test signal, especially in high frequency range. Moreover, the experimental data for MR-9000 type damper under harmonic excitation for currents between 1 (A) and 2 (A) can not be found in available literatures[119, 180, 181], and the maximum difference of the damping force for currents equal to 1 (A) and 2 (A) is around 10%[119, 180, 181]. Therefore for the sake of model accuracy, the working current range for MR-9000 type damper in this dissertation will be limited between 0.0 (A) and 1.0 (A).

The difference of the damping force (Δf) measured at point "D" shown in Figure 6.4 for two set of harmonic test signals with same excitation frequency (ω= 1Hz) and different excitation amplitude (X_1=1 (cm) and X_2=1.5 (cm)) under different input current are evaluated using the modified Bouc-Wen model[181] and the results are listed in Table 6.7.

Table 6.7 The damping force difference (Δf) at point "D" (Figure 6.4) for harmonic excitations (frequency ω=1 (Hz), amplitudes X_1=1 (cm) and X_2=1.5 (cm) (ΔX=0.5 cm)).

Frequency=1	Current (A)						
(Hz)	0	0.2	0.4	0.5	0.6	0.8	1
f_1 (N) (X_1)	53733.60	85682.03	124382.33	138908.61	150895.80	168471.99	179358.38
f_2 (N) (X_2)	70935.12	106418.27	151090.99	167410.25	180598.59	199176.87	209767.18
$\Delta f = f_2 - f_1$(N)	17201.52	20736.24	26708.66	28501.64	29702.79	30704.88	30408.8

Based on the data provided in Table 6.7, one can utilize Equation (6.16) to evaluate the parameter γ with respect to the input current. The results are shown in Figure 6.7. A second order polynomial function, as given in Equation (6.17), has been used to interpolate the data.

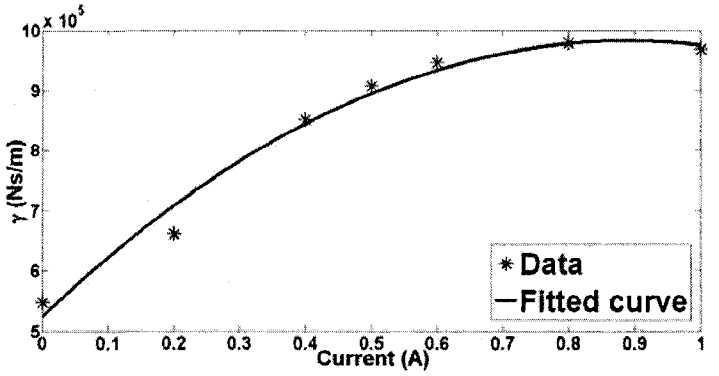

Figure 6.7 Variations of parameter γ with the input current.

$$\gamma(i) = p_1 i^2 + p_2 i + p_3 \tag{6.17}$$

where parameters p_1, p_2 and p_3 are identified using the least-square method[182] and found to be -5.796×10^5 ($N\ s\ m^{-1}\ A^{-2}$), 1.029×10^6 ($N\ s\ m^{-1}\ A^{-1}$) and 5.247×10^5 ($N\ s\ m^{-1}$), respectively.

As discussed before, the parameter β/α is frequency and amplitude independent. Thus, utilizing Equation (6.15), the data provided in Table 6.7, and the evaluated parameter γ, one can easily obtain the current relationship for the parameter β/α as:

$$\frac{\beta}{\alpha}(i) = f - \gamma(i) X \times \omega - f_0 \tag{6.18}$$

The variation of the parameter β/α with respect to the current is shown in Figure 6.8 and again a second order polynomial function, as described in Equation (6.19), is used to fit the data.

$$\frac{\beta}{\alpha}(i) = q_1 i^2 + q_2 i + q_3 \tag{6.19}$$

where parameters q_1, q_2 and q_3 are again evaluated using the least square method[182] and found to be -5.103×10^4 (NA^{-2}), 1.518×10^5 (NA^{-1}) and 1.83×10^4 (N), respectively.

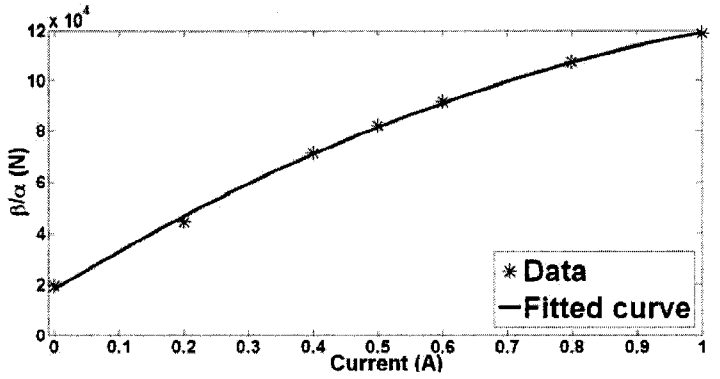

Figure 6.8 Variations of parameter β/α with the input current.

6.4.3 Estimation of characteristic parameter "δ"

The parameter δ can be estimated through point "E" shown in Figure 6.4. Based on the investigation presented in Section 6.3, the inner state (y) at point "E" is equal (close) to 1. Thus, Equation (6.14) at point "E" can be simplified as:

$$f = \frac{\beta}{\alpha}(i) + \delta X + f_0 \tag{6.20}$$

The parameter β/α is independent of the frequency and amplitude, as proven in Section 6.4.2, and hence, based on Equation (6.20), if the parameter δ is independent of the excitation amplitude, the damping force difference (Δf) under two harmonic excitation signals with same frequency and different amplitude for the same input current should be proportional to the difference of amplitude (ΔX) as:

$$\Delta f = \delta(X_2 - X_1) = \delta \Delta X \tag{6.21}$$

And also, if parameter δ is independent of the excitation frequency, Δf defined in Equation (6.21) should also be the same under different excitation frequency with fixed ΔX. Here, the selected test signals are similar to those provided in Tables 6.3 and 6.5, and the input current is set to zero. The results obtained from the modified Bouc-Wen

model[181] are summarized in Table 6.8, in which the ΔX and Δf have the same definitions as those provided in Tables 6.3 and 6.4 and also defined in Equation (6.21).

Table 6.8 The damping force difference (Δf) at point "E" (Figure 6.4) for two sets of test signal as presented in Tables 6.3 and 6.5 for input current of 0 (A).

Amplitude difference (Table 6.3)	Frequency (Hz)					
	0.5	1	2	5	7.5	10
ΔX=0.25(cm)	507.4073	501.0564	496.5099	495.807	508.0312	495.1521
ΔX=0.5(cm)	1009.6208	999.2709	993.0594	991.035	1015.6646	990.0009
ΔX=1(cm)	2016.3592	1997.0383	1987.4742	1981.7836	2031.1314	1979.8507
ΔX=1.5(cm)	3023.6956	2995.1283	2980.9948	2972.599	3046.6429	2969.7347
ΔX=2(cm)	4031.1925	3993.9021	3974.5578	3963.3433	4062.1657	3959.5874
ΔX=2.5(cm)	5038.756	4991.51	4967.9065	4953.3797	5077.692	4949.0786

Examination the results provided in Table 6.8 reveals that Δf is nearly constant with respect to the variation of the frequency under fixed ΔX, and also Δf is proportional to ΔX in each excitation frequency. Thus, it can be concluded that the parameter δ is independent of frequency and amplitude.

Therefore, one can utilize Equation (6.21) and the same current test signal utilized in Table 6.7 to evaluate the current dependency of the parameter δ. Figure 6.9 illustrates the variation of the parameter δ with the increase of input current. It should be noted that to study the parameter δ in small current range, the input current 0.1 (A) was added to those listed in Table 6.7.

It can be seen from Figure 6.9 that there is no significant change in δ for the values of current above 0.2 (A), and it is difficult to provide one simple function to interpolate the variations of δ with current especially for the current smaller than 0.1 (A). This is mainly

due to the fact that the dynamic behavior described by the modified Bouc-Wen model[181] is very complex for the input current below 0.1 (*A*). To better clarify this issue, Figure 6.10 shows the simulation results obtained through the modified Bouc-Wen model[181], as shown in Equations (6.1)-(6.6) and Table 6.2, for the harmonic excitation with frequency of 1 (*Hz*) and amplitude of 0.01 (*m*) for the input currents of 0, 0.05, 0.1 and 0.2 (*A*), respectively.

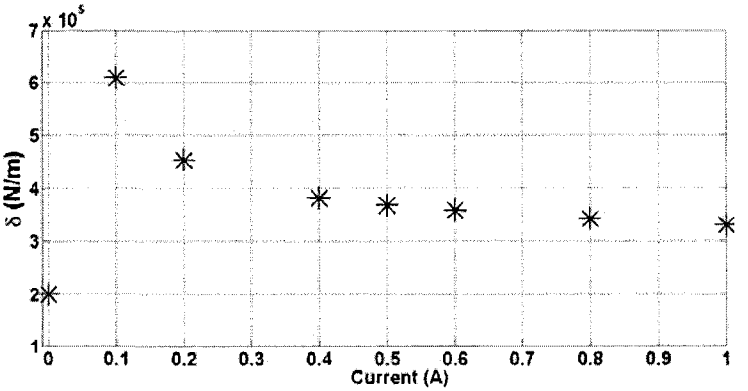

Figure 6.9 Variation of parameter δ versus current.

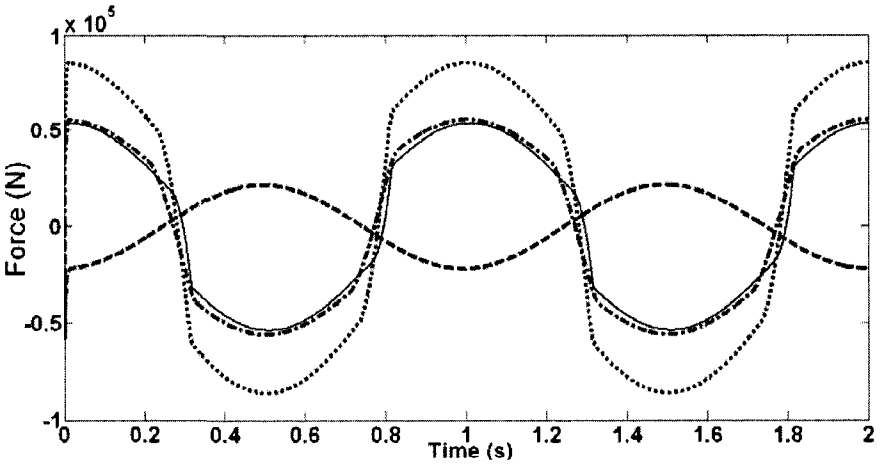

Figure 6.10 Simulation results for the modified Bouc-Wen Model[181] under harmonic excitation with frequency 1 of (*Hz*), amplitude of 0.01 (*m*), Solid, dashed, dashed-dotted and dotted lines represent input currents equal to 0, 0.05, 0.1 and 0.2 (*A*), respectively.

It can be seen from Figure 6.10 that the damping force for the input current of 0.05 (A) does not have the same pattern as those for other current inputs. Moreover, with the increase of the input current, the strength of the magnetic field will be increased and subsequently, the damping forces generated by the MR-damper are expected to naturally be increased. Obviously, based on Figure 6.10, this trend cannot be observed from the increase in the input current from 0 to 0.05 (A) by the modified Bouc-Wen model[181]

Based on the above investigations, it has been found that the value of parameter δ at the 0 (A) (δ =228234.84 $N\,m^{-1}$) will generate acceptable results as will be shown later.

6.4.4 Estimation of characteristic parameter "α"

As stated in Equation (6.7a), the inner state (y) depends on the parameter α. Thus, to estimate the parameter α, the inner state (y) for a whole period should first be obtained. To accomplish this, a typical harmonic excitation (frequency ω=1 (Hz), amplitude X=1 (cm)) under different current inputs (current i_1 =0.4 (A) and i_2=0.5 (A)) are utilized as the test signals. Now considering Equation (6.14) and above estimation for parameters δ, β/α and γ, the inner state (y) in a whole period can be estimated as:

$$y = \{f_2 - f_1 - [\gamma(i_2) - \gamma(i_1)]\dot{x}\} / (\frac{\beta}{\alpha}(i_2) - \frac{\beta}{\alpha}(i_1)) \tag{6.22}$$

where f_1 and f_2 present the MR-damper's damping force, obtained using the modified Bouc-Wen model[181], for current being equal to 0.4 (A) and 0.5 (A), respectively, under the same harmonic excitation. It should be noted that the parameter ε are assumed to be current independent (See Section 6.4.5) and the velocity ($\dot{x}$) for a whole period is known. Thus, inner state (y) for a whole period can be obtained using Equation (6.22). Based on

Equation (6.7a), the effect of the frequency and amplitude of harmonic excitation to the inner state (y) can be reflected through the velocity ($\dot{x}$). Furthermore, as shown above the parameter β/α is only current dependent, and hence it is possible to assume that the parameter α is independent of the frequency, amplitude, and current. Based on this assumption, the parameter α has been evaluated using the following optimal problem:

$$\begin{array}{rcl} \text{Find the design variables:} & \{\alpha\} & \\ \text{To minimize:} & [y(k+1)-y_e(k+1)]^2 & (6.23) \\ \text{Subjected to:} & 500 \leq \alpha \leq 10000 & \end{array}$$

where $y(k+1)$ represents the inner state (y) in the time index ($k+1$) obtained from Equation (6.22) evaluated through the modified Bouc-Wen model[181] and $y_e(k+1)$ represents the Fourth-Order Runge-Kutta (RK4)[183] simulation result of Equation (6.7a) for the inner state (y) in time index ($k+1$) under the design variable α. The constraint is selected based on the analysis presented in Section 6.3. The optimal problem is solved using the SQP optimization technique[88] and then repeated for the whole period. Finally, the estimated parameter α is found to be 2531.8 (m^{-1}). Figure 6.11 shows the comparison of the data for the inner state (y) based on Equation (6.22) obtained from the modified Bouc-Wen model[181] and that based on Equation (6.7a) under α of 2531.8 (m^{-1}).

It can be realized from Figure 6.11 that the estimated parameter α can provide accurate inner state (y) simulation result compared with the data obtained from the modified Bouc-Wen model[181]. As mentioned in Section 6.3, by suitably selecting parameter α the inner state (y) given in Equation (6.7a), is equal (close) to 1 between the time points "A" and "B" shown in Figure 6.3, and the parameter identification procedure presented in this chapter is based on this assumption. Here using the estimated parameter "α", this

behavior has been verified in Figure 6.12 and it must be noted that the time points "A" and "B" and the "dimensionless displacement" and "dimensionless velocity" in the caption of Figure 6.12 have the same definitions as those seen in Figure 6.3.

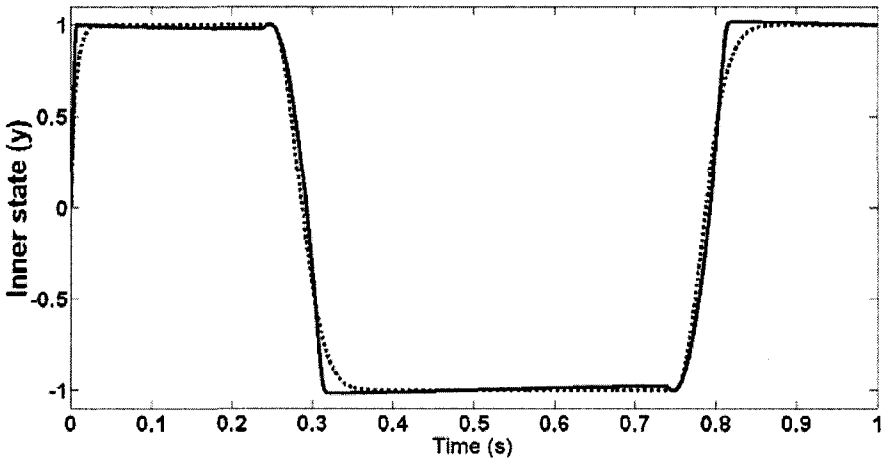

Figure 6.11 Inner state (y). Solid and dotted lines represent the result based on Equation (6.22) evaluated through the modified Bouc-Wen model[181] and the simulation result for Equation (6.7a) under α of 2531.8 (m^{-1}).

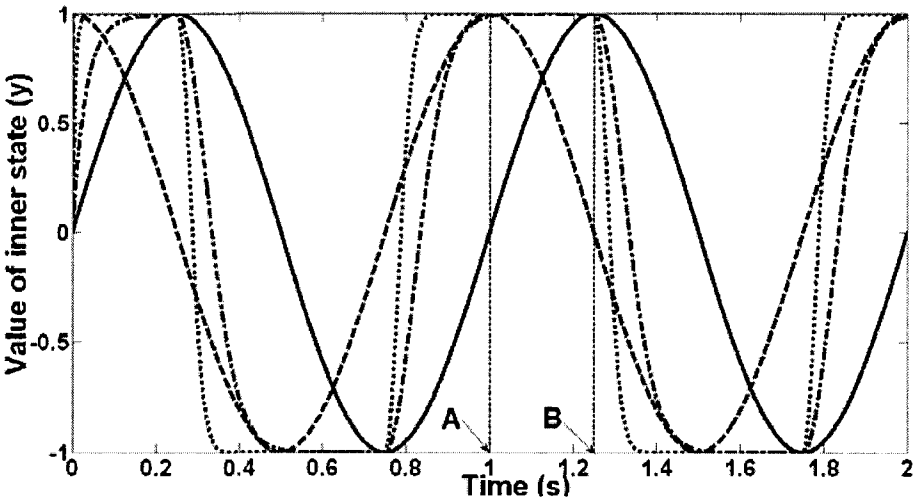

Figure 6.12 Simulation of Equation (6.7a) under harmonic excitation (frequency ω=1 (Hz), α=2531.8 (m^{-1})): Solid, dashed, dotted and dashed-dotted lines represent the dimensionless displacement, the dimensionless velocity and the inner state (y) with amplitude equal to 1 and 0.2 (cm), respectively.

One can find from Figure 6.12 that under this optimal parameter α of 2531.8 (m^{-1}), the inner state (y) will be equal (close) to 1 between the time points "A" and "B" for harmonic excitation with the amplitude bigger than around 2 (mm). Thus, the assumption made in Section 6.3 is acceptable for most of the MR-9000 type damper's working range.

6.4.5 Estimation of characteristic parameter "ε"

By rearranging Equation (6.14), one can easily obtain a function as:

$$f-(\frac{\beta}{\alpha})y-(\gamma)\dot{x}-\delta x-f_0=\varepsilon(\dot{x}-|\dot{x}|)y \tag{6.24}$$

Then let us define:

$$g(z/\varepsilon)=f-(\frac{\beta}{\alpha})y-(\gamma)\dot{x}-\delta x-f_0 \text{ and } \{z\}=\dot{x}-|\dot{x}|y \tag{6.25}$$

And thus based on the parameters evaluated in above sections, parameter $g(z/\varepsilon)$ and $\{z\}$ in Equation (6.25) can be easily obtained. Here, the least square parameter estimation method[182] will be adopted to evaluate the parameter ε, and the procedure can be expressed as:

$$g(z/\varepsilon)=\hat{\varepsilon}^T\{z\} \tag{6.26}$$

where $\hat{\varepsilon}$ represents the estimated value for parameter ε. Based on equation (6.26) one can obtain the estimated value for parameter ε under different input currents and the results has been illustrated in Figure 6.13.

Similar to the estimated parameter δ, one can easily find form Figure 6.13 that it is also difficult to provide one simple function to interpolate the variations of parameter ε versus

the input current, especially for the small range of the input current. Fortunately, the effect of value of parameter ε to the damping force is negligible in large MR-damper's working range. This can be verified by using Equation (6.14). The effect of parameter ε on the damping force of the MR-damper can be described as:

$$f_\varepsilon = \varepsilon(\dot{x} - |\dot{x}|y) \tag{6.27}$$

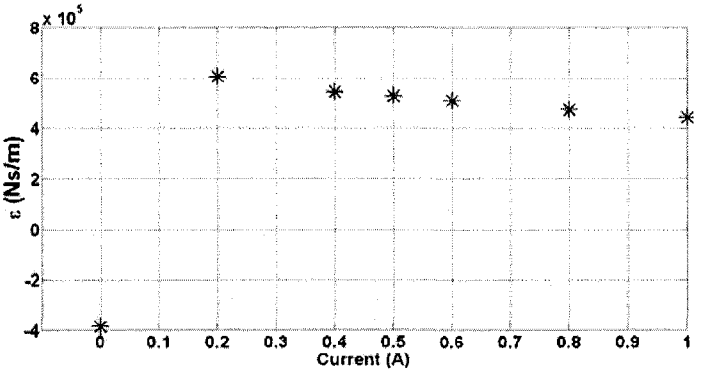

Figure 6.13 Estimated parameter ε versus the input current.

Based on the analysis of the inner state (y) in Section 6.3, one can easily find that the output f_ε would be close to zero in the working range (time point "A" to "B" shown in Figure 6.4). Here, it has been found that the value of parameter ε at 0.5 (A) (ε=526051.9562 ($N\,s\,m^{-1}$) will generate acceptable results as will be shown later.

6.5 Proposed LuGre Friction MR-damper Model

Using the estimated characteristic parameters, the proposed LuGre friction MR-damper model for MR-9000 type damper can be summarized as:

$$\frac{1}{\alpha}\dot{y} = \dot{x} - |\dot{x}|y \tag{6.28}$$

$$f = \frac{\beta}{\alpha} y + \gamma \dot{x} + \delta x + \frac{\varepsilon}{\alpha} \dot{y} + f_0 \tag{6.29}$$

$$\frac{\beta(i)}{\alpha} = q_1 i^2 + q_2 i + q_3 \text{ and } \gamma(i) = p_1 i^2 + p_2 i + p_3 \tag{6.30}$$

where i is the input current, and the other parameters are given in Table 6.9.

Table 6.9 Estimated characteristics parameters for the proposed LuGre friction model for MR-9000 type damper.

α	2531.8 (m^{-1})	q_2	1.518×10^5 (NA^{-1})
δ	228234.84 ($N\,m^{-1}$)	q_3	1.83×10^4 (N)
ε	526051.9562 ($N\,s\,m^{-1}$)	p_1	-5.796×10^5 ($N\,s\,m^{-1}A^{-2}$)
f_0	-111.1158 (N)	P_2	1.029×10^6 ($N\,s\,m^{-1}A^{-1}$)
q_1	-5.103×10^4 (NA^{-2})	p_3	5.247×10^5 ($N\,s\,m^{-1}$)

6.6 Validation of the Proposed Model

In this section, in order to verify the validity of the proposed LuGre friction model, the dynamic hysteretic behaviors of the MR-9000 type damper will be simulated using the proposed LuGre friction model and compared with those obtained using the modified Bouc-Wen model[181] under different test signals.

6.6.1 Harmonic excitation with frequency of 1 (*Hz*) and amplitude of 0.01(*m*) for different input currents

The dynamic performances of the MR-damper, which include the damping force versus the displacement, velocity and time under harmonic excitation with frequency of 1 (*Hz*), amplitude of 0.01 (*m*) under different input current evaluated using the proposed LuGre friction model and the modified Bouc-Wen model[181] are compared in Figure 6.14.

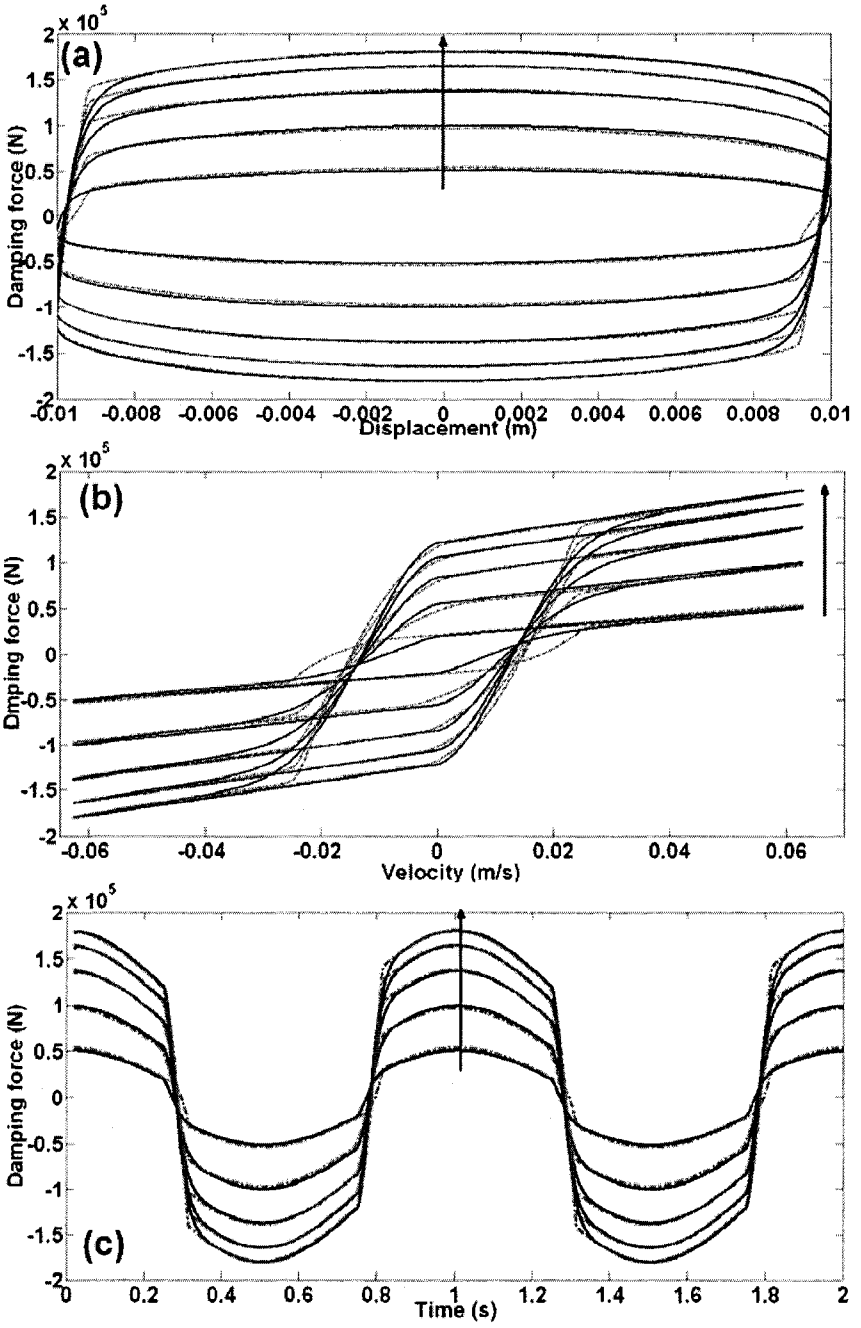

Figure 6.14 MR-damper's dynamic behavior comparison under harmonic excitation with frequency of 1 (*Hz*) and amplitude of 0.01 (*m*) for different input current. (a) Force-Displacement. (b) Force-Velocity. (c) Force-Time. Solid and dashed-dotted (red) lines represent the results obtained from the proposed LuGre friction model and the modified Bouc-Wen model[181], respectively. Along the arrow direction: current values are 0, 0.25, 0.5, 0.75 and 1 (*A*).

6.6.2 Harmonic excitation with frequency of 1 (*Hz*) and current of 0.5 (*A*) for different excitation amplitudes

Figure 6.15 compares the dynamic performances of MR-damper, which include the damping force versus the displacement, velocity and time under harmonic excitation with frequency of 1 (*Hz*) and the input current of 0.5 (*A*) for different excitation amplitudes evaluated using the proposed LuGre friction model and the modified Bouc-Wen model[181]. Here it should be noted that to facilitate the comparison, the "Dimensionless displacement" and "Dimensionless velocity" in Figure 6.15 represent the excitation displacement and velocity divided by their relative values of amplitude and maximum velocity, respectively.

6.6.3 Harmonic excitation with amplitude of 0.02 (*m*) and current of 0.5 (*A*) for different excitation frequencies

The dynamic performances of MR-damper, which include the damping force versus the displacement, velocity and time under harmonic excitation with the amplitude of 0.02 (*m*) and input current 0.5 (*A*) for different excitation frequencies evaluated using the proposed LuGre friction model and the modified Bouc-Wen model[181]are compared in Figure 6.16, in which the "Dimensionless velocity" represents the excitation velocity divided by their relative maximum values.

Based on above investigation for MR-damper's damping force under harmonic excitation with different frequency, amplitude and input current, one can realize that the predicted dynamic behavior for MR-9000 type damper using the proposed LuGre friction model agrees very well with that of the modified Bouc-Wen model[181] under harmonic excitation.

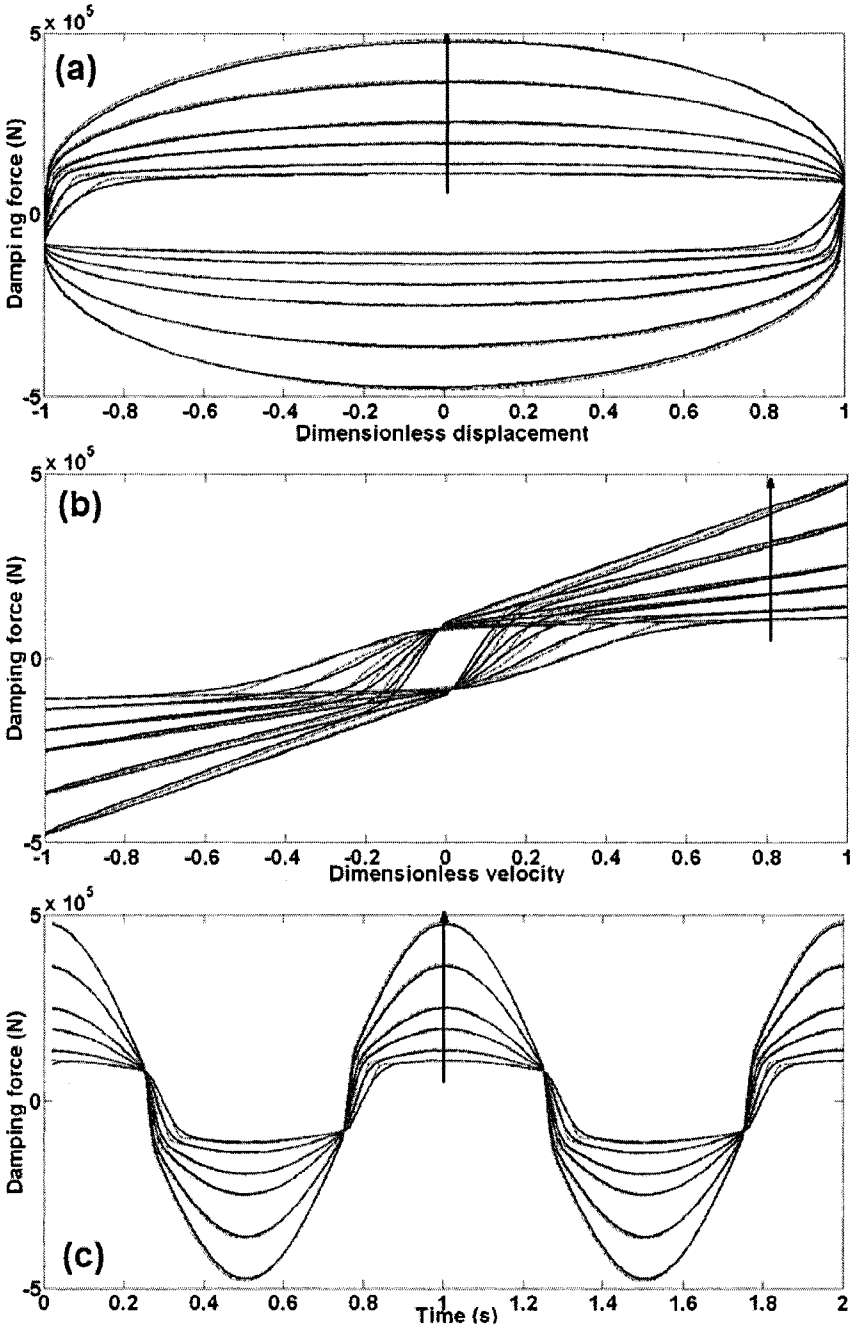

Figure 6.15 MR-damper's dynamic behavior comparison under harmonic excitation with frequency of 1 (*Hz*), different amplitude and input current of 0.5 (*A*). (a) Force-Displacement. (b) Force-Velocity. (c) Force-Time. Solid and dashed-dotted (red) lines represent the result obtained from the proposed LuGre friction model and the modified Bouc-Wen model[181], respectively. Along the arrow direction: amplitude values are 0.005, 0.01, 0.02, 0.03, 0.05 and 0.07 (*m*).

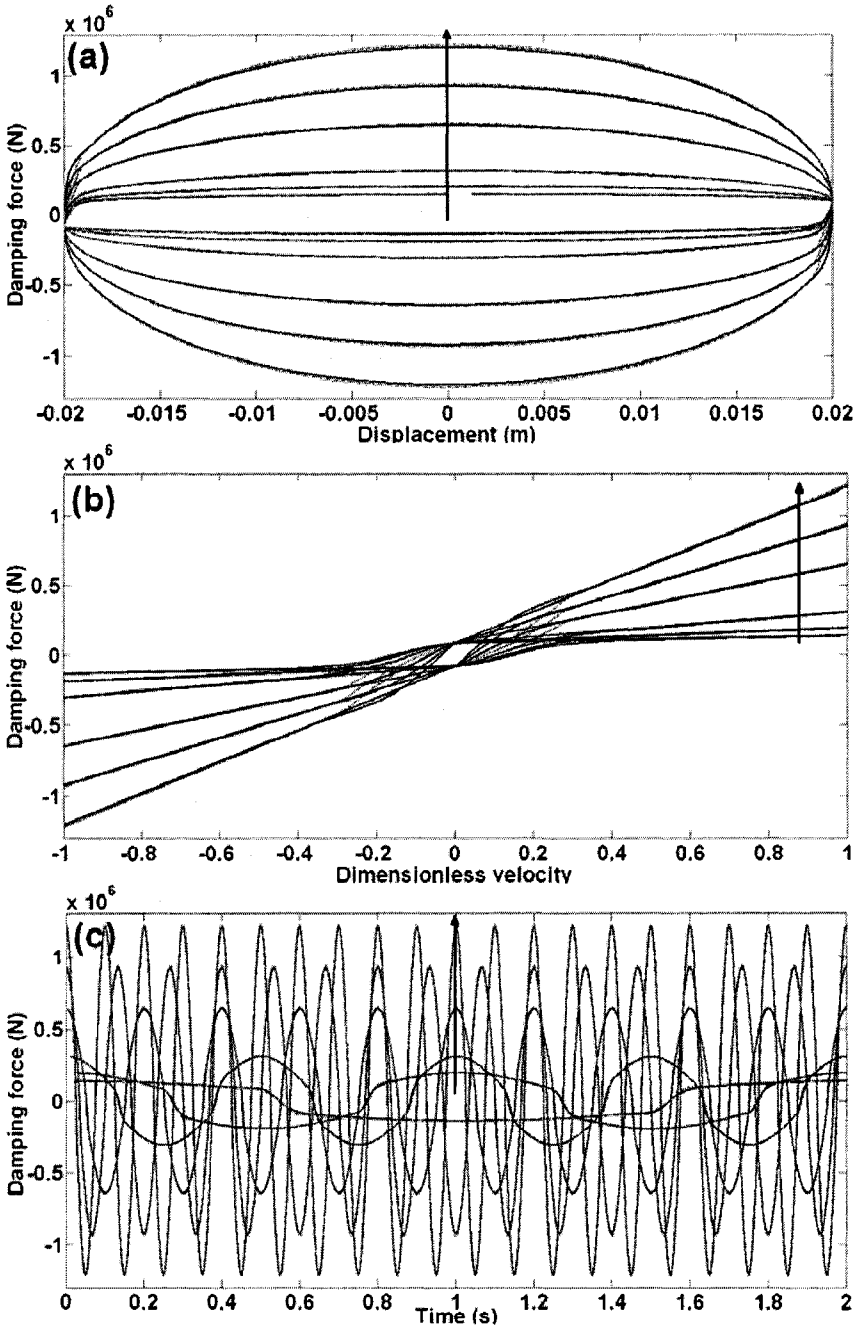

Figure 6.16 MR-damper's dynamic behavior comparison under harmonic excitation with Amplitude of 0.02 (*m*), different frequency and input current of 0.5 (*A*). (a) Force-Displacement. (b) Force-Velocity. (c) Force-Time. Solid and dashed-dotted (red) lines represent the result obtained from the proposed LuGre friction model and the modified Bouc-Wen model[181], respectively. Along the arrow direction: frequency values are 0.5, 1, 2, 5, 7.5 and 10 (*Hz*).

Furthermore, as mentioned before, in the low range of input current, the modified Bouc-Wen model[181] may not provide reasonable results. The proposed LuGre friction model can provide smooth transition under the low current range. To demonstrate this issue, Figure 6.17 illustrates the damping force evaluated using the proposed LuGre friction model and the modified Bouc-Wen model[181] for the harmonic excitation with frequency of 1 (*Hz*), amplitude *X* of 0.01 (*m*) and the input current of 0.05(*A*). The results show that the proposed LuGre model can predict more reasonable MR-damper's damping force in the low current range compared with the modified Bouc-Wen model[181].

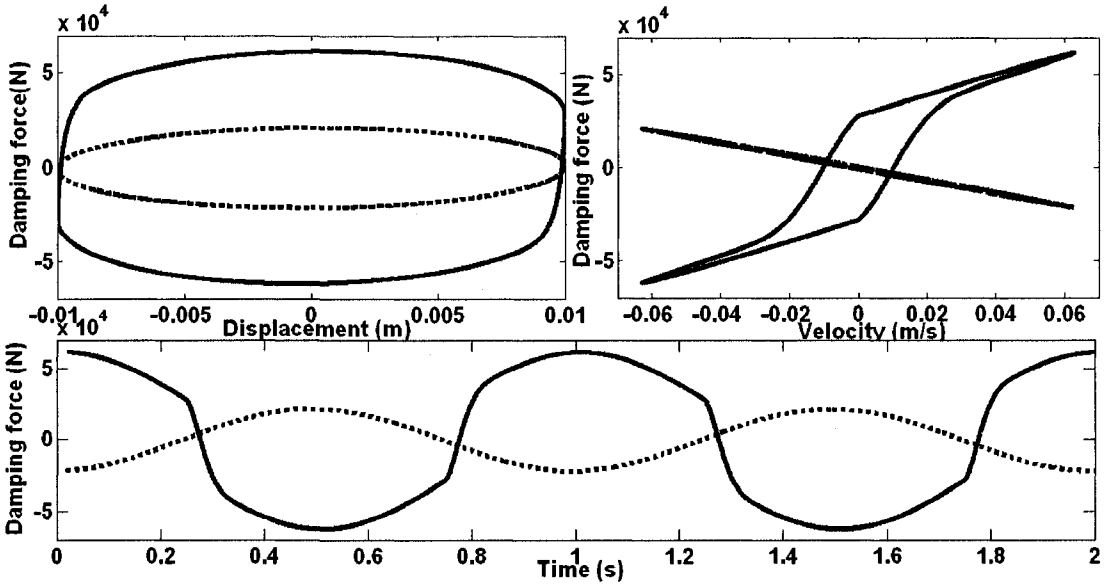

Figure 6.17 MR-damper's dynamic behavior comparison under harmonic excitation with amplitude of 0.01(*m*), frequency of 1(*Hz*) and current input of 0.05 (*A*). Solid and dotted lines represent the results obtained from the proposed LuGre friction model and the modified Bouc-Wen model[181].

6.6.4 Harmonic excitation with amplitude of 0.01 (*m*) and frequency of 1 (*Hz*) for continuously changing input current

Here the input current is assumed as a harmonic wave with the amplitude of 0.5(*A*), frequency of 1(*Hz*) and the bias 0.5 (*A*), as shown in Figure 6.18, which can cover the whole MR-damper's working current range.

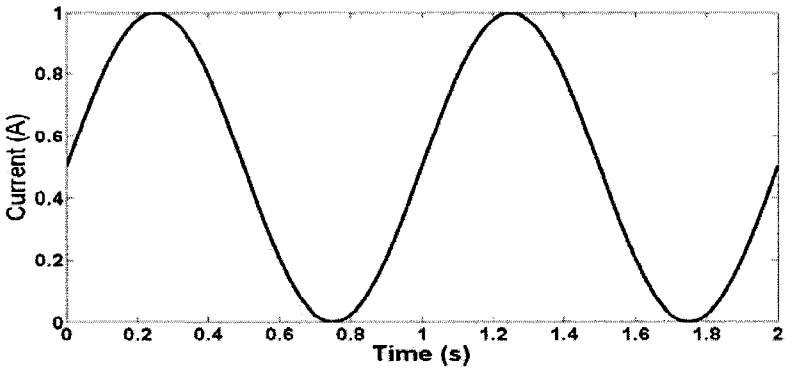

Figure 6.18 Test varying current input.

The simulation results for this test are shown in Figure 6.19 and it should be noted that in this simulation the step size is selected as 1×10^{-6} (*s*). One can realize from Figure 6.19 that the singularity occurs for the modified Bouc-Wen model[181], however, the proposed model does not experience this point. This singularity can be removed by selecting smaller simulation step size, but using the step size smaller than 1×10^{-6} (*s*) is computationally expensive. One may also realize that except the singularity point, the predicted damping force generated by the proposed LuGre friction model agrees very well with that obtained by the modified Bouc-Wen model[181].

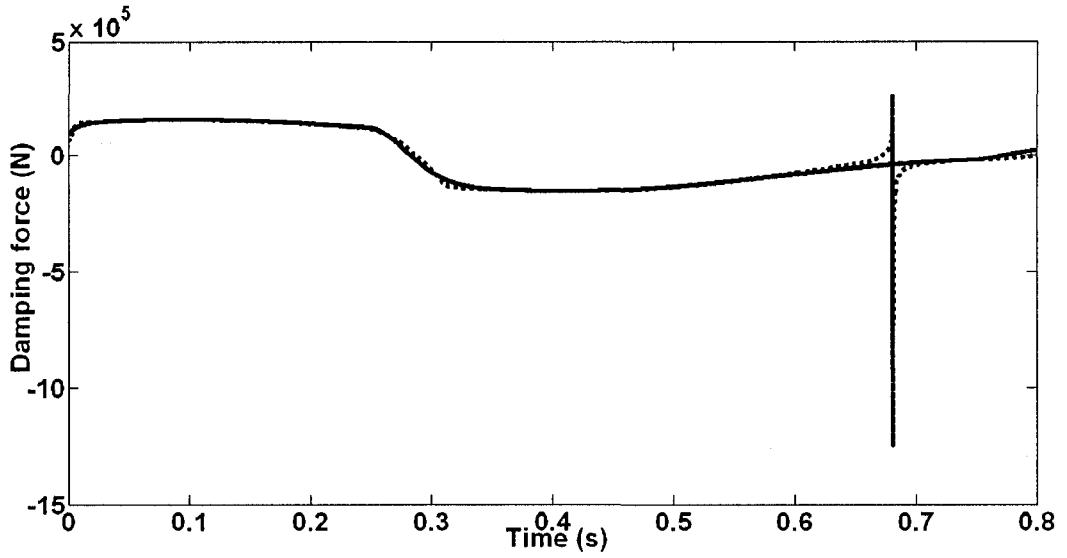

Figure 6.19 MR-damper's dynamic behavior comparison for harmonic excitation with frequency of 1 (*Hz*), amplitude of 0.01 (*m*) under harmonic current test signal with simulation step size of 1×10^{-6}(*s*). Solid and dotted lines represent the results obtained from the proposed LuGre friction model and the modified Bouc-Wen model[181], respectively.

The MR-damper's dynamic behavior under the same current test signal shown in Figure 6.18 but this time with simulation step size 1×10^{-4} (*s*) is illustrated in Figure 6.20. It can be seen that the modified Bouc-Wen model[181] is not capable to simulate the damping force properly, the proposed model can still provide accurate results for large simulation step size. Since the only controllable parameter in MR-damper is the input current, therefore, the dynamic behavior of MR-damper with changing input current is very important. However, as shown in Figures 6.19 and 6.20, the damping force generated by modified Bouc-Wen model for this low-frequency current signal does not produce reasonable results for relatively large simulation step size (10^{-4} *s*) or shows singularity for small step size (10^{-6} *s*).

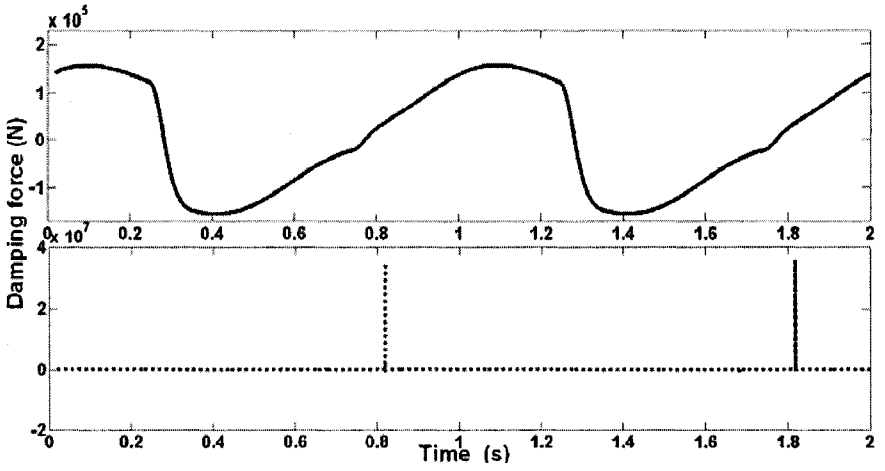

Figure 6.20 MR-damper dynamic behavior comparison for harmonic excitation with frequency of 1 (*Hz*), amplitude of 0.01 (*m*), and the test current shown in Figure 6.18, and the simulation step size of 1×10^{-4} (*s*) Solid and dotted lines represent the results obtained from the proposed LuGre friction model and the modified Bouc-Wen model[181], respectively.

6.6.5 Random excitation

The dynamic behavior of MR-damper under random excitation will be investigated in this section using the proposed model and the results will be compared with those obtained from the modified Bouc-Wen model[181]. The random signal in this test is a combination of 30 harmonic signals with frequency ranging from 0.01–10 (*Hz*), as illustrated in Figure 6.21, and the input current in this test is selected as 0.5 (*A*). The simulation results are shown in Figure 6.21, from which it can be realized that the generated damping force under this set of random excitation signal evaluated using the proposed LuGre friction model perfectly agrees with those obtained form the modified Bouc-Wen model[181].

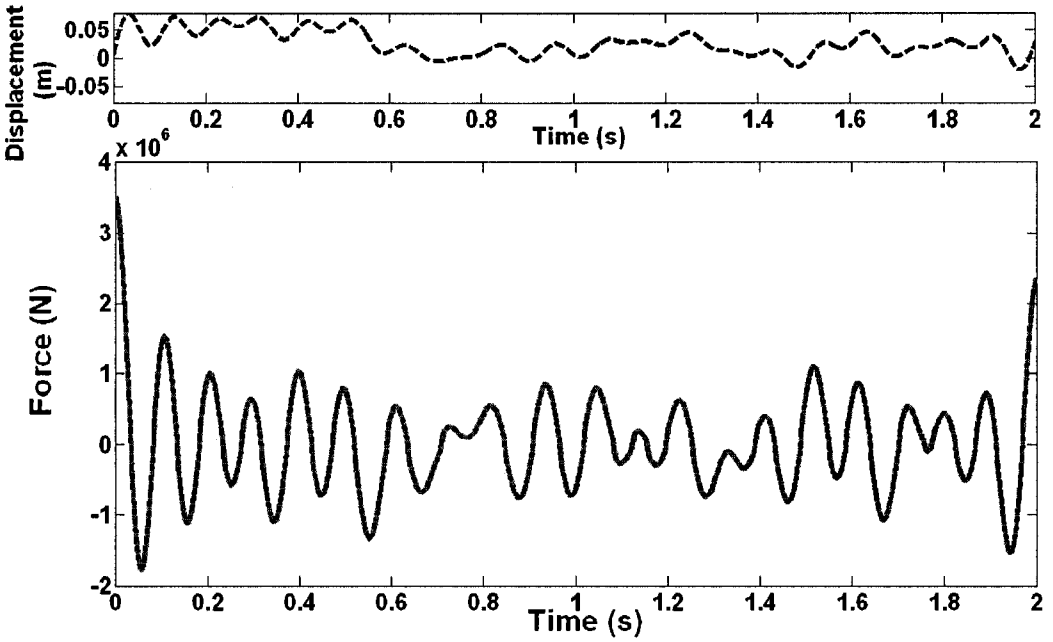

Figure 6.21 MR-damper's dynamic behavior comparisons under random excitation. Solid and dotted (red) lines represent the results obtained from the proposed LuGre friction model and the modified Bouc-Wen model[181], respectively. Dashed line represents the random excitation signal.

In summary, the MR-damper's damping force predicted by the proposed LuGre friction model and the modified Bouc-Wen model[181] under harmonic excitation, random excitation, and different kind of input currents have been compared. The results show that compared with the modified Bouc-Wen model[181], the proposed LuGre friction model can provide accurate simulation results and easily be utilized in practical semi-active vibration control applications.

6.7 Conclusions and Summary

A simple hysteresis model based on the LuGre friction model has been developed to predict the dynamic behavior of large-scale MR-damper accurately and efficiently. It has

been shown that the predicted dynamic behavior of MR-damper, using the proposed model agrees very well with those obtained using the modified Bouc-Wen model[181] for MR-9000 type damper under different working conditions (harmonic excitation with different frequency and amplitude, changing current, and random excitation). Although the proposed LuGre friction model is based on the simulation data of modified Bouc-Wen model[181], the evaluation procedure provided in this dissertation can easily be applied to the experimental data.

It has also been illustrated that the proposed model is stable (no singularity point) and computationally more efficient than the modified Bouc-Wen model[181]. Since the only controllable parameter in the MR-damper is the input current, in the next chapter (Chapter 6) an effective inverse MR-damper model based on the proposed LuGre friction model will be presented, which can be readily utilized in the design of semi-active vibration suppression devices.

CHAPTER 7

SEMI-ACTIVE MASS DAMPER DESIGN USING MAGNETO-RHEOLOGICAL FLUID DAMPERS

7.1 Introduction

As the damping and stiffness of an optimally designed Tuned Mass Damper (TMD) system can not change with different excitation condition, the effectiveness of the TMD system is restricted to its tuned frequency. Subsequently, it provides limited vibration suppression performance for the random type excitation or excitation frequency far away from its tuned natural frequency. The so-called Active Mass Damper (AMD) or Semi-Active Mass Damper (SAMD), in which a controllable device (full-active or semi-active) will be added to or replace the damper in the TMD system, is developed to overcome the restriction of the TMD system and also improve the vibration suppression performance around the TMD's tuned natural frequency. The detail introductions about the AMD and SAMD systems have been presented in Chapter 1.

The Magneto-Rheological (MR) fluid damper is one of the most promising semi-active devices and the detailed introductions about its development, modeling and control methodologies have also been presented in Chapters 1 and 6. Here it should be noted that most of researches related to MR-damper's application are mainly focused on the base isolation structure, for instance, Dyke *et al*[92] and Dyke[94] installed the MR-damper between the base of building structures and the ground; Wang *et al*[134] studied the vehicle

suspension system using MR-damper; Dominguez *et al*[148] replaced one element of truss structure with MR-damper. For this type of application, the simple "*on-off*" control method can provide good performance, as the "over-damping" phenomenon, in which the MR-damper becomes too strong to suppress the vibratory energy, may not happen under suitably selected MR-damper. However, for SAMD system using MR-damper, which is seldom reported by researchers, the simple "*on-off*" control method may not work, as the working principle of SAMD is to dissipate energy through MR-damper's moving induced by the movement of the attached small mass. Obviously, to maximize the energy dissipation through MR-damper, it is required not only to control the damping force but also to allow the free movement of the attached small mass. It should be noted that the damping force provided by MR-damper in "*on*" condition may become too large to allow the free movement of the small attached mass, and subsequently, the MR-damper may not dissipate energy efficiently.

Based on the above discussions, this chapter will present a methodology to utilize the MR-damper as the semi-active device in the SAMD system to suppress the structural vibration effectively. The proposed methodology consists of four steps: (1) an inverse MR-damper model will be developed based on the LuGre friction model proposed in Chapter 6 for MR-9000 type damper and proposed by Jimenez and Alvarez[136] for RD-1005-3 type MR-damper; (2) an effective Boolean algebra methodology will be provided to calculate command current based on the proposed inverse MR-damper model; (3) H_2/LQG control design method will be utilized to design the controller for AMD system; (4) a vibration suppression strategy will be developed to provide effective vibratory suppression capacity for SAMD system using MR-damper. Finally numerical examples

will be presented to compare the effect of SAMD with MR-damper using the proposed control methodology with those using different vibration control methodologies available in published literatures and that of optimal TMD and AMD systems.

7.2 MR-Damper and Inverse MR-Damper Models

The LuGre friction MR-damper model has been presented in Chapter 6 as:

$$\frac{1}{\alpha}\dot{y} = \dot{x} - |\dot{x}|\, y \tag{7.1}$$

$$f = \frac{\beta}{\alpha} y + \gamma\dot{x} + \delta x + \frac{\varepsilon}{\alpha}\dot{y} + f_0 \tag{7.2}$$

$$\frac{\beta(i)}{\alpha} = q_1 i^2 + q_2 i + q_3 \text{ and } \gamma(i) = p_1 i^2 + p_2 i + p_3 \tag{7.3}$$

where i is the input current. The characteristic parameters in Equations (7.1)-(7.3) for MR-9000 type damper have been listed in Table 6.9, and for RD-1005-3 type MR-damper will be presented in Table 7.1[136].

Table 7.1 Estimated characteristics parameters for the LuGre friction model for RD-1005-3 type MR-damper[136].

α	3.2 (mm^{-1})	q_2	833.85 (N/A)
δ	1.03 ($N\,mm^{-1}$)	q_3	14.72 (N)
ε	0.6 ($N\,s\,mm^{-1}$)	p_1	-10.80 ($N\,s\,mm^{-1}A^{-2}$)
f_0	-45.82 (N)	p_2	17.75 ($N\,s\,mm^{-1}A^{-1}$)
q_1	0 (NA^{-2})	p_3	0.5 ($N\,s\,mm^{-1}$)

To obtain the best vibration suppression performance using MR-damper, it is required to obtain the precise MR-damper's input current control. Assuming that the required control force is known, the problem is how to derive the MR-damper's command current to generate the damping force as close as the required control force. The so called inverse

MR-damper model is developed based on this requirement. The inverse MR-damper model is developed based on the LuGre friction model given in Equations (7.1)-(7-3). Rearranging Equations (7.1)-(7-3), one can easily obtain a simple binomial function as:

$$ai^2 + bi + c = f \tag{7.4}$$

where $a = p_1\dot{x} + q_1 y$, $b = q_2 y + p_2\dot{x}$, $c = (q_3 - \varepsilon|\dot{x}|)y + (p_3 + \varepsilon)\dot{x} + \delta x + f_0$. Parameter i represents the command current. Therefore, the inverse MR-damper model can be expressed as the following optimization problem:

Find the design variables:	command current (i).	
To minimize:	$J=\|u-f\|$	(7.5)
Subjected to:	$0 \le i \le 1$	

where parameter u represents the required control force. Here it should be emphasized that for the safety purpose, the working current for both types of MR-dampers is restricted in the range of [0.0, 1.0] (A). It may be a simple and direct approach to use formal optimization techniques to solve the optimization problem established in Equation (7.5), however it is computationally expensive compared to the computational time required to obtain the structural response and thus not effective for real time vibration control applications. As the objective function of this optimization problem is a simple binomial function, an effective calculating method based on the Boolean algebra has been developed to obtain the command current based on this optimization problem. It is difficult to clearly express the developed Boolean algebra methodology for solving the optimization problem established in Equation (7.5) in one simple figure, thus the logic algebra form, as shown in Figure 7.1, has been utilized to represent the proposed Boolean algebra methodology. Based on Figure 7.1, one can easily replace the logic relationship

with the Boolean algebra to obtain the solution for the optimization problem given in Equation (7.5).

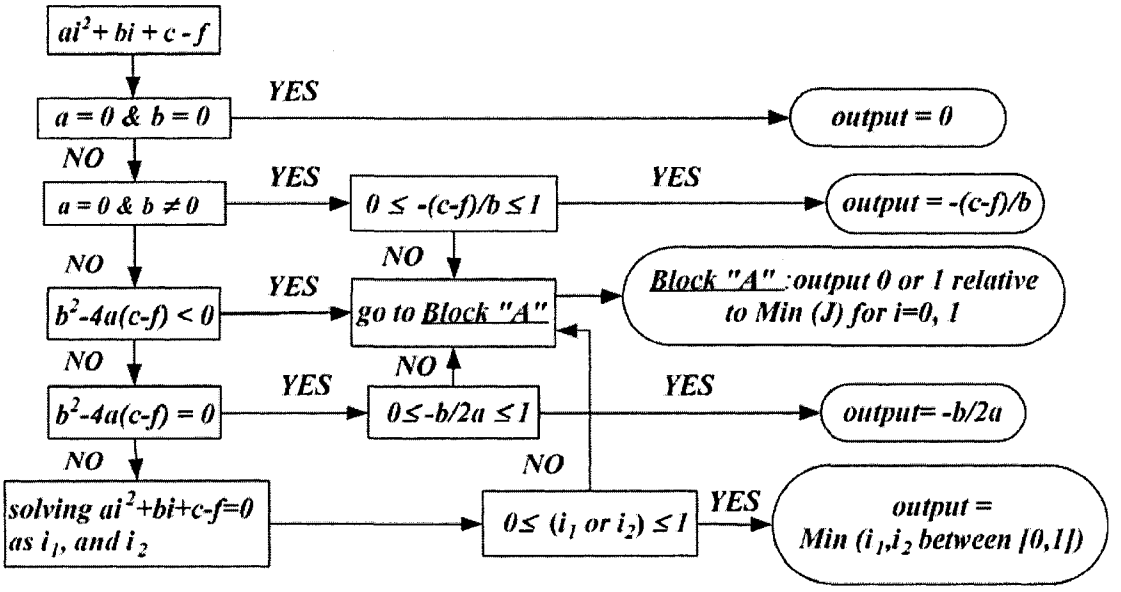

Figure 7.1 The solution of optimization problem established in Equation (7.5).

The proposed calculation method has been tested in the numerical examples and compared with the formal optimization techniques. It is found that the developed calculation method based on Boolean algorism is at least 10 times faster than the traditional optimization techniques, and can be effectively and easily used in simulation.

7.3 H_2/LQG Optimal Control Method Based on the Active Mass Damper

Linear Quadratic optimal controller design method is adopted by many researchers in structural vibration suppression area. However, most of studies are based on the Linear Quadratic Regulator (LQR) method, which assumes that all of the state variables can be measured directly. In practical application the structural displacement and velocity are not absolute, and depend on their relative measured references. Furthermore, it is difficult

to measure all of the state variables directly in real application. Therefore, the controller design that is based on directly measured displacement and velocity is impractical.

Other linear quadratic controller design methods, such as Linear Quadratic Gaussian (LQG) and H_2, utilize a state estimate to evaluate the state variables, and thus it is more practical in real application. As the accelerometers can provide accurate measurements of absolute acceleration, and it is easy to be installed in any place on the whole structure, more and more researchers have adopted acceleration feedback to design the controller. Here first a general introduction of the H_2 controller will be presented and then the H_2/LQG controller design method, which will be utilized to design the controller in this chapter, will be introduced. The governing equations for a general vibratory problem can be expressed as:

$$[M]\{\ddot{q}\}+[C]\{\dot{q}\}+[K]\{q\}=[M][E_s]\ddot{x}_g+[Q_s]\{F\}+[P_s]\{f\} \tag{7.6}$$

where $[M]$, $[C]$ and $[K]$ are the structural mass, damping and stiffness matrices, respectively. $[E_s]$, $[Q_s]$ and $[P_s]$ are the direction matrices related to base acceleration ($\ddot{x}_g$), external force vector $\{F\}$ and control force vector $\{f\}$, respectively. Parameters $\{q\}$, $\{\dot{q}\}$ and $\{\ddot{q}\}$ are the displacement, velocity and acceleration vectors, respectively. The equations of motion stated in Equation (7.6), can be transferred to the state-space form as:

$$\{\dot{x}\}=[A]\{x\}+[E]\ddot{x}_g+[Q]\{F\}+[P]\{f\} \tag{7.7}$$

where $\{x\}$ is the state vector $\{q,\dot{q}\}^T$, and

$$[A]=\begin{bmatrix}[0] & [I]\\ -[M]^{-1}[K] & -[M]^{-1}[C]\end{bmatrix},\ [E]=\begin{bmatrix}[0]\\ [E_s]\end{bmatrix},\ [Q]=\begin{bmatrix}[0]\\ [M]^{-1}[Q_s]\end{bmatrix},\ [P]=\begin{bmatrix}[0]\\ [M]^{-1}[P_s]\end{bmatrix} \tag{7.8}$$

Based on the equations of motion stated in Equation (7.7), the control problem for a general dynamic system can be expressed as:

$$\{\dot{x}\} = [A]\{x\} + [B_1]\{w\} + [B_2]\{f\} \tag{7.9a}$$

$$\{y\} = [C_1]\{x\} + [D_{11}]\{w\} + [D_{12}]\{f\} \tag{7.9b}$$

$$\{z\} = [C_2]\{x\} + [D_{21}]\{w\} + [D_{22}]\{f\} \tag{7.9c}$$

and the controller is defined as:

$$\{f\} = [G]\{z\} \tag{7.9d}$$

where $\{x\}$, $\{y\}$ and $\{z\}$ are the state-space vector, dynamic system output vector and measured vector, respectively; $\{f\}$ is the control force; $\{w\}$ represents the base excitation $\{\ddot{x}_g\}$ and/or external force $\{F\}$ depended on different loading conditions; $[G]$ is the controller and $[B_1]$, $[B_2]$, $[C_1]$, $[C_2]$, $[D_{11}]$, $[D_{12}]$, $[D_{21}]$ and $[D_{22}]$ are all the direction matrices. The H_2 controller design is essentially an optimization problem[184], in which the solution is based on two Algebraic Riccati Equation (ARE)[86, 184-186] as:

$$[A]^T[X] + [X][A] - ([X][B_2] + [N])[R]^{-1}([B_2]^T[X] + [N]^T) + [Q] = 0 \tag{7.10}$$

where $[R] = [D_{12}]^T[D_{12}]$, $N = [C_1]^T[D_{12}]$ and $[Q] = [C_1]^T[C_1]$;

$$[Y][A]^T + [A][Y] - ([Y][C_2]^T + [S])[R_e]^{-1}([C_2][Y] + [S]^T) + [Q_e] = 0 \tag{7.11}$$

where $[R_e] = [D_{21}][D_{21}]^T$, $[S] = [B_1][D_{21}]^T$ and $[Q_e] = [B_1][B_1]^T$. Assuming the solution of Equations (7.10) and (7.11), can be stated as $[X]$ and $[Y]$, respectively, then a full-state feedback $[K]$ and Kalman estimate $[L]$ can be obtained as:

$$[K] = [R]^{-1}([B_2]^T[X] + [N]^T) \text{ and } [L] = ([Y][C_2]^T + [S])[R_e]^{-1} \tag{7.12}$$

Finally the controller $[G]$ can be expressed in transfer matrix form as:

$$[G]=\left[\begin{array}{c|c}[A_k] & [B_k] \\ \hline [C_k] & [D_k]\end{array}\right] \tag{7.13}$$

where

$$[A_k]=[A]-[B_2][K]-[L][C_2]+[L][D_{22}][K],\ [B_k]=[L],\ [C_k]=-[K] \text{ and } [D_k]=[0] \tag{7.14}$$

This is the standard H_2 controller design method. It should be noted that the standard H_2 controller design approach is based on the assumption that the matrix $[D_{11}]$ is zero. A transformation method from $[D_{11}]$ non-zero to zero was proposed by Zhou *et al* [186] as:

$$[A_k]=[A]-[B_2][K]-[L][C_2]+[L][D_{22}][K]+[B_2][D_E][C_2],$$
$$[B_k]=[L]+[B_2][D_E],\ [C_k]=-[K]-[D_E][C_2] \text{ and } [D_k]=-[D_E] \tag{7.15}$$

where $[D_E]=[D_{12}]^T[D_{11}][D_{21}]^T$. From the introduction of H_2 controller design approach, one can easily find that this controller design method is very flexible. Using the same measured parameters provided in Equation (7.9c), one can easily design different controller through changing the system output equation stated in Equation (7.9b), in order to obtain suitable controller based on different design requirement. Here it should be noted the LQR controller is one of the special cases of the standard H_2 controller, in which the measure vector $\{z\}$ and dynamic system output vector $\{y\}$ are both equal to the state-space vector $\{x\}$. This means that in Equations (7.9) the matrices $[D_{11}]$, $[D_{12}]$, $[D_{21}]$ and $[D_{22}]$ are all null matrices and matrices $[C_1]$, $[C_2]$ are both identity matrices.

The standard H_2 controller does not take into account the processing and measured noises. The LQG controller considers these two kinds of noise with covariance. The H_2 controller design based on LQG framework is presented by Chiang and Safonov[187].

Dyke[94] and Spencer Jr *et al*[188] utilized H_2 controller design method based on LQG framework (H_2/LQG) to design the controller for SAMD system using hydraulic actuator, and then they studied the building structural base isolation system with MR-damper using the H_2/LQG controller[92, 94]. As mentioned above, the standard H_2 controller design consists of one full-state feedback and one Kalman estimate. In H_2/LQG controller, one basically designs the Kalman estimate using LQG framework, which considers both the processing and measured noises. Let us go back to system dynamic equations stated in Equations (7.9). The full-state feedback for H_2/LQG controller is based on Equations (7.9a) and (7.9b) as:

$$\{\dot{x}\} = [A]\{x\} + [B_2]\{f\} \tag{7.16a}$$

$$\{y\} = [C_1]\{x\} + [D_{12}]\{f\} \tag{7.16b}$$

The Kalman estimate (based on LQG framework) for H_2/LQG controller is based on Equations (7.9a) and (7.9c), as:

$$\{\dot{x}\} = [A]\{x\} + [B_1]\{w\} + [B_2]\{f\} \tag{7.17a}$$

$$\{z\} = [C_2]\{x\} + [D_{21}]\{w\} + [D_{22}]\{f\} + v_n \tag{7.17b}$$

where v_n is the measured noise.

An important issue for LQG, H_2 and H_2/LQG controller designs is the stability analysis. The standard LQR controller has at least 60^o phase margin and 6 (dB) gain margin. However there are no guaranteed stability margins for other linear quadratic controller design methods, thus the stability properties of the controller especially for the proposed H_2/LQG controller should be verified. The stability properties of controller includes: ($[A]$, $[B_2]$, $[C_2]$) should be stablizable and detectable; the controller should be stable itself and

can internally stabilize the controlled plant and also provide suitable stability margin. The ([A], [B_2], [C_2]) stabilizable and detectable properties and stability of the controller itself may be easily checked though the eigenvalue analysis of matrices [[A]-[B_2][K]], [[A]-[L][C_2]] and [A_k] stated in Equations (7.12)-(7.15). If all the eigenvalue stay in the half left plan ([[A]-[B_2][K]], [[A]-[L][C_2]] and [A_k] are Hurwitz matrices), then the ([A], [B_2], [C_2]) are stabilizable and detectable and controller is stable. Internal stability analysis can be checked using the following method[186]. The equations of motion stated in Equations (7.9), can be expressed as Linear Fractional Transformation (LFT) form as:

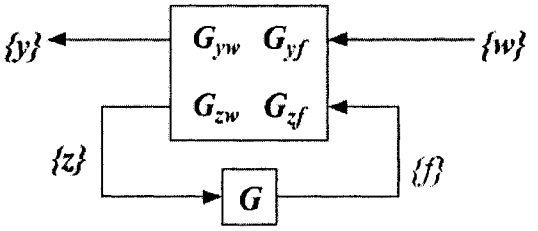

Figure 7.2 Linear Fractional Transformation (LFT) form for controller design problem.

where [G_{yw}], [G_{yf}], [G_{zw}] and [G_{zf}] are the transformation matrices from input {w} to output {y}, input {f} to output {y}, input {w} to output {z} and input {f} to output {z}, respectively. Based on Equations (7.9), all of these transformation matrices can be expressed in the transfer matrix form as:

$$[G_{yw}]=\left[\begin{array}{c|c}[A] & [B_1] \\ \hline [C_1] & [D_{11}]\end{array}\right],\ [G_{yf}]=\left[\begin{array}{c|c}[A] & [B_2] \\ \hline [C_1] & [D_{12}]\end{array}\right],[G_{zw}]=\left[\begin{array}{c|c}[A] & [B_1] \\ \hline [C_2] & [D_{21}]\end{array}\right] \text{ and}$$

$$[G_{zf}]=\left[\begin{array}{c|c}[A] & [B_2] \\ \hline [C_2] & [D_{22}]\end{array}\right] \tag{7.18}$$

and controller [G] has the same form as stated in Equation (7.13). Now let us establish the following matrix as[186]:

$$[\hat{A}]=\begin{bmatrix}[A] & [0]\\ [0] & [A_k]\end{bmatrix}+\begin{bmatrix}[B_2] & [0]\\ [0] & [B_k]\end{bmatrix}\begin{bmatrix}[I] & -[D_k]\\ -[D_{22}] & [I]\end{bmatrix}^{-1}\begin{bmatrix}[0] & [C_k]\\ [C_2] & [0]\end{bmatrix} \tag{7.19}$$

If and only if $[\hat{A}]$ is a Hurwitz matrix, the controller $[G]$ can internally stabilize the sub-plant $[G_{zf}]$ and then the controlled plant[186]. The stability margin can also be checked through the Bode diagram for the open loop transfer function as:

$$H_{open} = -[G][G_{zf}] \tag{7.20}$$

7.4 Developed Control Methodology

In Section 7.2, the inverse MR-damper model for RD-1005-3 and MR-9000 type MR-dampers and their respective calculation method has been proposed. Section 7.3 presented the H_2/LQG controller design method. Here the inverse MR-damper model will be combined with the H_2/LQG controller to present an effective vibration control strategy for SAMD system using MR-damper. The schematic and essential issues of this proposed control strategy (Controller A) is shown in Figure 7.3 and the design methodology can be summarized as:

Step 1: Following the method presented in Chapters 3 and 4, an optimal TMD system will be designed first.

Step 2: Based on the optimally designed TMD system, a SAMD system will be designed, in which the damper of optimal TMD system will be replaced by the selected MR-damper.

Step 3: The controller will be designed using H_2/LQG method presented in Section 7.3.

Step 4: The designed H_2/LQG controller is combined with the inverse MR-damper model to establish a control methodology for SAMD system using MR-damper.

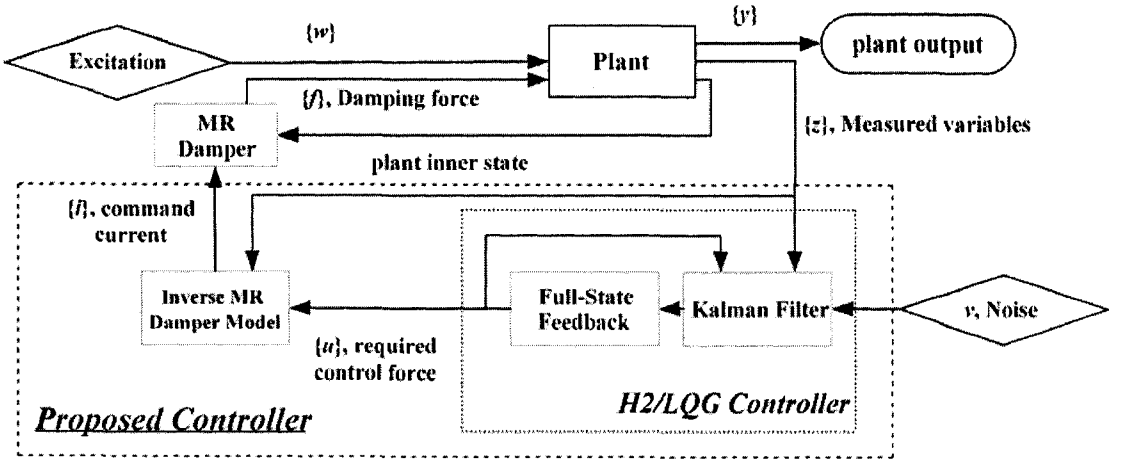

Figure 7.3 Semi-Active Mass Damper (SAMD) system using MR-damper with the proposed controller (Controller A).

The Clipped-Optimal controller for MR-damper was first proposed by Dyke *et al*[92] for the base isolation structure, and then many researchers utilized the same method or its modifications. Here the essential issues of the Clipped-Optimal controller[92] will also be utilized in the SAMD design, as illustrated in Figure 7.4, and also named as Clipped-Optimal controller (Controller B).

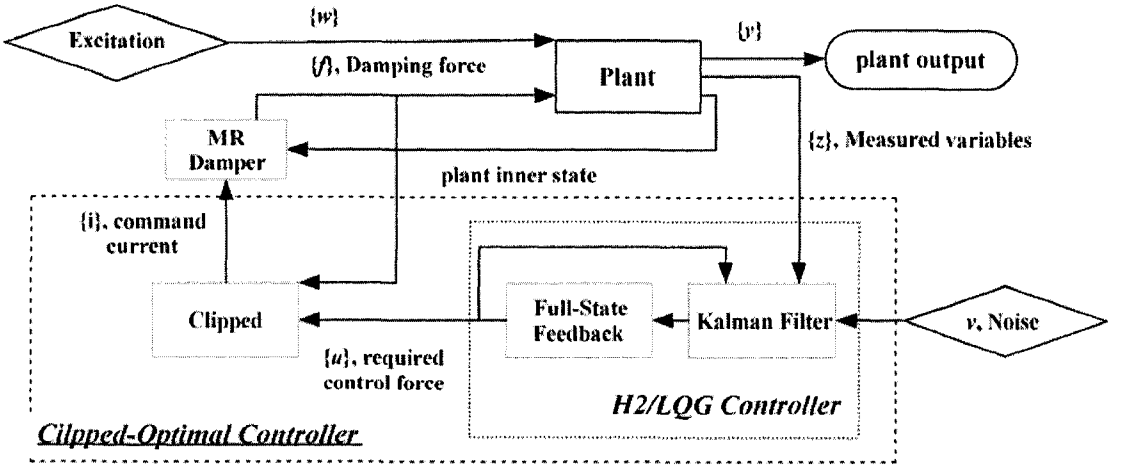

Figure 7.4 Semi-Active Mass Damper (SAMD) system using MR-damper with Clipped-Optimal controller (Controller B).

In Figure 7.4, the "Clipped" is based on the following mathematical method as[92]:

$$i = i_{\max} H\{(u - f)f\} \tag{7.21}$$

where i_{max} is the MR-damper's maximum working current, which is equal to 1 (A) in this dissertation. $H\{.\}$ is the Heaviside step function.

In this dissertation, we also combined the proposed controller shown in Figure 7.3 with Clipped-Optimal controller and named it as Inverse-Clipped-Optimal controller (Controller C), as shown in Figure 7.5.

The vibration suppression performance of the three control methodologies discussed above will be studied and compared through numerical examples. Two kinds of numerical examples have been provided. In Section 7.5, a three floors building model will be investigated and RD-1005-3 type MR-damper will be utilized in the SAMD design. The beam-type structures' SAMD system using MR-9000 type damper will be presented in the Section 7.6.

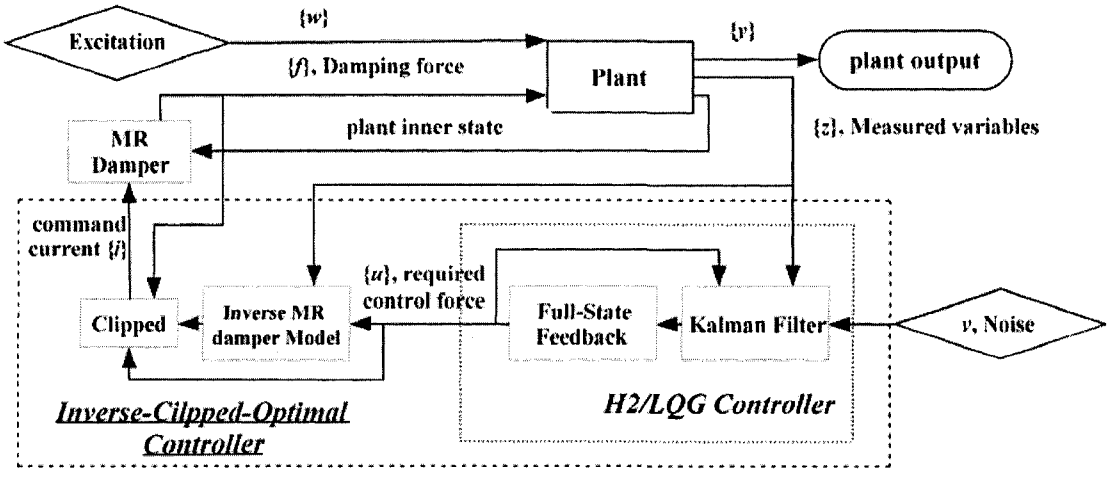

Figure 7.5 Semi-Active Mass Damper (SAMD) system using MR-damper with Inverse-Clipped-Optimal controller (Controller C).

As to illustrate the performance of the proposed control methodologies for SAMD system using MR-damper, one should compare the vibration suppression performances for uncontrolled structure; structure with optimal TMD; structure with SAMD using MR-damper under MR-damper's "fail-safe" condition; structure with SAMD using MR-damper with the proposed controller designs and also structure with AMD. Therefore, in the numerical examples, all the vibration suppression methodologies mentioned above will be investigated.

7.5 Numerical Example 1—Building-Type Structures

A three-floor building model subjected to base excitation, as shown in Figure 7.6, will be utilized to clarify the validity of the proposed SAMD design.

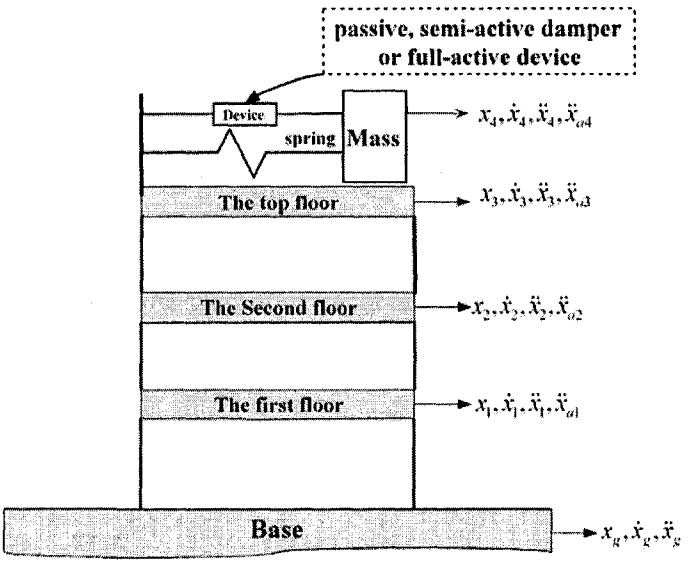

Figure 7.6 Three-floor building model for TMD, AMD and SAMD design.

In Figure 7.6, $\ddot{x}_{a,}$ presents the absolute acceleration and x, $\dot{x}$ and $\ddot{x}$ are the relative (relative to the base) displacement, velocity and acceleration, respectively. The building model with two set of model parameters will be investigated in this section. The

parameters of the Building model 1 (Section 7.5.1) are taken from Dyke *et al*[92, 94], and the Building model 2 (Section 7.5.2) is utilized to clarify robustness property of the proposed control methods.

7.5.1 Building model 1

In this section, the parameters for the three-floor building model shown in Figure 7.6 are taken from Dyke *et al*[92, 94] and the equations of motion for this building model under base excitation can be described using Equation (7.6), in which the displacement vector $\{x\}$, velocity vector $\{\dot{x}\}$ and accelerator vector $\{\ddot{x}\}$ are all measured relative to the base and

$$[M]=\begin{bmatrix}98.3 & 0 & 0\\ 0 & 98.3 & 0\\ 0 & 0 & 98.3\end{bmatrix}(Kg),\ [C]=\begin{bmatrix}175 & -50 & 0\\ -50 & 100 & -50\\ 0 & -50 & 50\end{bmatrix}(Ns/m),$$
$$[K]=\begin{bmatrix}12 & -6.84 & 0\\ -6.84 & 13.7 & -6.84\\ 0 & -6.84 & 6.84\end{bmatrix}10^5(N/m),\ [E_s]=-\begin{bmatrix}1\\1\\1\end{bmatrix},\ \{F\}=0 \text{ and } \{f\}=0 \tag{7.22}$$

7.5.1.1 *TMD, AMD and SAMD design approaches*

The equations of motion of structure with an attached TMD in the top floor under base excitation can also be expressed as the form stated in Equation (7.6), by defining:

$$[M]=\begin{bmatrix}98.3 & 0 & 0 & 0\\ 0 & 98.3 & 0 & 0\\ 0 & 0 & 98.3 & 0\\ 0 & 0 & 0 & m\end{bmatrix}(Kg),\ [C]=\begin{bmatrix}175 & -50 & 0 & 0\\ -50 & 100 & -50 & 0\\ 0 & -50 & 50+C_{TMD} & -C_{TMD}\\ 0 & 0 & -C_{TMD} & C_{TMD}\end{bmatrix}(\frac{Ns}{m})$$
$$\{F\}=\{f\}=0,[K]=\begin{bmatrix}12 & -6.84 & 0 & 0\\ -6.84 & 13.7 & -6.84 & 0\\ 0 & -6.84 & 6.84+K_{TMD} & -K_{TMD}\\ 0 & 0 & -K_{TMD} & K_{TMD}\end{bmatrix}10^5(\frac{N}{m}),\ [E_s]=-\begin{bmatrix}1\\1\\1\\1\end{bmatrix} \tag{7.23}$$

where the mass (m) of the TMD and AMD systems is selected as 10% of the total mass of the main structure; the linear viscous damper and stiffness of TMD are represented by C_{TMD} and K_{TMD}, which are the design variables.

Transferring Equation (7.6), to the state-space form described in Equation (7.7), with the parameters defined in Equation (7.8), and then utilizing the optimization procedure provided in Chapter 3, one can easily obtain the optimal damping factor (ξ_{TMD}) and frequency ratio (f_{TMD}) defined in Equation (3.14) as 0.1903 and 0.8403, respectively. Here it should be noted that the RMS of the top floor's relative displacement (relative to the base) has been selected as the objective function, as the first vibration mode is dominant mode in this example. Subsequently, the linear viscous damper and stiffness for the optimal TMD system would be 323.3 (Ns/m) and 24475(N/m), respectively.

Next, the damper of the developed optimal TMD system will be replaced by an active device to establish an AMD system and the controller for the AMD system will be designed following the procedure stated in Section 7.3. The equations of motion for the controller design can also be expressed as the form stated in Equation (7.6), by defining:

$$[M]=\begin{bmatrix}98.3 & 0 & 0 & 0\\ 0 & 98.3 & 0 & 0\\ 0 & 0 & 98.3 & 0\\ 0 & 0 & 0 & 29.49\end{bmatrix}(Kg),\ [C]=\begin{bmatrix}175 & -50 & 0 & 0\\ -50 & 100 & -50 & 0\\ 0 & -50 & 50 & 0\\ 0 & 0 & 0 & 0\end{bmatrix}(\frac{Ns}{m}),\ \{F\}=0(N),$$

$$[K]=\begin{bmatrix}12 & -6.84 & 0 & 0\\ -6.84 & 13.7 & -6.84 & 0\\ 0 & -6.84 & 6.84+0.245 & -0.245\\ 0 & 0 & -0.245 & 0.245\end{bmatrix}10^5(\frac{N}{m}),[E_s]=-\begin{bmatrix}1\\1\\1\\1\end{bmatrix}\text{ and }[P_s]=\begin{bmatrix}0\\0\\1\\-1\end{bmatrix} \quad (7.24)$$

Transferring Equation (7.6) to the state-space form provided in Equations (7.9), by defining:

$$[A]=\begin{bmatrix}[0] & [I]\\ -[M]^{-1}[K] & -[M]^{-1}[C]\end{bmatrix},\ [B_1]=\begin{bmatrix}[0]\\ [E_s]\end{bmatrix},\ [B_2]=\begin{bmatrix}[0]\\ [M]^{-1}[P_s]\end{bmatrix},$$
$$[C_1]=\begin{bmatrix}-[P_1][M]^{-1}[K] & -[P_1][M]^{-1}[C]\\ 0\ 0\ 1\ 0 & 0\ 0\ 0\ 0\end{bmatrix},\ [D_{11}]=[0\ \ 0\ \ 0\ \ 0]^T,\ [D_{12}]=\begin{bmatrix}[P_1][M]^{-1}[P_s]\\ 0\end{bmatrix}, \quad (7.25)$$
$$[C_2]=\begin{bmatrix}0\ 0\ -1\ 1 & 0\ 0\ 0\ 0\\ -[P_2][M]^{-1}[K] & -[P_2][M]^{-1}[C]\end{bmatrix},\ [D_{21}]=\begin{bmatrix}0\\ 0\end{bmatrix} \text{ and } [D_{22}]=\begin{bmatrix}0\\ [P_2][M]^{-1}[P_s]\end{bmatrix}$$

where $[M]$, $[C]$, $[K]$, $[P_s]$ and $[E_s]$ have been defined in Equation (7.24). In this example, the absolute acceleration of all three floors and the relative displacement (relative to the base) of top floor are selected as the system output vector $\{y\}$ stated in Equation (7.9b). The absolute acceleration of top floor and the relative displacement (between the top floor and the attached mass) are selected as the measured vector $\{z\}$ stated in Equation (7.9c). Thus, the matrices $[P_1]$ and $[P_2]$ in Equations (7.25) can be defined as:

$$[P_1]=\begin{bmatrix}1 & 0 & 0 & 0\\ 0 & 1 & 0 & 0\\ 0 & 0 & 1 & 0\end{bmatrix} \text{ and } [P_2]=[0\ \ 0\ \ 1\ \ 0] \quad (7.26)$$

H_2/LQG method is utilized to design the controller based on the system parameters stated in Equations (7.25). A full-state feedback will be designed based on Equations. (7.10), (7.12) and (7.16) with the definitions of $[Q]=[C_1]^T[C_1]$, $[R]=3[D_{12}]^T[D_{12}]$ and $[N]=[C_1]^T[D_{12}]$. The Kalman filter will be designed based on Equations (7.11), (7.12) and (7.17) with the definitions of $[Q_e]=r[I]$, $[R_e]=[I]$ and $[S]=[0]$. Here, the autocovariance of measurement noise ($E(v_n v_n^T)=R_v[I]$) and the process noise ($E(\ddot{x}_g \ddot{x}_g^T)=R_g[I]$) are both assumed to be identically distributed and statistically independent Gaussian white noise with the ratio ($r=R_g/R_v=25$), furthermore the covariance between excitation processing and measurement noise processes is assumed to

be zero. Finally the H_2/LQG controller can be obtained using Equation (7.13) and (7.14), as matrix $[D_{11}]$ stated in Equations (7.25) is a null matrix.

The controller stability analysis based on eigenvalue analysis of $[A_k]$, as stated in Equation (7.14), the internally stabilizing analysis based on Equation (7.19), the full-state feedback $[K]$ stability analysis based on the eigenvalue analysis of matrix $[[A]-[B_2][K]]$ and the Kalman filter $[L]$ stability analysis based on the eigenvalue analysis of matrix $[[A]-[L][C_2]]$ have been conducted. All test matrices are Hurwitz matrices. The stability margin analysis, as stated in Equation (7.20), is shown in Figure 7.7.

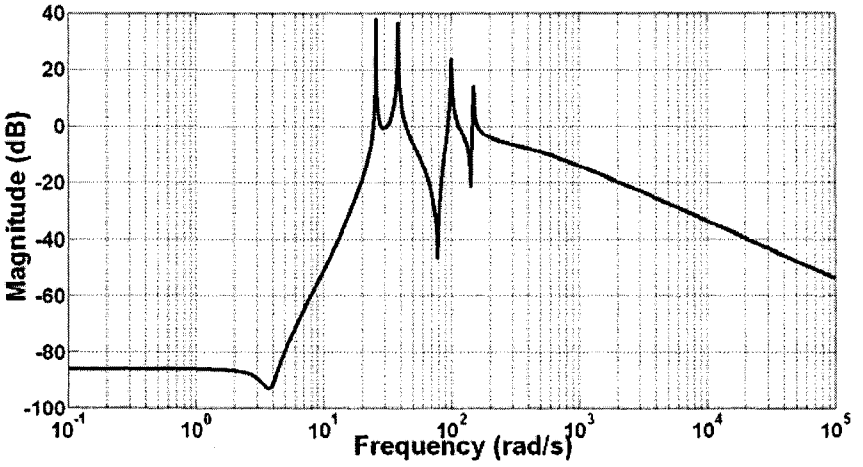

Figure 7.7 Open-loop stability margin analysis for Build model 1.

Based on experience study for this building model proposed by Dyke[94] and Spencer Jr *et al*[95], the numerical model matches the experimental data very well for excitation frequencies below 35 (*Hz*) (about 220 *rad/s*), which is after the natural frequency of the third vibration mode (148.5 *rad/s*). However, significant modeling errors occur at higher frequencies due to un-modeled dynamic properties. Herein, the controller design was considered to be acceptable for implementation if the magnitude of the open loop gain at

high frequencies (higher than 35 (*Hz*)) was less than -5 (dB)[94, 95]. Based on this, the designed H_2/LQG controller provides at least -5.2 (dB) for the frequency more than 32 (*Hz*), as illustrated in Figure 7.7, so the designed controller is considered to be acceptable.

Figure 7.8 illustrates the frequency domain response (Bode diagram) for uncontrolled structure, structure with optimal TMD and AMD system using the developed H_2/LQG controller.

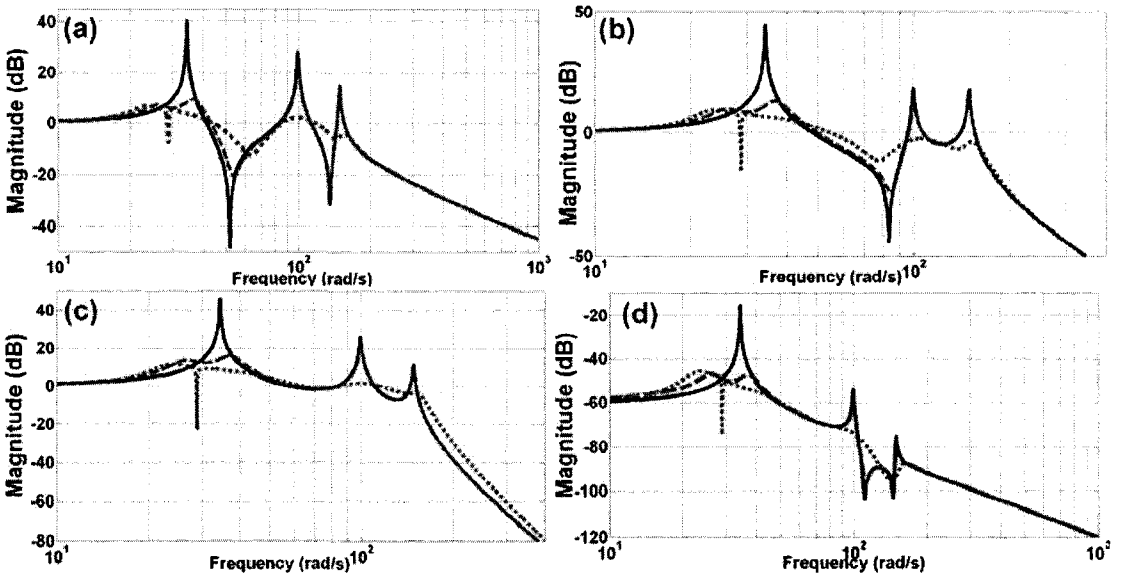

Figure 7.8 The structural frequency domain response (Bode diagram). (a) The first floor absolute acceleration. (b) The second floor absolute acceleration. (c) The top floor absolute acceleration. (d) The top floor relative displacement (relative to base). Solid, dashed (brown) and dotted (red) lines represent uncontrolled structure and structure with optimal TMD and AMD system, respectively.

Examination of the results shown in Figure 7.8 reveals that: (1) the optimal TMD system attenuates vibrations effectively around the original structural first natural frequency, which is the dominant mode in this example; (2) The AMD system not only can provide better vibration suppression performance than the optimal TMD system around its tuned

frequency but also it can effectively suppress the vibration due to higher modes (in this example the effect of AMD can provide significant attenuation up to the third natural frequency); (3) as expected after the third vibration mode no significant control force exists, and thus the response for structures with AMD system almost coincides with uncontrolled structure. As discussed in Chapter 1, the designed AMD system may be unpractical, as it is very difficult to find a suitable device which can provide the active force required by the controller. In the next part the SAMD system using MR-damper will be introduced.

Following the proposed methodology presented in Section 7.4 and summarized in Figure 7.3, the developed H_2/LQG controller has been combined with the proposed inverse MR-damper model (RD-1005-3 type MR-damper) to provide command current to MR-damper and subsequently to provide damping force to the main structure. To make the simulation close to the real application, before applying the proposed control method for the SAMD system using MR-damper, the H_2/LQG controller should be transferred to discrete-time form utilizing the z-transform method as:

$$s = 2f_z \frac{z-1}{z+1} \tag{7.27}$$

where f_z is the sampling frequency. In the simulation, the time step size is selected as 10^{-4} (s), and controller sampling frequency (measured signal sampling rate) is chosen as 1 (KHz), which can provide enough time for the controller to calculate the command current. Using this sampling frequency, the H_2/LQG controller, as stated in Equation (7.13), can be transferred to the discrete-time form as:

$$\{x(KT+T)\} = [A_d]\{x(KT)\} + [B_d]\{z(KT)\}\ ;\ u(KT) = [C_d]\{x(KT)\} + [D_d]\{z(KT)\} \quad (7.28)$$

where $T=1/f_z$, and matrices $[A_d]$, $[B_d]$, $[C_d]$ and $[D_d]$ are the bilinear transformation form for matrices $[A_k]$, $[B_k]$, $[C_k]$ and $[D_k]$, as stated in Equation (7.13), respectively.

A typical uniform ($\pm 50\ m/s^2$) random signal is applied onto the structural base. Based on the properties of RD-1005-3 type MR-damper[122, 136], the MR-damper's relative displacement is limited to ±20 (*mm*), and the maximum damping force is limited to ±2700 (*N*). The structural response comparison in time domain between structure with the SAMD system using MR-damper utilizing Controller A illustrated in Figure 7.3 and uncontrolled structure; structure with the optimal TMD and AMD using H_2/LQG controller are illustrated in Figures 7.9-7.11, respectively. Table 7.2 summarized the RMS of response for these different cases.

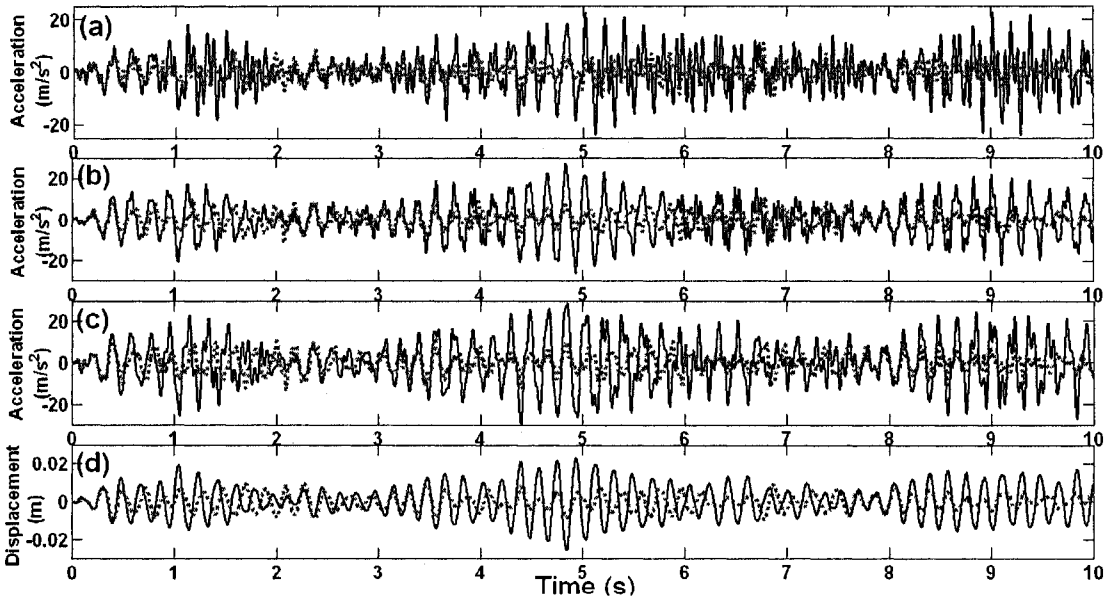

Figure 7.9 Structural response comparison. (a) The first floor absolute acceleration. (b) The second floor absolute acceleration. (c) The top floor absolute acceleration. (d) The top floor relative (relative to base) displacement. Solid and dotted (red) lines represent uncontrolled structure and structure with SAMD using MR-damper with Controller A, respectively.

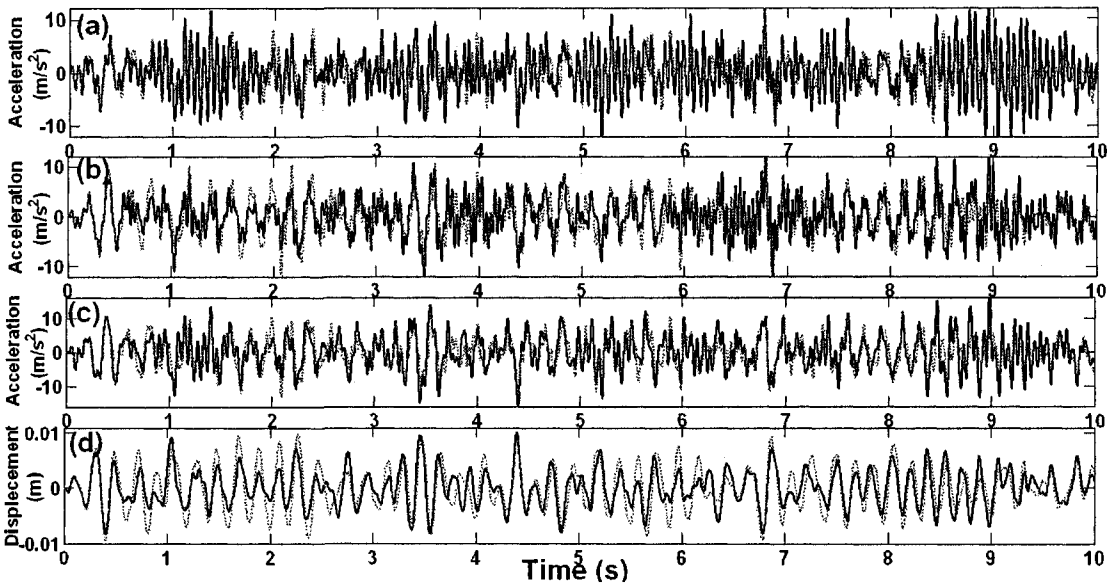

Figure 7.10 Structural response comparison. (a) The first floor absolute acceleration. (b) The second floor absolute acceleration. (c) The top floor absolute acceleration. (d) The top floor relative (relative to base) displacement. Solid and dotted (red) lines represent structure with optimal TMD and SAMD using MR-damper with Controller A, respectively.

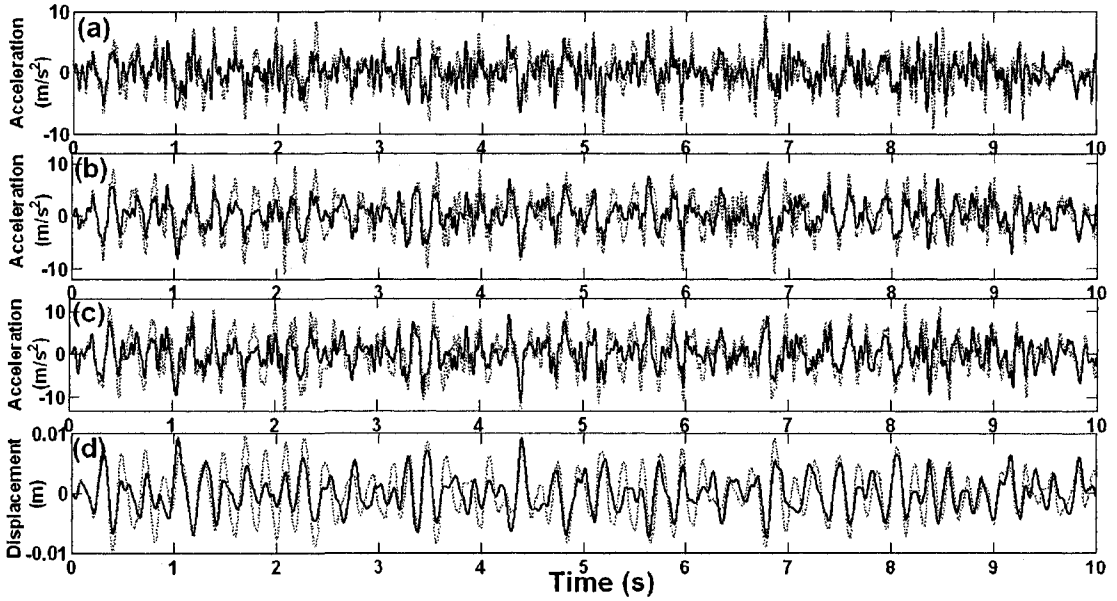

Figure 7.11 Structural response comparison. (a) The first floor absolute acceleration. (b) The second floor absolute acceleration. (c) The top floor absolute acceleration. (d) The top floor relative (relative to base) displacement. Solid and dotted (red) lines represent structure with AMD and SAMD using MR-damper with Controller A, respectively.

From Figures 7.9–7.11 and Table 7.2, one can find that: (1) the optimal TMD system can decrease the RMS about 42.2%, 56.5%, 52.47% and 61.63% for the first, second and top

floors' absolute acceleration responses and the top floor's relative displacement response, respectively, compared with uncontrolled structure; (2) compared with the optimal TMD system, the SAMD system decreases the RMS about 30.2%, 6.77%, and 13.92% for the first, second and top floors' absolute acceleration responses, respectively; (3) the AMD system provide the best vibration suppression effectiveness. Compared with the optimal TMD system, the AMD decreases the RMS about 47.62%, 33.47%, and 38.33% for the first, second and top floors' absolute acceleration responses, respectively; (4) the vibration suppression performance of the SAMD system with MR-damper using Controller A can match those of AMD well. This issue can also be realized through Figure 7.12, from which one can find that the MR-damper with Controller A can provide the damping force $\{f\}$ very close to the H_2/LQG controller requiring control force $\{u\}$.

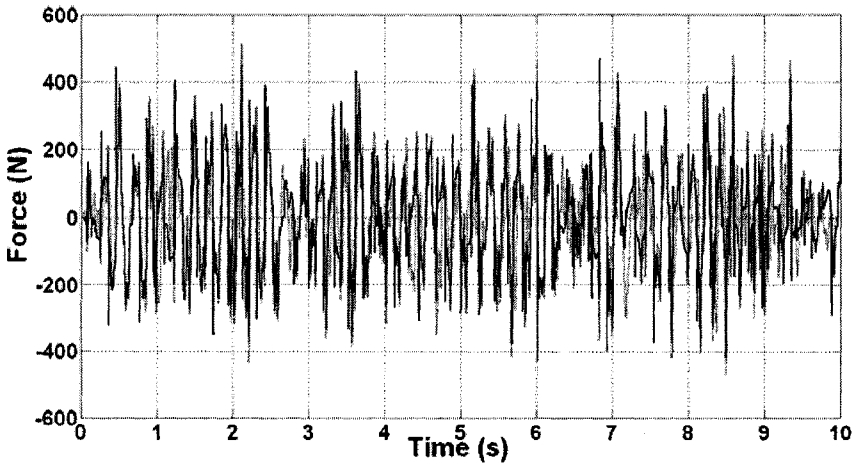

Figure 7.12 H_2/LQG controller command control force ($\{u\}$) and MR-damper damping force ($\{f\}$). Solid and dotted (red) lines represent $\{u\}$ and $\{f\}$, respectively.

7.5.1.2 SAMD using MR-damper in its "fail-safe" condition

MR-damper can provide fail-safe protection, meaning that if the controller is failed, the MR-damper can still act as a passive damper. In this example, two cases will be

considered as the MR-damper's fail-safe conditions: "*passive-off*" means the command current of MR-damper is hold as 0 (*A*); "*passive-on*" represents the case when the command current is hold as its maximum value, which is 1 (*A*) in this example. Utilizing the same random signal and discrete methodology as those presented in above section, the simulation results for the structural responses have been obtained and shown in Figures 7.13 and 7.14, which compare the structural response for SAMD with MR-damper using Controller A and MR-damper's "*passive-off*" and "*passive-on*" condition, respectively.

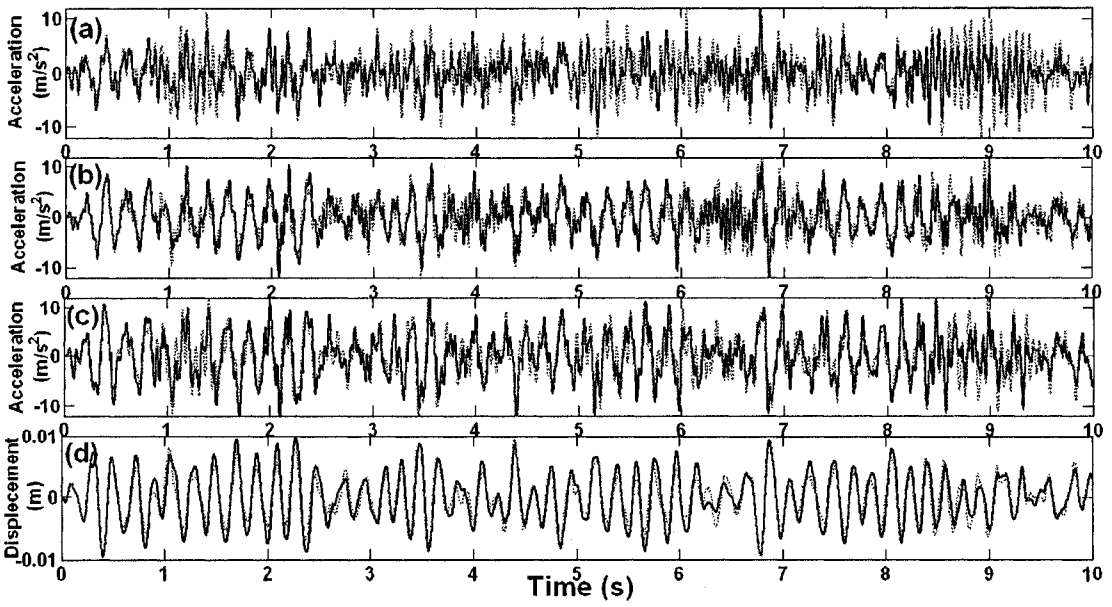

Figure 7.13 Structural response comparison. (a) The first floor absolute acceleration. (b) The second floor absolute acceleration. (c) The top floor absolute acceleration. (d) The top floor relative (to base) displacement. Solid and dotted (red) lines represent structure with SAMD using MR-damper with Controller A and MR-damper's "*passive-off*" condition, respectively.

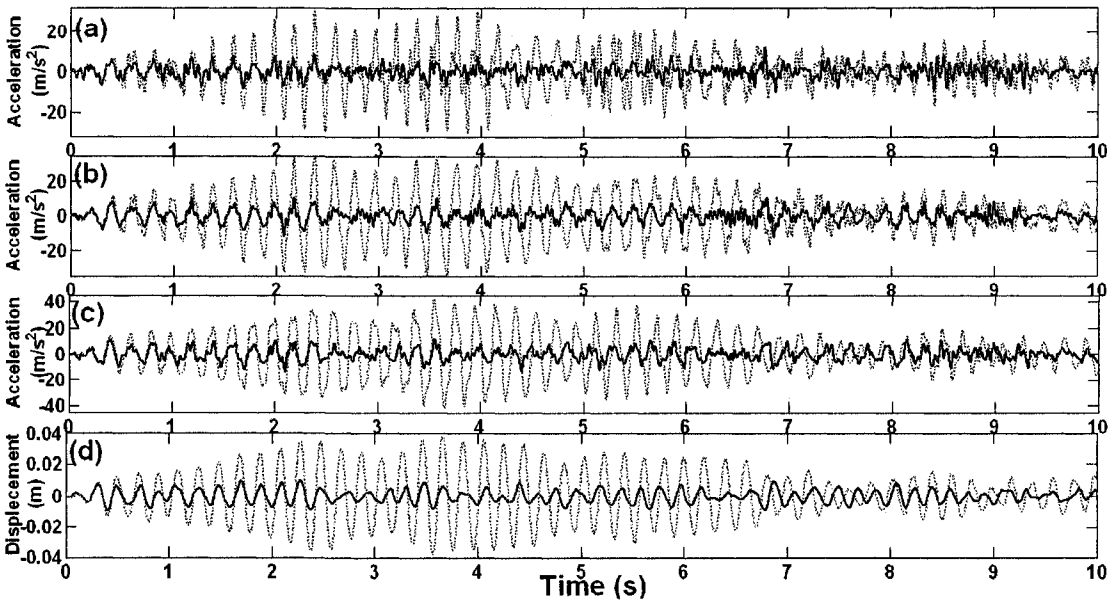

Figure 7.14 Structural response comparison. (a) The first floor absolute acceleration. (b) The second floor absolute acceleration. (c) The top floor absolute acceleration. (d) The top floor relative (to base) displacement. Solid and dotted (red) lines represent structure with SAMD using MR-damper with Controller A and MR-damper's *"passive-on"* condition, respectively.

From Figures 7.13 and 7.14, one can realize that MR-damper exactly provides the fail-safe protection performance for *"passive-off"* condition in this example, and also the *"passive-on"* case can not suppress the structural vibration effectively compared with uncontrolled structure. This is mainly due to the fact that the RD-1005-3 type MR-damper provides too much equivalent viscous damping in *"passive-on"* condition with respect to the selected mass of the SAMD system. To clarify this issue one should analysis the dynamic property of MR-damper model as listed in Equations (7.1)-(7.3) and Table 7.1. It can be found that when the command current is set to zero, MR-damper provides the minimum viscous damping coefficient about 1100 (*Ns/m*). Compared with the viscous damping coefficient in the optimal TMD system, which is 323.3 (*Ns/m*), the minimum damping coefficient provided by the selected MR-damper is too strong to

suppress vibration effectively. This property can also be found from Figure 7.15, from which one can realize that the selected MR-damper almost dose not move in the "*passive-on*" condition and the relative displacement of MR-damper with Controller A shown in Figure 7.3 are almost the same as those in MR-damper's "*passive-off*" condition.

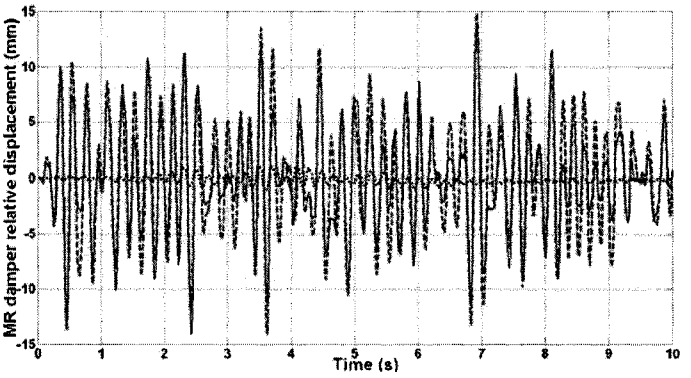

Figure 7.15 MR-damper relative displacement for different cases. Solid, dashed (red) and dotted lines represent MR-damper using Controller A, MR-damper's "*passive-off*" and "*passive-on*" condition, respectively.

In this study RD-1005-3 type MR-damper is utilized as the semi-active device for the SAMD system, thus selecting the suitable mass for the designed SAMD system related to this special type of MR-damper becomes very important. Generally the mass of the TMD or SAMD systems should not be more than 10% of the total mass of main structure; otherwise the TMD or SAMD systems will significantly change the main structural property. However, small mass will make RD-1005-3 type MR-damper become too strong to allow the mass moving freely to dissipate energy. Basically the selected mass should make the damping coefficient of the optimally designed TMD system located around the equivalent damping coefficient that the selected MR-damper can provide. The so-called equivalent damping coefficient is respected to the "*passive-off*" and "*passive-on*" conditions of the MR-damper. Thus the SAMD system with the selected MR-damper

using Controller A can provide the best vibration suppression effectiveness, which will be illustrated in Section 7.5.2. Furthermore, based on above discussion, one can also find that the simple "*on-off*" control methodology may not be suitable for the SAMD system using MR-damper.

7.5.1.3 SAMD using MR-damper with different control methodologies

The performance of different control methodologies presented in Section 7.4 will be investigated in this section. The same uniform random signal used in previous sections is utilized to excite the structure at the base. Figure 7.16 shows the structural responses in time domain for structure with different control methodologies. It should be noted that in this example the structural response using MR-damper with Controllers A and C are very close. Figure 17 illustrates the command current signals for these three control methodologies. Table 7.2 also summarized the RMS of response for different cases.

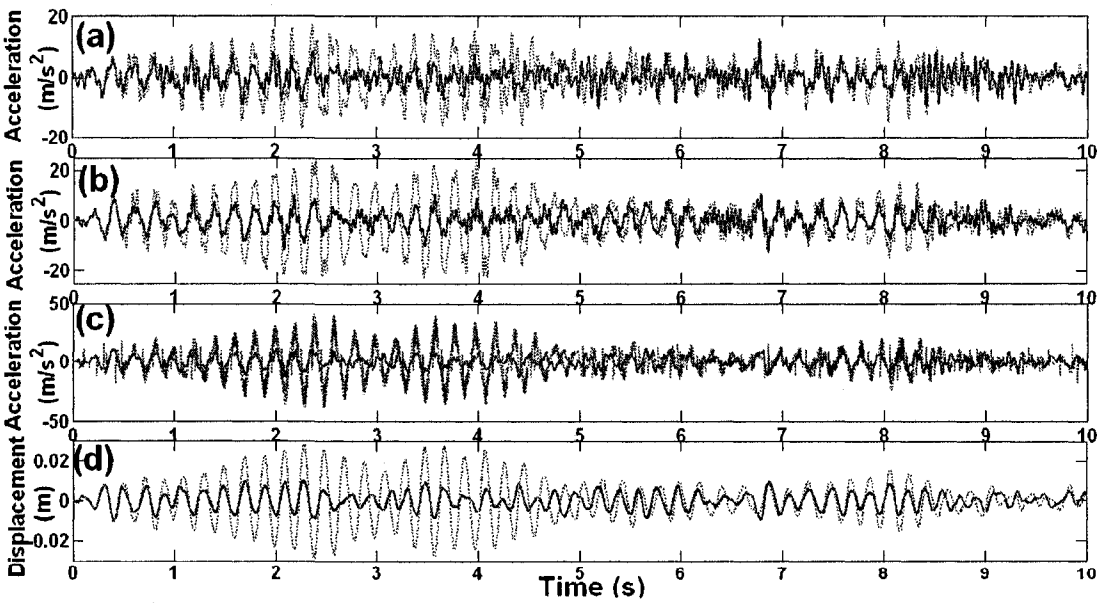

Figure 7.16 Structural response comparison. (a) The first floor absolute acceleration. (b) The second floor absolute acceleration. (c) The top floor absolute acceleration. (d) The top floor relative (relative to base) displacement. Solid, dotted(blue) and dashed (red) lines represent SAMD Structure using MR-damper with Controllers A, B and C, respectively. Note: Solid and dashed (red) lines are very close.

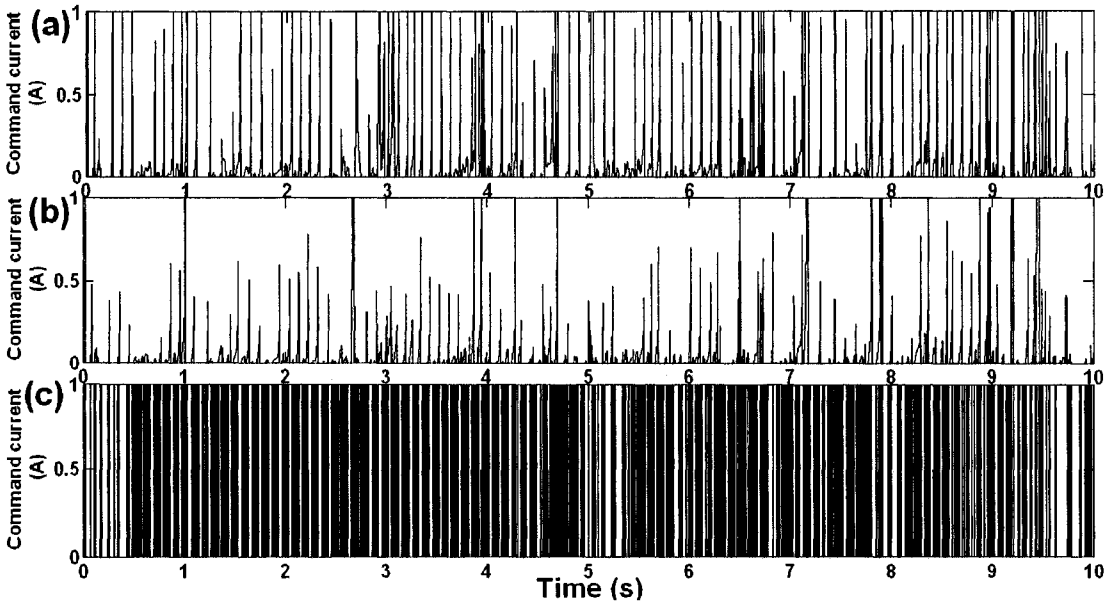

Figure 7.17 Command current comparison: (a) SAMD Structure with Controller A. (b) SAMD Structure with Controller C. (c) SAMD Structure with Controller B.

From Figures 7.16 and 7.17 and also Table 7.2, one can easily realize that: (1) the Clipped-Optimal controller (Controller B) illustrated in Figure 7.4 can not provide effective vibration suppression performance in this example; (2) the proposed Inverse-Clipped-Optimal controller (Controller C) illustrated in Figure 7.5 can improve the vibration suppression performance compared with the proposed controller (Controller A) illustrated in Figure 7.3 about 4%. However this small performance improvement is associated with the cost of an extra force sensor; (3) the MR-damper's command current using Controller B oscillates between 0 and 1 in a very high frequency, which subsequently causes the MR-damper's magnetic field to be changed in high frequency which is not practical for the MR-damper devices; (4) the MR-damper command current using Controllers A and C, is much smoother than that for Controller B, thus it would be more practical in real application. Based on the above discussion, it can be concluded that

the Controller A, as illustrated in Figure 7.3, and Controller C, as illustrated in Figure 7.5, are both acceptable controller designs in this example.

7.5.1.4 Summary of the results for Building model 1

Table 7.2 summarizes the RMS of structural responses for the simulation results presented in the above sections. Therefore, one can clearly verify the conclusion made in above sections from Table 7.2.

Table 7.2 RMS of response for different cases. Case A: *Uncontrolled structure.* Case B: *Structure with optimal TMD.* Case C: *Structure with SAMD under MR-damper's "passive-off" condition.* Case D: *Structure with SAMD under MR-damper's "passive-on" condition.* Case E: *Structure with SAMD using Controller A.* Case F: *Structure with SAMD using Controller B.* Case G: *Structure with SAMD using Controller C.* Case H: *Structure with AMD using developed H_∞/LQG controller.*

Control Strategies	1^{st} floor absolute acceleration (m/s^2)	2^{nd} floor absolute acceleration (m/s^2)	Top floor absolute acceleration (m/s^2)	Top floor relative displacement (mm)
Case A	7.3148	8.8649	10.9402	8.6
Case B	4.2268	3.8567	5.1999	3.3
Case C	3.6669	3.5943	4.4800	3.41
Case D	9.1772	12.9676	16.1391	15.71
Case E	2.9505	3.5957	4.4760	4.0
Case F	5.6345	8.3643	10.9801	10.1854
Case G	2.8275	3.3963	4.2459	3.8049
Case H	2.2141	2.5658	3.2070	3.0

7.5.2 Building model 2

In the previous example, we have shown that as the minimum damping coefficient of RD-1005-3 type MR-damper is too strong for the given mass of the designed SAMD

system, the vibration suppression effectiveness for SAMD with MR-damper using Controller A and the MR-damper's "*passive-off*" condition is almost the same and also the MR-damper's "*passive-on*" condition can not suppress structural vibration effectively. This example is presented to demonstrate those issues and also test the robustness property of the Controllers A and C. In this example the mass of the building model will be increased 10 times than that in Building model 1 (Section 7.5.1). The mass of TMD and AMD systems is still selected as the 10% of the total mass of building. Subsequently, it would be also 10 times of that in the previous example.

7.5.2.1 TMD, AMD and SAMD design approaches

Following exactly the same procedures presented in Section 7.5.1, an optimal TMD system has been designed for Building model 2. The optimal TMD parameters for the spring stiffness and viscous damping coefficient are 24585 (*N/m*) and 1031.1 (*Ns/m*), respectively. One can find that the viscous damping coefficient for this designed optimal TMD is now closed to the viscous damping coefficient (1100 *Ns/m*) at the "*passive-off*" condition for RD-1005-type MR-damper. The H_2/LQG controller has been designed following the same procedure and definitions presented in Section 7.5.1, and it should be noted that in this example the parameter $[R]$, which was utilized to design the full-state feedback $[K]$, is defined as $[R] = 2[D_{12}]^T[D_{12}]$. Stability analysis has been performed and all of the test matrices are Hurwitz matrices. Figure 7.18 provides the open-loop stability margin analysis.

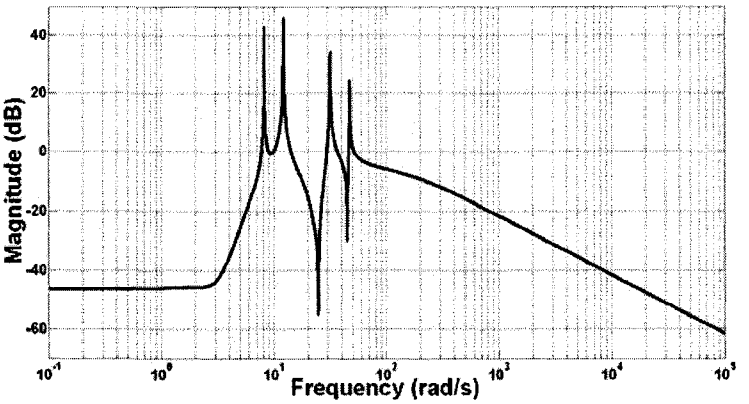

Figure 7.18 Open-loop stability margin analysis for Building model 2.

Based on the same comment provided in Building model 1 (Section 7.5.1), one can find that the design controller is acceptable for implementation, since after the third natural frequency (47 *rad/s*), the magnitude of the open loop gain was less than -5 (dB)[94,95]. Figure 7.19 illustrates the frequency domain response for uncontrolled structure, structure with the optimal TMD and AMD with the developed H_2/LQG controller.

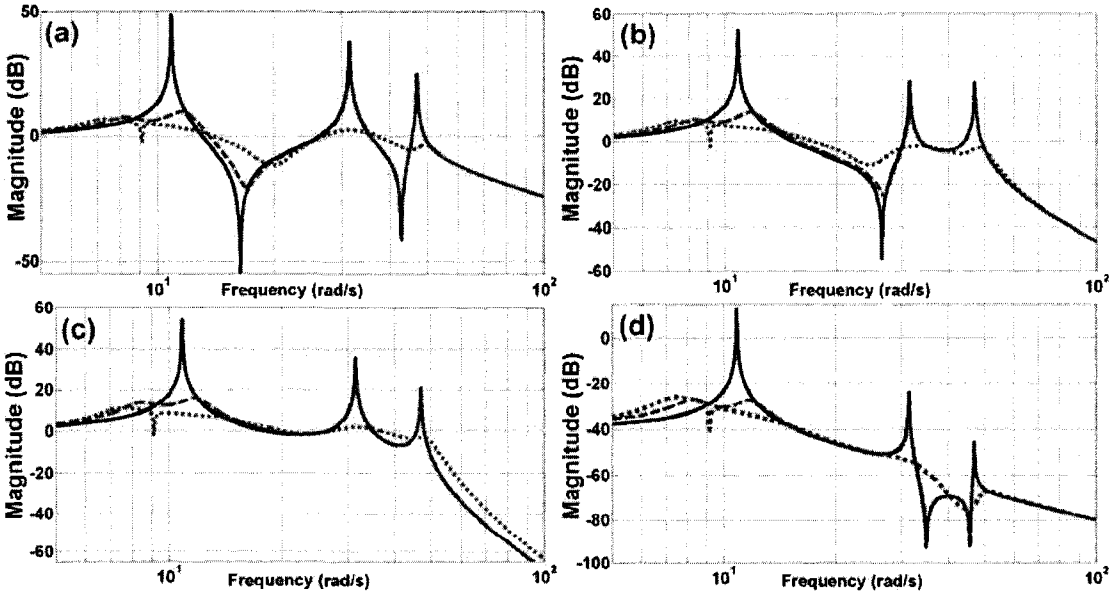

Figure 7.19 The structural frequency response/base excitation. (a) The first floor absolute acceleration. (b) The second floor absolute acceleration. (c) The top floor absolute acceleration. (d) The top floor relative displacement (relative to base). Solid, dashed (brown) and dotted (red) lines represent uncontrolled structure and structure with optimal TMD and AMD system, respectively.

The same conclusion can be drawn from Figure 7.19 as those from Figure 7.8. Using the same uniform random test signal, sampling rate (1 *KHz*) and discrete method as those utilized in Section 7.5.1, the simulation results for uncontrolled structure, structure with SAMD system using MR-damper with the Controller A, optimal TMD and AMD systems are compared in Figures 7.20–7.22, respectively. Table 7.3 summarized the RMS of responses for these different cases.

From Figures 7.20–7.22 and Table 7.3, one can easily find that: (1) the optimal TMD system can decrease the RMS about 45.99%, 52.48%, 56.63% and 71.43% for the first, second and top floors' absolute acceleration responses and the top floor's relative displacement response, respectively, compared with uncontrolled structure; (2) the SAMD system also provides better vibration suppression effectiveness than the optimal TMD structure. Compared with the optimal TMD system, SAMD decreases the RMS about 53.43%, 34.75%, and 30.15% for the first, second and top floors' absolute acceleration responses, respectively; (3) the AMD system provide the best vibration suppression effectiveness. Compared with the optimal TMD system, the ideal full-active AMD decreases the RMS about 64.63%, 56.09%, and 50.16% for the first, second and top floors' absolute acceleration responses, respectively. Comparing the results with those illustrated in Figure 7.9-7.11 and Table 7.2 for Building model 1 (Section 7.5.1), one can also find that in this example, the SAMD system can provide much better vibration performance than the optimal TMD system. This is mainly due to the fact that the damping factor provided by RD-1005-3 type MR-damper is suitable for the mass of SAMD system presented in this section, which confirms again the conclusion made in Building model 1 (Section 7.5.1).

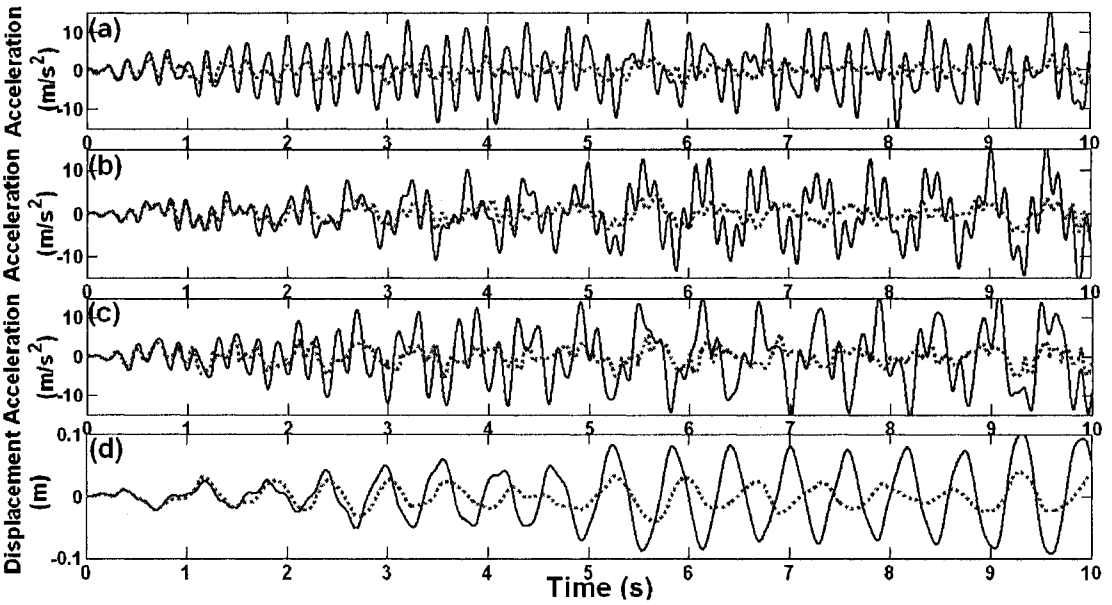

Figure 7.20 Structural response comparison. (a) The first floor absolute acceleration. (b) The second floor absolute acceleration. (c) The top floor absolute acceleration. (d) The top floor relative (relative to base) displacement. Solid and dotted (red) lines represent uncontrolled structure and structure with SAMD using MR-damper with Controller A, respectively.

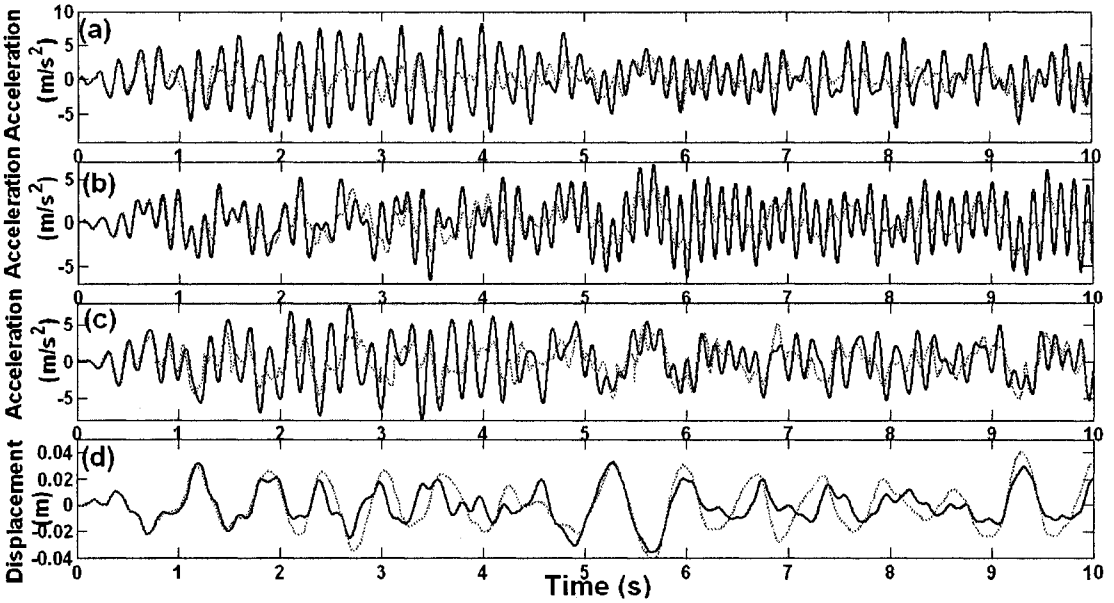

Figure 7.21 Structural response comparison. (a) The first floor absolute acceleration. (b) The second floor absolute acceleration. (c) The top floor absolute acceleration. (d) The top floor relative (relative to base) displacement. Solid and dotted (red) lines represent structure with optimal TMD and SAMD using MR-damper with Controller A, respectively.

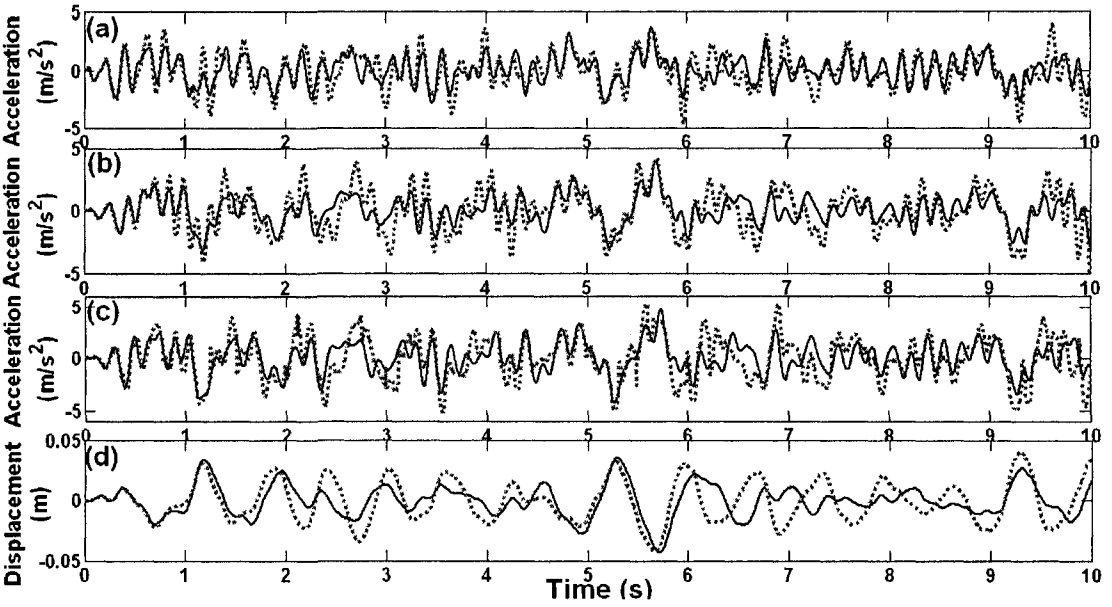

Figure 7.22 Structural response comparison. (a) The first floor absolute acceleration. (b) The second floor absolute acceleration. (c) The top floor absolute acceleration. (d) The top floor relative (relative to base) displacement. Solid and dotted (red) lines represent structure with AMD and SAMD using MR-damper with Controller A, respectively.

7.5.2.2 SAMD using MR-damper in its "fail-safe" condition

Similar to Building model 1 (Section 7.5.1), MR-damper's fail-safe condition will be investigated in this section for Building model 2 utilizing the same random excitation signal. The simulation results are shown in Figure 7.23, which compares the first, second and top floors' absolute acceleration and the top floor's relative displacement responses for SAMD with MR-damper using Controller A, "*passive-off*" and "*passive-on*" conditions. Table 7.3 summarizes the RMS of responses for different cases.

Comparing Figure 7.23 with Figures 7.13 and 7.14, one can find significant difference between these two examples. In this example, the MR-damper's "*passive-off*" and "*passive-on*" condition can both provide good "fail-safe" property and the vibration suppression performance of MR-damper using Controller A is better than the fail-safe

conditions, which confirm the robustness of Controller A and also the conclusion made in the Building model 1 (Section 7.5.1).

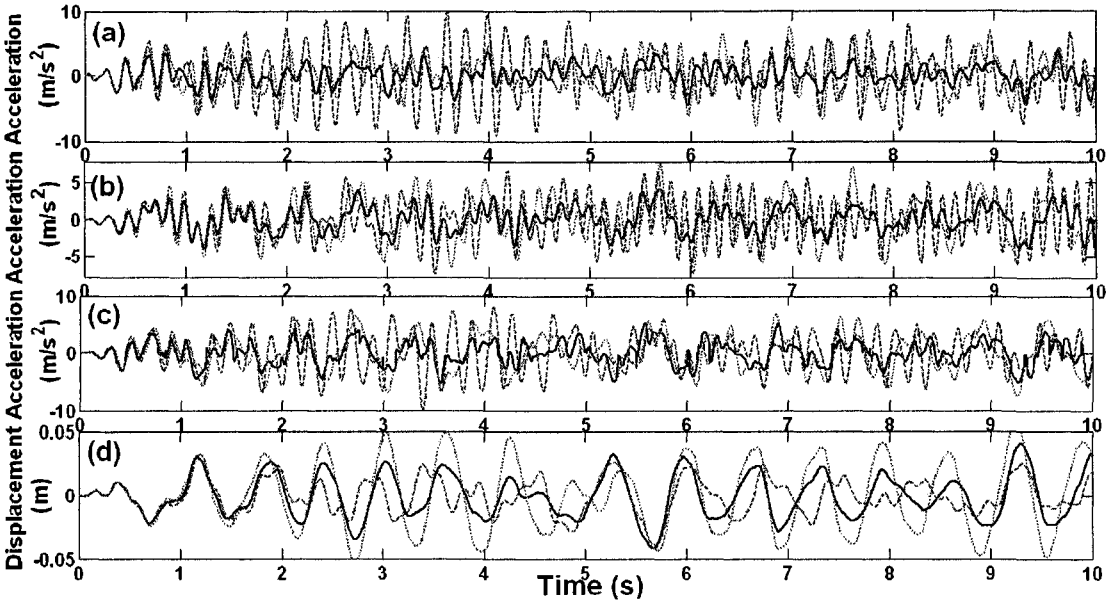

Figure 7.23 Structural response comparison. (a) The first floor absolute acceleration. (b) The second floor absolute acceleration. (c) The top floor absolute acceleration. (d) The top floor relative (relative to base) displacement. Solid, dashed (blue) and dotted (red) lines represent structure with SAMD using MR-damper with Controller A, and MR-damper's "*passive-off*" and "*passive-on*" conditions, respectively.

7.5.2.3 SAMD using MR-damper with different control methodologies

The vibration suppression performance comparisons for SAMD system using MR-damper with different control methodologies for Building model 2 are provided in Figure 7.24 and Table 7.3 summarizes the RMS of responses for each case. It can be realized that in this example three different kinds of control methodologies provide almost the same vibration suppression performance. Furthermore, comparing the results in this example with those in Building model 1, it can be found that the Controllers A and C are very robust compared with the Controller B. Moreover, examining Figure 7.24 carefully, one can also find that the top floor absolute acceleration has been a little unstable under

Controller B. The command current comparisons for these three different kinds of control methodologies are illustrated in Figure 7.25.

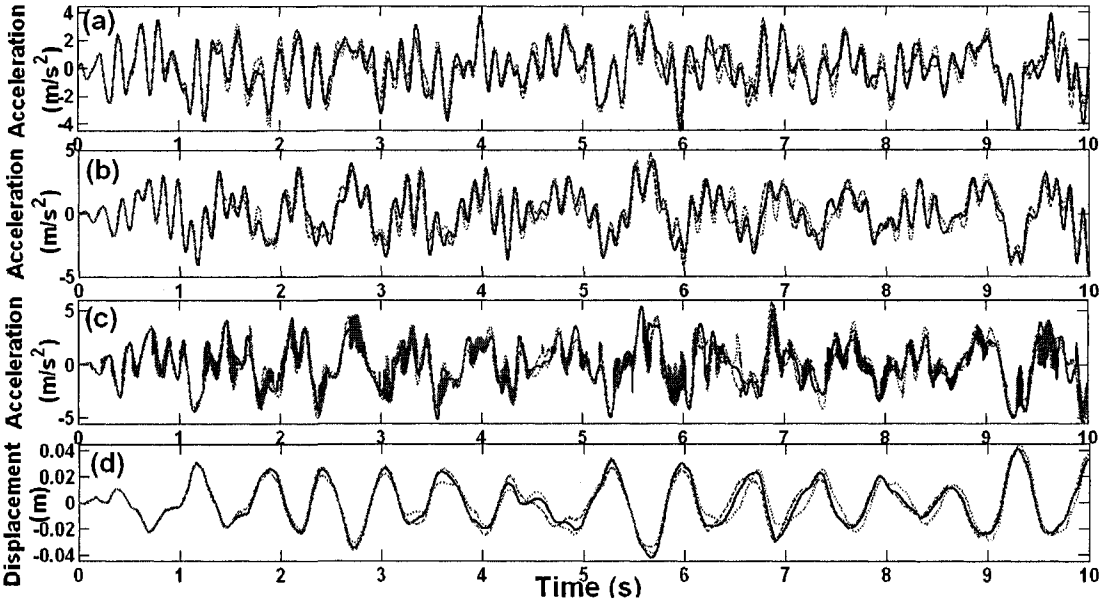

Figure 7.24 Structural response comparison. (a) The first floor absolute acceleration. (b) The second floor absolute acceleration. (c) The top floor absolute acceleration. (d) The top floor relative (relative to base) displacement. Solid, dashed (blue) and dotted (red) lines represent SAMD Structure with Controllers A, B and C, respectively.

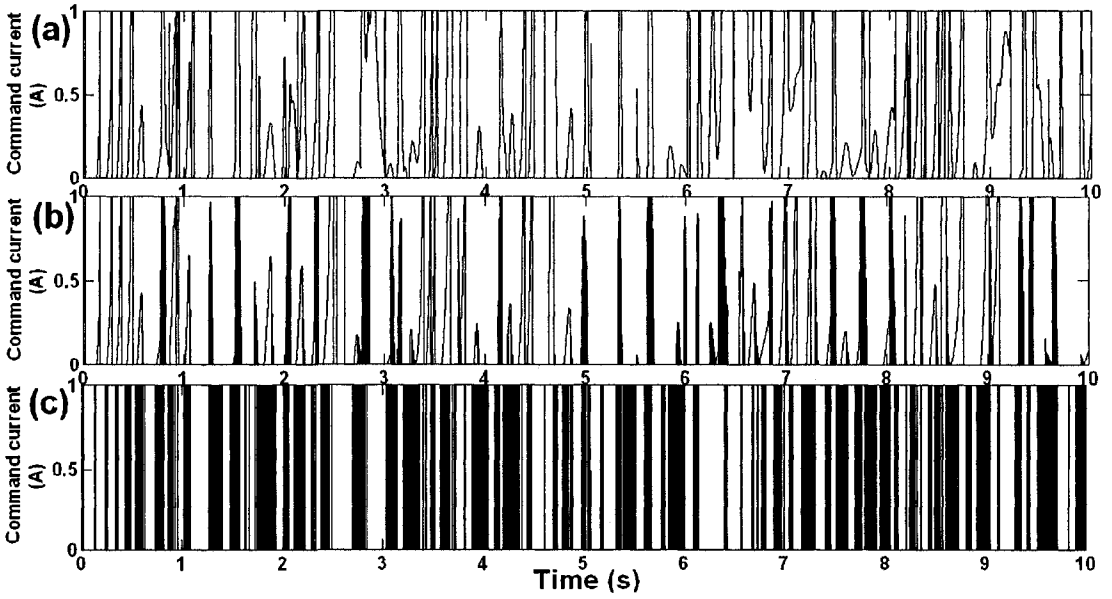

Figure 7.25 Command current comparison: (a) SAMD Structure with Controller A stated in Figure 7.3. (b) SAMD Structure with Controller C stated in Figure 7.5. (c) SAMD Structure with Controller B stated in Figure 7.4.

From Figure 7.25, one can obtain the same conclusion as those for Figure 7.17. Based on above observations, it can be realized that the Controllers A and C are the best control methodologies for the SMAD structure using MR-damper.

7.5.2.4 Summary of the results for Building model 2

Table 7.3 summarizes the RMS of structural response for the simulation results presented in the above sections for Building model 2, from which one can clearly verify the conclusions presented above.

Table 7.3 RMS of response for different cases. Case A: *Uncontrolled structure.* Case B: *Structure with optimal TMD.* Case C: *Structure with SAMD under MR-damper's "passive-off" condition.* Case D: *Structure with SAMD under MR-damper's "passive-on" condition.* Case E: *Structure with SAMD using Controller A).* Case F: *Structure with SAMD using Controller B.* Case G: *Structure with SAMD using Controller C.* Case H: *Structure with AMD using developed H_2/LQG controller.*

Control Strategies	1st floor absolute acceleration (m/s^2)	2nd floor absolute acceleration (m/s^2)	Top floor absolute acceleration (m/s^2)	Top floor relative displacement (mm)
Case A	6.0196	5.4393	6.7841	45.5
Case B	3.2511	2.5850	2.9424	13
Case C	3.9228	2.8397	3.3498	13.7
Case D	2.6096	2.7627	3.0498	26.7
Case E	1.5119	1.5812	2.0025	16.4
Case F	1.5139	1.6866	2.0554	17
Case G	1.4941	1.6344	2.0447	16.6
Case H	1.1499	1.1350	1.4665	13.2

The other advantage for using the proposed SAMD design procedures, as illustrated in Figures 7.3 and 7.5, is that all components can be assembled as a compact module. Two sensors are needed in Controller A, as stated in Figure 7.3: (1) accelerometer can be

installed on the case of MR-damper, which will provide the same measured signal as that placed in the top floor; (2) Linear Variable Displacement Transducer (LVDT) can be installed between the case and the acting rod of MR-damper, which will give us the same measured signal as the relative displacement between top floor and the attached mass. One extra force sensor is required to measure the damping force generated by MR-damper for Controller C, which can also be installed inside the MR-damper. Therefore, for different structural parameters of performance requirement, the only thing needed to be changed is the controller, which is represented by $[A_d]$, $[B_d]$, $[C_d]$ and $[D_d]$ as stated in Equation (5.28).

7.6 Numerical Example 2—Beam-Type Structures

The control methodologies for SAMD system using MR-damper has been testified through the above two building models. In this section, the vibration suppression of beam-type structures using SAMD technology with MR-damper will be presented. The Timoshenko beam with the mid-span attached TMD presented in Chapter 3 will be considered in this section. The geometrical and physical properties of the Timoshenko beam have been listed in Table 3.1.

7.6.1 TMD, AMD and SAMD design approaches

The beam studied in Chapter 3 has been assumed to have no structural damping, as the main purpose of Chapter 3 is to testify the validity of the finite element methodology for studying the Timoshenko beam with the attached TMD system. In this section, the beam's damping factor will be assumed to be 2% for all vibration modes. Therefore, following the same procedure provided in Chapter 3 and selecting the RMS of beam's

mid-span transverse response (w) as objective function and assuming mass ratio of the attached TMD to be μ=0.07, one can find that the frequency ratio (f_{TMD}) and damping factor (ξ_{TMD}) for the optimal TMD would be 0.8861 and 0.1968, respectively. Subsequently the spring stiffness (K_{TMD}) and viscous damping (C_{TMD}) of the attached optimal TMD would be 9.9611×10^7 (N/m) and 12.48×10^5(Ns/m), respectively. The validity of this set of optimal TMD's parameters will be illustrated through the frequency domain response (Bode diagram) comparison, which will be shown in Figure 7.27. Here it should be noted that the value of viscous damping of the attached optimal TMD is located inside the proposed LuGre friction model for MR-9000 type damper's working range, as illustrated in Equations (6.28)-(6.30) and Table 6.9. Therefore, the MR-9000 type damper will be selected to design the SAMD system in this example.

Next, the damper of the proposed optimal TMD system will be replaced by an active device to establish an AMD system and the controller for the AMD system will be designed following the procedure provided in Section 7.3. The equations of motion can also be expressed as the form stated in Equation (7.6), by defining:

$$[M]=\begin{bmatrix}[M_{ww}] & [0] & [0]\\ [0] & [M_{\psi\psi}] & [0]\\ [0] & [0] & M_{TMD}\end{bmatrix},\ [C]=\begin{bmatrix}[C_{ww}] & [0] & [0]\\ [0] & [0] & [0]\\ [0] & [0] & 0\end{bmatrix},\ \ddot{x}_g=0,$$

$$[K]=\begin{bmatrix}[K_{ww}]+[K_{wTMD}] & [K_{w\psi}] & -[K_{zTMD}]\\ [K_{w\psi}]^T & [K_{\psi\psi}] & [0]\\ -[K_{zTMD}]^T & [0] & K_{TMD}\end{bmatrix},\ [P_s]=\begin{Bmatrix}-\{C\_pic\}\\ 1\end{Bmatrix}\ \text{and} \tag{7.29}$$

$$\{F(t)\}=\left\{\sum_{element}\left[\int_{-1}^{1}\left([N(\eta)]f(\eta,t)\bar{J}(\eta)\right)d\eta,\ \ \{0\}_{\psi},\ \ 0\right]\right\}^T$$

where K_{TMD} is the spring stiffness of designed optimal TMD system, which is equal to 9.9611×10^7 (N/m), $\{C\_pic\}$ is the matrix to pick up the beam's mid-span values, which

can be defined as $\left\{ \sum_{element} [N(\eta_{TMD})] \right\}$, and the other parameters has been defined in Equations (3.7). Here it should be noted that the loading is applied uniformly perpendicular to the central line of beam. For simplifying expression, one can assumed the loading as unit value and thus the result obtained from $\{F(t)\}$ stated in Equation (7.29) would be equal to the direction matrix $[Q_s]$, as stated in Equation (7.7).

In Chapter 3 the beam with clamped-clamped boundary condition has been modeled using 7 Timoshenko beam elements with 4 nodes per element, thus the beam model has total of 40 degree of freedom. In fact, it is un-necessary to design a controller taking into account all of the degree of freedom. In this section the first five vibration modes of Timoshenko beam will be utilized to design the controller for the AMD system. This is due to the following facts that: (1) no matter how many numbers of elements one selected, un-modeled dynamic properties in high vibration mode exist; (2) the AMD is designed based on the optimal TMD system, which was tuned to the first vibration mode (dominant mode) in this example, obviously the effect of the AMD would be also around the first vibration mode; (3) if studying higher vibration modes is require, it is better to follow the methodology proposed in Chapter 4 to design other TMD system based on higher vibration mode and then go to the AMD design; (4) although in theory one can directly design controller for the AMD system utilizing the Timoshenko beam's finite element model, but definitely in the high frequency range the required control force will be outside of the MR-9000 type damper's working range.

Based on the above discussions, total six modes of the Timoshenko beam with the attached Tuned Mass system will be utilized to design the controller of the AMD system,

as the first mode of Timoshenko beam has been modified to two modes by the attached Tuned Mass system. Therefore, one can easily utilize the eigenvector of ($[M]^{-1}[K]$), as shown in Equation (7.29), to pick up the first six modes which will be utilize to calculate the beam nodal displacement as:

$$\{q\} = [V_e]\{e_1 \cdots e_6\}^T \tag{7.30}$$

where $[V_e]$ represents the first six eigenvectors, and e_i represents the response of the i^{th} mode. Thus, the equations of motion for the controller design can be expressed as Equations (7.7)-(7.9), by defining:

$$[A] = \begin{bmatrix} [0] & [I] \\ -[M_e]^{-1}[K_e] & -[M_e]^{-1}[C_e] \end{bmatrix},\ [B_1] = \begin{bmatrix} [0] \\ [M_e]^{-1}[V_e]^T\{Q_s\} \end{bmatrix},$$

$$[B_2] = \begin{bmatrix} [0] \\ [M_e]^{-1}[V_e]^T[P_s] \end{bmatrix}, \tag{7.31}$$

$$[C_1] = [P_1][V_e][A],\ [D_{11}] = [P_1][V_e][B_1],\ [D_{12}] = [P_1][V_e][B_2],$$

$$[C_2] = [P_2][V_e][A],\ [D_{21}] = [P_2][V_e][B_1] \text{ and } [D_{22}] = [P_2][V_e][B_2]$$

where $[M_e]=[V_e]^T[M][V_e]$, $[C_e]=[V_e]^T[C][V_e]$ and $[K_e]=[V_e]^T[K][V_e]$. In this example, the beam mid-span's acceleration and displacement are selected as the system output vector $\{y\}$, as stated in Equation (7.9b). The beam mid-span's acceleration and the relative displacement (between beam mid-span and the attached mass) are selected as the measured vector $\{z\}$, as stated in Equation (7.9c). Therefore, the directional matrices $[P_1]$ and $[P_2]$ can be defined as:

$$[P_1] = \begin{bmatrix} [\{C\_pic\} & 0] & \{0\} \\ \{0\} & [\{C\_pic\} & 0] \end{bmatrix} \text{ and } [P_2] = \begin{bmatrix} [\{C\_pic\} & -1] & \{0\} \\ \{0\} & [\{C\_pic\} & 0] \end{bmatrix} \tag{7.32}$$

H_2/LQG method is utilized to design the controller based on the system parameters stated in Equations (7.31) and (7.32). A full-state feedback will be designed based on Equations (7.10) and (7.16) with the definitions:

$$[Q]=1.5e^3[W_1C_1]^T[W_1C_1],\ [R]=5e^3[D_{12}]^T[D_{12}] \text{ and } [N]=[W_1C_1]^T[D_{12}] \tag{7.33}$$

where $[W_1]$=[5×10^3, 0; 0, 1]. Finally the full-state feedback $[K]$ defined in Equation (7.12) is equal to $[R]^{-1}([B_2]^T[X]+[N]^T)$. The Kalman filter will also be designed based on Equations (7.11) and (7.17) with the definitions:

$$[Q_e]=r[I],\ [R_e]=1e^{-10}\begin{bmatrix}0.1 & 0\\ 0 & 2000\end{bmatrix} \text{ and } [S]=[0] \tag{7.34}$$

Here, the autocovariance of measurement noise, $E(v_nv_n^T)=R_v[I]$, and the process noise, $E(ff^T)=R_g[I]$, are both assumed to be identically distributed and statistically independent Gaussian white noise with the ratio, $r=R_g/R_v=1\times10^4$, furthermore the covariance between excitation processing and measurement noise processes is assumed to be zero. Then the Kalman estimate $[L]$ defined in Equation (7.12) is equal to $[L]=([Y][C_2]^T+[S])[R_e]^{-1}$. Finally the H_2/LQG controller can be obtained using Equation (7.13) and (7.15), as in this example the matrix $[D_{11}]$ is not a null matrix.

The controller stability analysis based on eigenvalue analysis of $[A_k]$, as stated in Equation (7.14), the internally stabilizing analysis based on Equation (7.19), the full-state feedback $[K]$ stability analysis based on the eigenvalue analysis of matrix $[[A]-[B_2][K]]$ and the Kalman filter $[L]$ stability analysis based on the eigenvalue analysis of matrix $[[A]-[L][C_2]]$ have been conducted. All test matrices are Hurwitz matrices. The stability margin analysis, as stated in Equation (7.20), has been shown in Figure 7.26, which

includes the Bode diagram of open loop for design model, as stated in Equations (7.31) and that for the beam finite element model, as stated in Equation (7.29)

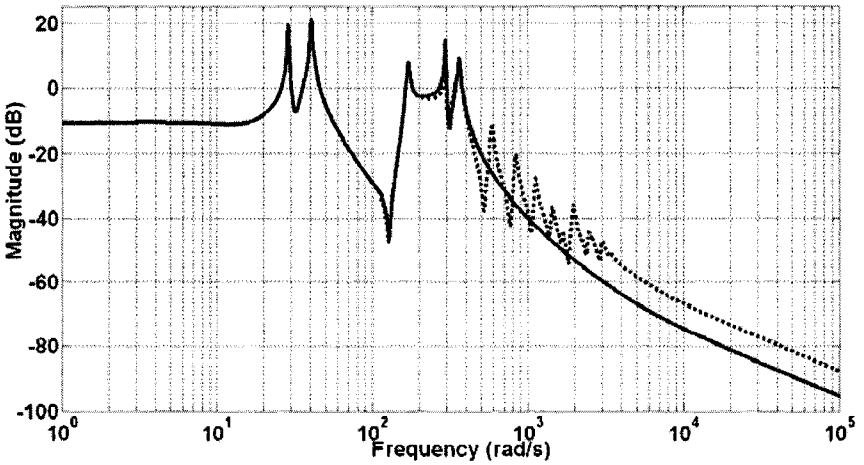

Figure 7.26 Open-loop stability margin analysis. Solid and dotted lines represent the open loop Bode diagram for design model and beam's finite element model.

From Figure 7.26, one can easily find that: (1) as expected, the open loop Bode diagram for design model is perfectly agreed with that for beam's finite element model below 400(*rad/s*), which is right after the beam's fifth natural frequency (359.64 *rad/s*), as listed in Table 3.2; (2) above 400 (*rad/s*), both design model and beam's finite element model provide at least -10 (dB) margin, which means no control force after the beam's 5^{th} vibration mode. Based on above analysis, it can be found that the proposed H_2/LQG controller is acceptable.

Figure 7.27 illustrates the frequency domain response (Bode diagram) for uncontrolled structure, structure with the optimal TMD and AMD system using the proposed H_2/LQG controller. Examination of the results reveals that: (1) the optimal TMD attenuates vibrations effectively around the original structural first natural frequency; (2) the AMD system can provide better vibration suppression performance than the optimal TMD

system around its tuned frequency as well as enlarge its vibration suppression frequency range (in this example the effect of AMD can provide significantly attenuation up to the 5th natural frequency (359.64 *rad/s*); (3) after the 5th vibration mode, no control force exists.

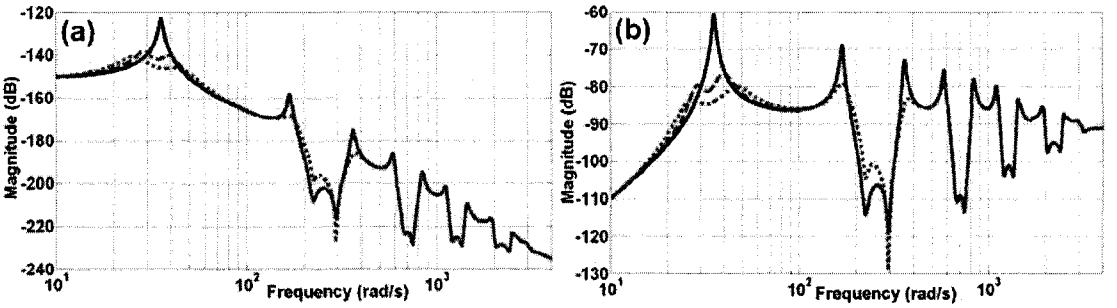

Figure 7.27 The structural frequency response/excitation. (a) The beam mid-span displacement. (b) The beam mid-span acceleration. Solid dashed (brown) and dotted (red) lines represent uncontrolled structure and structure with optimal TMD and AMD system, respectively.

As discussed before, the proposed AMD may be unpractical due to the difficulty to find a suitable device to produce the required control force. Considering this, MR-9000 type damper will be utilized to design the SAMD system. The whole procedure for the SAMD design has been summarized in Section 7.4 and illustrated in Figure 7.3. Again before applying the proposed control method for SAMD system using MR-damper, the H_2/LQG controller has been transferred to discrete-time form utilizing the *z*-transform method as those shown in Equations (7.27) and (7.28).

A typical uniform ($\pm 7\times10^5$ *N*) random signal is utilized as excitation signal for the uniformly distributed loading and a Butterworth low-pass filter was utilized to filter out the excitation for frequency higher than 500 (*rad/s*). Based on the properties of MR-9000

type damper[122, 181], the MR-damper's relative displacement is limited to ±8 (*cm*), and the maximum damping force is limited to $\pm 2\times 10^5$ (*N*). The structural response comparisons for structure with SAMD using MR-damper with Controller A, with uncontrolled structure, structure with optimal TMD and AMD using H_2/LQG controller have been illustrated in Figures 7.28-7.30, respectively. Table 7.4 also summarizes the RMS of responses for these different cases.

From Figures 7.28–7.30 and Table 7.4, one can easily find that: (1) the optimal TMD system can decrease the RMS about 64.28% and 29.84% for the beam mid-span displacement and acceleration responses, respectively, compared with uncontrolled structure; (2) the AMD system provides the best vibration suppression effectiveness. Compared with the optimal TMD system, the AMD system decreases the RMS about 20.87% and 31.27% for the beam mid-span displacement and acceleration responses, respectively.

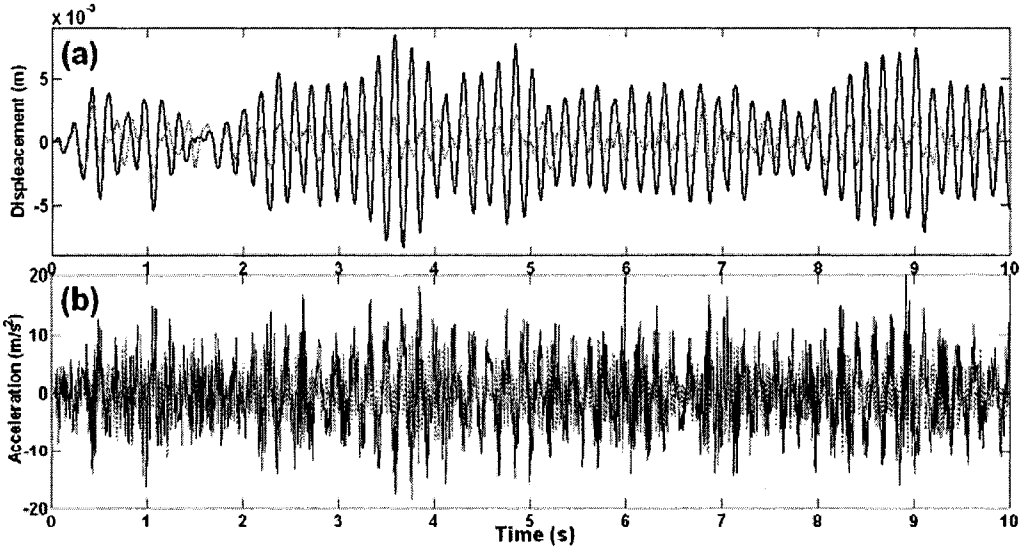

Figure 7.28 Structural response comparison. (a) The beam mid-span's displacement. (b) The beam mid-span's acceleration. Solid and dotted (red) lines represent uncontrolled structure and structure with SAMD using MR-damper with Controller A, respectively.

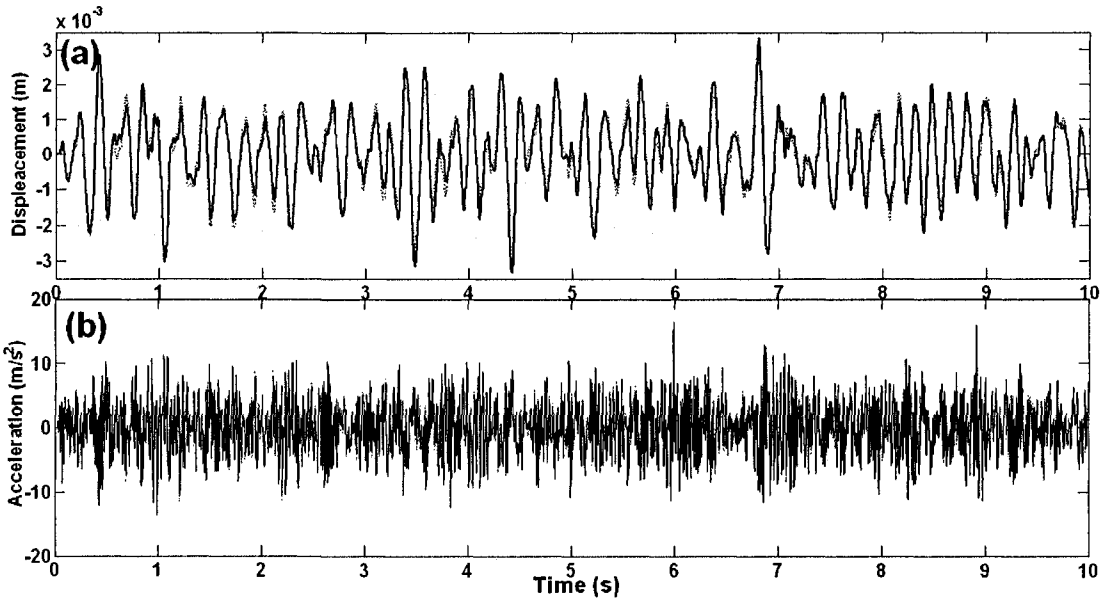

Figure 7.29 Structural response comparison. (a) The beam mid-span's displacement. (b) The beam mid-span's acceleration. Solid and dotted (red) lines represent structure with optimal TMD and SAMD using MR-damper with Controller A, respectively.

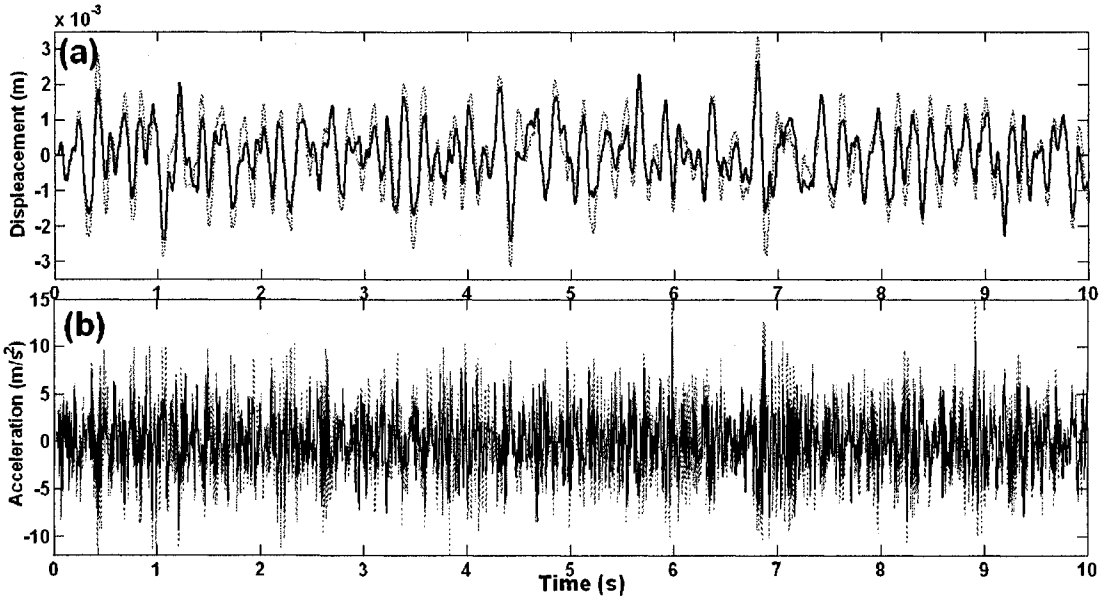

Figure 7.30 Structural response comparison. (a) The beam mid-span's displacement. (b) The beam mid-span's acceleration. Solid and dotted (red) lines represent structure with AMD and SAMD using MR-damper with Controller A, respectively.

One can also find from Figures 7.28-7.30 that the SAMD system also provides better vibration suppression effectiveness than the optimal TMD system but not significantly. This is mainly due to the fact that the H_2/LQG controller requiring control force $\{u\}$ has gone beyond the MR-damper's working range, which can be illustrated through Figure 7.31

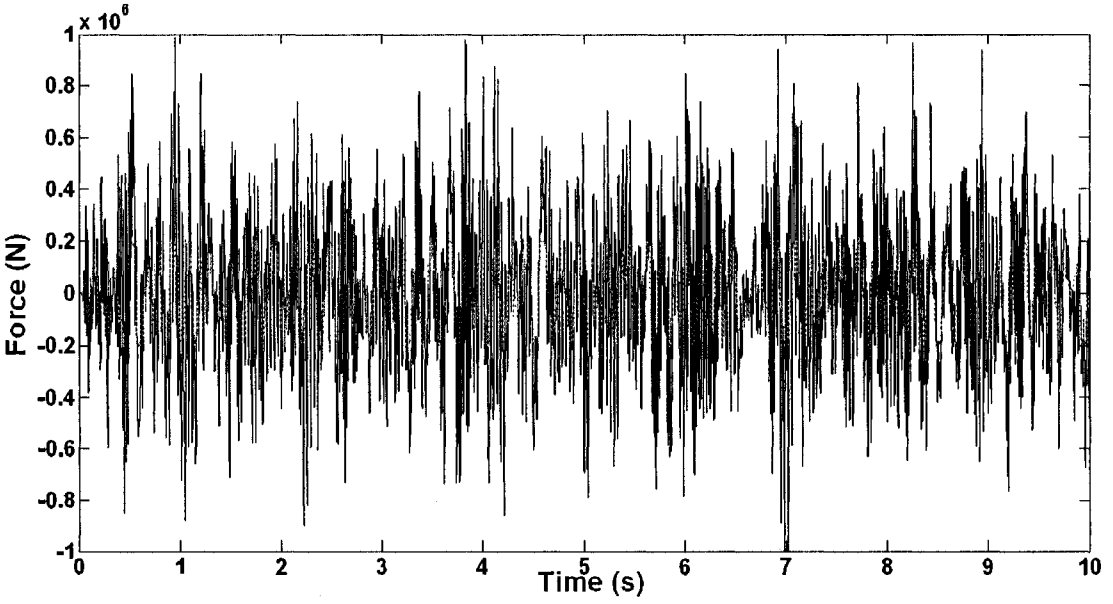

Figure 7.31 H_2/LQG controller command control force $\{u\}$ and MR-damper damping force $\{f\}$. Solid and dotted (red) lines represent $\{f\}$ and $\{u\}$, respectively.

7.6.2 SAMD using MR-damper in its "fail-safe" condition

Similar to the study presented in Section 7.5, MR-damper's fail-safe condition will be investigated in this section utilizing the same random excitation as that adopted above. The simulation results are show in Figure 7.32, which compares the beam mid-span acceleration and displacement responses for SAMD using MR-damper with Controller A and MR-damper's "*passive-off*" and "*passive-on*" condition. Table 7.4 summarizes the RMS of responses for different cases.

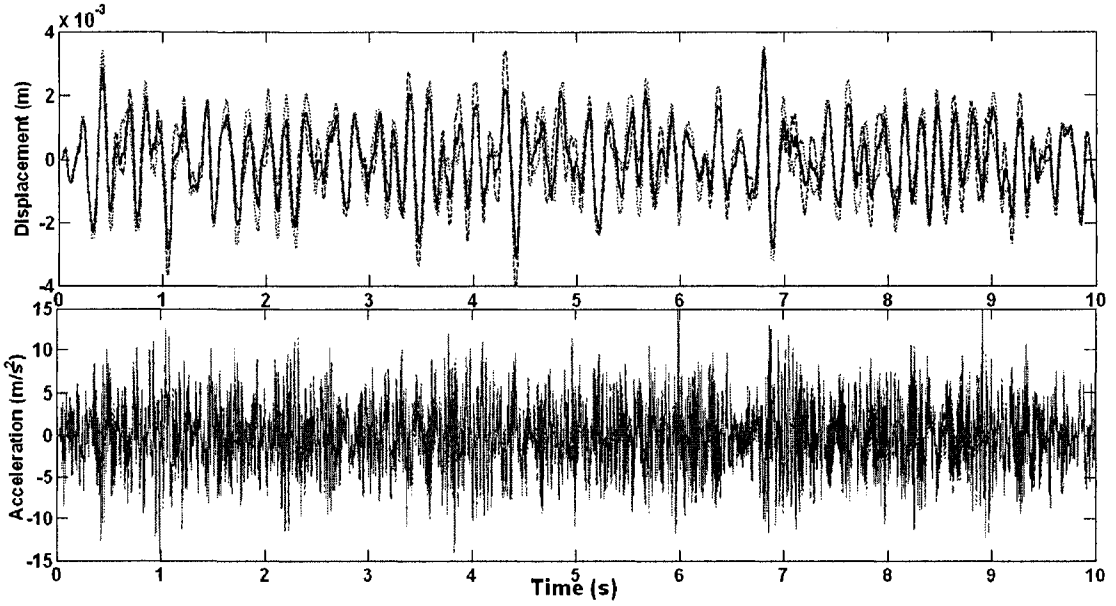

Figure 7.32 Structural response comparison. (a) The beam mid-span's displacement. (b) The beam mid-span's acceleration. Solid, dashed (blue) and dotted (red) lines represent structure with SAMD using MR-damper with Controller A and MR-damper's "*passive-off*" and "*passive-on*" conditions, respectively.

From Figure 7.32 and Table 7.4, one can find that the MR-damper's "*passive-off*" and "*passive-on*" condition can both provide good fail-safe property and the vibration suppression performance of MR-damper using Controller A, is better than the fail-safe conditions, which confirms the robustness of Controller A.

7.6.3 SAMD using MR-damper with different control methodologies

The vibration suppression performance comparisons for SAMD system with different control methodologies have been provided in Table 7.4, from which one can find that the results are very close. However Similar to the study for building models, one still can find that the command current signal, as illustrated in Figure 7.33, for the Clipped-Optimal controller (Controller B) would also oscillate between 0 and 1 in a very high

frequency, and subsequently causes the MR-damper's magnetic field to be changed with high frequency, which is not practical for the MR-damper devices, as illustrated in Figure 7.33.

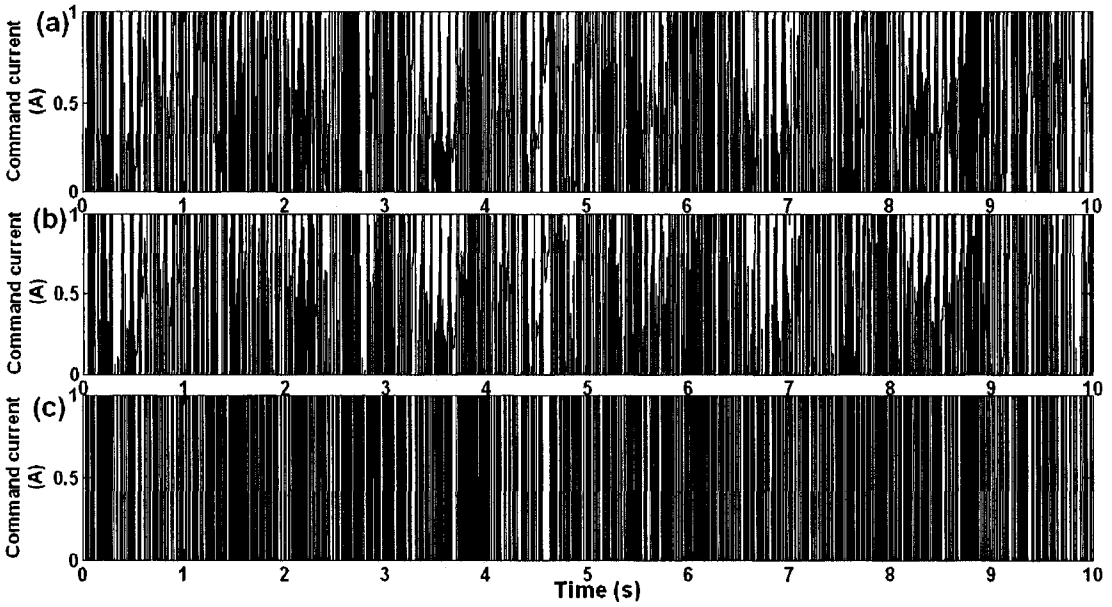

Figure 7.33 Command current comparison: (a) SAMD Structure with Controller A. (b) SAMD Structure with Controller C. (c) SAMD Structure with Controller B.

Based on the above discussion, it can be realized that the Controllers A and C are the best design control methodologies for the SMAD structure using MR-damper.

7.6.4 Summary of the results for the Beam model

Table 7.4 summarizes the RMS of structural response for the simulation results presented in above sections, from which one can clearly verify the conclusions presented above.

Compared with those presented in Section 7.5.2 for building model using RD-1005-3 type MR-damper, one can easily find that in this example the effect of the SAMD design using MR-9000 type damper is not significantly better than the optimal TMD design. The

main reason is due to the MR-damper's properties, which can be summarized in Table 7.5.

Table 7.4 RMS of response for different cases. Case A: *Uncontrolled structure.* Case B: *Structure with optimal TMD.* Case C: *Structure with SAMD under MR-damper's "passive-off" condition.* Case D: *Structure with SAMD under MR-damper's "passive-on" condition.* Case E: *Structure with SAMD using Controller A.* Case F: *Structure with SAMD using Controller B.* Case G: *Structure with SAMD using Controller C.* Case H: *Structure with AMD using H_∞/LQG controller.*

Control Strategies	Mid-span displacement (*mm*)	Mid-span Acceleration (m/s^2)
Case A	3.279	5.6492
Case B	1.2	3.8475
Case C	1.165	4.0181
Case D	1.198	3.8478
Case E	1.036	3.6434
Case F	1.039	3.6501
Case G	1.036	3.6311
Case H	0.8	2.7114

Table 7.5 Optimal TMD design and MR-damper equivalent viscous damping comparison.

Examples	Viscous damping (*Ns/m*)	Equivalent viscous damping for MR-damper (*Ns/m*)			
	Optimal TMD	RD-1005-3		MR-9000	
		Min	Max	Min	Max
Section 7.5.2	1031.1	1100	8050		
Section 7.6	12.48×10^5			10.50×10^5	15.00×10^5

It can be easily found from Table 7.5 that compared with the viscous damping for the optimal TMD design the equivalent viscous damping provided by MR-9000 type damper can only be changed in very small range. Therefore, it provides limited vibration suppression performance for SAMD design but as shown even with this narrow damping range, compared with the optimal TMD design, the SAMD design using MR-9000 type

damper can still provide superior vibration suppression performance in both its fail-safe condition and using Controllers A and C, thus one can make conclusion that the proposed SAMD design methodology is very effective for both types of MR-dampers..

7.7 Conclusions and Summary

This chapter presents a comprehensive investigation on vibration suppression using Semi-Active Mass Damper (SAMD) technology. A design approach for SAMD using MR-damper has been proposed in which the H_2/LQG controller design method is combined with the inverse MR-damper model to provide effective current control for the MR-damper input command currents. It has been shown that the proposed control method is robust as well as flexible. One can easily design different controllers depending on different system requirement based on this proposed controller design approach.

The effectiveness of proposed methodology has been compared with different conditions also with different controller design method available in published literatures through illustrated examples. It is found that SAMD using MR-damper with proposed control methodologies is robust and can provide good vibration suppression effectiveness.

CHAPTER 8

CONCLUSIONS AND RECOMMENDATIONS FOR FUTURE WORKS

8.1 Conclusions

A comprehensive framework is presented for vibration suppression of beam-type structures using the optimal Tuned Mass Damper (TMD) technology and Semi-Active Mass Damper (SAMD) technology using Magneto-Rheological (MR) fluid damper. This work improves the design procedure for vibration suppression of beam-type structures using optimally designed TMD system through the development of the finite element analysis methodology and consequently the design optimization algorithm. It also demonstrates the functionality and performance of vibration suppression using TMD technology and the validity of MR-damper utilized as the semi-active device for a designed SAMD system.

The finite element models for the general curved beam have been developed. The governing differential equations of motion for the curved beam are derived using the extended Hamilton principle and then transferred to the finite element form using proposed elements. The Gauss Quadrate technique and the curvilinear integral applied on the central line of curvilinear for curved beam are used to evaluate the required matrices numerically. A '4-node' Lagrangian type curved beams element with 3-degree of freedom per node has been developed to solve the curved beam model including the

effects of the extensibility of the curved axis, the shear deformation and the rotary inertia and a novel '2-node' curved beams element with 3-degree of freedom per node has been developed to solve the curved beam model excluding the effects of the extensibility of the curved axis, the shear deformation and the rotary inertia. Results obtained are in excellent agreement with those available in published literatures. It has been shown that the effects of the axial extensibility, shear deformation and rotary inertia are quite significant[21].

The developed beam's finite element models were then combined with the attached TMD system, to investigate the optimal TMD design strategy for beam-type structures. To testify the validity of the developed optimization design approach and methodology, first the uniform Timoshenko beam with attached TMD has been studied and the results are found to be in excellent agreement with those reported in literatures. Furthermore, the study has been extended to the curved beam structure in the same way. As the dynamic properties for the curved beam model has multiple dominant modes, a set of multiple TMD system design has been proposed to suppress the vibration effectively and the validity of optimal TMD parameters has been testified through the response comparison and the sensitivity analysis based on small deviation from the optimal values. Finally, based on the numerical results, a design principle (framework) for beam-type structures' vibration suppression using TMD technology has been established.

The random vibration matrix analysis methodology has been utilized to obtain the value of the objective function. This methodology allows us to solve the dynamic problem as one first order differential equation and can obtain the random criterions (variance, covariance) for all state variables. The validity of this methodology in optimal TMD design has also been testified through numerical examples.

A hybrid optimization methodology, which combines the global optimization method based on Genetic Algorithm (GA) and the powerful local optimization method based on Sequential Quadratic Programming (SQP), has been developed and then utilized to find the optimally designed parameters of the TMD system for curved beam-type structures. The validity of the proposed GA and hybrid optimization methodology has been verified through the GA convergence analysis and can also be proven by the proposed design principle for beam-type structures with the attached TMD system, as that shown in Chapter 4.

The MR-damper has been selected as the semi-active damper for a SAMD design. Based on the investigation of different numerical models for the MR-damper available in published literatures, the LuGre friction model is utilized to model the dynamic behavior the large-scale MR-damper. A LuGre friction model for MR-9000 type damper has been developed. The MR-damper's dynamic properties obtained through the proposed model under different type excitations and also input currents have been compared with those obtained form Bouc-Wen model proposed by Yang *et al*[181]. Perfect agreements can be found between these two models. Furthermore, it has been shown that the proposed model is easily to be used than the Bouc-Wen model proposed by Yang *et al*[181].

Based on MR-damper's LuGre friction model, an effective inverse MR-damper model has been proposed, which can be readily to design controller. The controller for Active Mass Damper (AMD) system is designed based on the H_2/LQG methodology and then combined with the Inverse-MR-damper model to provide effective vibration suppression performance using SAMD technology with MR-damper.

The major components of the present work and important observations are summarized as following:

- **Design Optimization of TMD system for beam-type structures**
  - ✓ Development of reliable curved beam element to investigate the dynamic property for general curved beam-type structures using finite element method.
  - ✓ Formulating the beam-type structures with the attached Tuned Mass Damper (TMD) system using finite element method.
  - ✓ Developing a hybrid optimization methodology, which combines the global optimization method based on GA and the powerful local optimization method based on SQP, to obtain the optimal design for vibration suppression of beam-type structures using TMD technology.

The validity of the developed curved beam element to investigate the dynamic property of curved beam has been proven in Chapter 2 through comparing the results with those in available literatures. Through the investigation provided in Chapters 3 and 4, and also the experimental investigation presented in Chapter 5, the effectiveness of utilizing the finite element methodology to design TMD system for beam-type structures and the developed optimization approach have been verified. The finite element method provides a straight forward way to study the general beam with attached TMD, and then one can easily extend the study to beam with different boundary conditions.

- **Magneto-Rheological (MR) fluid damper modeling**
  - ✓ Developing a LuGre friction model to model the dynamic behavior of large-scale MR-damper (MR-9000 type damper [122]).
  - ✓ Development an inverse MR-damper model based on the proposed LuGre friction model, which can be readily used in the design of semi–active vibration suppression devices

The dynamic behaviors of MR-9000 type damper have been evaluated using the proposed LuGre friction model and then the results were compared with those obtained by the Bouc-Wen model[181]. It has been shown that the proposed model can simulate the MR-damper's dynamic behavior accurately and also can be easily used to design the controller.

- **Vibration Suppression**
  - ✓ The effectiveness of vibration suppression for beam-type structures using the optimally designed MTMD system has been verified through the numerical investigation and experimental study.
  - ✓ The vibration suppression performance for Semi-Active Mass Damper (SAMD) design using the MR-damper has been presented and compared with other available control methodology.

The validity of the proposed SAMD design firstly testified through a classical building type structures and then extended to the beam-type structures, which has been presented in Chapter 7. Different vibration suppression strategies has been compared, which includes the uncontrolled structure; structure with optimally designed TMD system; structure with AMD system; structure with SAMD system

using MR-damper with the proposed control methodologies; structure with SAMD system under MR-damper's "*fail-safe*" condition; and also structure with SAMD system using MR-damper with different control methodologies.

8.2 Publications

Based on the conclusions and results obtained from the present work, the following articles have been prepared and published/submitted in refereed journals/conferences:

✓ **Journal papers published or accepted:**

- Yang, F., Sedaghati, R. and Esmailzadeh, E., "Free in-plane vibration of general curved beams using finite element method", *Journal of Sound and Vibration*, In press (doi:10.1016/j.jsv.2008.04.041).
- Yang, F., Sedaghati, R. and Esmailzadeh, E., "Vibration suppression of non-uniform curved beam under random loading using optimal Tuned Mass Damper", *Journal of Vibration and Control,* In press (doi: 10.1177/1077546308091220).
- Yang, F., Sedaghati, R. and Esmailzadeh, E., "Development of LuGre friction model for large-scale Magneto-Rheological fluid dampers", *Journal of Intelligent Material Systems and Structures.* 2008, tentatively Accepted.

✓ **Journal papers under review:**

- Yang, F., Sedaghati, R. and Esmailzadeh, E., "Vibration control of structures under random base excitations using active and semi-active mass damper", *Journal of Sound and Vibration.* Under review.

- Yang, F., Sedaghati, R. and Esmailzadeh, E., "Optimal vibration suppression of Timoshenko beam with Tuned Mass Damper using finite element method", *ASME Journal of Vibration and Acoustics.* Under review.

✓ **Conference papers:**

- Yang, F., Sedaghati, R. and Esmailzadeh, E., "A new LuGre friction model for MR-9000 type MR damper", *Proceedings of ASME International Mechanical Engineering congress and Exposition,* Boston, Massachusetts, USA, 2008.
- Yang, F., Sedaghati, R. and Esmailzadeh, E., "Seismic response controlled structure with semi-active mass-damper", *Proceedings of ASME International Mechanical Engineering congress and Exposition,* Boston, Massachusetts, USA, 2008.
- Yang, F., Sedaghati, R. and Esmailzadeh, E., "Passive vibration control of Timoshenko beam using optimal Tuned Mass Dampers", *Proceedings of 21st Canadian congress of applied mechanics,* Toronto Canada, 2007.
- Yang, F., Sedaghati, R. and Esmailzadeh, E., "In-plane free vibration of curved beam using finite element method", *Proceedings of ASME International Engineering Technical Conference,* Las Vegas, Nevada, USA, 2007.
- Yang, F., Sedaghati, R. and Esmailzadeh, E., "Random vibration suppression of non-uniform curved beam using optimal tuned mass damper", *Proceedings of ASME International Engineering Technical Conference,* Las Vegas, Nevada, USA, 2007.

8.3 Recommendations for Future Works

The present work established a framework for design and application of optimal Tuned Mass Damper (TMD) and Semi-Active Mass Damper (SAMD) in beam-type structures for vibration suppression applications. The scope of this work can be further extended in the following aspects:

Structural elements: The numerical model for Magneto-Rheological (MR) fluid dampers can be extended especially for the small displacement range, as those presented in Chapter 6.

Mathematical modeling: To improve the accuracy of mathematical model for the Magneto-Rheological (MR) fluid damper, the dynamic performance of the MR-damper's electromagnet should also be considered, which includes the current driver's properties; the coil configuration and its amplifier saturation voltage for MR-damper's multi-stage electromagnetic coil.

Control methodologies: Other control methodologies should also be investigated, such as the Fuzzy logic control method and the PID controller. Furthermore, it is a good idea to combine the dynamic properties of the Magneto-Rheological (MR) fluid damper with the original structures, and then design a controller directly to adjust the control current.

Semi-Active Devices: Application of other type of semi-active devices such as variable orifice hydraulic actuator, Active Variable Stiffness, Tuned Liquid Column Damper, and Electro-Rheological dampers could also be investigated.

Experimental works: In order to achieve the higher level of confidence and reliability, further experimental work is required to demonstrate the functionality and performance of optimal Tuned Mass Damper (TMD) design. Particularly, effectiveness of the optimal TMD in general curved beam-type structures under different random excitations is of great importance. Moreover, the experimental study regarding the SAMD system using MR-damper is needed.

Design optimization: The application of the global optimization methodology based on Genetic Algorithm can be improved by suitably selecting its optimization parameters. Furthermore, other type of global optimization methodology such as Simulated Annealing should also be investigated to illustrate the efficiency of the design optimization procedure and to facilitate the procedure of designing optimal TMD system for beam-type structures.

REFERENCES

1. Fitzpatrick, T., Dallard, P., Bourva, S. L., Low, A., Smith, R. R. and Willford, M., *Linking London: the Millennium Bridge*, The Royal Academy of Engineering, London, 2001, ISBN 1871634997.

2. Agoston, M. K., *Computer Graphics and Geometric Modeling*, Springer, London, 2005.

3. Cook, R. D., Malkus, D. S. and Plesha, M. E., *Concepts and Applications of finite element Analysis*, John Wiley & Sons, New York, 2002.

4. Meirovitch, L., *Principles and Techniques of vibrations*, Prentice-Hall, New Jersey, 1997.

5. Thomas, D. L., Wilson, J. M. and Wilson, R. R., "Timoshenko beam finite elements", *Journal of Sound and Vibration*, Vol. 31(3), 1973, 315-330.

6. Thomas, J. and Abbas, B. A. H., "Finite element model for dynamic analysis of Timoshenko beam", *Journal of Sound and Vibration*, Vol. 41(3), 1975, 291-299.

7. Dawe, D. J., "A finite element for the vibration analysis of Timoshenko beams", *Journal of Sound and Vibration*, Vol. 60(1), 1978, 11-20.

8. Davis, R., Henshell, R. D. and Warburton, G. B., "A Timoshenko beam element", *Journal of Sound and Vibration*, Vol. 22(4), 1972, 475-487.

9. Ansys ®, *Theory Reference-Chapter 12. Shape functions*,

10. Reddy, N. J., "On locking-free shear deformable beam finite elements", *Computer Methods in Applied Mechanics and Engineering*, Vol. 149, 1997, 113-132.

11. Mukherjee, S., Reddy, J. N. and Krishnamoorthy, C. S., "Convergence properties and derivative extraction of the superconvergent Timoshenko beam finite element", *Computer Methods in Applied Mechanics and Engineering*, Vol. 190, 2001, 3475-3500.

12. Henrych, J., *The Dynamics of Arches and Frames,* Elsevier, New York, 1981.

13. Auciello, N. M. and De Rosa, M. A., "Free vibrations of circular arches: A Review", *Journal of Sound and Vibration,* Vol. 176(4), 1994, 433-458.

14. Laura, P. A. A. and Verniere De Irassar, P. L., "A note on in-plane vibrations of arch-type structures of non-uniform cross-section: the case of linearly varying thickness", *Journal of Sound and Vibration,* Vol. 124(1), 1988, 1-12.

15. Schmidt, R., "Technique for estimating natural frequencies", *Journal of Engineering Mechanics,* Vol. 109(2), 1983, 654-657.

16. Bert, C. W., "Application of a version of the Rayleigh technique to problems of bars, beams, columns, membranes and plates", *Journal of Sound and Vibration,* Vol. 119(2), 1987, 317-326.

17. Raithel, A. and Franciosi, C., "The stability of arches in Lagrangian approach", *International Journal of Solids and Structures*, Vol. 21(5), 1985, 427-446.

18. Tong, X., Mrad, N. and Tabarrok, B., "In-plane vibration of circular arches with variable cross-sections", *Journal of Sound and Vibration,* Vol. 212(1), 1998, 121-140.

19. Veletsos, A. S., Austin, W. J., Lopes Pereira, C. A. and Wung, S. J., "Free in-plane vibrations of circular arches", *Journal of Engineering Mechanics ASCE,* Vol. 98, 1972, 311-329.

20. Lee, S. Y. and Hsiao, J. Y., "Free in-plane vibrations of curved nonuniform beams", *ACTA Mechanica,* Vol.155, 2002 173-189.

21. Chidamparam, P. and Leissa, A. W., "Influence of centrerline extensibility on the in-plane free vibrations of loaded circular arches", *Journal of Sound and Vibration,* Vol. 183(5), 1995, 779-795.

22. Austin, W. J. and Veletsos, A. S., "Free vibration of arches flexible in shear", *Journal of Engineering Mechanics, ASCE*, Vol. 99, 1973, 735-753.

23. Irie, T., Yamada, G., and Takahashi, I., "The steady state in-plane response of a curved Timoshenko beam with internal damping", *Ingenieur-Archiv*, Vol. 49, 1980, 41-49.

24. Issa, M. S., Wang, T. M. and Hsiao, B. T., "Extensional vibrations of continuous circular curved beams with rotary inertia and shear deformation, I: free vibration", *Journal of Sound and Vibration*, Vol. 114(2), 1987, 297-308.

25. Kang, K., Bert, C. W. and Striz, A. G., "Vibration analysis of shear deformable circular arches by the differential quadrature method", *Journal of Sound and Vibration*, Vol. 181(2), 1995, 353-360.

26. Tseng, Y. P., Huang, C. S. and Lin, C. J., "Dynamic stiffness analysis for in-plane vibrations of arches with variable curvature", *Journal of Sound and Vibration*, Vol. 207(1), 1997, 15-31.

27. Kreyszig, E., *Advanced engineering matiematics-9th edition,* John Wiley & Sons, New York, 2006.

28. Yildirim, V., "A computer program for the free vibration analysis of elastic arcs", *Computers and Structures*, Vol. 62(3), 1997, 475-485.

29. Shores, T. S., *Applied Linear Algebra and Matrix Analysis,* Springer, New York, 2007.

30. Tüfekçí, E. and Arpaci, A., "Exact solution of in-plane vibrations of circular arches with account taken of axial extension, transverse shear and rotatory inertia effects", *Journal of Sound and Vibrations*, Vol. 209(5), 1998, 845-856.

31. Tüfekçí, E. and Ozdemirci, O., "Exact solution of in-plane vibration of a stepped circular arch", *Journal of Sound and Vibrations*, Vol. 295, 2006, 725-738

32. Rubin, M. B. and Tüfekçí, E., "Three-dimensional free vibrations of a circular arch using the theory of Cosserat point", *Journal of Sound and Vibrations*, Vol. 286, 2005, 799-816.

33. Rubin, M. B., "Numerical solution procedures for nonlinear elastic rods using the theory of a Coosserat point", *International Journal of Solids and Structures*, Vol. 38, 2001, 4395-4473.

34. Rubin, M. B., "On the theory of Cosserat point and its application to the numerical solution of continuum problems", *Journal of Applied Mechanics, ASME*, 52, 1985, 368-372.

35. Oh, S. J., Lee, B. K. and Lee, I. W., "Natural Frequencies of non-circular arches with rotatory inertia and shear deformation", *Journal of Sound and Vibration*, Vol. 219(1), 1999, 23-33.

36. Petyr, M., and Fleischer, C. C., "Free vibration of a curved beam", *Journal of Sound and Vibration*, vol. 18(1), 1971, 17-30.

37. Davis, R., Henshell, R. D. and Warburton, G. B., "Constant curvature beam finite elements for in-plane vibration", *Journal of Sound and Vibration*, Vol. 25, 1972, 561-576.

38. Dawe, D. J., "Curved finite elements for the analysis of shallow and deep arches", *Computers & Structures*, Vol. 4, 1974, 559-580.

39. Balasubramanian, T. S. and Prathap, G., "A field consistent higher-order curved beam element for static and dynamic analysis of stepped arches", *Computers & Structures*, Vol. 33(1), 1989, 281-288.

40. Friedman, Z. and Kosmatka, J. B., "An accurate two-node finite element for shear deformable curved beams", *International Journal for Numerical Methods in Engineering*, Vol. 41, 1998, 473-498.

41. Raveendranath, P., Singh, G. and Pradhan, B., "Free vibration of arches using a curved beam element based on a coupled polynomial displacement field", *Computers & Structures*, Vol. 78, 2000, 583-590.

42. Litewka, P. and Rakowski, J., "Free vibrations of shear-flexible and compressible arches by FEM", *International Journal for Numerical Methods in Engineering*, Vol. 52, 2001, 273–286.

43. Eisenberger, M. and Efraim, E., "In-plane vibrations of shear deformable curved beams", *International Journal for Numerical Methods in Engineering*, Vol. 52, 2001, 1221-1234.

44. Wu, J. S. and Chiang, L. K., "Free vibration analysis of arches using curved beam elements", *International Journal for Numerical Methods in Engineering*, Vol. 58, 2003, 1907-1936.

45. Ribeiro, P., "A *p*-version, first order shear deformation, finite element for geometrically non-linear vibration of curved beams", *International Journal for Numerical Methods in Engineering*, Vol. 61, 2004, 2696-2715.

46. ÖztÜrk, H., Yeşilyurt, İ. and Sabuncu, M., "In-plane stability analysis of non-uniform cross-sectioned curved beams", *Journal of Sound and Vibration*, Vol. 296, 2006, 277-291.

47. Zhu, Z. H. and Meguid, S. A., "Vibration analysis of a new curved beam element", *Journal of Sound and Vibration*, Vol. 309, 2008, 86-95.

48. Frahm, H., *Device for damping vibration of bodies,* U.S. Patent No. 989,958, 1911.

49. Den Hartog, J. P., *Mechanical Vibrations*, McGraw-Hill, New York, 1956.

50. Crandall, S. H. and Mark, W. D., *Random Vibration in Mechanical Systems*, Academic Press, New York, 1963.

51. Warburton, G. B. and Ayorinde, E.O., "Optimum absorber parameters for simple systems", *Earthquake Engineering and Structural Dynamics*, Vol. 8(3), 1980, 197-217.

52. Warburton, G. B., "Optimum absorber parameters for various combinations of response and excitation parameters", *Earthquake Engineering and Structural Dynamics,* Vol. 10(3), 1982, 381-401.

53. Thomson, W. T. and Dahleh, M. D., *Theory of vibration with applications*, Prentice Hall, New Jersey, 1998.

54. Kwok, K. C. S. and Samali, B., "Performance of tuned mass dampers under wind loads", *Engineering Structures*", Vol. 17(9), 1995, 655-667.

55. Rana, R. and Soong. T. T., "Parametric study and simplified design of tuned mass dampers", *Engineering Structures*, Vol. 20(3), 1998, 193-204.

56. Rüdinger, F., "Tuned mass damper with fractional derivative damping", *Engineering Structures*, Vol. 28, 2006, 1774-1779.

57. Hadi, M. N. S. and Arfiadi, Y., "Optimum design of absorber for MDOF structures", *Journal of Structural Engineering*, Vol. 124(11), 1998, 1272-1280.

58. Hwang, J. S., Kim, H. and Kim, J., "Estimation of the modal mass of a structure with a tuned-mass damper using H-infinity optimal model reduction", *Engineering Structures,* Vol. 28, 2006, 34-42.

59. Lee, C. L., Chen, Y. T., Chung, L. L. and Wang, Y. P., "Optimal design theories and applications of tuned mass dampers", *Engineering Structures,* Vol. 28, 2006, 43-53.

60. Marano, G. C., Greco, R., Trentadue, F. and Chiaia, B., "Constrained reliability-based optimization of linear tuned mass dampers for seismic control", *International Journal of Solids and Structures*, Vol. 44, 2007, 7370-7388.

61. Nishimura, I., Yamada, T., Sakamoto, M., and Kobori, T., "Control performance of active-passive composite tuned mass damper", *Smart Materials and Structures*, Vol. 7, 1998, 637-653.

62. Lewandowski, R. and Grzymislawska, J., "Dynamic behaviour of composite mass damper for control of wind-excited vibration", *AMAS workshop on Smart Materials and Structures, SMART'03*, Jadwisin, 2003, 131-140.

63. Li, C. and Zhu, B., "Estimating double tuned mass dampers for structures under ground acceleration using a novel optimum criterion", *Journal of Sound and Vibration*, Vol. 298, 2006, 280-297.

64. Xu, K. and Igusa, T., "Dynamic characteristics of multiple substructures with closely spaced frequencies", *Earthquake Engineering & Structural dynamics*, Vol. 21(12), 1992, 1059-1070.

65. Igusa, T. and Xu, K., "Vibration control using multiple tuned mass dampers", *Journal of Sound and vibration,* Vol. 175(4), 1994, 491-503.

66. Kareem, A. and Kline, S., "Performance of multiple mass dampers under random loading", *Journal of Structural Engineering*, Vol. 121(2), 1995, 348-361

67. Joshi, A. S. and Jangid, R. S., "Optimum parameters of multiple tuned mass dampers for base-excited damped system", *Journal of Sound and Vibration*, Vol. 202(5), 1997, 657-667.

68. Li, C., "Optimum multiple tuned mass dampers for structures under the ground acceleration based on DDMF and ADMF", *Earthquake Engineering and Structural Dynamics*, Vol. 31, 2002, 897-919,

69. Li, C. and Qu, W., "Optimum properties of multiple tuned mass dampers for reduction of translational and torsional response of structures subject to ground acceleration", *Engineering Structures*, Vol. 28, 2006, 472-294.

70. Li, H. N. and Ni, X. L., "Optimization of non-uniformly distributed multiple tuned mass damper", *Journal of Sound and Vibration*, Vol. 308, 2007, 80-97.

71. Febbo, M. and Vera, S. A., "Optimization of a two degree of freedom system acting as a dynamic vibration absorber", *Journal of Vibration and Acoustics*, Vol. 130, 2008, [DOI: 10.1115/1.2827368].

72. Zuo, L. and Nayfeh, S. A., "Minmax optimization of multi-degree-of-freedom tuned mass dampers", *Journal of Sound and Vibration*, Vol. 272, 2004, 893-908

73. Zuo, L. and Nayfeh, S. A., "Optimization of the individual stiffness and damping parameters in multiple-tuned-mass-damper systems", *Journal of Vibration and Acoustics*, Vol. 127, 2005, 77-83.

74. Zuo, L. and Nayfeh, S. A., "The two-degree-of-freedom Tuned-Mass Damper for suppression of single-mode vibration under random and harmonic excitation", *Journal of Vibration and Acoustics*, Vol. 128, 2006, 56-65.

75. Jacquot, R. G., "Optimal dynamic vibration absorbers for general beam systems", *Journal of Sound and Vibration*, Vol. 60(4), 1978, 535-542.

76. Manikanahally, D. N. and Crocker, M. J., "Vibration absorbers for hysterestically damped mass-loaded beams", *Journal of Vibration and Acoustics*, Vol. 113, 1991, 116-122.

77. Gu, M., Chen, S. R. and Chang, C. C., "Parametric study on multiple tuned mass dampers for buffeting control of Yangpu Bridge", *Journal of Wind Engineering and Industrial Aerodynamics,* Vol. 89, 2001, 987-1000.

78. Yau, J. D. and Yang, Y. B., "A wideband MTMD system for reducing the dynamic response of continuous truss bridges to moving train loads", *Engineering Structures,* Vol. 26, 2004, 1795-1807.

79. Yau, J. D. and Yang, Y. B., "Vibration reduction for cable-stayed bridges traveled byhigh-speed trains", *Finite Element in Analysis and Design*, Vol. 40, 2004, 341-359.

80. Kwon, S. D. and Park, K. S., "Suppression of bridge flutter using tuned mass dampers based on robust performance design", *Journal of Wind Engineering and Industrial Aerodynamics*, Vol. 92, 2004, 919-934.

81. Chen, Y. H. and Chen, D. S., "Timoshenko beam with tuned mass dampers to moving loads", *Journal of Bridge Engineering*, Vol. 9(2), 2004, 167-177.

82. Chen, Y. H. and Huang Y. H., "Timoshenko beam with tuned mass dampers and its design curves" *Journal of Sound and Vibration*, Vol. 278, 2004, 873-888.

83. Esmailzadeh, E. and Jalili, N., "Optimum design of vibration absorbers for structurally damped Timoshenko beams", *Journal of Vibration and Acoustics.* Vol. 120, 1998, 833-841.

84. Younesian, D., Esmailzadeh, E and Sedaghati, R., "Passive vibration control of beams subjected to random excitations with peaked PSD", *Journal of Vibration and Control*, Vol. 12(9), 2006, 941-953.

85. Wu, J. J., "Free vibration analysis of beams carrying a number of two-degree-of-freedom spring-damper-mass systems", *Finite Elements in Analysis and Design,* Vol. 40, 2004, 363-381.

86. Matlab, http://www.mathworks.com/products/matlab/.

87. Wirsching, P. H., *Random Vibrations: Theory and Practice*, John Wiley & Sons, New York, 1995.

88. Arora, J. S., *Introduction to Optimal Design*, Mcgraw-Hill, New York, 1989.

89. Rao, S. S., *Engineering Optimization: Theory and Practice*, John Wiley & Sons, New York, 1996.

90. Nishimura, I., Kobori, T., Sakamoto, M., Koshika, N., Sasaki, K. and Ohrui, S., "Active tuned mass damper", *Smart Materials and Structures*, Vol. 1(4), 1992, 306-311.

91. Chang, C. C. and Yang, H. T. Y., "Control of buildings using active tuned mass dampers", *Journal of Engineering Mechanics*, Vol. 121(3), 1995, 355-366.

92. Dyke, S. J., Spencer Jr, B. F., Sain, M. K. and Carlson, J. D., "Modeling and control of Magnetorheological dampers for seismic response reduction", *Smart Materials and Structures*, Vol. 5(5), 1996, 565-575.

93. Niu, M. C. Y., *Airframe Structural Design: Practical design information and data on aircraft structures*, Conmilit, Hong Kong, 1999.

94. Dyke, S. J., "Acceleration feedback control strategies for active and semi-active control systems: modeling, algorithm development, and experimental verification," Ph.D thesis, University of Notre Dame, Notre Dame, Indiana, USA, 1996.

95. Spencer Jr, B. F., Dyke, S. J. and Deoskar, H. S., "Benchmark problems in structural control: Part 1-Active mass driver system", *Earthquake Engineering and Structural Dynamics*, Vol. 27, 1998, 1127-1139.

96. Zhuang, W., "Optimal design analysis of a semi-active tuned mass hydraulic damper for structural control," M.S thesis, University of Oklahoma, Oklahoma, USA, 1999.

97. Zhuang, W., Leming, S., Kuehn, J., Zeng, H. and Stalford, H., "Semi-active tuned mass damper design for balcony vibration control", *Proceedings of American Control Conference,* Chicago, Illinois, 2000, 3560-3564.

98. Nasu, T., Kobori, T., Takahashi, M., Niwa, N. and Ogasawara, K., "Active variable stiffness system with non-resonant control", *Earthquake Engineering and Structural Dynamics*, Vol. 30, 2001, 1597-1614.

99. Leavitt, J., Jabbari, F. and Boborw, J. E., "Optimal control and performance of variable stiffness devices for structural control", *2005 American Control Conference*, Portland, OR, USA, 2005, 2499-2504.

100. Renzi, E. and De Angelis, M., "Optimal semi-active control and non-linear dynamic response of variable stiffness structures", *Journal of Vibration and Control*, Vol. 11(10), 2005, 1253-1289.

101. Nagarajaiah, S., *Structural vibration damper with continuous variable stiffness*, US Patent No. 9098969, 2002.

102. Agrawal, A. "Response of semi-active variable stiffness and damping systems to pulse type excitations: analysis and experimental study", M.S Thesis, Rice University, Houston, Texas, USA, 2004.

103. Varadarajan, N. and Nagarajaiah, S., "Wind response control of building with variable stiffness tuned mass damper using empirical mode decomposition/Hilbert transform", *Journal of Engineering Mechanics*, Vol. 130(4), 2004, 451-458.

104. Sun, L. M., Fujino, Y., Pacheco, B. M. and Chaiseri, P., "Modelling of tuned liquid damper (TLD)", *Journal of Wind Engineering and Industrial Aerodynamics*, Vol. 43, 1992, 1883-1894.

105. Hitchcock, P. A., Kwok, K. C. S. and Watkins, R. D., "Characteristics of liquid column vibration absorbers (LCVA)-1", *Engineering Structures*, Vol. 19(2), 1997, 126-134.

106. Hitchcock, P. A., Kwok, K. C. S. and Watkins, R. D., "Characteristics of liquid column vibration absorbers (LCVA)-2", *Engineering Structures*, Vol. 19(2), 1997, 135-144.

107. Gao, H., Kwok, K. C. S. and Samali, B., "Optimization of tuned liquid column dampers", *Engineering Structures*, Vol. 19(6), 1997, 476-486.

108. Yalla, S. K., Kareem, A. and Kantor, J. C., "Semi-active tuned liquid column dampers for vibration control of structures", *Engineering Structures*, Vol. 23. 2001, 1469-1479.

109. Yalla, S. K. and Kareem, A., "Semiactive tuned liquid column dampers: experimental study", *Journal of Structural Engineering*, Vol. 129(7), 2003, 960-971.

110. Hochrainer, M. J., "Tuned liquid column damper for structural control", *ACTA Mechanica*, Vol.175, 2005, 57-76.

111. Chen, Y. H. and Ko, C. H., "Active tuned liquid column damper with propellers", *Earthquake Engineering and Structural Dynamics*, Vol. 32, 2003, 1627-1638.

112. Wang, J. Y., Ni, Y. Q., Ko, J. M. and Spencer Jr, B. F., "Magneto-rheological tuned liquid column dampers (MR-TLCDs) for vibration mitigation of tall buildings: modeling and analysis of open-loop control", *Computers and Structures*, Vol. 83, 2005, 2023-2034.

113. Mcclamroch, N. H. and Gavin, H. P., "Electrorheological dampers and semi-active structural control", *Proceedings of the 34th Conference on Decision & Control,* New Orleans, LA, 1995, 3528-2533.

114. Winslow, W. M., "Induced fibration of suspensions", *Journal of Applied Physics*, Vol. 20, 1949, 1137-1140.

115. Makris, N., Burton, S. A. and Taylor, D. P., "Electrorheological damper with annular ducts for seismic protection applications", S*mart Materials & Structures*, Vol. 5. 1996, 551-564.

116. Wang, X. and Gordaninejad, F., "Dynamic modeling of semi-active ER/MR fluid dampers", *Proceedings of SPIE Conference on Smart Materials and Structures,* Ed. Daniel J. Inman, Vol. 4331, 2001, 82-91.

117. Bitman, L., Choi, Y. T. and Wereley, N. M., "Electrorheological damper analysis using an eyring constitutive relationship," *Journal of Intelligent Material Systems and Structures*, Vol. 13, 2002, 633-639.

118. Stanway, R., "Smart Fluids: current and future developments", *Materials Science and Technology*, Vol. 20(8), 2004, 931-939.

119. Yang, G., *Large-scale magnetorheological fluid damper for vibration mitigation: modeling, testing and control*, Ph.D Thesis, University of Notre Dame, Notre Dame, Indiana, USA, 2001.

120. Sims, N. D., Stanway, R. and Johnson, A. R., "Vibration control using smart fluids: A state-of-the-art review", *The Shock and vibration Digest*, Vol.31, 1999, 195-203.

121. Ashour, O., Rogers, C. A. and Kordonsky, W., "Magnetorhelolgical fluids: Materials, Characterization, and Devices", *Journal of Intelligent Material System and Structures*, Vol. 7, 1996, 123-130.

122. www.Lord.com. LORD Company website.

123. Stanway, R., Sproston, J. L. and Strvens, N. G., "Non-linear modeling of an electro-rheological vibration damper", *Journal of Electrostatics*, Vol. 20, 1987, 167-184.

124. Stanway, R., Sproston, J. L. and EL-Wahed, A. K., "Applications of electro-rheological fluids in vibration control: a survey", *Smart Materials & Structures*, Vol. 5, 1996, 464-482.

125. Peel, D. J, Stanway, R., and Bullough, W. A., "Dynamic modeling of an ER vibration damper for vehicle suspension applications", *Smart Materialss and Structures*, Vol. 5, 1996, 591-606.

126. Gamota, D. R., and Filisko, F. E., "Dynamic mechanical studies of electroheological materials: moderate frequencies," Journal of Rheology, Vol. 35(3), 1991, 399-425.

127. Wereley, N. M., Li, P., and Kamath, G. M., "Idealized hysteresis modeling of electrorheological and magnetorheological dampers", *Journal of Intelligent Material Systems and Structures*, Vol. 9(8), 1998, 642-649.

128. Spencer Jr, B. F., Dyke, S. J., Sain, M. K., and Carlson, J. D., "Phenomenological model for magnetorheological dampers", *Journal of Engineering Mechanics*, Vol. 123(3), 1997, 230-238.

129. Wen, Y. K., "Method of random vibration of hysteretic system", *Journal of Mechanic Engineering, ASCE*, Vol. 102(2), 1976, 249-263.

130. Li, W. H., Yao, G. Z., Chen, G., Teo, S. H. and Yap, F. F., "Testing and steady state modeling of a linear MR damper under sinusoidal loading", *Smart Materials & Structures*, Vol. 9, 2000, 95-102.

131. Choi, S. B., and Lee, S. K., "A hysteresis model for the field-dependent damping force of a magnetorheological damper", *Journal of Sound and Vibration*, Vol. 245(2), 2001, 375-383.

132. Oh, H. U. and Onoda, J., "An experimental study of a semiactive magneto-rheologican fluid variable damper for vibration suppression of truss structures", *Smart Materials and Structures*, Vol. 11, 2002, 156-162.

133. Wang, E. R., Ma, X. Q., Rakheja, S. and Su, C. Y., "Analysis of a semi-active MR-damper with hysteretic and asymmetric properties", *Proceedings of the American Control Conference,* Denver, Colorado, 2003, 4920-4925.

134. Wang, E. R., Ma, X. Q., Rakheja, S. and Su, C. Y., "Force tracking control of vehicle vibration with MR-dampers", *Proceedings of 2005 IEEE International Symposium on Intelligent Control*, Limassol, Cyprus, 2005, 995-1000.

135. Jimenez, R. and Alvarez, L., "Real time identification of structures with magnetorheological dampers", *Proceedings of the 41st IEEE Conference on Decision and Control*, Las Vegas, Nevada, USA, 2002, 1017-1022.

136. Jimenez, R., and Alvarez I, L., "LuGre friction model for a magnetorheological damper", *Structural Control and Health Monitoring*, Vol. 12, 2005, 91-116

137. Xia, P. Q., "An inverse model of MR damper using optimal neural network and system identification", *Journal of Sound and Vibration*, Vol. 266, 2003, 1009-1023.

138. Kim, H. S., Roschke, P. N., Lin, P. Y. and Loh, C. H., "Neuro-fuzzy model of hybrid semi-active base isolation system with FPS bearings and an MR damper", *Engineering Structures*, Vol. 28(7), 2006, 947-958.

139. Dominguez, A., Sedaghati, R., and Stiharu, I., "Modelling the hysteresis phenomenon of magnetorheological dampers", *Smart Materials and Structures*, Vol. 13, 2004, 1351-1361.

140. Dominguez, A., Sedaghati, R. and Stiharu, I., "A new dynamic hysteresis model for magnetorheological dampers," *Smart Materials and Structures*, Vol. 15, 2006, 1179-1189.

141. Jin, G., Sain, M. K. and Spencer Jr, B. F., "Nonlinear black box modeling of MR-dampers for civil structural control", *IEEE Transactions on Control Systems Technology*. Vol. 13(3) 2005, 345-355.

142. Wang, L. X. and Kamath, H., "Modelling hysteretic behaviour in magnetorheological fluids and dampers using phase-transition theory", *Smart Materials and Structures*, Vol. 15, 2006, 1725-1733.

143. Ikhouane, F. and Dyke, S. J., "Modeling and identification of a shear mode magnetorheological damper", *Smart Materials and Structures*, Vol. 16, 2007, 605-616.

144. Shivaram, A. C. and Gangadharan, K. V., "Statistical modeling of a magento-rheological fluid damper using the design of experiments approach", *Smart Materials and Structures*, Vol. 16, 2007, 1310-1314.

145. Leitmann, G., "Semiactive control for vibration attenuation", *Journal of Intelligent Material Systems and Structure*s, Vol. 5, 1994, 841-846.

146. Mcclamroch, N. H. and Gavin, H. P., "Closed loop structural control using electrorheological dampers", *Proceedings of the American Control Conference,* Seattle, Washington, 1995, 4173-4177.

147. Jansen, L. M. and Dyke, S. J., "Semi-active control strategies for MR dampers: a comparative study", *Journal of Engineering Mechanics*, Vol. 126(8), 2000, 795-803.

148. Domingues, A., Sedaghati, R. and Stiharu, I., "Semi-Active vibration control of adaptive structures using magnetorheological dampers", *AIAA Journal*, Vol. 44(7), 2006, 1563-1571.

149. Zhang, J. and Roschke, P. N., "Active control of a tall structure excited by wind", *Journal of Wind Engineering and Industrial Aerodynamics*, Vol. 83, 1999, 209-223.

150. Chang, C. C. and Zhou, L., "Neural network emulation of inverse dynamics for a magnetorheological damper", *Journal of Structural Engineering*, Vol. 128(2), 2002, 231-239.

151. Tsang, H. H., Su, R. K. L. and Chandler, A. M., "Simplified inverse dynamics models for MR fluid dampers", *Engineering Structures*, Vol. 28, 2006, 327-341.

152. Battaini, M., Casciati, F. and Faravelli, L., "Fuzzy control of structural vibration, an active mass system driven by a fuzzy controller", *Earthquake Engineering and Structural Dynamics*, Vol. 27, 1998, 1267-1276.

153. Schurter, K. C. and Roschke, P. N., "Neuro-fuzzy control of structures using acceleration feedback", *Smart Materials and Structures*, Vol. 10, 2001, 770-779.

154. Choi, K. M., Cho, S. W., Jung, H. J. and Lee, I. W., "Semi-active fuzzy control for seismic response reduction using magnetorhelolgical dampers", *Earthquake Engineering and Structural Dynamics*, Vol. 33. 2004, 723-736.

155. Liu, Y., Gordaninejad, F., Evrensel, C. A., Hitchcock, G. and Wang, X., "Variable structure system based fuzzy logic control of bridge vibration using fail-safe magneto-rheological fluid dampers", *Proceedings of SPIE Conference on Smart Materials and Structures*, San Diego, 2002,

156. Wilson, C. M. D. and Abdullah, M. M., "Structural vibration reduction using fuzzy control of magnetorheological dampers", *ASCE Structural Congress*, New York, 2005

157. Wilson, C. M. D. and Abdullah, M. M., "Fuzzy control of magnetorheological dampers in civil structures", *6th European Conference on Structural Dynamics*, Paris, 2005.

158. Zhou, L. Chang, C. C. and Wang, L. X., "Adaptive fuzzy control for nonlinear building magnetorheological damper system", *Journal of Structural Engineering*, Vol. 129(7), 2003, 905-913.

159. Reigles, D. G. and Symans, M. D., "Supervisory fuzzy control of a base-isolated benchmark building utilizing a neuro-fuzzy model of controllable fluid viscous dampers", *Structural Control and Health Monitoring*, Vol. 13, 2006, 724-747.

160. Kim, H. S. and Roschke, P. N., "Design of fuzzy logic controller for smart base isolation system using genetic algorithm", *Engineering Structures*, Vol. 28, 2006, 84-96.

161. Arslan, A. and Kaya, M., "Determination of fuzzy logic membership function using genetic algorithms", *Fuzzy Sets and Systems*, Vol. 118, 2001, 297-306.

162. Zhu, W. Q. and Ying, Z. G., "An optimal nonlinear feedback control strategy for randomly excited structural systems", *Nonlinear Dynamics*, Vol. 24, 2001, 31-51.

163. Ying, Z. G., Zhu, W. Q. and Soong, T. T., "A stochastic optimal semi-active control strategy for ER/MR dampers", *Journal of Sound and Vibration*, Vol. 259(1), 2003, 45-62.

164. Cheng, H., Zhu, W. Q. and Ying, Z. G., "Stochastic optimal semi-active control of hysteretic systems by using a magneto-rheological damper", *Smart Materials and Structures*, Vol. 15, 2006, 711-718.

165. Dyke, S. J., Spencer Jr, B. F., Sain, M. K. and Carlson, J. D., "An experimental study of MR dampers for seismic protection", *Smart Materials and Structures*, Vol. 7, 1998, 693-703.

166. Yoshioka, H., Ramallo, J. C. and Spencer Jr, B. F., "Smart base isolation strategies employing magnetorheological dampers", *Journal of Engineering Mechanics*, Vol. 128(5), 2002, 540-551.

167. Yoshida, O. and Dyke, S. J., "Seismic control of a nonlinear benchmark building using Smart dampers", *Journal of Engineering Mechanics*, Vol. 130(4), 2004, 386-392.

168. Sakai, C., Ohmori, H. and Sano, A., "Modeling of MR damper with hysteresis for adaptive vibration control," *Proceedings of the 41st IEEE Conference on Decision and Control*, Maul, Hawaii, USA, 2003, 3840-3845.

169. Rosinger, H. E. and Ritchie, I. G., "On Timoshenko's correction for shear in vibrating isotropic beams", *Journal of Applied Physics*, Vol. 10, 1977, 1461-1466.

170. Stephen, N. G., "Discussion: "Shear Coefficients for Timoshenko Beam theory"", *Journal of Applied Mechanics*, Vol. 68, 2001, 959-961.

171. Chidamparam, R. and Leissa, A. W., "Vibrations of planar curved beams, rings and arches", *Applied Mechanics Reviews*, Vol. 46(9), 1993, 467-483.

172. Auciello, N. M. and Ercolano, A., "A general solution for dynamic response of axially loaded non-uniform Timoshenko beams", *International Journal of Solids and Structures*, Vol. 41, 2004, 4861-4874.

173. Eisenberger, M., "Dynamic stiffness matrix for variable cross-section Timoshenko beams", *Communications in Numerical Methods in Engineering*, Vol. 11(6), 1995, 507-513.

174. Rossi, R. E., Laura, P. A. A. and Guitierrez, R. H., "A note on transverse vibrations of a Timoshenko beam of non-uniform thickness clamped at one end and carrying a concentrated mass at the other", *Journal of Sound and Vibration,* Vol. 143(3), 1990, 491-502.

175. Irie, T., Yamada, G. and Tanaka, K., "Natural frequencies of in-plane vibrations of arcs", *Journal of Applied Mechanics, ASME*, Vol.50, 1983, 449-452.

176. Lutes, L. D. and Sarkani, S., *Random vibration: analysis of structural and mechanical systems.* Amsterdam; Boston: Elsevier, 2004.

177. Holland, J., *Adaptation in Natural and Artificial System*, Ann Ardor: University of Michigan Press, 1975.

178. Goldberg, D., *Genetic Algorithms in Search, Optimization, and Machine Learning, Reading*, Addison_Wesley, MA, 1989.

179. Haupt, R. L. and Haupt, S. E., *Practical Genetic Algorithms, Second Edition,* John Wiley & Sons. Inc, Hoboken, New Jersey, 2004.

180. Yang, G., Spencer Jr, B. F., Jung, H. J. and Carlson, J. D., "Dynamic modeling of large-scale magnetorheological damper systems for civil engineering applications", *Journal of Engineering Mechanics.* Vol. 130(9), 2004, 1107-1114.

181. Yang, G., Spencer Jr, B. F., Carlson, J. D. and Sain, M. K., "Large-scale MR fluid dampers: modeling and dynamic performance considerations" *Engineering Structures.* Vol. 24, 2002, 309-323.

182. Strang, G., *Introduction to Applied Mathematics*, Wellesley-Cambridge Press, Wellesley, MA. 1986.

183. Atkinson, K. E., *An Introduction to Numerical Analysis*, Willey, New York, 1989.

184. Doyle, J. C., Glover, K., Khargonekar, P. P. and Francis, B. A., "State-space solutions to standard H_2 and H_∞ control problems," *IEEE Transactions on Automatic Control*, Vol. 34(8), 1989, 831-847.

185. Zhou, K. and Khargonekar, P. P., "An algebraic Riccati equation approach to H_∞ optimization," Systems & control letters, Vol. 11(2), 1988, 85-91,

186. Zhou, K., Doyle, J. C. and Glover, K., *Robust and optimal control*, Prentice Hall, Englewood Cliffs, New Jersey, 1996.

187. Chiang, R. Y. and Safonov, M. G., Robust-control toolbox, The Mathworks.

188. Spencer Jr, B. F., Suhardjo, J. and Sain, M. K., "Frequency domain optimal control strategies for aseismic protection", *Journal of Engineering Mechanics*, Vol. 120(1), 1994, 135-158.

189. Jha, A., Sedaghati, R. and Bhat, R., "Analysis and dynamic testing of structures subjected to vibration and shock using scale models", *Canadian Aeronautics and Space Journal*, Vol. 52(3), 2006, 95-108.

APPENDIX A:

Timoshenko beam's mass, stiffness and damping sub-matrices

$$[M_{ww}] = \sum_{element} \left\{ \int_{-1}^{1} \left[\gamma [N(\eta)]^T A(\eta) [N(\eta)] \bar{J}(\eta) \right] d\eta \right\} \tag{A.1}$$

$$[M_{\psi\psi}] = \sum_{element} \left\{ \int_{-1}^{1} \left[\gamma [N(\eta)]^T I(\eta) [N(\eta)] \bar{J}(\eta) \right] d\eta \right\} \tag{A.2}$$

$$[K_{ww}] = \sum_{element} \left\{ \int_{-1}^{1} \left[k_q G [B(\eta)]^T A(\eta) [B(\eta)] \bar{J}^{-1}(\eta) \right] d\eta \right\} \tag{A.3}$$

$$[K_{\psi\psi}] = \sum_{element} \left\{ \int_{-1}^{1} \left[E [B(\eta)]^T I(\eta) [B(\eta)] \bar{J}^{-1}(\eta) \right] d\eta + \int_{-1}^{1} \left[k_q G [N(\eta)]^T A(\eta) [N(\eta)] \bar{J}(\eta) \right] d\eta \right\} \tag{A.4}$$

$$[K_{w\psi}] = [K_{\psi w}]^T = - \sum_{element} \left\{ \int_{-1}^{1} k_q G \left[[B(\eta)]^T A(\eta) [N(\eta)] \right] d\eta \right\} \tag{A.5}$$

where $A(\eta) = [N(\eta)]\{A\}$, $I(\eta) = [N(\eta)]\{I\}$ and γ represent the density of material; $\bar{J} = dx/d\eta$ is the Jacobian between the natural coordinates and the physical coordinates.

APPENDIX B:

Sub-matrices of mass and stiffness in Equations (2.12)

$$[M_{ww}] = \sum_{element} \left\{ \int_{-1}^{1} [\gamma [N(\eta)]^T A(\eta)[N(\eta)] \bar{J}_c(\eta)] d\eta \right\} \tag{B.1}$$

$$[M_{uu}] = \sum_{element} \left\{ \int_{-1}^{1} [\gamma [N(\eta)]^T A(\eta)[N(\eta)] \bar{J}_c(\eta)] d\eta \right\} \tag{B.2}$$

$$[M_{\psi\psi}] = \sum_{element} \left\{ \int_{-1}^{1} [\gamma [N(\eta)]^T I(\eta)[N(\eta)] \bar{J}_c(\eta)] d\eta \right\} \tag{B.3}$$

$$[K_{ww}] = \sum_{element} \left\{ \int_{-1}^{1} \left[[k_q GA(\eta)[B(\eta)]^T [B(\eta)] \bar{J}_c^{-1}(\eta) + \frac{EA(\eta)}{\rho(\eta)^2} [N(\eta)]^T [N(\eta)] \bar{J}_c(\eta) \right] d\eta \right\} \tag{B.4}$$

$$[K_{wu}] = \sum_{element} \left\{ \int_{-1}^{1} \left[\frac{EA(\eta)}{\rho(\eta)} [N(\eta)]^T [B(\eta)] - \frac{k_q GA(\eta)}{\rho(\eta)} [B(\eta)]^T [N(\eta)] \right] d\eta \right\} \tag{B.5}$$

$$[K_{w\psi}] = \sum_{element} \left\{ - \int_{-1}^{1} [k_q GA(\eta)[B(\eta)]^T [N(\eta)]] d\eta \right\} \tag{B.6}$$

$$[K_{uu}] = \sum_{element} \left\{ \int_{-1}^{1} \left[EA(\eta)[B(\eta)]^T [B(\eta)] \bar{J}_c^{-1}(\eta) + \frac{k_q GA(\eta)}{\rho(\eta)^2} [N(\eta)]^T [N(\eta)] \bar{J}_c(\eta) \right] d\eta \right\} \tag{B.7}$$

$$[K_{u\psi}] = \sum_{element} \left\{ \int_{-1}^{1} \left[\frac{k_q GA(\eta)}{\rho(\eta)} [N(\eta)]^T [N(\eta)] \bar{J}_c(\eta) \right] d\eta \right\} \tag{B.8}$$

$$[K_{\psi\psi}] = \sum_{element} \left\{ \int_{-1}^{1} [EI(\eta)[B(\eta)]^T [B(\eta)] \bar{J}_c^{-1}(\eta) + k_q GA(\eta)[N(\eta)]^T [N(\eta)] \bar{J}_c(\eta)] d\eta \right\} \tag{B.9}$$

where $A(\eta) = [N(\eta)]\{A\}$, $I(\eta) = [N(\eta)]\{I\}$ and $[B(\eta)] = d[N(\eta)]/d\eta$. The Jacobian $\bar{J}_c(\eta)$ can be evaluated through:

$$\bar{J}_c(\eta) = \frac{ds}{d\eta} = \sqrt{(\frac{dx}{d\eta})^2 + (\frac{dy}{d\eta})^2} = \sqrt{([B(\eta)]\{X\})^2 + ([B(\eta)]\{Y\})^2} \tag{B.10}$$

and the radius $\rho(\eta)$ can be evaluated through the following equation:

$$\frac{1}{\rho(\eta)}=\frac{d^2y/dx^2}{\{1+(dy/dx)^2\}^{1.5}}=\frac{\frac{d\eta}{dx}\frac{d}{d\eta}(\frac{dy/d\eta}{dx/d\eta})}{\{1+(\frac{dy/d\eta}{dx/d\eta})^2\}^{1.5}}=\frac{\frac{1}{[B(\eta)]\{X\}}\frac{d}{d\eta}(\frac{[B(\eta)]\{Y\}}{[B(\eta)]\{X\}})}{\{1+(\frac{[B(\eta)]\{Y\}}{[B(\eta)]\{X\}})^2\}^{1.5}}=$$
$$\frac{\frac{1}{[B(\eta)]\{X\}}\{\frac{[D(\eta)]\{Y\}[B(\eta)]\{X\}-[B(\eta)]\{Y\}[D(\eta)]\{X\}}{[D(\eta)]\{X\}}\}}{\{1+(\frac{[B(\eta)]\{Y\}}{[B(\eta)]\{X\}})^2\}^{1.5}} \quad \text{(B.11)}$$

where $[D(\eta)]=d[B(\eta)]/d\eta$. Here it should be noted that as the evaluation for the radius requires second order differential respected to the natural coordinate (η), the polynomial interpolation function for the geometrical condition should at least 3 order, which means the Lagrangian type shape function need at least 4 nodes.

APPENDIX C:

Governing differential equations of motion for Curved beam model (Case 2)

Based on Equations (2.13) and (2.14), the variation in kinetic and potential energies can be expressed as:

$$\delta T = \underbrace{\int_L \gamma(s)A(s)\frac{\partial w(s,t)}{\partial t}\frac{\partial}{\partial t}(\delta w(s,t))ds}_{Part1} + \underbrace{\int_L J(s)\frac{\partial \psi(s,t)}{\partial t}\frac{\partial}{\partial t}(\delta \psi(s,t))ds}_{Part2} \tag{C.1}$$

$$\delta V = \underbrace{\int_L EI(s)\frac{\partial \psi(s,t)}{\partial s}\frac{\partial}{\partial s}(\delta \psi(s,t))ds}_{Part3} \tag{C.2}$$

Substituting the deformation relationship for Case 2, as listed in Table 2.1 to Equations (C.1) and (C.2), and then utilizing the Hamilton principle, as stated in Equation (2.6), the following expressions for each part shown in Equations (C.1) and (C.2) can be obtained:

For *Part 1*:

$$\begin{aligned}&\int_{t_1}^{t_2}\int_L \gamma(s)A(s)\frac{\partial w(s,t)}{\partial t}\frac{\partial}{\partial t}(\delta w(s,t))dsdt \\ &= \int_L\left\{\gamma(s)A(s)\frac{\partial w(s,t)}{\partial t}\delta w(s,t)\Big|_{t_1}^{t_2} - \int_{t_1}^{t_2}\gamma(s)A(s)\frac{\partial w^2(s,t)}{\partial t^2}\delta w dt\right\}ds\end{aligned} \tag{C.3}$$

For *Part 2*:

$$\begin{aligned}&\int_{t_1}^{t_2}\int_L J(s)\frac{\partial \psi(s,t)}{\partial t}\frac{\partial}{\partial t}(\delta \psi(s,t))dsdt \\ &= \int_L\left\{J(s)\frac{\partial \psi(s,t)}{\partial t}\delta \psi(s,t)\Big|_{t_1}^{t_2} - \int_{t_1}^{t_2}J(s)\frac{\partial \psi^2(s,t)}{\partial t^2}\delta \psi dt\right\}ds\end{aligned} \tag{C.4}$$

For *Part 3*:

$$
\begin{aligned}
&\int_{t_1}^{t_2}\int_L EI(s)\frac{\partial\psi(s,t)}{\partial s}\frac{\partial}{\partial s}(\delta\psi(s,t))dsdt \\
&=\int_L\{\int_{t_1}^{t_2} EI(s)\frac{\partial(\frac{\partial w(s,t)}{\partial s}-\frac{u(s,t)}{\rho(s)})}{\partial s}\frac{\partial}{\partial s}(\delta(\frac{\partial w(s,t)}{\partial s}-\frac{u(s,t)}{\rho(s)}))dt\}ds \\
&=\int_{t1}^{t2}\int_L EI(s)\frac{\partial^2 w(s,t)}{\partial s^2}\delta(\frac{\partial^2 w(s,t)}{\partial s^2})-\frac{EI(s)}{\rho(s)}\frac{\partial^2 w(s,t)}{\partial s^2}\frac{\partial}{\partial s}\delta u(s,t) \\
&\quad-\frac{EI(s)}{\rho(s)}\frac{\partial u(s,t)}{\partial s}\delta(\frac{\partial^2 w(s,t)}{\partial s^2})+\frac{EI(s)}{\rho^2(s)}\frac{\partial u(s,t)}{\partial s}\frac{\partial}{\partial s}\delta u(s,t)dsdt \\
&=\int_{t1}^{t2}\left\{\begin{array}{l}\{\delta(\frac{\partial w(s,t)}{\partial s})EI(s)\frac{\partial^2 w(s,t)}{\partial s^2}\Big|_L-\delta w(s,t)\frac{\partial}{\partial s}(EI(s)\frac{\partial^2 w(s,t)}{\partial s^2})\Big|_L+ \\ \int_L\frac{\partial^2}{\partial s^2}(EI(s)\frac{\partial^2 w(s,t)}{\partial s^2})\delta(w(s,t))ds\}\end{array}\right\}dt+ \\
&\quad\int_{t1}^{t2}\left\{-\delta u(s,t)\frac{EI(s)}{\rho(s)}\frac{\partial^2 w(s,t)}{\partial s^2}\Big|_L+\int_L\frac{\partial}{\partial s}(\frac{EI(s)}{\rho(s)}\frac{\partial^2 w(s,t)}{\partial s^2})\delta u(s,t)ds\right\}dt+ \\
&\quad\int_{t1}^{t2}\left\{\begin{array}{l}-\frac{\partial}{\partial s}(\delta w(s,t))\frac{EI(s)}{\rho(s)}\frac{\partial u(s,t)}{\partial s}\Big|_L+\delta w(s,t)\frac{\partial}{\partial s}(\frac{EI(s)}{\rho(s)}\frac{\partial u(s,t)}{\partial s})\Big|_L \\ -\int_L\frac{\partial^2}{\partial s^2}(\frac{EI(s)}{\rho(s)}\frac{\partial u(s,t)}{\partial s})\delta(w(s,t))\end{array}\right\}dt+ \\
&\quad\int_{t1}^{t2}\left\{\delta u(s,t)\frac{EI(s)}{\rho^2(s)}\frac{\partial u(s,t)}{\partial s}\Big|_L-\int_L\frac{\partial}{\partial s}(\frac{EI(s)}{\rho^2(s)}\frac{\partial u(s,t)}{\partial s})\delta u(s,t)ds\right\}dt
\end{aligned}
\tag{C.5}
$$

Combining Equations (C.3)-(C.5) together and canceling the part related to the boundary conditions then rearranging the equation respected to the δw and δu separately. Finally one can obtain the governing differential equations of motion as stated in Equations (2.15). Here it should be noted in Equation (C.5), the following assumption has been made:

$$\rho(s)\frac{\partial}{\partial s}u(s,t)>>u(s,t)\frac{\partial}{\partial s}\rho(s) \tag{C.6}$$

APPENDIX D:

Shape function for curved beam model (Case 2)

Based on Equation (2.19), one can easily obtain the following equations:

$$du(\eta)/d\eta = C_1 + 2C_2\eta + 3C_3\eta^2 + 4C_4\eta^3 + 5C_5\eta^4 \tag{D.1}$$

$$d^2u(\eta)/d\eta^2 = 2C_2 + 6C_3\eta + 12C_4\eta^2 + 20C_5\eta^3 \tag{D.2}$$

Then utilizing Equations (2.19), (2.20), (D.1) and (D.2), the deflection of nodes i and j can be expressed as:

$$\{U_i \quad W_i \quad \Psi_i \quad U_j \quad W_j \quad \Psi_j\}^T = [NC]\{C_0 \quad C_1 \quad C_2 \quad C_3 \quad C_4 \quad C_5\}^T \tag{D.3}$$

Finally the shape function $[NN]$ can be obtained through:

$$[NN] = \{1 \quad \eta \quad \eta^2 \quad \eta^3 \quad \eta^4 \quad \eta^5\} \times [NC]^{-1} \tag{D.4}$$

Here it should be noted that for circular beams, as the radius $\rho(\eta)$ and the Jacobian $\bar{J}_c(\eta)$ is constant in one element, the matrix $[NC]$, as shown in Equations (D.3) and (D.4) is identical. However for non-circular beams, the radius $\rho(\eta)$ and Jacobian $\bar{J}_c(\eta)$ are related to the geometrical coordinate properties, thus the matrix $[NC]$ is also related to η. This is one of the challengers of the proposed methodology and has been successfully solved through the Gauss Quadrate technique, in which only the parameters of the Gaussian point would be evaluated, thus the whole procedure can be summarized as: the radius and Jacobian in Gaussian points would be evaluated, and then substituted to Equations (D.3) and (D.4) to obtain the shape function in one Gaussian points, finally, one can obtain the mass and stiffness matrices for one element.

APPENDIX E:

Equations of motion in finite element form for curved beam model (Case 2)

The governing differential equations of motion as stated in Equations (2.15) and (2.16)

$$\underbrace{m(s)\frac{\partial^2 w(s,t)}{\partial t^2}}_{Part1}+\underbrace{\frac{\partial^2}{\partial s^2}\left\{EI(s)\frac{\partial^2 w(s,t)}{\partial s^2}\right\}}_{Part2}-\underbrace{\frac{\partial^2}{\partial s^2}\left(\frac{EI(s)}{\rho(s)}\frac{\partial u(s,t)}{\partial s}\right)}_{Part3}=0 \tag{E.1}$$

$$\underbrace{m(s)\frac{\partial^2 u(s,t)}{\partial t^2}}_{Part4}+\underbrace{\frac{\partial}{\partial s}\left(\frac{EI(s)}{\rho(s)}\frac{\partial^2 w(s,t)}{\partial s^2}\right)}_{Part5}-\underbrace{\frac{\partial}{\partial s}\left(\frac{EI(s)}{\rho^2(s)}\frac{\partial u(s,t)}{\partial s}\right)}_{Part6}=0 \tag{E.2}$$

Substituting the deformation relationship $w(s)=-\rho(s)\partial u(s)/\partial s$ in Table 2.1 for Case 2, and applying the Galerkin weighted residual technique, the following expressions for each part shown in Equations (E.1) and (E.2) can be obtained: Here, for simplifying the expression, in the following equations, the parts related to the boundary conditions have been cancelled.

For *Part 1*

$$\begin{aligned}&\int_L \delta w(s,t)m(s)\frac{\partial^2 w(s,t)}{\partial t^2}ds=\int_L\{-\rho(s)\frac{\partial}{\partial s}\delta u(s,t)m(s)(-\rho(s)\frac{\partial^3 u(s,t)}{\partial t^2\partial s})\}ds\\&=\sum_{element}\delta^T\{q\}\int_{-1}^{1}\left\{(-\rho(\eta)\frac{d[NN(\eta)]^T}{\bar{J}_c(\eta)d\eta})\gamma A(\eta)(-\rho(\eta)\frac{d[NN(\eta)]}{\bar{J}_c(\eta)d\eta})\right\}\bar{J}_c(\eta)d\eta\{q\}\ddot{g}(t)\end{aligned} \tag{E.3}$$

For *Part 2*

$$\begin{aligned}&\int_L \delta w(s,t)\frac{\partial^2}{\partial s^2}\left\{EI(s)\frac{\partial^2 w(s,t)}{\partial s^2}\right\}ds\cong\int_L\frac{\partial^2\delta w(s,t)}{\partial s^2}EI(s)\frac{\partial^2 w(s,t)}{\partial s^2}ds\\&=\int_L\{-\rho(s)\frac{\partial^3\delta u(s,t)}{\partial s^3}EI(s)(-\rho(s)\frac{\partial^3 u(s,t)}{\partial s^3})\}ds\\&=\sum_{element}\delta^T\{q\}\int_{-1}^{1}\left\{(-\rho(\eta)\frac{d^3[NN(\eta)]^T}{\bar{J}_c{}^3(\eta)d\eta^3})EI(\eta)(-\rho(\eta)\frac{d^3[NN(\eta)]}{\bar{J}_c{}^3(\eta)d\eta^3})\right\}\bar{J}_c(\eta)d\eta\{q\}g(t)\end{aligned} \tag{E.4}$$

For *Part 3*

$$\int_L \delta w(s,t)(-\frac{\partial^2}{\partial s^2}(\frac{EI(s)}{\rho(s)}\frac{\partial u(s,t)}{\partial s}))ds \cong \int_L \frac{\partial^2 \delta w(s,t)}{\partial s^2}(-\frac{EI(s)}{\rho(s)}\frac{\partial u(s,t)}{\partial s}))ds = \int_L \{-\rho(s)\frac{\partial^3 \delta u(s,t)}{\partial s^3}(-\frac{EI(s)}{\rho(s)}\frac{\partial u(s,t)}{\partial s}))\}ds$$
$$= \sum_{element} \delta^T\{q\} \int_{-1}^{1} \left\{(-\rho(\eta)\frac{d^3[NN(\eta)]^T}{\bar{J}_c{}^3(\eta)d\eta^3})(-\frac{EI(\eta)}{\rho(\eta)})(\frac{d[NN(\eta)]}{\bar{J}_c(\eta)d\eta})\right\}\bar{J}_c(\eta)d\eta\{q\}g(t) \tag{E.5}$$

For *Part 4*

$$\int_L \delta u(s,t)m(s)\frac{\partial^2 u(s,t)}{\partial t^2}ds = \sum_{element} \delta^T\{q\} \int_{-1}^{1} \{[NN(\eta)]^T \gamma A(\eta)[NN(\eta)]\}\bar{J}_c(\eta)d\eta\{q\}\ddot{g}(t) \tag{E.6}$$

For *Part 5*

$$\int_L \delta u(s,t)\frac{\partial}{\partial s}(\frac{EI(s)}{\rho(s)}\frac{\partial^2 w(s,t)}{\partial s^2})ds \cong -\int_L \frac{\partial}{\partial s}\delta u(s,t)\frac{EI(s)}{\rho(s)}\frac{\partial^2 w(s,t)}{\partial s^2}ds = -\int_L \frac{\partial}{\partial s}\delta u(s,t)\frac{EI(s)}{\rho(s)}(-\rho(s)\frac{\partial^3 u(s,t)}{\partial s^3})ds$$
$$= \sum_{element} \delta^T\{q\} \int_{-1}^{1} \left\{-(\frac{d[NN(\eta)]^T}{\bar{J}_c(\eta)d\eta})\frac{EI(\eta)}{\rho(\eta)}(-\rho(\eta)\frac{d^3[NN(\eta)]}{\bar{J}_c{}^3(\eta)d\eta^3})\right\}\bar{J}_c(\eta)d\eta\{q\}g(t) \tag{E.7}$$

For *Part 6*

$$\int_L \delta u(s,t)\frac{\partial}{\partial s}(-\frac{EI(s)}{\rho^2(s)}\frac{\partial u(s,t)}{\partial s})ds \cong \int_L \frac{\partial}{\partial s}\delta u(s,t)\frac{EI(s)}{\rho^2(s)}\frac{\partial u(s,t)}{\partial s}ds$$
$$= \sum_{element} \delta^T\{q\} \int_{-1}^{1} \left\{(\frac{d[NN(\eta)]^T}{\bar{J}_c(\eta)d\eta})\frac{EI(\eta)}{\rho^2(\eta)}\frac{d[NN(\eta)]}{\bar{J}_c(\eta)d\eta}\right\}\bar{J}_c(\eta)d\eta\{q\}g(t) \tag{E.8}$$

where $A(\eta)$= $[N(\eta)]\{A\}$, $I(\eta)$= $[N(\eta)]\{I\}$. The shape function $N(\eta)$ and $NN(\eta)$ and Jacobian matrix $\bar{J}_c(\eta)$ have been defined in Equations (2.10), (2.21) and (B.10), respectively. Then combining Equations (E.3)-(E.8) together one can easily obtain the equations of motion in finite element form, as stated in Equations (2.21)-(2.24). Here it should be noted that the derivative procedure are based on the same assumption, as stated in Equation (C.6).

APPENDIX F:

Sub-matrices in Equations (3.7)

$$[C_{wTMD}]=[N(\eta_{TMD})]^T C_{TMD}[N(\eta_{TMD})] \tag{F.1}$$

$$[K_{wTMD}]=[N(\eta_{TMD})]^T K_{TMD}[N(\eta_{TMD})] \tag{F.2}$$

$$[C_{zTMD}]=[N(\eta_{TMD})]^T C_{TMD} \tag{F.3}$$

$$[K_{zTMD}]=[N(\eta_{TMD})]^T K_{TMD} \tag{F.4}$$

$$[C_{ww}]=\sum_{element}\left\{\int_{-1}^{1}\left[C[N(\eta)]^T[N(\eta)]\bar{J}(\eta)\right]d\eta\right\} \tag{F.5}$$

where η_{TMD} represents the position of attached TMD system in the natural coordinate. Therefore, utilizing η_{TMD}, one can easily extend the study to multiple Tuned Mass Damper (TMD) condition. $N(\eta)$ represents the shape function, which was defined in Equation (2.3).

APPENDIX G:

Derivative procedure for Equation (3.13)

The equations of motion in state-space form, as shown in Equation (3.10), can be expressed:

$$\{\dot{z}(t)\}+[A_s]\{z(t)\}=\{Q(t)\} \tag{G.1}$$

Post-multiplying $\{z(s)\}^T$, and then taking the expect value for Equation (G.1), one can easily obtain:

$$C_{\dot{z}z}(t,s)+[A_s]C_{zz}(t,s)=C_{Qz}(t,s) \tag{G.2}$$

where Symbol $C_{..}$ represent the autocorrelation, and they are defined as:

$$C_{\dot{z}z}(t,s)=E[\dot{z}(t)z^T(s)],\ C_{zz}(t,s)=E[z(t)z^T(s)] \text{ and } C_{QQ}(t,s)=E[Q(t)Q^T(s)] \tag{G.3}$$

It should be noted that in this dissertation autocorrelation is equal to the autocovariance, as the mean value is assume to be zero. One can utilize the symmetry property of the autocorreleaton function, or pre-multiplying $\{z(s)\}$ to the transpose of Equation (G.1), to obtain:

$$C_{z\dot{z}}(s,t)+C_{zz}(s,t)[A_s]^T=C_{zQ}(s,t) \tag{G.4}$$

Adding Equations (G.2) and (G.4) together as:

$$C_{z\dot{z}}(s,t)+C_{\dot{z}z}(t,s)+C_{zz}(s,t)[A_s]^T+[A_s]C_{zz}(t,s)=C_{zQ}(s,t)+C_{Qz}(t,s) \tag{G.5}$$

Now, let us focus on the right part of Equation (G.5), and considering the general solution of Equation (G.1) can be expressed as:

$$\{z(t)\}=\{z(t_0)\}+\int_{t0}^{t}\{Q(u)\}du-[A_s]\int_{t_0}^{t}\{z(u)\}du \tag{G.6}$$

Again, pre-mutiplying $\{Q(t)\}$ to the transpose of Equation (G.6), one can obtain:

$$C_{Qz}(s,t) = C_{Qz}(s,t_0) + \int_{t0}^{t} C_{QQ}(s,u)du - \int_{t_0}^{t} C_{Qz}(s,u)du[A_s]^T \tag{G.7}$$

Here, $\{z(t_0)\}$ represents the initial response, and obviously it is un-correlated with the $\{Q(t)\}$, which represents the force at time t after t_0. The same analytical methodology can be applied the last part of Equation (G.7), in which s represent the time after t. Therefore Equation (G.7) can be simplified as:

$$C_{Qz}(s,t) = \int_{t0}^{t} C_{QQ}(s,u)du \tag{G.8}$$

Again, following the same methodology, as the derivate procedure for Equation (G.8) or utilizing the symmetry property of the autocorrelation function, one can also obtain:

$$C_{zQ}(t,s) = \int_{t0}^{s} C_{QQ}(t,v)dv \tag{G.9}$$

Then, substituting Equations (G.8) and (G.9) to Equation (G.5), it may be obtained:

$$C_{z\dot{z}}(s,t) + C_{\dot{z}z}(t,s) + C_{zz}(s,t)[A_s]^T + [A_s]C_{zz}(t,s) = \int_{t0}^{t} C_{QQ}(s,u)du + \int_{t0}^{s} C_{QQ}(t,v)dv \tag{G.10}$$

Assuming the autocorrelation function for a random excitation can be expressed in a general form as:

$$C_{QQ}(u,v) = 2\pi S_0(u)\delta(u-v) \tag{G.11}$$

The following equation can be obtained through integrating Equation (G.11) for $t > s > t_0$:

$$\int_{t_0}^{t}\int_{t_0}^{s} C_{QQ}(u,v)dvdu = 2\pi \int_{t_0}^{t} S_0(u)H(u-s)du = 2\pi \int_{t_0}^{t} S_0(u)du \tag{G.12}$$

Now differentiating Equation (G.12) for both t and s, one can obtain:

$$\int_{t_0}^{t} C_{QQ}(s,u)du + \int_{t_0}^{s} C_{QQ}(v,t)dv = 2\pi S_0(t) \tag{G.13}$$

Next, let us focus on the left side of Equation (G.10), and take the derivative of autocolleration $C_{zz}(t,s)$, one can obtain:

$$\frac{d}{dt}C_{zz}(t,s) = C_{\dot{z}z}(t,s) + C_{z\dot{z}}(s,t) \tag{G.14}$$

Now, substituting Equations (G.13) and (G.14) to Equation (G.10), one may obtain:

$$\frac{d}{dt}C_{zz}(t,s) + C_{zz}(s,t)[A_s]^T + [A_s]C_{zz}(t,s) = 2\pi S_0(t) \tag{G.15}$$

For a stationary random process, the correlation is only depended on the time interval between t and s. Furthermore let us assuming the excitation is a whiter noise with Power Spectrum density (PSD) function S_0, and autocolleration function of a white noise is $2\pi S_0\delta(t)$. Finally Equation (G.15) can be simplified as:

$$C_{zz}[A_s]^T + [A_s]C_{zz} = 2\pi S_0 \tag{G.16}$$

APPENDIX H:

Sub-matrices in Equations (4.4)

$$[K_{wwTi}] = \left[[N(\eta)]^T [N(\eta)] K_{TMD} \cos^2(\alpha(\eta))\right]_{\eta=\eta_{TMDi}} \tag{H.1}$$

$$[K_{wuTi}] = \left[[N(\eta)]^T [N(\eta)] K_{TMD} \cos(\alpha(\eta)) \sin(\alpha(\eta))\right]_{\eta=\eta_{TMDi}} \tag{H.2}$$

$$[K_{uuTi}] = \left[[N(\eta)]^T [N(\eta)] K_{TMD} \sin^2(\alpha(\eta))\right]_{\eta=\eta_{TMDi}} \tag{H.3}$$

$$[K_{uzi}] = -\left[[N(\eta)]^T K_{TMD} \sin(\alpha(\eta))\right]_{\eta=\eta_{TMDi}} \tag{H.4}$$

$$[K_{wzi}] = -\left[[N(\eta)]^T K_{TMD} \cos(\alpha(\eta))\right]_{\eta=\eta_{TMDi}} \tag{H.5}$$

$$[C_{ww}] = \sum_{element} \int_{-1}^{1} C_w [N(\eta)]^T [N(\eta)] \bar{J}_c(\eta) d\eta \tag{H.6}$$

$$[C_{uu}] = \sum_{element} \int_{-1}^{1} C_u [N(\eta)]^T [N(\eta)] \bar{J}_c(\eta) d\eta \tag{H.7}$$

$$[C_{wwTi}] = \left[[N(\eta)]^T [N(\eta)] C_{TMD} \cos^2(\alpha(\eta))\right]_{\eta=\eta_{TMDi}} \tag{H.8}$$

$$[C_{wuTi}] = \left[[N(\eta)]^T [N(\eta)] C_{TMD} \cos(\alpha(\eta)) \sin(\alpha(\eta))\right]_{\eta=\eta_{TMDi}} \tag{H.9}$$

$$[C_{uuTi}] = \left[[N(\eta)]^T [N(\eta)] C_{TMD} \sin^2(\alpha(\eta))\right]_{\eta=\eta_{TMDi}} \tag{H.10}$$

$$[C_{uzi}] = -\left[[N(\eta)]^T C_{TMD} \sin(\alpha(\eta))\right]_{\eta=\eta_{TMDi}} \tag{H.11}$$

$$[C_{wzi}] = -\left[[N(\eta)]^T C_{TMD} \cos(\alpha(\eta))\right]_{\eta=\eta_{TMDi}} \tag{H.12}$$

where $\cos(\alpha(\eta))$ and $\sin(\alpha(\eta))$ can be evaluated through

$$\cos(\alpha(\eta_{TMDi})) = [B(\eta_{TMDi})]\{X\} / \bar{J}_c(\eta_{TMDi}) \tag{H.13}$$

$$\sin(\alpha(\eta_{TMDi})) = [B(\eta_{TMDi})]\{Y\} / \bar{J}_c(\eta_{TMDi}) \tag{H.14}$$

APPENDIX I:

Curved beam mid-span tangential displacement (u) and rotation (ψ) response comparison

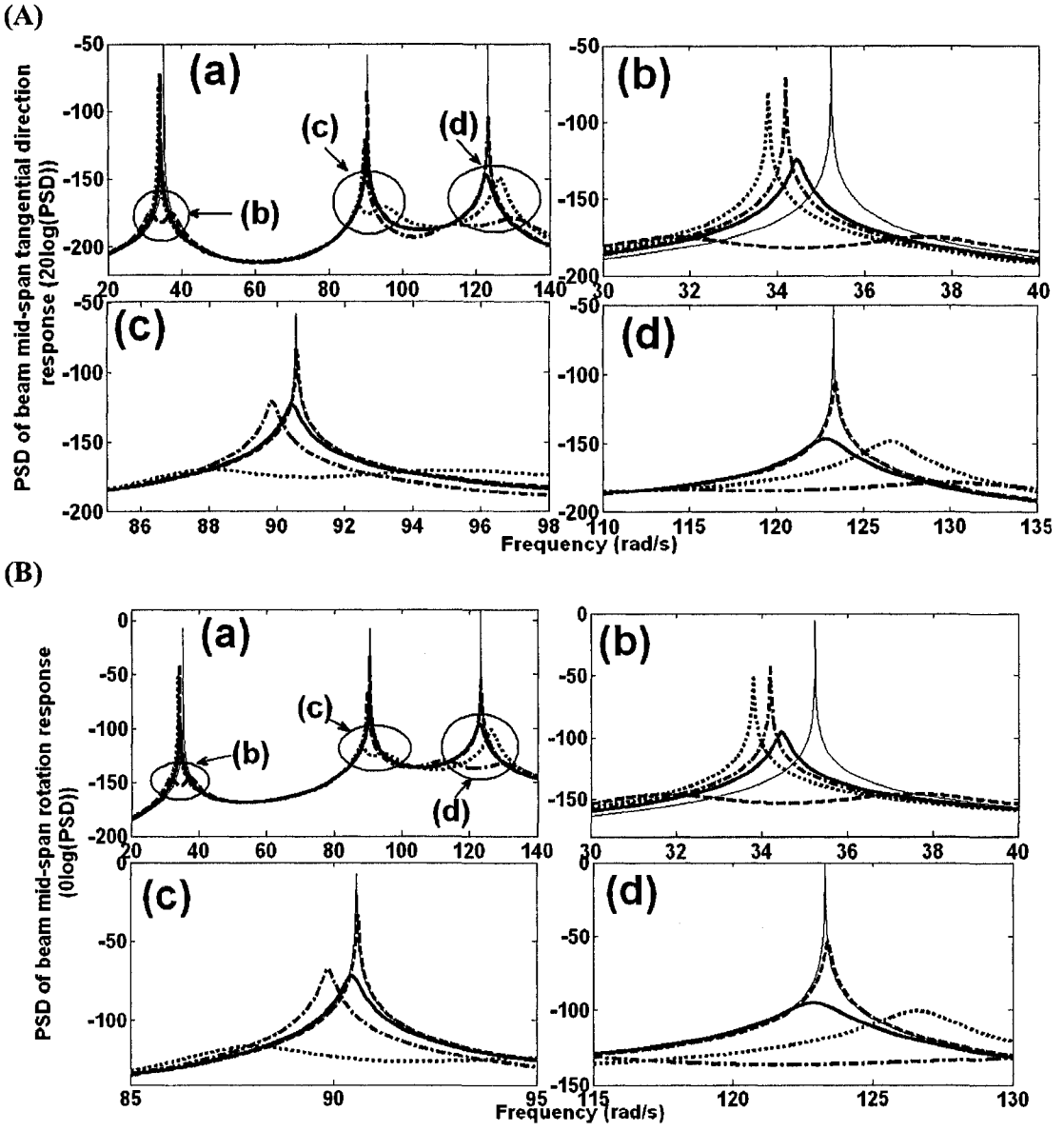

Figure I.1 Beam mid-span response. (A) Tangential displacement (u). (B) Rotation (ψ). (a) Frequency range 20-140 (*rad/s*). (b) Around the 2nd natural frequency. (c) Around the 4th natural frequency. (d) Around the 5th natural frequency. Solid (light), dashed, dotted, dashed-dotted and solid lines represent uncontrolled structure, structure with optimal TMD Case a in Table 4.4, Case b in Table 4.6, Case c in Table 4.5 and Case d in Table 4.4, respectively.

APPENDIX J:

Response comparison and sensitivity analysis for optimal DTMD based on 2nd mode

(A)

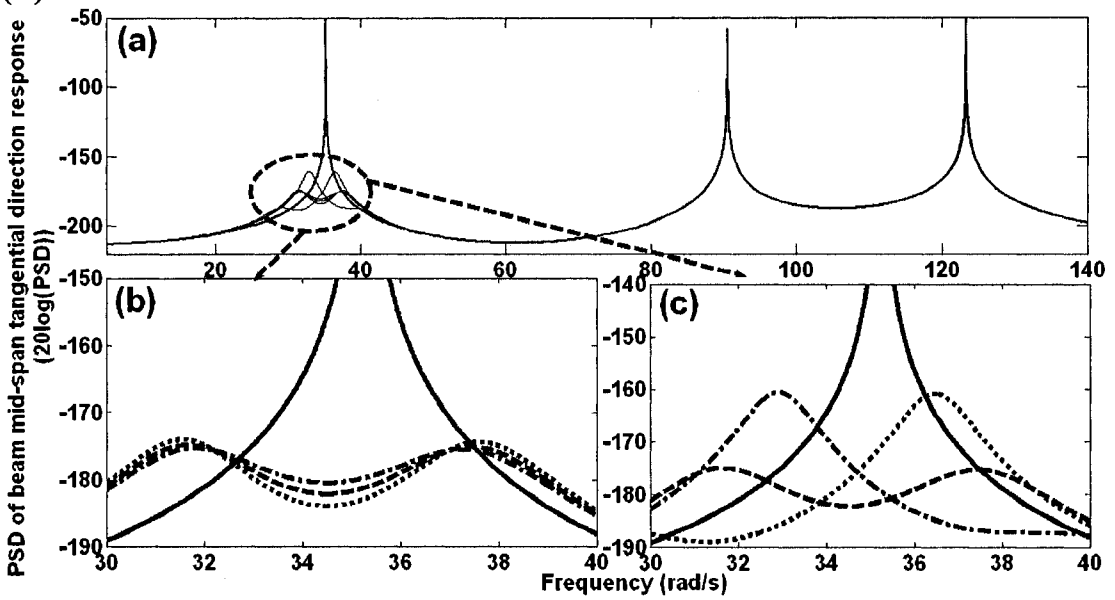

(B)

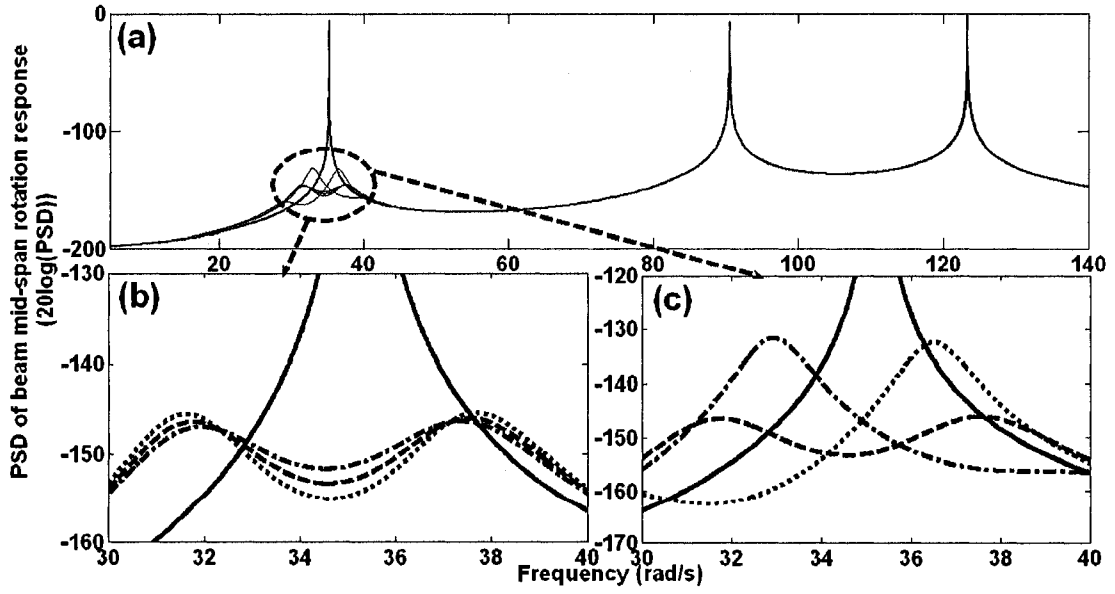

Figure J.1 The curved beam's response comparison. (A) Tangential displacement (u). (B) Rotation (ψ). (a) Frequency range 5-140 (*rad/s*). (b) Sensitivity analysis for optimal damping factor. (c) Sensitivity analysis for optimal frequency ratio. Solid, dashed, dotted and dashed-dotted lines represent uncontrolled structure, structure with optimal DTMD, as stated in Table 4.9, structure with DTMD having -10% and +10% deviations from designed optimal values, respectively.

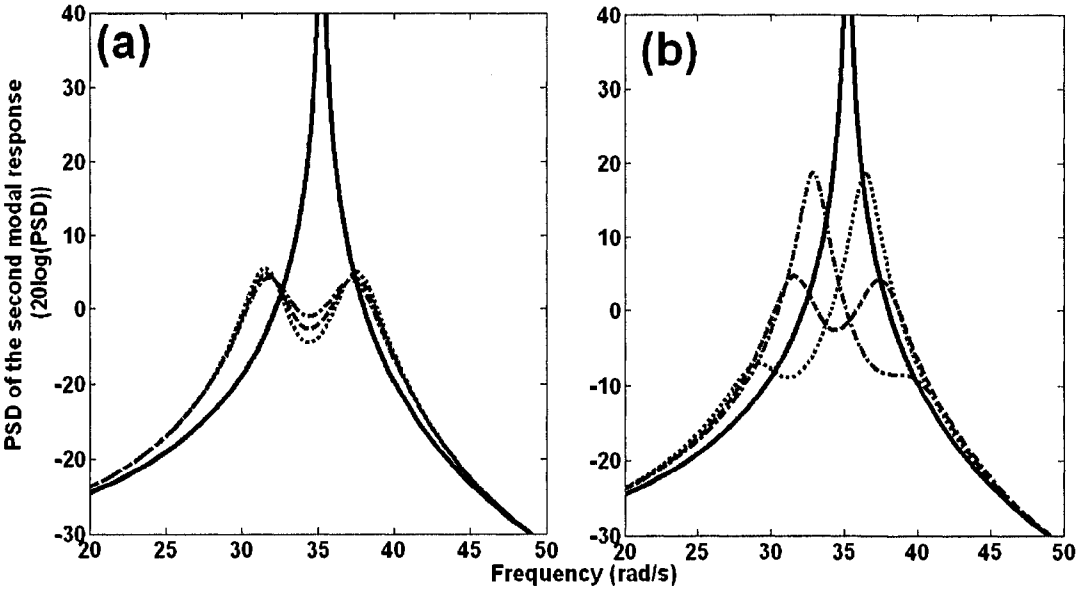

Figure J.2 The curved beam's 2nd vibration modal response comparison. (a) Sensitivity analysis for optimal damping factor. (b) Sensitivity analysis for optimal frequency ratio. Solid, dashed, dotted and dashed-dotted lines represent uncontrolled structure, structure with optimal DTMD, as stated in Table 4.9, structure with DTMD having -10% and +10% deviations from designed optimal values, respectively.

APPENDIX K:

Response comparison and sensitivity analysis for optimal DTMD based on 4th mode

(A)

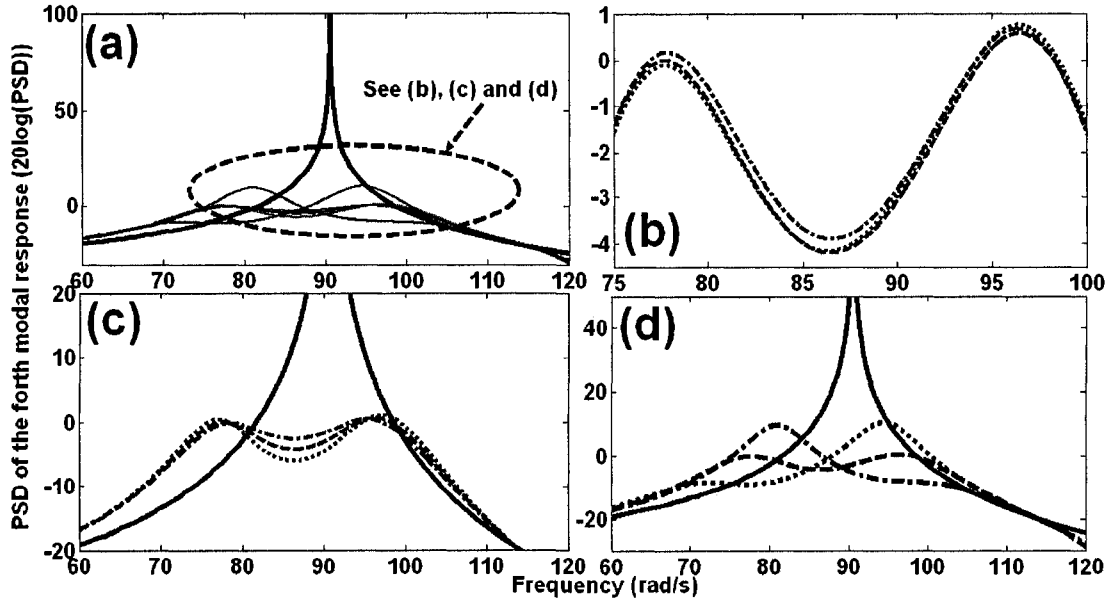

(B)

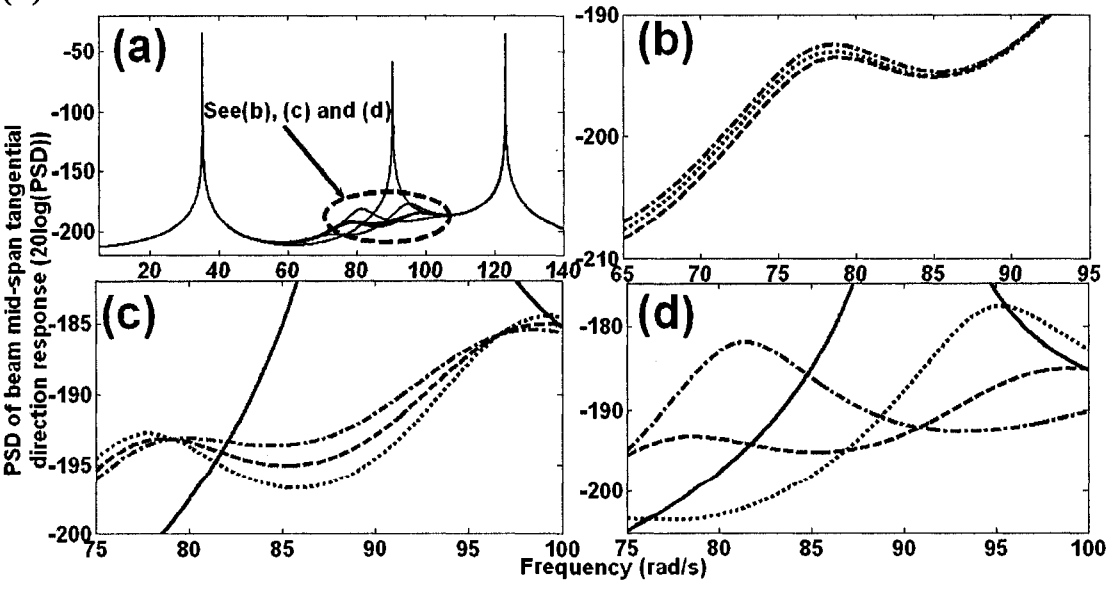

(C)

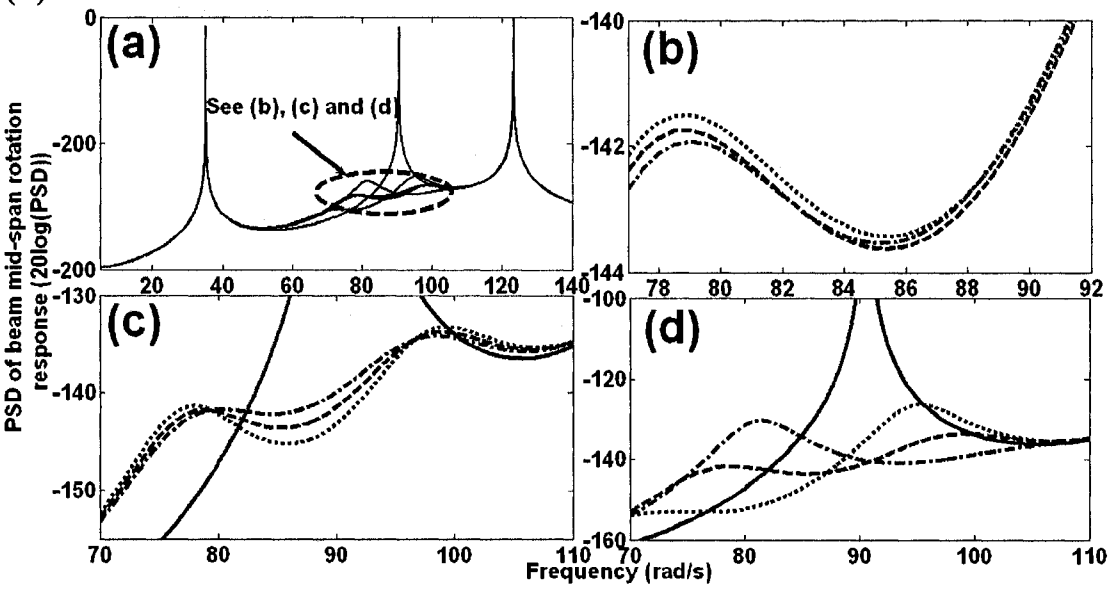

Figure K.1 PSD of the curved beam's response comparison. (A) The 4th mode. (B) Tangential displacement (u). (C) Rotation (ψ). (a) Sensitivity analysis for optimal damping factor. (b) Sensitivity analysis for optimal frequency ratio. Solid, dashed, dotted and dashed-dotted lines represent uncontrolled structure, structure with optimal DTMD, as stated in Table 4.11, structure with DTMD having -10% and +10% deviations from designed optimal values, respectively.

APPENDIX L:

Response comparison and sensitivity analysis for optimal two symmetrical DTMD based on 5th mode

(A)

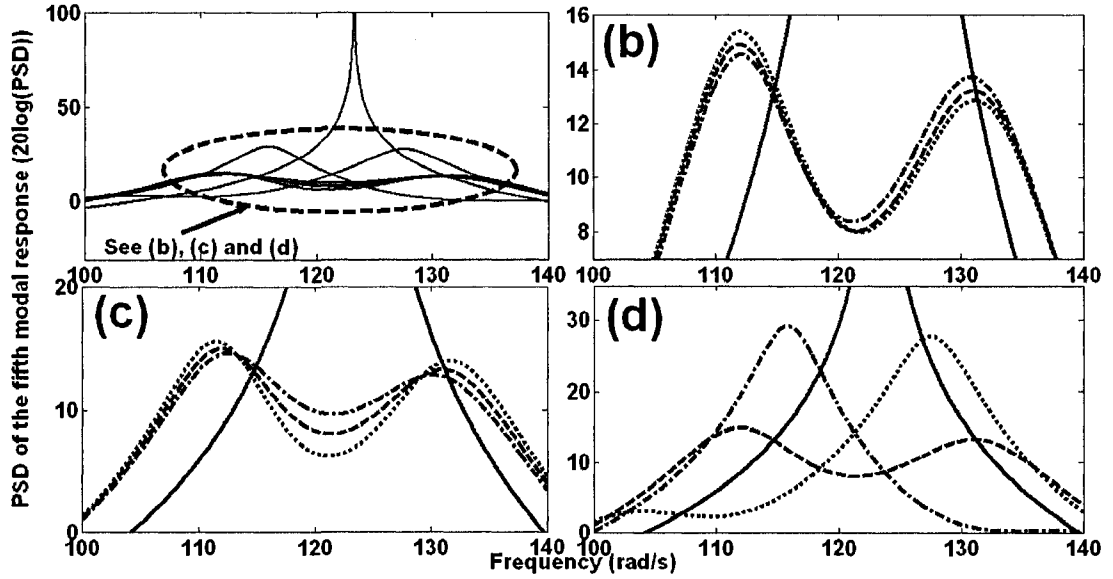

(B)

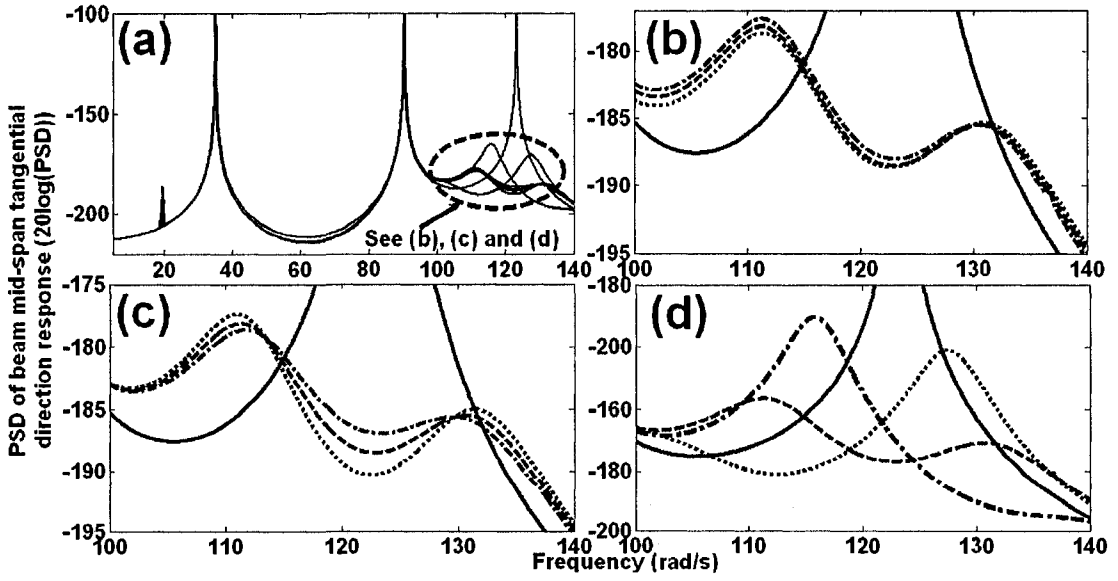

(C)

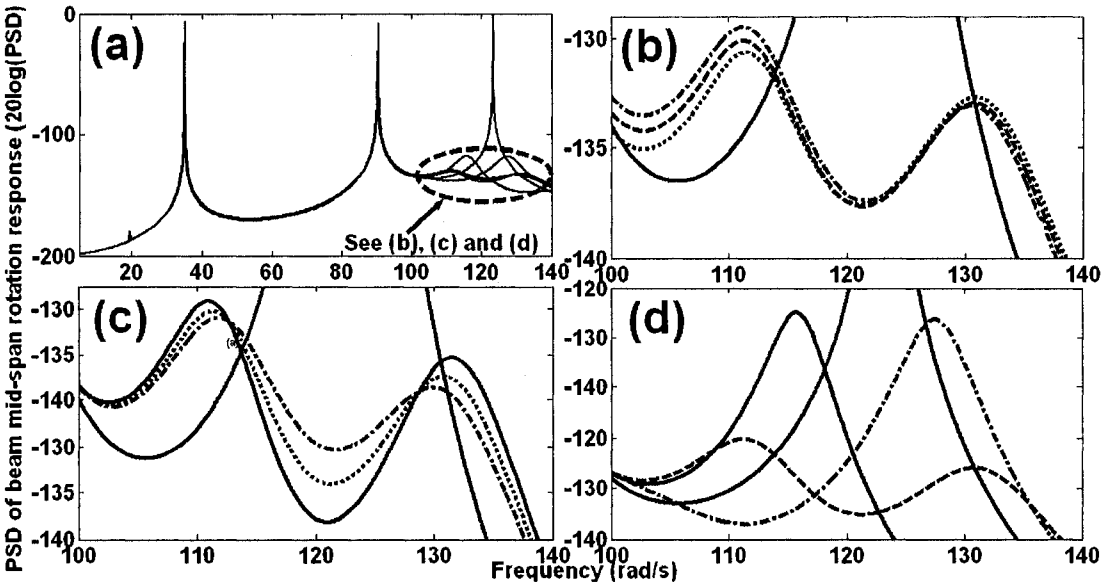

Figure L.1 PSD of curved beam's response comparison. (A) The 5th mode. (B) Tangential displacement (u). (C) Rotation (ψ). (a) Sensitivity analysis for optimal damping factor. (b) Sensitivity analysis for optimal frequency ratio. Solid, dashed, dotted and dashed-dotted lines represent uncontrolled structure, structure with optimal DTMD, as stated in Table 4.13, structure with DTMD having -10% and +10% deviations from designed optimal values, respectively.

APPENDIX M:

Response comparison and sensitivity analysis for optimal three DTMD design method (1) based on 5th mode.

(A)

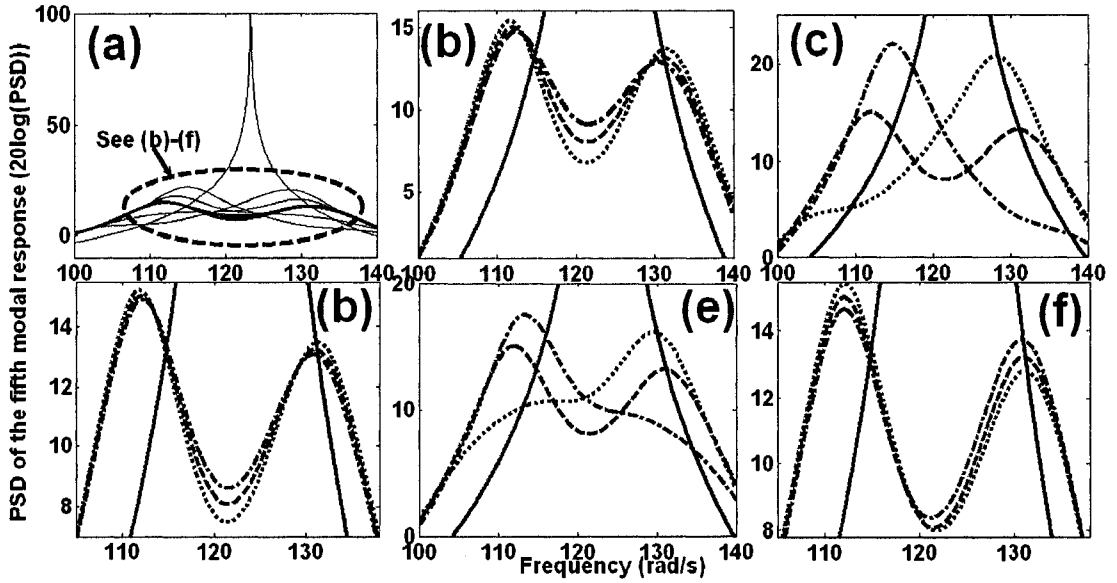

(B)

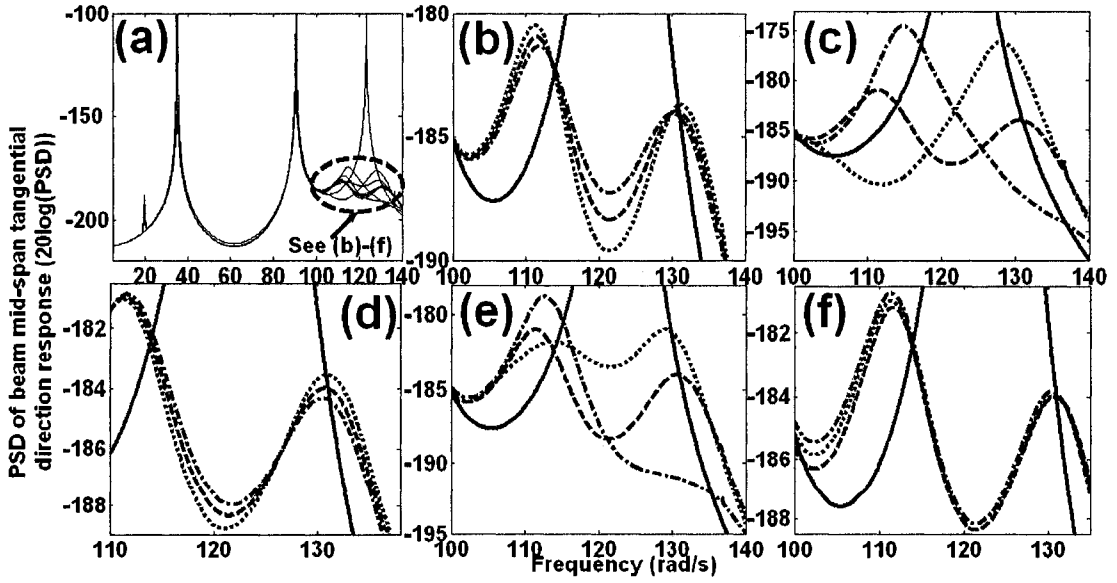

(C))

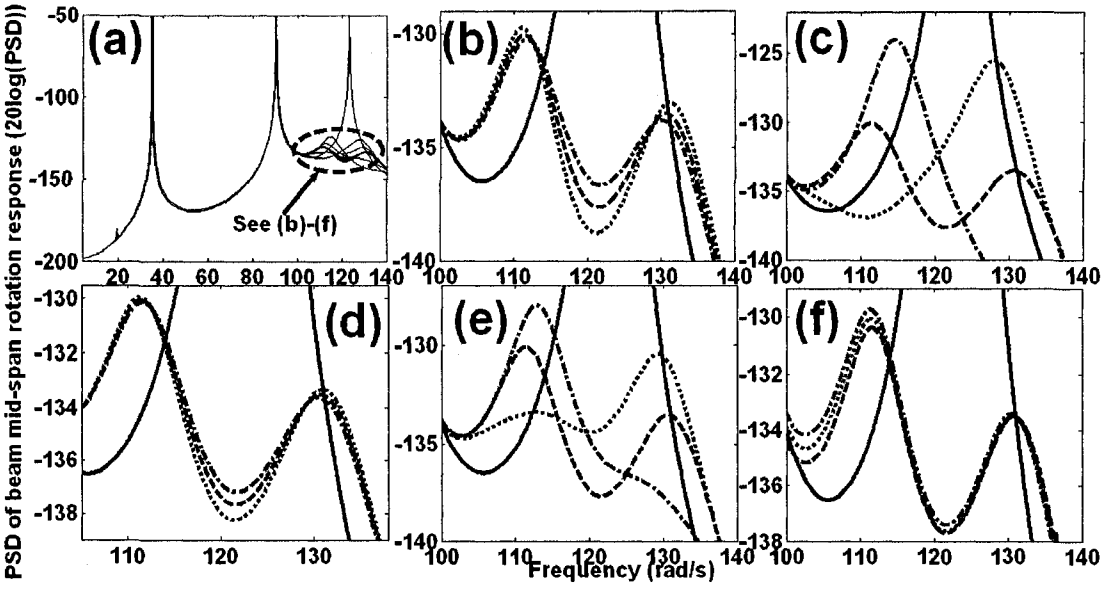

Figure M.1 PSD of curved beam's response comparison for three DTMD design Method (1) with mass ratio (μ) 0.005 for each TMD. (A) The 5th mode. (B) Tangential displacement (u). (C) Rotation (ψ). (a) Frequency range 5-140 (*rad/s*). (b) Sensitivity analysis for optimal damping factor for the two symmetrical TMD. (c) Sensitivity analysis for optimal frequency ratio for the two symmetrical TMD. (d) Sensitivity analysis for optimal damping factor for the mid-span TMD. (e) Sensitivity analysis for optimal frequency ratio for the mid-span TMD. (f) Sensitivity analysis for optimal position for the two symmetrical TMD. Solid, dashed, dotted and dashed-dotted lines represent uncontrolled structure, structure with optimal DTMD, as stated in Table 4.15, structure with DTMD having -10% (-0.1) and +10% (+0.1) deviations from designed optimal values, respectively.

APPENDIX N:

Response comparison and sensitivity analysis for optimal three DTMD design method (2) based on 5th mode

(A)

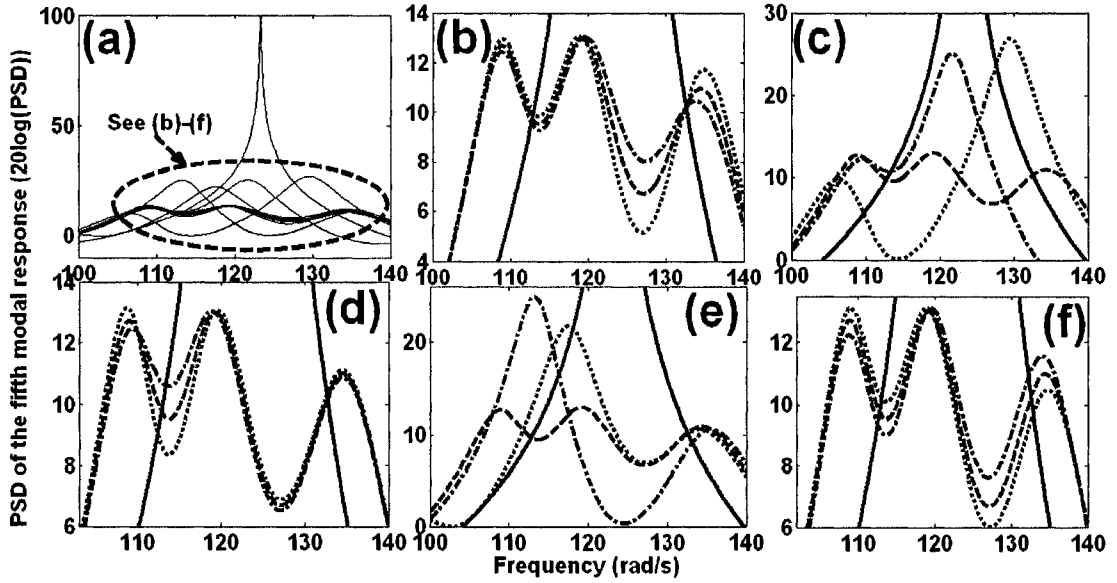

(B

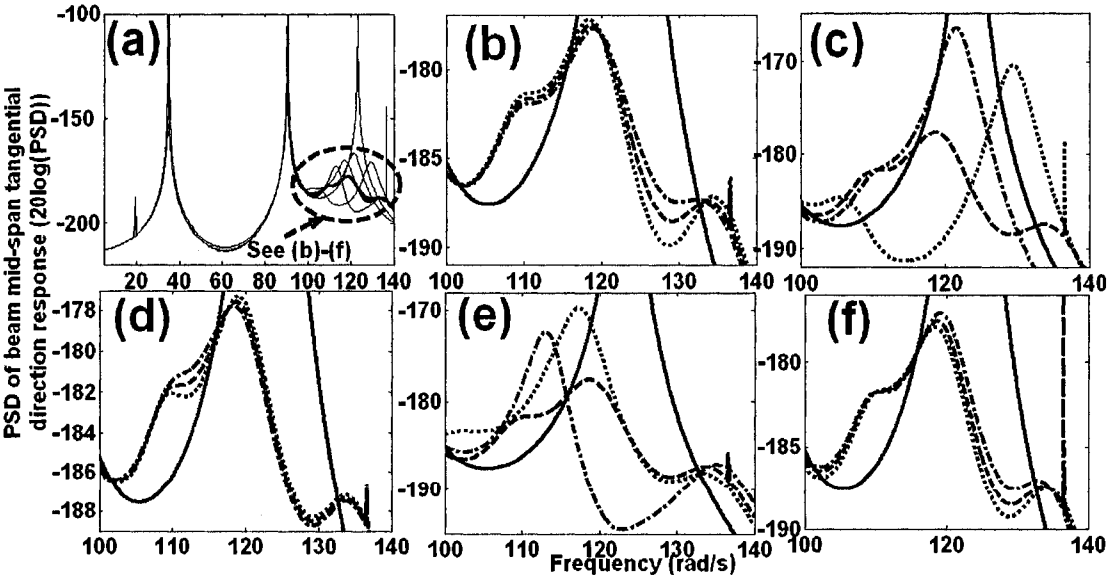

(C))

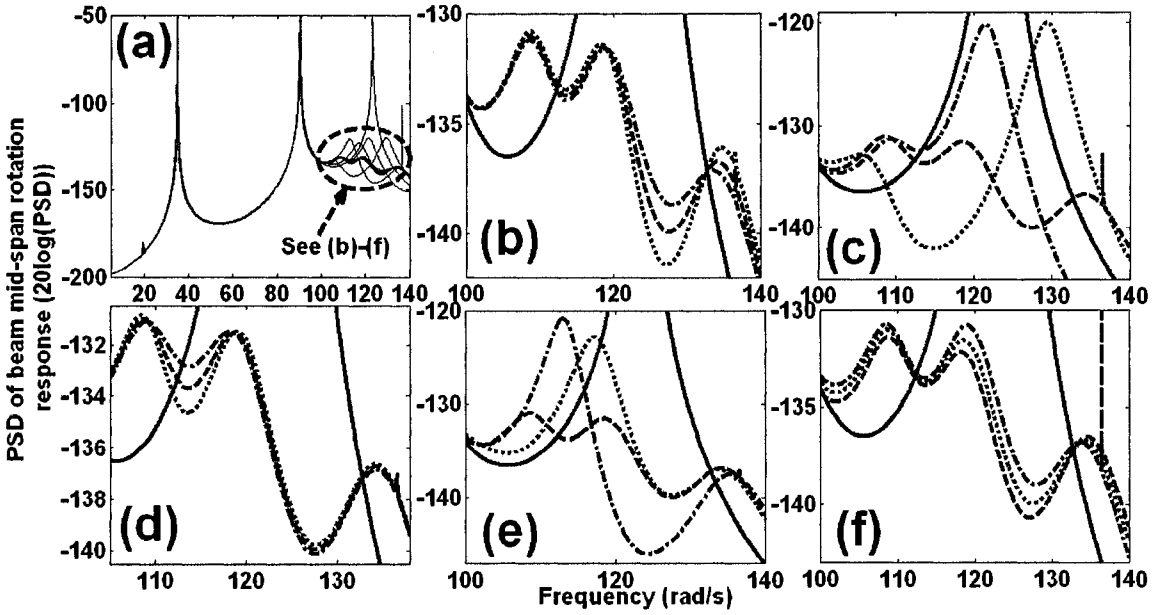

Figure N.1 PSD of curved beam's response comparison) for three DTMD design Method (2) with mass ratio (μ) 0.005 for each TMD. (A) The 5th mode. (B) Tangential displacement (*u*). (C) Rotation (*ψ*). (a) Response in 5-140 (*rad/s*) frequency range. (b) Sensitivity analysis for optimal damping factor for the two symmetrical TMD. (c) Sensitivity analysis for optimal frequency ratio for the two symmetrical TMD. (d) Sensitivity analysis for optimal damping factor for the mid-span TMD. (e) Sensitivity analysis for optimal frequency ratio for the mid-span TMD. (f) Sensitivity analysis for optimal position for the two symmetrical TMD. Solid, dashed, dotted and dashed-dotted lines represent uncontrolled structure, structure with optimal DTMD, as stated in Table 4.18, structure with DTMD having -10% (-0.1) and +10% (+0.1) deviations from designed optimal values, respectively.